GENERAL ATOMIC

GA-A14046
UC-77

HTGR FUELS AND CORE DEVELOPMENT PROGRAM

QUARTERLY PROGRESS REPORT FOR THE PERIOD ENDING AUGUST 31, 1976

Prepared under
Contract E(04-3)-167
Project Agreement No. 17
for the San Francisco Operations Office
U.S. Energy Research and Development Administration

GENERAL ATOMIC PROJECT 3224 DATE PUBLISHED: SEPTEMBER 24, 1976

DISCLAIMER

QUARTERLY REPORT SERIES

GA-4072-December, 1962, through February, 1963
GA-4350-March, 1963, through May, 1963
GA-4569-June, 1963, through August, 1963
GA-4937-September, 1963, through November, 1963
GA-5104-December, 1963, through February, 1964
GA-5366-March, 1964, through May, 1964
GA-5618-June, 1964, through August, 1964
GA-5866-September, 1964, through November, 1964
GA-6113-December, 1964, through February, 1965
GA-6418-March, 1965, through May, 1965
GA-6671-June, 1965, through August, 1965
GA-6869-September, 1965, through November, 1965
GA-7010-December, 1965, through February, 1966
GA-7181-March, 1966, through May, 1966
GA-7396-June, 1966, through August, 1966
GA-7553-September, 1966, through November, 1966
GA-7801-December, 1966, through February, 1967
GA-7981-March, 1967, through May, 1967
GA-8200-June, 1967, through August, 1967
GA-8356-September, 1967, through November, 1967
GA-8530-December, 1967, through February, 1968
GA-8662-March, 1968, through May, 1968
GA-8860-June, 1968, through August, 1968
GA-9090-September, 1968, through November, 1968
GA-9227-December, 1968, through February, 1969
GA-9372-March, 1969, through May, 1969
GA-9660-June, 1969, through August, 1969
GA-9815-September, 1969, through November, 1969
GA-9944-December, 1969, through February, 1970
GA-10088-March, 1970, through May, 1970
GA-10288-June, 1970, through August, 1970
GA-10399-September, 1970, through November, 1970
GA-10501-December, 1970, through February, 1971
GA-10661-March, 1971, through May, 1971
Gulf-GA-A10784-June, 1971, through August, 1971
Gulf-GA-A10930-September, 1971, through November, 1971
Gulf-GA-A10999-December, 1971, through February, 1972
Gulf-GA-A12150-March, 1972, through May, 1972
Gulf-GA-A12222-June, 1972, through August, 1972
Gulf-GA-A12422-September, 1972, through November, 1972
Gulf-GA-A12515-December, 1972, through February, 1973
Gulf-GA-12599-March, 1973, through May, 1973
Gulf-GA-A12725-June, 1973, through August, 1973
Gulf-GA-A12818-September, 1973, through November, 1973
GA-A12916-December, 1973, through February, 1974
GA-A13030-March, 1974, through May, 1974
GA-A13126-June, 1974, through August, 1974
GA-A13253-September, 1974, through November, 1974
GA-A13353-December, 1974, through February, 1975
GA-A13444-March, 1975, through May, 1975
GA-A13592-June, 1975, through August, 1975
GA-A13737-September, 1975, through November, 1975
GA-A13804-December, 1975, through February, 1976
GA-A13941-March, 1976, through May, 1976

ABSTRACT

This publication continues the quarterly report series on the HTGR Fuels and Core Development Program. The Program covers items of the base technology of the High-Temperature Gas-Cooled Reactor (HTGR) system. The development of the HTGR system will, in part, meet the greater national objective of more effective and efficient utilization of our national resources. The work reported here includes studies of reactions between core materials and coolant impurities, basic fission product transport mechanisms, core graphite development and testing, the development and testing of recyclable fuel systems, and physics and fuel management studies. Materials studies include irradiation capsule tests of both fuel and graphite. Experimental procedures and results are discussed and, where appropriate, the data are presented in tables, graphs, and photographs. More detailed descriptions of experimental work are presented in topical reports; these are listed at the end of the report.

INTRODUCTION

This report covers the work performed by the General Atomic Company under U.S. Energy Research and Development Administration Contract E(04-3)-167, Project Agreement No. 17. This Project Agreement calls for support of basic technology associated with the fuels and core of the gas-cooled, nuclear power reactor systems. The program is based on the concept of the High-Temperature Gas-Cooled Reactor (HTGR) developed by the General Atomic Company.

Characteristics of advanced large HTGR designs include:

1. A single-phase gas coolant allowing generation of high-temperature, high-pressure steam with consequent high-efficiency energy conversion and low thermal discharge.

2. A prestressed concrete reactor vessel (PCRV) offering advantages in field construction, primary system integrity, and stressed member inspectability.

3. Graphite core material assuring high-temperature structural strength, large temperature safety margins, and good neutron economy.

4. Thorium fuel cycle leading to U-233 fuel which allows good utilization of nuclear resources and minimum demands on separative work.

These basic features are incorporated into the 330-MW(e) prototype Fort St. Vrain reactor which is currently undergoing prestartup testing.

CONTENTS

FIGURES

FIGURES (Continued)

FIGURES (Continued)

FIGURES (Continued)

FIGURES (Continued)

TABLES

TABLES (Continued)

TABLES (Continued)

TABLES (Continued)

4. HTGR FISSION PRODUCT MECHANISMS
189a NO. SU001

TASK 100: FISSION PRODUCT TRANSPORT

Subtask 110: Fission Gas Release

It is evident that gas phase diffusion is involved in the release of fission gas from fuel rods. This means that the ambient gas pressure has an effect on fission gas release. Release by gas phase diffusion is dominant at low temperatures ($\lesssim$1000 K) for all short-lived isotopes (with half-life $\lesssim$5 d) and contributes significantly at higher temperatures to the release of isotopes with half-lifes less than ~4 h. Evidence for the contribution of gas phase diffusion has been obtained from (1) an analysis of fission gas release data obtained from reactor, capsule, and loop (high pressure) tests and TRIGA (low pressure) tests* and (2) TRIGA tests designed specifically to determine the contribution of gas phase diffusion.

Analysis of Fission Gas Release Data

An analysis of fission gas release data was made in terms of half-life dependence according to the equation

$$(R/B)_{ij} = A_j(\tau_i)^n \quad , \tag{4-1}$$

where R/B is the ratio of release rate to birth rate for a given fission gas nuclide at steady state and at a given temperature, A_j is a constant for each element j, τ_i is the half-life of isotope i, and n is a constant.

*TRIGA tests consist of fission gas release measurements performed in a King furnace facility mounted in a TRIGA reactor at General Atomic.

The values of n derived from in-pile (reactor, capsule, and loop) measurements and from TRIGA tests are compared in Fig. 4-1 for the krypton isotopes (see Ref. 4-1 for sources of the data).

The comparison in Fig. 4-1 demonstrates that the values of n derived from the TRIGA test data are consistently smaller than those derived from the in-pile data. The prominent difference between the measurements from which the data are derived is the gas pressure; for TRIGA tests, the pressure was only 0.24 MPa, whereas for the in-pile measurements the pressure was between 2.0 and 2.84 MPa except as noted in Fig. 4-1. On this basis, a contribution to the measured fractional release of fission gas from gas phase diffusion was postulated.

The data of Fig. 4-1 have a large associated uncertainty; nevertheless, a gas phase contribution is consistent with the data. The gas phase contribution would be expected to be larger at low temperatures since the temperature dependence of bulk diffusion which contributes at high temperature is much greater than that of gas phase diffusion.

A comparison of the values of n from in-pile and TRIGA test data for xenon leads to the same conclusions as presented above for the krypton data.

TRIGA Tests to Determine the Contribution of Gas Phase Diffusion

To conclusively establish the contribution of gas phase diffusion, fission gas release (R/B) measurements were performed in the TRIGA test facility. These tests were designed on the basis of the gas diffusion coefficient being inversely proportional to $P\sqrt{m^*}$, where P is the total pressure and m^* is the reduced mass as defined by

$$\frac{1}{m^*} = \frac{1}{m_1} + \frac{1}{m_2} \quad , \tag{4-2}$$

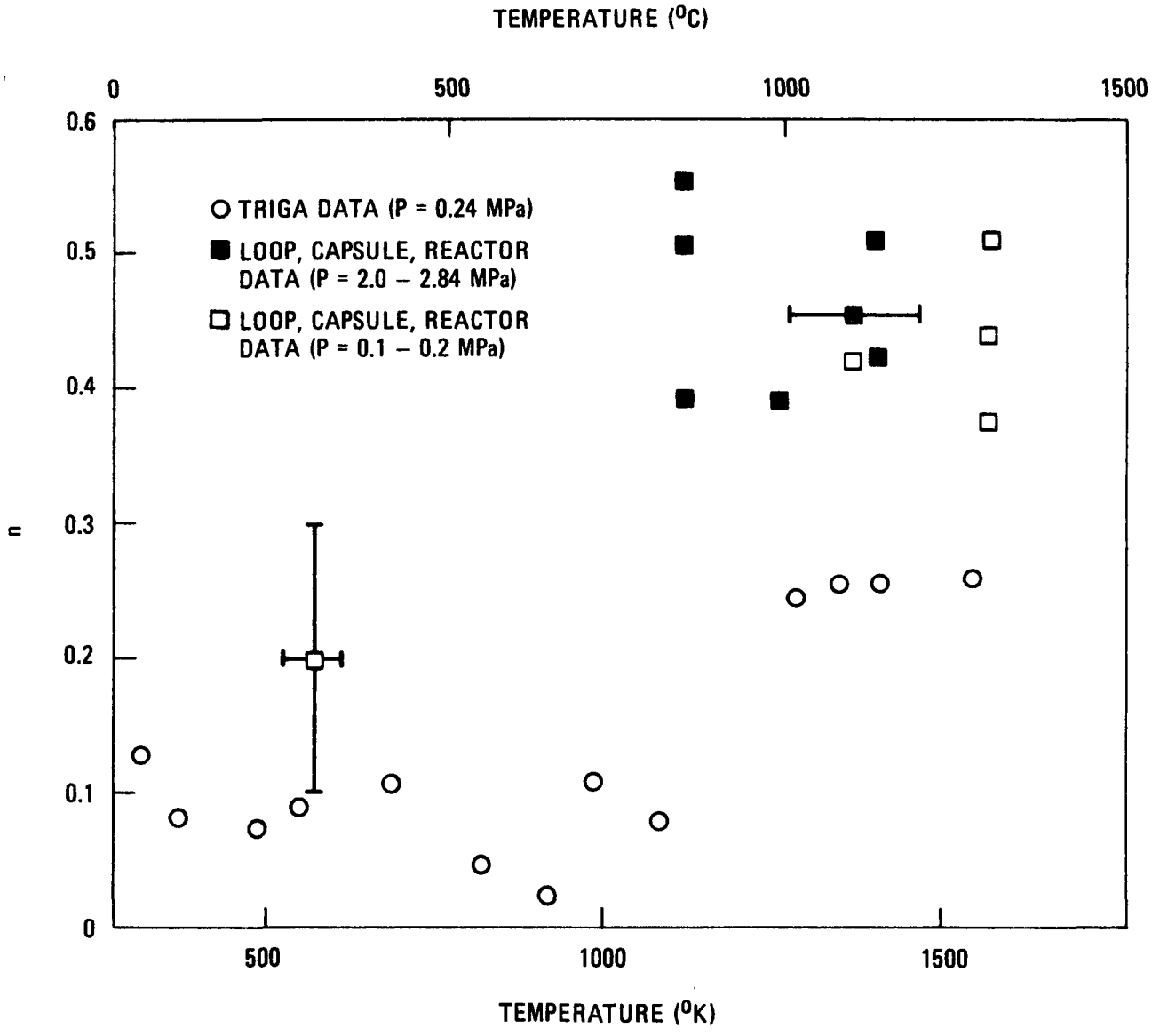

Fig. 4-1. Comparison of n values derived from in-pile and TRIGA test data for krypton

where m_1 is the atomic weight of the fission gas element and m_2 is the atomic weight of the diluent (or carrier) gas (Ref. 4-2). Accordingly, the fractional release (R/B) should be a function of $P\sqrt{m^*}$ if gas phase diffusion contributes significantly; furthermore, the fractional release should decrease as $P\sqrt{m^*}$ increases.

In the TRIGA tests, helium and neon were used as carrier gases at pressures of 0.18 and 0.30 MPa (1.8 and 3.0 atm). (The use of other noble gases as carrier gases was prevented either by licensing or procedural restrictions. The pressure of 0.30 MPa was the maximum allowable.) Thus the range of values of $P\sqrt{m^*}$ was between 0.35 and 1.22 MPa in the tests for the release of krypton isotopes. A loose mixture of bare UC_2 kernels (200-μm diameter) and ground fuel rod matrix material was used. Bare kernels were used to provide relatively large fractional releases thereby permitting more accurate measurements. The tests were conducted at low temperature (in the range 295 to 305 K) since the effect of gas phase diffusion was expected to be more pronounced at low temperature.

The results of the TRIGA tests are shown in Fig. 4-2 for krypton-87 and -89 nuclides. These results conclusively establish that gas phase diffusion is involved in fission gas release under the conditions of the tests. The curves drawn in Fig. 4-2 were calculated with an equation developed to account quantitatively for the contribution of gas phase diffusion to the total fractional release of fission gases (Ref. 4-1). These curves exhibit the expected dependence of R/B on $P\sqrt{m^*}$. Curves for other isotopes of krypton (Kr-85m and Kr-88) and for isotopes of xenon (Xe-138 and Xe-139) show similar trends, although the extent of change in R/B is a function of the half-life of the isotope.

Subtask 140: Diffusion of Fission Product Metals in Graphite

Diffusion of Cesium in Graphite

A permeation method is being used to study cesium transport through H-451 graphite, which is the current reference graphite for the large HTGR.

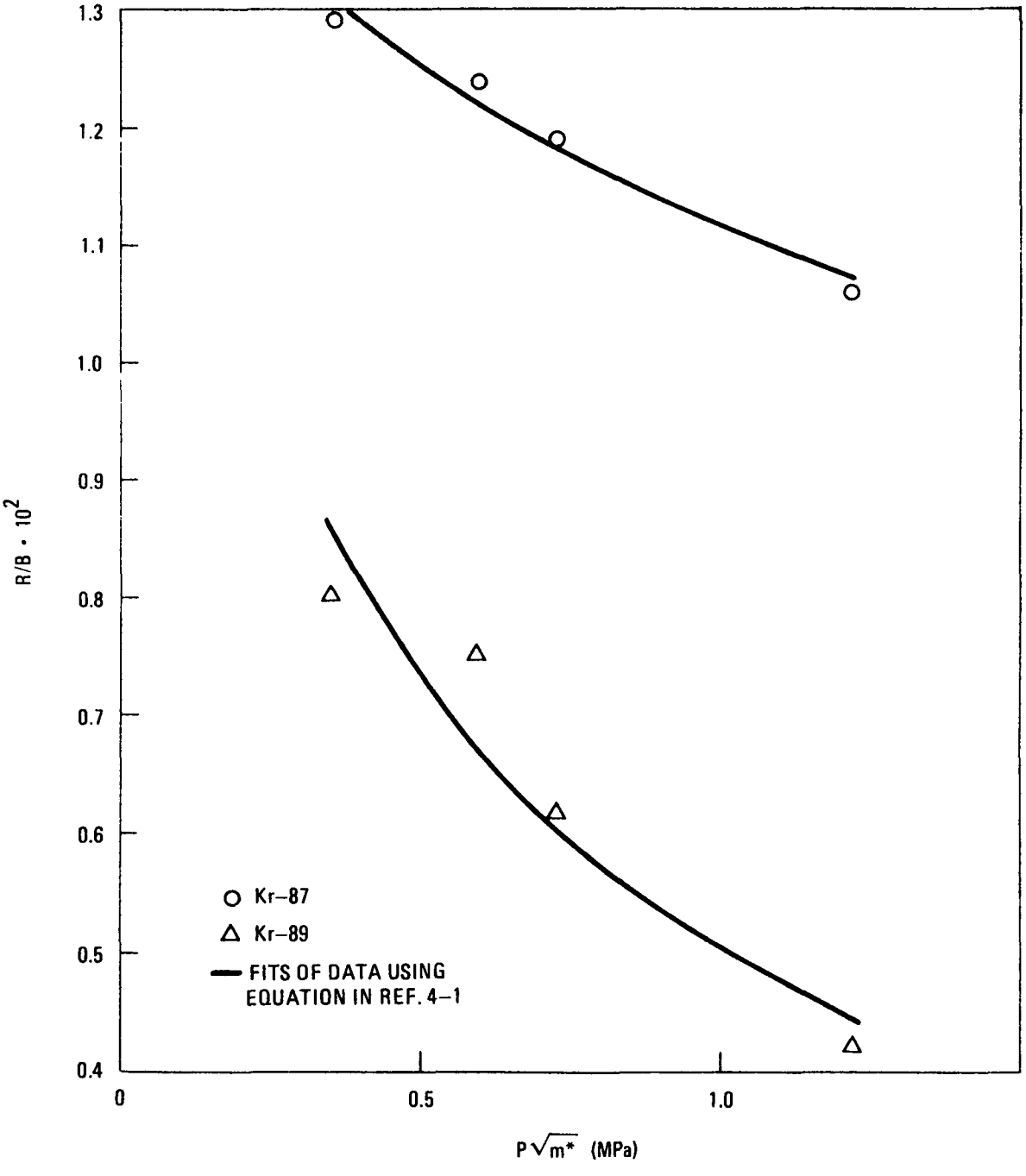

Fig. 4-2. Fractional release (R/B) of krypton isotopes as a function of pressure and reduced mass

The basic method was described and preliminary results were presented in an earlier report (Ref. 4-3).

The preliminary results showed that the rate of transport across the graphite, as reflected in the permeation coefficient, is very dependent on the atmosphere present during the process, with traces of oxidizing agent having a greatly accelerating effect. It was also very apparent that the transport was non-Fickian in the sense that the rate of cesium uptake was very slow compared to the rate of permeation whereas the time lag of permeation was very short. Furthermore, the cesium content of the graphite could be separated into two components: one readily built up and readily removable, presumably adsorbed on the internal surfaces of the graphite, and the other slowly built up and difficult to remove, presumably sorbed within the crystallites of the graphite. Because of this slow uptake of cesium by the graphite, profile measurements on samples subjected to short experiments are meaningless in evaluating permeation rates.

The objective of the present work was to improve the method to permit measurement of well-defined permeation coefficients. The results of this work are presented below. Improvements made in the method are described, and permeation coefficient data obtained to date for cesium in H-451 graphite are presented and discussed. It is shown that the data are consistent and yield an activation energy of 140 kJ/mole (33 kcal/mole). The results of permeation experiments performed on char-loaded graphite are also included.

Method. The basic method (described in Ref. 4-3) uses highly sorptive, char-loaded graphite as the source and sink in measuring the transport of cesium across a barrier sleeve of the graphite to be studied. The source is a small rod that is completely enclosed in the sleeve, which is closed with tightly fitting plugs. This in turn is enclosed in the cylindrical sink, the ends of which are also tightly closed with caps. Thus, cesium has to travel through the graphite sleeve to reach the sink. These parts are illustrated in Fig. 4-2 of Ref. 4-3.

Several changes which permitted the measurement of well-defined permeation coefficients have been introduced in the method. These changes were mainly:

1. The diffusion assembly was annealed in a closed crucible of char-loaded graphite to prevent cross-contamination.

2. The reducing atmosphere required was provided by a nonflammable gas mixture consisting of 8% hydrogen in helium. This mixture was used for safety reasons instead of the flammable mixture of H_2/CO used previously (Ref. 4-3). The gas was dried with a molecular sieve and a liquid nitrogen trap and was used at approximately atmospheric pressure during the anneals.

3. Between anneals the samples were handled in a specially designed glove box that could be evacuated so that the samples were never exposed to air or moisture. After an anneal, the quartz tube containing the sample was evacuated and placed in the glove box, which was evacuated and flushed with the helium-hydrogen gas mixture three times. All disassembly and assembly operations were performed within the glove box, and any samples removed were either sealed within the box in three nestled jars (two polypropylene and one screw cap glass with an O-ring seal) or in one polypropylene vial within a ground-glass-stoppered weighing bottle with a well-greased joint. The latter was used for radioactivity counting. Prior to experimental use, the samples were heated to 1470 K for a short time in the helium-hydrogen atmosphere. The difference that this "sterile" handling of the specimen made was readily seen in the ease of evacuation during heating as the amount of desorbing gases was rendered negligible.

4. A carefully calibrated scintillator/pulse-height analyzer counting system gave increased reproducibility in the latest experiments.

The permeability coefficient π is defined for our purposes by

$$J = \pi \frac{\Delta C}{\Delta X} \quad , \tag{4-3}$$

where C is the concentration of the sample at surfaces separated by ΔX and J is the transport across the surface per unit time and unit area. As explained previously (Ref. 4-3), taking the various geometrical factors into account and assuming that at the same stoichiometric concentration the activity of the cesium in char-loaded graphite is 10 times lower than in the H-451 graphite studied, one obtains

$$\pi = 3.0 \times 10^{-9} \frac{Q}{sh} \ (m^2/sec) \quad , \tag{4-4}$$

where Q and s are the total activities of the sink and source, respectively, in the same units (e.g., cpm) and h is the duration of the anneal in hours.

Transport in H-451 Graphite. Table 4-1 gives the results for four assemblies of source and sleeve, with new sinks in each anneal. It can be seen that on the whole the permeation coefficients are quite consistent within each group and independent of time for anneals of 2, 6, and 18 hours. Short anneals of 40 minutes, however, yield significantly higher values of the permeation coefficient. This is attributed tentatively to the fact that the sink may be imperfect, and having accumulated some cesium, it offers a slight resistance to transport leading to a slightly excessive accumulation of cesium in the sleeve. A fresh sink at first rapidly absorbs this excess before coming to a more steady condition and thus leads to slightly excessive transport in the beginning. Hence, results of the short anneals are not included in the averages.

Considering the remaining values at 1143 K, the five marked by asterisks are obviously higher than the rest. Statistical analysis shows that they differ from the average of the others by more than five times the

TABLE 4-1
PERMEATION COEFFICIENTS FOR CESIUM IN H-451 GRAPHITE AT 1143 K

Duration (hours)	Permeation Coefficient, π ($m^2/s \times 10^{-12}$)	
	Assembly Ha	Assembly Hb
6	1.75	3.01
6	1.56	2.83
6	1.53	3.02
2	2.81*(a)	3.47
18	1.73	3.14
2	2.05*	4.06*
	Avg 1.64	Avg 3.11
	±0.082 (5.0%)	±0.231 (7.4%)
	Assembly Ia	Assembly Ib
6	5.47*	3.68
6	3.46	3.23
6	3.49	3.32
2	4.24	6.14*
18	3.44	3.94
2	3.83	3.87
0.67	(6.23)(b)	(5.10)
6	3.31	3.75
	Avg 3.63	Avg 3.63
	±0.182 (5.0%)	±0.23 (6.3%)

(a) Values marked with asterisks were not averaged for reasons given in the text.

(b) Values in parentheses were not averaged because of short anneal time (see text).

standard deviation of these. Thus they clearly do not belong to the same family of data and should not be averaged with the other values. The fact that they are all high suggests radioactive contamination during the difficult manipulations in the glove box, but direct proof of this is not available.

The remaining values of 1143 K have been averaged; the average value, together with the standard deviation, is shown for each assembly. These deviations amount to between 5 and 7.4%, with an average of 6% which seems satisfactory.

Two of the assemblies gave very concordant values at 3.63×10^{-12} m^2/sec, another was somewhat lower at 3.1×10^{-12} m^2/sec, and the fourth was appreciably lower at 1.64×10^{-12} m^2/sec. These are clearly significant differences between the assemblies, and preliminary indications are that they are mostly due to differences between sleeves (graphite samples). Considering the general variability of graphite samples, this variation is not unexpected; in fact it is quite small.

Two assemblies (Ha and Hb) were run at three different temperatures. Table 4-2 and Fig. 4-3 show the results with respect to the influence of temperature. For one assembly (Hb), the points obtained at the three temperatures (928, 1143, and 1288 K) lie very close to a straight line on the Arrhenius plot (Fig. 4-3) and define an activation energy of 140 kJ/mole (33 kcal/mole). For the other assembly (Ha), the 928 and 1143 K points lie on a parallel line, but the 1288 K point seems clearly high and should probably be disregarded.

It can be noted that the present permeation coefficients at 1143 K agree reasonably with the values reported previously (Ref. 4-3); however, the present activation energy is higher than the previous value of 111 kJ/mole (26.5 kcal/mole) derived from the line in Fig. 4-3 of Ref. 4-3.

Transport Through Char-Loaded Graphite. Some experiments were performed on char-loaded graphite because of its importance in our method of

TABLE 4-2
TEMPERATURE DEPENDENCE OF PERMEATION COEFFICIENTS
FOR CESIUM IN H-451 GRAPHITE

Temp (K)	Duration (hours)	Permeation Coefficient, π ($m^2/s \times 10^{-12}$)	
		Assembly Ha	Assembly Hb
928	72	0.0445	0.0801
1143	2 to 18	1.64[(a)]	3.11[(a)]
1288	2	16.6[(b)]	19.6

[(a)] Averages from Table 4-1.

[(b)] This value is not in good accord with the other values (see text).

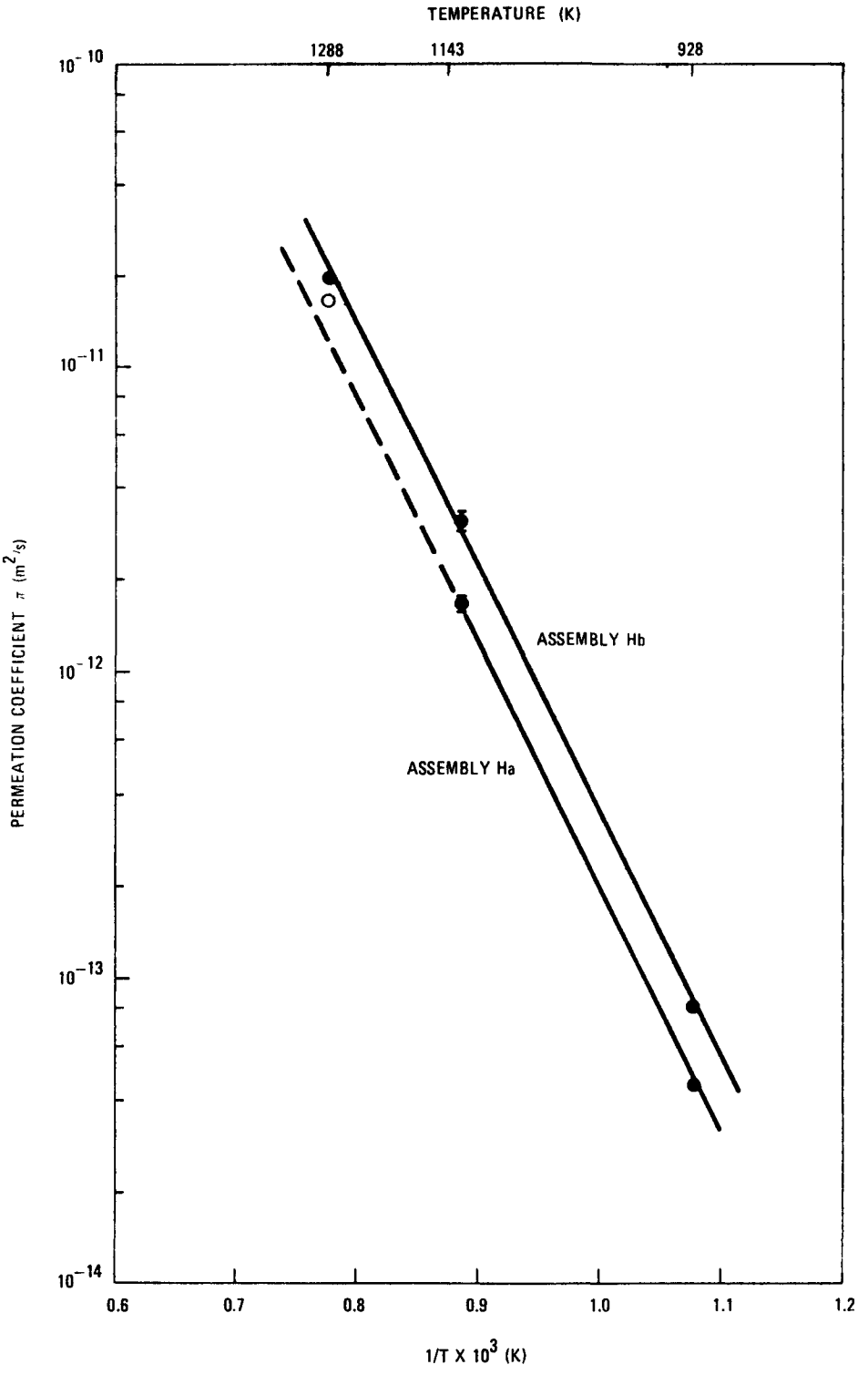

Fig. 4-3. Temperature dependence of permeation coefficient data for cesium in H-451 graphite

studying transport through ordinary graphite and also because of its potential value as a reactor material. The method was similar to that described above but was adapted to the high sorptivity of this material. The geometry of source and sink was reversed; i.e., a small rod acted as the sink and a large hollow cylinder as the source. Thus there was a relatively large reservoir of cesium available during the experiment. The assembly was enclosed in a niobium crucible with a slip cover of the type normally used in the preparation of sources in order to reduce cesium losses to a minimum. The crucible, in turn, was clamped in a char-loaded crucible with a screw closure to reduce outside contamination. The experiments were conducted at 1338 K.

Table 4-3 shows the results, which are also plotted in Figs. 4-4 and 4-5. In Fig. 4-4 a time lag is clearly evident, followed by a constant rate of permeation. As shown by Fig. 4-5, loading of the sleeve was still in progress at the end of the experiments, but conforms reasonably well to the initial part of the standard loading curve for a solid sphere as given by Crank (see Fig. 6.4 in Ref. 4-4). (Fitting of the loading curve is discussed further below.) The anticipated equilibrium loading is calculated on the basis that the source and sleeve are of the same material and that the sleeve should reach 67% of the value it would have at equilibrium because its inner surface is kept at zero concentration by the regularly renewed sink.*

---

*The expression for steady-state content of a cylindrical membrane is not given by Crank (Ref. 4-4) but can be derived readily as follows. When C_1 at r = a is kept zero and C_2 at r = b is constant, Crank's expression 5.4 gives

$$C = C_2 \ln(r/a)/\ln(b/a)$$

The total content (M) per unit length of the cylinder is found by integration

$$M = \int_a^b C 2\pi r \, dr = \frac{2C_2}{\ln(b/a)} \int_a^b r \ln(r/a) \, dr \quad .$$

The equilibrium content (M_o) of a hollow cylinder exposed to concentration C_2 is simply per unit length

$$M_o = C_2(b^2 - a^2) \quad ,$$

which gives

$$\frac{M}{M_o} = \frac{1}{f^2 - 1} \left[f^2 + \frac{f^2 - 1}{2 \ln f} \right] ,$$ where f stands for b/a. In our case f = 3 so that $M/M_o = 0.67$.

TABLE 4-3
PERMEATION AND LOADING OF CHAR-LOADED GRAPHITE AT 1338 K

Duration (hours)		Loading (μCi)			
		Sink			
Incremental	Cumulative	Incremental	Cumulative	Sleeve	Source
24	--	0.0214	--	23.8	(526)[a]
24	48	0.0669	0.0883	--	--
24	72	0.185	0.273	--	--
24	96	0.287	0.560	52.6	--
27.5	123.5	0.445	1.005	63.5	486
48	171.5	0.630	1.64	73.9	460

[a] This value is questionable.

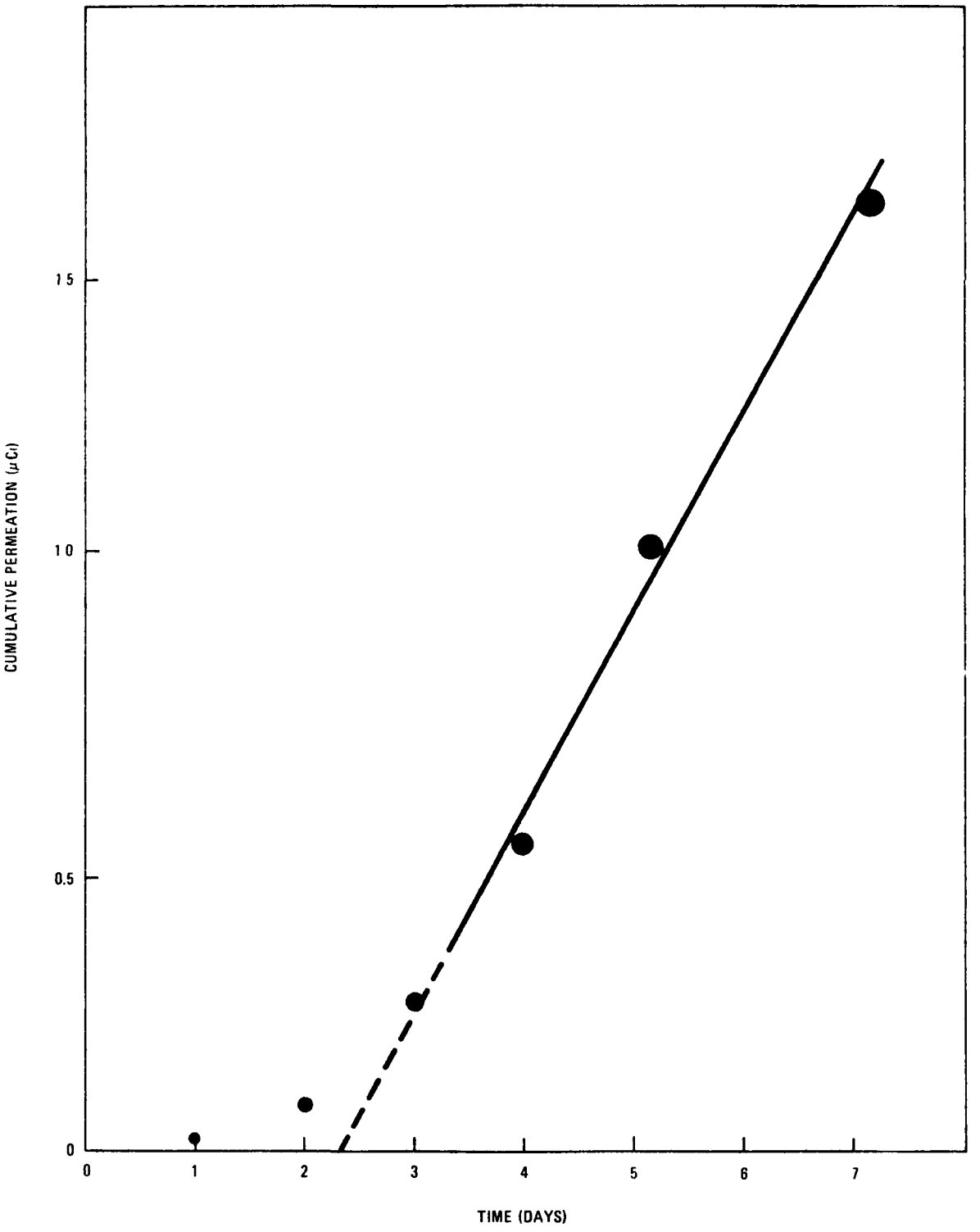

Fig. 4-4. Time dependence of cumulative permeation (or flux)

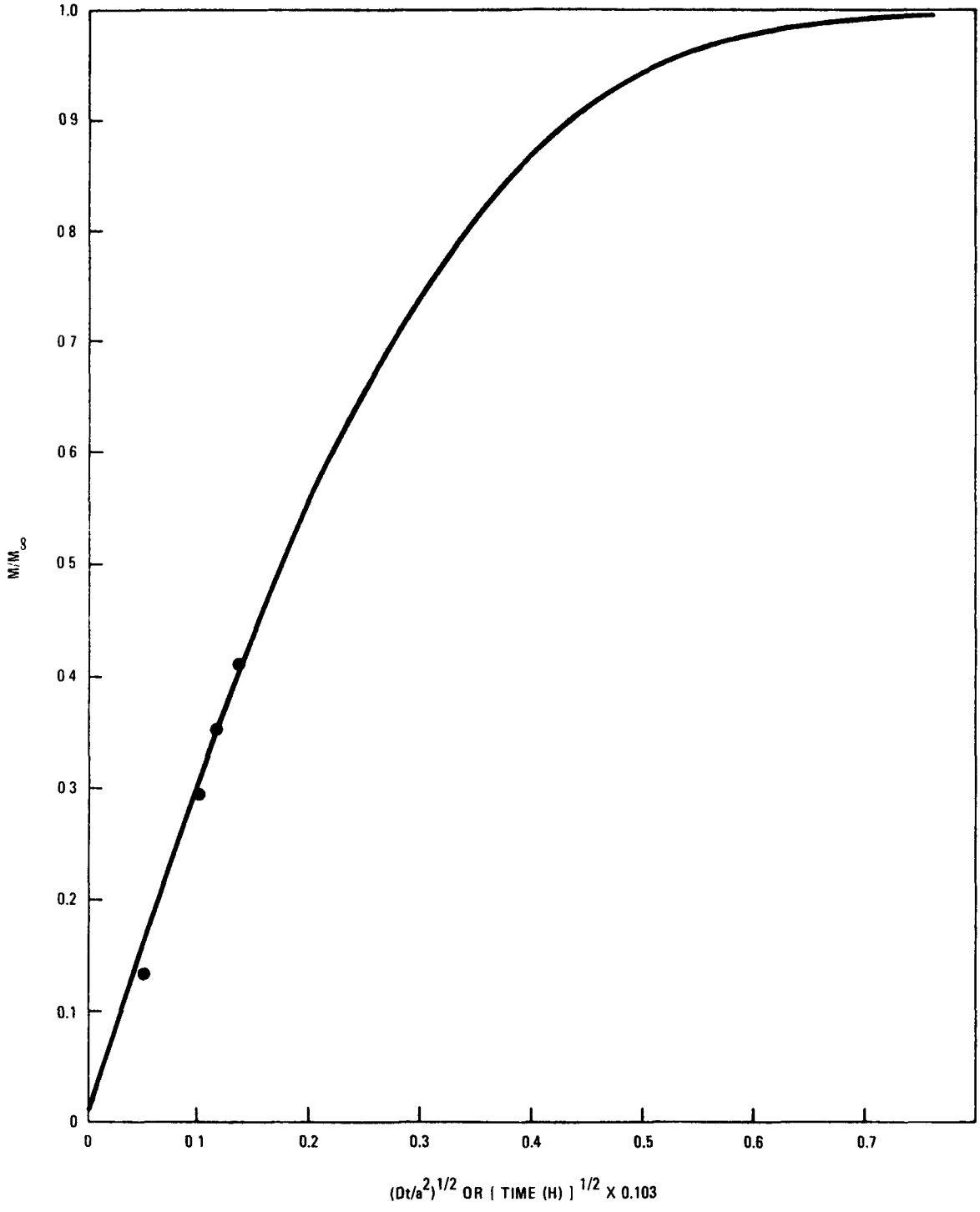

Fig. 4-5. Fractional loading (M/M_{∞}) of sleeve (graphite) sample as a function of normalized time

The time lag, the steady permeation slope, and the loading curve can each be converted to a diffusion coefficient. In a Fickian solid these three values must be the same within experimental error. In our case they are clearly different, thus confirming again the non-Fickian nature of graphite.

The time lag is 2.3 days. For a hollow cylinder this is related to the diffusion coefficient by

$$D_t = (b^2 - a^2)/6L \quad , \tag{4-5}$$

where D_t is the diffusion coefficient derived from time lag, L is the time lag, and a and b are the inner and outer radii of the cylinder (1.59 and 4.76 mm, respectively). Thus,

$$D_t = 1.7 \times 10^{-11} \ m^2/s \quad .$$

The constant slope of Fig. 4-4 is related to the diffusion coefficient, which is also the permeation coefficient, by

$$D \equiv \pi = \frac{Q}{C} \frac{\log(b/a)}{(2\pi)L} \frac{1}{t} \quad . \tag{4-6}$$

In our case the second right-hand term is 11.2 as before (Ref. 4-3), and C equals the source concentration, s/6.4, the source activity divided by the weight of the source. Thus,

$$\pi = 6.6 \times 10^{-10} \frac{Q}{sd} \ m^2/s \quad , \tag{4-7}$$

where d is the time in days. The experimental slope in these units is 4.8×10^{-3}/day so that the permeation coefficient is

$$\pi = 3.2 \times 10^{-12} \ m^2/s \quad .$$

Fitting of the loading curve in Fig. 4-5 involved the selection of the proper scale of the abcissa, i.e., selection of a diffusion coefficient for loading. This was done by fitting the highest point to the curve given for loading of solid spheres by Crank. The rationale of using the sphere is twofold: the expression for the hollow cylinder is very complex and is presumably not applicable since the takeup is by carbon crystallites of irregular shape bathed by a steady concentration of surface sorbed cesium. The sphere is probably as good an approximation of the irregular shape as is available. The $D' = D/a^2$ thus obtained is 3×10^{-8} s^{-1}. If the radius of the crystallites is of the order of 0.1 μm (1000 angstroms) D would be 3×10^{-22} m^2/s.

Another approximation of the loading curve would be to consider the cylindrical membrane as being flat, in which case an apparent D of 5×10^{-13} m^2/s would be obtained.

Any discrepancy between the permeability coefficient obtained from the slope of the steady rate permeation and the apparent diffusion coefficient obtained from the time lag can be accounted for if one assumes that the actual diffusion path is only a fraction of the total cross section of the sample and that the diffusion path has dead-end branches.

Limiting diffusion to only a part of the cross section, as represented by Fig. 4-6a, does not affect the lag time but reduces the flux and therefore the diffusion coefficient calculated on the basis of the total area. Providing dead-end diffusion paths, as represented by Fig. 4-6b, does not affect the steady-state diffusion rate but does extend the time lag in direct proportion to the dead-end volume provided (Ref. 4-5). The former can account for a higher diffusion coefficient based on lag time than on permeation and the latter accounts for the opposite situation.

In the graphite case, it is likely that both factors are present, the diffusion path being only a small part of the total cross section and being complicated in shape with many dead-end branches, as represented by Fig. 4-6c. In addition, this path is interspersed with nearly impermeable crystallites which give a very slow loading rate.

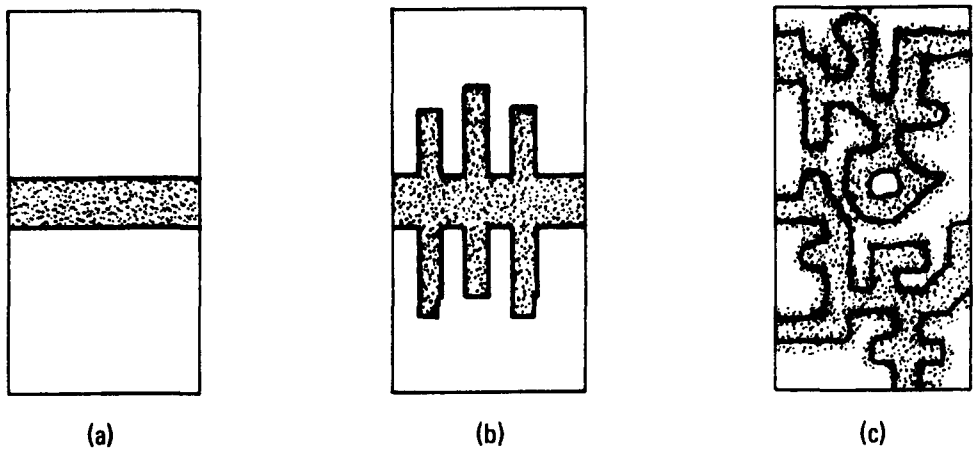

Fig. 4-6. Schematic presentation of how (a) reduction of cross section does not affect time lag but reduces the rate of permeation, (b) addition of dead-end volume increases the time lag, and (c) a greatly reduced cross section with dead-end pores and very slow diffusion into bulk material can account for the behavior of graphite

TASK 200: FISSION PRODUCT TRANSPORT CODES

Subtask 220: Code Validation

COPAR Code Validation Utilizing Out-of-Pile Anneal Test Data

Accurate predictions of fission product metal release from HTGR coated fuel particles are a necessary prerequisite for in-pile fission product transport characterization. Metallic release is controlled by the interaction of numerous physical phenomena, including fission product recoil, decay, diffusion, sorption, and vaporization. These and other effects have been reviewed and included in the recently developed COPAR (COated PARticle release) computer code (Refs. 4-6, 4-7). An important adjunct to development of the code is the comparison of COPAR predictions with observed fission metal release from particles. In this manner, the applicability of the modeling assumptions used to characterize the release behavior can be validated.

Accordingly, a study has been performed to validate the COPAR code. The release of cesium and strontium from bare fuel kernels and coated particles was modeled, and comparisons of predicted and measured release were made. Results confirm that the code is sufficiently flexible in its programming to provide accurate predictions of metallic release from coated particles. A summary of the validation work is presented below; Ref. 4-8 is a detailed report of the work.

Cesium and strontium release data derived from the out-of-pile post-irradiation anneal (PIA) test method (Ref. 4-9), including results for (1) bare ThO_2 kernels, (2) PyC coated $(xTh,U)C_2$, $(xTh,U)O_2$, and (3) ThO_2 particles, was modeled with the COPAR code. Cesium and strontium release data were selected for use in the analysis because a significant body of data has been gathered on time-dependent release of these metals. Their behavior has been extensively characterized because the radionuclides Sr-90 and Cs-137 are important from the standpoint of reactor design and operation.

Analysis of the time-dependent cesium release from both bare kernels and coated particles revealed that a fraction of the cesium inventory in the particles was rapidly released. This "rapid release fraction" was found to be larger than the predicted release resulting solely from Fickian diffusion of cesium in the coatings or kernel of the particle at the elevated temperature of the PIA tests. The rapid release fraction is felt to result from the diffusion of cesium from grain surfaces within nonhomogeneous kernel materials known to be present in irradiated fuel particles. Since this phenomenon may have a significant effect on observed cesium release during postulated HTGR temperature excursions, a "double kernel" adaptation of the COPAR model was formulated to simulate this behavior. This model was found to provide accurate representations of the observed out-of-pile release for a variety of temperature conditions. .

The release of strontium during out-of-pile anneal tests was found to be adequately described using the COPAR model as previously programmed. It should be noted, however, that the limited time of observed strontium release (resulting from the decay of 9.7 h Sr-91, the radionuclide monitored in the PIA tests) makes this conclusion tentative since release at long times could not be measured.

TASK 300: FISSION PRODUCT DATA ANALYSIS

Subtask 310: Fission Product Data Review

Fission Product Data Status and Needs

An evaluation of the status of fission product transport data and the need for additional data has been made. This evaluation, which is an update of an earlier, more extensive evaluation (Ref. 4-10), reflects the findings of recent reviews of fission gas transport data (Ref. 4-1) and cesium transport data (Ref. 4-11).

On the basis of the earlier and present evaluations, it is concluded that the most pressing needs for additional data are as follows:

1. The strongest need continues to be for sorption data for iodine and cesium on primary circuit metals. These data must include the effect of the surface condition of the metals on sorptivity and must be applicable to sorbate pressures in the range 10^{-4} to 10^{-8} Pa (10^{-9} to 10^{-13} atm).

2. A study of the phenomenon of rapid release of cesium from ThO_2 fuel kernels is needed. The study should include the development and validation of a suitable model. A study is also needed of the release of cesium from ThO_2 kernels at extended times.

3. Studies of the diffusion of cesium in graphite need to be continued. An apparent reduction of cesium transport in-pile, as compared to that out-of-pile, needs to be verified and quantified. These needs are understandable considering that:

   a. Cesium diffusion in graphite is very complex.

   b. The largest uncertainty for cesium release into the primary circuit of the HTGR arises from the uncertainty in cesium transport in graphite (Ref. 4-12).

4. In the area of fission gas release, work is needed to:

   a. Verify that constrained failed fuel particles are representative of failed particles in fuel rods.

   b. Determine the extent of fission gas release when particles fail.

   c. Establish the effect of fuel hydrolysis on fission gas release.

   d. Study fission gas release under temperature transient conditions.

5. A particularly important need is for more information on the in-pile transport behavior of fission products. Such information, for example, will be derived from operation of the Fort St. Vrain HTGR. (See Task 900 for information gained from Fort St. Vrain during the initial rise-to-power.)

In addition to the above needs, which relate mainly to the normal operation of HTGR systems, more information is needed on the transport behavior of fission products under postulated accident conditions. For example, additional information is needed on the release of fission products from intact and failed fuel particles at temperatures above 2000 K to reduce uncertainties in the analysis of the postulated accident involving loss of forced circulation (Ref. 4-13). This information is being provided by studies in progress at General Atomic under the ERDA Safety Program.

Recent information relating to data status and needs for the various areas of fission product transport data are presented in the following sections.

Fission Product Plateout Data. As stated in the earlier evaluation (Ref. 4-10), plateout data are needed for the sorption of iodine on graphite and the sorption of iodine and cesium on low- and high-alloy metals. Of particular interest is the sorption of iodine on T-22 steel; reduction in the uncertainty associated with this sorption is quite important for the accurate prediction of the circulating activity of iodine. Strontium and tellurium plateout data are also of interest.

The sorption of cesium on Incoloy 800 has recently been measured (Ref. 4-6). The sorption data were obtained using as-received (degreased) samples in the temperature range 673 to 1090 K and the pressure range 10^{-5} to 1 Pa. The dependence of cesium sorptivity on the vapor pressure at constant temperature and on the temperature at constant vapor pressure is not strong; the variations in sorptivity are of the order of ten. Additional measurements using samples exposed to HTGR atmospheres are desirable in assessing the applicability of the new data.

The need for additional iodine and cesium plateout data for representative reactor plateout surfaces was demonstrated by a recent analysis (Ref. 4-6) of plateout behavior in the CPL-2/1 loop experiment carried out in the French Cadarache Pegase loop. Calculated and observed shapes of iodine plateout profiles were found to be in good agreement, but calculated levels of deposited iodine were appreciably lower than observed values. For cesium, calculated and observed plateout profile shapes and levels of deposition were in good agreement when the sorption data used in the analysis were representative of the loop materials. It was concluded that the reference GA method for calculating plateout distribution (PAD code) is acceptable, provided accurate surface temperatures and appropriate sorption isotherms (measured on representative materials) are utilized as input for the calculations.

Metallic Fission Product Release Data. Since the previous evaluation (Ref. 4-10), additional information on metallic fission product release has been developed from in-pile experiments on cesium transport (Ref. 4-6) and a review of cesium transport data (Ref. 4-11).

Release from Kernels. The review of cesium transport data (Ref. 4-11) showed that release of cesium from oxide kernels (ThO_2 and UO_2) is relatively small at temperatures below 1473 K, and release is predominately by recoil over the range of FIMA values up to 12%. However, data on ThO_2 kernels obtained from postirradiation anneal (PIA) experiments often show an initial, rapid release of cesium. This has been attributed to the difference between the irradiation and anneal conditions (Ref. 4-11); this interpretation is supported by comparisons between the PIA experiments and measurements on the in-pile release of cesium from UO_2 kernels into the coatings of intact, TRISO coated particles. Under HTGR conditions of a steady or declining temperature, a rapid release of cesium is not expected; however, under temperature transient (rise) conditions, a rapid release may become important. Additional data are needed to establish the importance of rapid release. The development and experimental validation of a suitable model incorporating this phenomenon has been accomplished (see Subtask 220).

Migration in Particle Coatings. The diffusion coefficient of cesium in low-temperature isotropic (LTI) pyrocarbon has been shown to correlate with the cesium concentration at the inner surface of the pyrocarbon coating (Ref. 4-11); with increasing burnup, the latter concentration increases and the diffusion coefficient increases. Apparently these increases are greatest at low FIMA values (<20%) and reach a limit at FIMA values greater than 20%. It is estimated that the pyrocarbon diffusion coefficient is increased by a factor of about 2 at 7% FIMA as a result of the described phenomenon. The increase is accounted for in the uncertainty assigned to the diffusion coefficient. A further analysis of the phenomenon is desirable (1) to understand the basis of the correlation, (2) to assess the importance of the correlation, and (3) to reduce the uncertainty associated with the diffusion coefficient.

This phenomenon also apparently applies to the diffusion of strontium in pyrocarbon. Further investigation is needed to substantiate this.

At present, the cesium release from failed fissile particles is calculated in reactor analyses on the basis of immediate and complete release of the cesium inventory in the particles. However, unpublished preliminary data on cesium release from laser-drilled (simulated failed) BISO coated ThO_2 particles indicate a delay in cesium release; as expected, this delay is smaller than the delay observed in cesium release from intact BISO coated ThO_2 particles. Analogously, a delay in the release of cesium from failed constrained fissile particles can be anticipated. Since the cesium release from an HTGR core has a significant contribution from cesium released from failed fissile particles, measurements of the release of cesium from failed fissile particles for HTGR operating conditions are needed. These measurements can be used to determine the extent by which the core release of cesium will be reduced by taking into account the delay in cesium release from failed fissile particles.

Migration in Graphite. Recent experiments have confirmed the reduction in cesium transport in-pile as compared to that in out-of-pile experiments (Ref. 4-6). The in-pile experiments were conducted in the same

sample assembly as used in companion out-of-pile experiments and demonstrated an increased uptake of cesium by the graphite and concomitant decreased transport through the graphite compared to that found in out-of-pile experiments. This is consistent with the observed increase in cesium sorptivity with irradiation of the graphite as deduced from Knudsen cell mass spectrometer measurements on irradiated graphite (Ref. 4-11).

Fission Gas Release. Further analysis of the fission gas release data has revealed that gas phase diffusion is involved in fission gas release from fuel rods (see Subtask 110 and Ref. 4-1). Gas phase diffusion dominates fission gas release at low temperatures ($\lesssim$1000 K) and contributes significantly to the release of the shorter-lived isotopes (half-life $\lesssim$4 h) in the temperature range of HTGR normal operating conditions. The gas phase diffusion contribution to fission gas release from fuel rods has been conclusively demonstrated in recent tests in the TRIGA facility.

TASK 600: COOLANT IMPURITY/CORE MATERIAL INTERACTION

Subtask 620: Reaction of Steam with Core Structural Materials

Rate Constants for the Reaction of Water with H-451 Graphite

Summary. The reaction rate of H-451 graphite with water vapor has been studied at water concentrations in the range of 45 to 3000 Pa (450 to 30,000 μatm), at added hydrogen concentrations from 0 to 1000 Pa, and at temperatures from 1093 to 1253 K. A weight-loss method utilizing automatic recording microbalances was employed. Helium was the carrier gas. Values of the rate constants K_1, K_2, and K_3, as defined by the Langmuir-Hinshelwood equation, were derived from the reaction rate data. The results show that a single set of rate constants is not valid over the wide range of water concentration. The rate constant values change significantly at water concentrations around 300 Pa. The results also show that hydrogen sorption on graphite is slow and has a profound effect on the apparent reaction rate. Rate constant values for H-451 graphite are recommended for the high range of water concentration, where the most reliable

data were obtained. The recommended rate constant values are compared with former values used in the OXIDE-3 code. Further work is required to obtain rate constants for H-451 graphite at low water vapor concentrations and to establish the effect on reaction rate of the slow hydrogen sorption on graphite.

Introduction. The extent of the reaction of water vapor with the core graphite in an HTGR is calculated (predicted) utilizing computer codes, such as the OXIDE-3 code (Ref. 4-14) and the GOP code (Ref. 4-15), and appropriate input reaction rate data. Input data used in the codes have consisted of reaction rates for graphites other than H-451 graphite, which is the reference fuel element graphite for the large HTGR. A study is being performed to provide input reaction rate data for the reaction of water vapor with the reference graphite; the results obtained to date from this study are presented in this report.

The reaction of graphite with water vapor is controlled by chemical interactions and also by mass transport in the porous graphite structure. This report deals only with the chemical interactions. Two water vapor concentration regions are of interest from the reactor standpoint: high concentrations, up to 1000 kPa (10 atm) water vapor, such as could occur in the event of a large steam leak, and low concentrations, up to 50 Pa (500 μatm), such as could occur during normal operation.

While some controversy exists on the mechanisms involved in the reaction of water vapor with graphite, it is generally agreed that the chemical aspects of the reaction can be represented by the Langmuir-Hinshelwood equation

$$R = \frac{K_1 P_{H_2O} F_b F_c}{1 + K_2 P_{H_2}^n + K_3 P_{H_2O}} , \qquad (4\text{-}8)$$

where K_1, K_2, and K_3 are rate constants, n is a constant, P_{H_2O} and P_{H_2} are partial pressures of water vapor and hydrogen, respectively, F_b corrects

the rate for the effect of burnoff, and F_c corrects the rate for the effect of catalysis. The effect of catalysis is not considered in this report.

Theory. It is generally agreed (Refs. 4-16 through 4-18) that the oxidation of graphite by water vapor consists of three distinct processes:* (1) sorption of water molecules on active carbon sites, (2) chemical reaction of the sorbed water to form H_2 and CO, and (3) inhibition of water sorption by competitive sorption of H_2 molecules. Process (1) can be expressed by

$$H_2O(g) + C_f \underset{j_1}{\overset{i_1}{\rightleftharpoons}} C(H_2O) \quad , \tag{4-9}$$

where C_f and $C(H_2O)$ denote free and occupied sites and i and j are reaction rate constants for the forward and reverse reactions. Following process 4-9 sorbed water reacts with the solid phase to form carbon monoxide and hydrogen as expressed by

$$C(H_2O) \xrightarrow{j_3} CO + H_2 + aC_f \quad , \tag{4-10}$$

where a is an integer having values from 0 to 2. If $a > 1$ (observed in the earlier stages of oxidation), the number of reaction sites increases as the reaction proceeds, leading to increased reaction rates. If $a < 1$ (observed only during the final stages of the oxidation process), the graphite becomes less reactive as the reaction proceeds. Thus, the reaction rate is affected by burnoff (i.e., the extent of oxidation).

Previous studies have concluded that hydrogen molecules compete with water vapor molecules for the available sites (Refs. 4-16 and 4-17). Thus, included in the denominator of Eq. 4-8 is a term which reflects the rates of adsorption and desorption of hydrogen on graphite (process 4-10) as expressed by

*Transport considerations are neglected in this treatment.

$$C_f + H_2(g) \underset{j_2}{\overset{i_2}{\rightleftharpoons}} C(H_2) \quad . \tag{4-11}$$

These three processes form the basis for the Langmuir-Hinshelwood equation

$$\text{Rate} = \frac{\dfrac{i_1 j_3}{j_1 + j_3} P_{H_2O}}{1 + \dfrac{i_2}{j_2} P^n_{H_2} + \dfrac{i_1}{j_1 + j_3} P_{H_2O}} \quad . \tag{4-12}$$

It is apparent that if j_1, the rate of evaporation of water molecules from the surface, is negligible, $K_1 = i_1$, $K_2 = i_2/j_2$, and $K_3 = i_1/j_3$.

Experimental Procedure. The test procedure involves the use of automatic recording microbalances with which instantaneous reaction rates are measured by sample weight-loss determinations. Figure 4-7 is a diagram of the apparatus. Selected graphite specimens are supported by a platinum wire from the balance beam in a nonreactive container at constant temperature and exposed to a measured partial pressure of water vapor for a known period of time. Water vapor is transported via a carrier gas composed of either inert helium or a mixture of helium and hydrogen. Water vapor is added to the carrier gas by passing the inlet stream over water (or ice) maintained at constant temperature with an FTS refrigeration system. Moisture levels are determined by use of EG&G dew point or MEECO electrolytic type moisture monitors.

It was found that reaction rates increased with increasing flow but reached a relatively constant value at from 5.0 to 17 cm^3/s. Accordingly, all measurements reported herein were performed at 8.3 cm^3/s, which is equivalent to a linear velocity of 16 cm/s at 1173 K.

The sample temperatures were maintained at ±5 K with the use of SCR-controlled resistance furnaces. Temperatures were measured with sheathed Chromel-Alumel thermocouples read with an IRCON digital output amplifier.

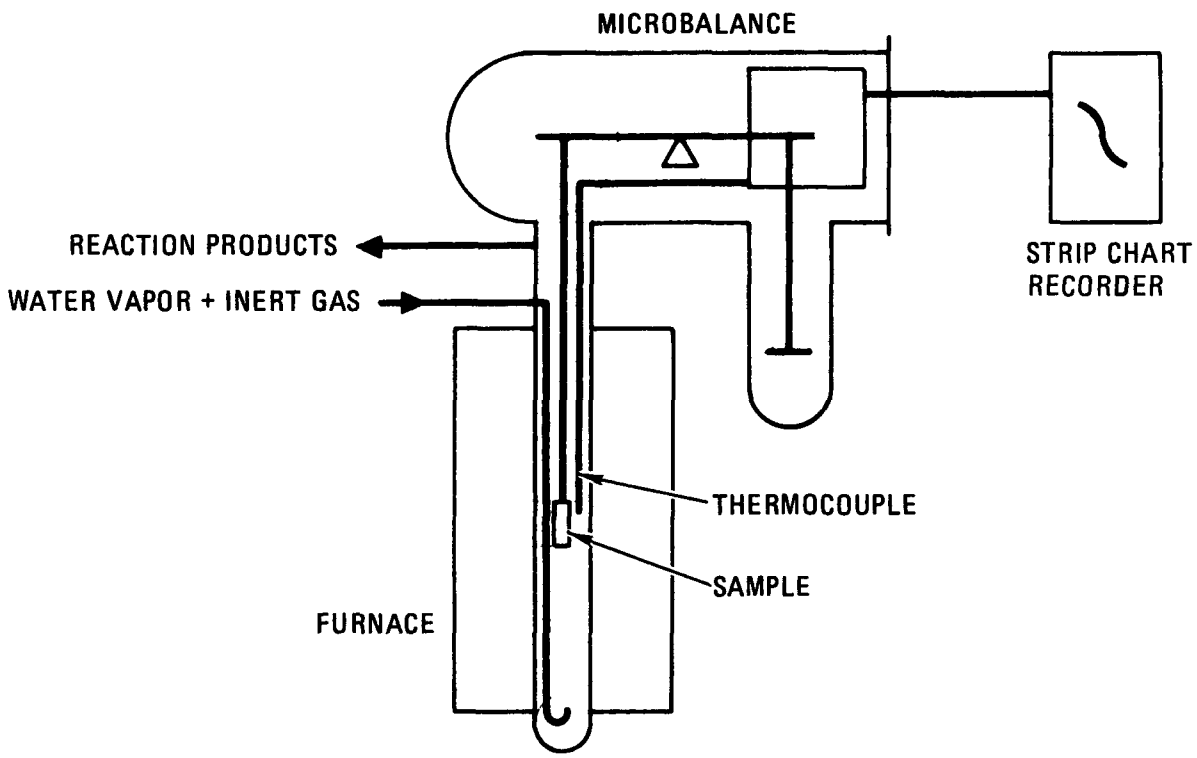

Fig. 4-7. Typical apparatus for continuous weight loss determination of graphite oxidation by moisture in inert gas

In order to minimize the effects of mass transfer or inpore diffusion on the reaction rates, thin disks or cylinders were used. A series of tests were performed to determine whether samples of such dimensions would be controlled by either chemical effects or mass transport. These tests involved performing rate studies at temperatures up to 1253 K on disks of increasing thickness from 1.6 to 12.7 mm. These tests showed that volumetric reaction rates under all conditions were constant for disks of thickness 3.2 mm or less. In addition it was found that under certain conditions, namely high moisture content or high hydrogen concentration, thicker samples exhibited minimal mass transport contribution. Reaction rate constants of similar magnitude were found for both thin (3.2 mm) disks and thicker cylinders (12.7 mm diameter). (See Fig. 4-14 in section "Determination of K_1.") Almost all rate data were determined using 3.2-mm-thick disks. In a few cases, where mass transfer conditions permitted, 12.7-mm-diameter cylinders were used.

Samples were taken from near the center of a log of preproduction H-451 graphite. The density of the samples ranged from 1.69 to 1.70 Mg/m^3. Using spectrochemical techniques, the total metallic impurity content of the graphite was found to be typically below 200 ppm; iron impurity levels ranged from <1 to 6 ppm.

A typical experimental run involved exposing a graphite sample to a given gas mixture of H_2O, H_2, and He at a single temperature until the weight-loss rate (reaction rate) stabilized. After prespecified burnoffs were attained, moisture levels were changed by adjusting the temperature of the refrigerated saturator at the gas inlet. It was found that at constant hydrogen partial pressure, reaction rates stabilized within 1 or 2 hours. Long equilibration times (up to 24 hours or more) were necessary whenever temperature or hydrogen content was changed. This phenomenon was determined to be due to slow hydrogen sorption equilibration, which caused apparent reaction rates to diminish with time. This phenomenon is discussed in more detail in the section "Determination of K_2."

Values of the constant n and rate constants K_1, K_2, and K_3 are obtained from the slopes of isothermal plots of the reaction rate data treated in accord with relationships derived from Eq. 4-8. Since all three rate constants increase with burnoff, values of the constants were corrected to a constant burnoff of 1%.

Determination of Reaction Rate Constants. Values were determined for the following reaction rate constants: burnoff factor F_b, hydrogen exponent n, and K_1, K_2, and K_3, as discussed below.

Determination of Burnoff Factor F_b. The burnoff factor F_b is determined from plots of relative reaction rate versus percent burnoff, where the rate data are normalized to unity at 1% burnoff. Figures 4-8 through 4-10 show the burnoff data. The increase in reaction rate with burnoff is more rapid at lower temperatures. For example, at 5% burnoff F_b is 4, 2.6, and 2.5 for 1093, 1173, and 1253 K, respectively.

The above determined values of F_b differ with the presently accepted F_b value of 1.5 at 5% burnoff used in the OXIDE-3 code. However, no change in the value of F_b (for use in the OXIDE code) is recommended on the basis of the present data. This is because in the reactor, due to high He pressures, burnoff will be largely surface oriented, and the F_b term is likely to be quite different from that found in these laboratory experiments.

All reaction rate constant data reported herein are corrected to 1% burnoff using the laboratory-derived burnoff correlations given in Figs. 4-8 through 4-10.

Determination of Hydrogen Exponent n. As reported in Ref. 4-14, the value of n can be determined by rearranging Eq. 4-8 to give

$$\ln\left(\frac{1}{R_{ss}} - \frac{1}{R_o}\right) = \ln\left(\frac{K_2}{K_1 P_{H_2O}}\right) + n \ln P_{H_2} \quad , \tag{4-13}$$

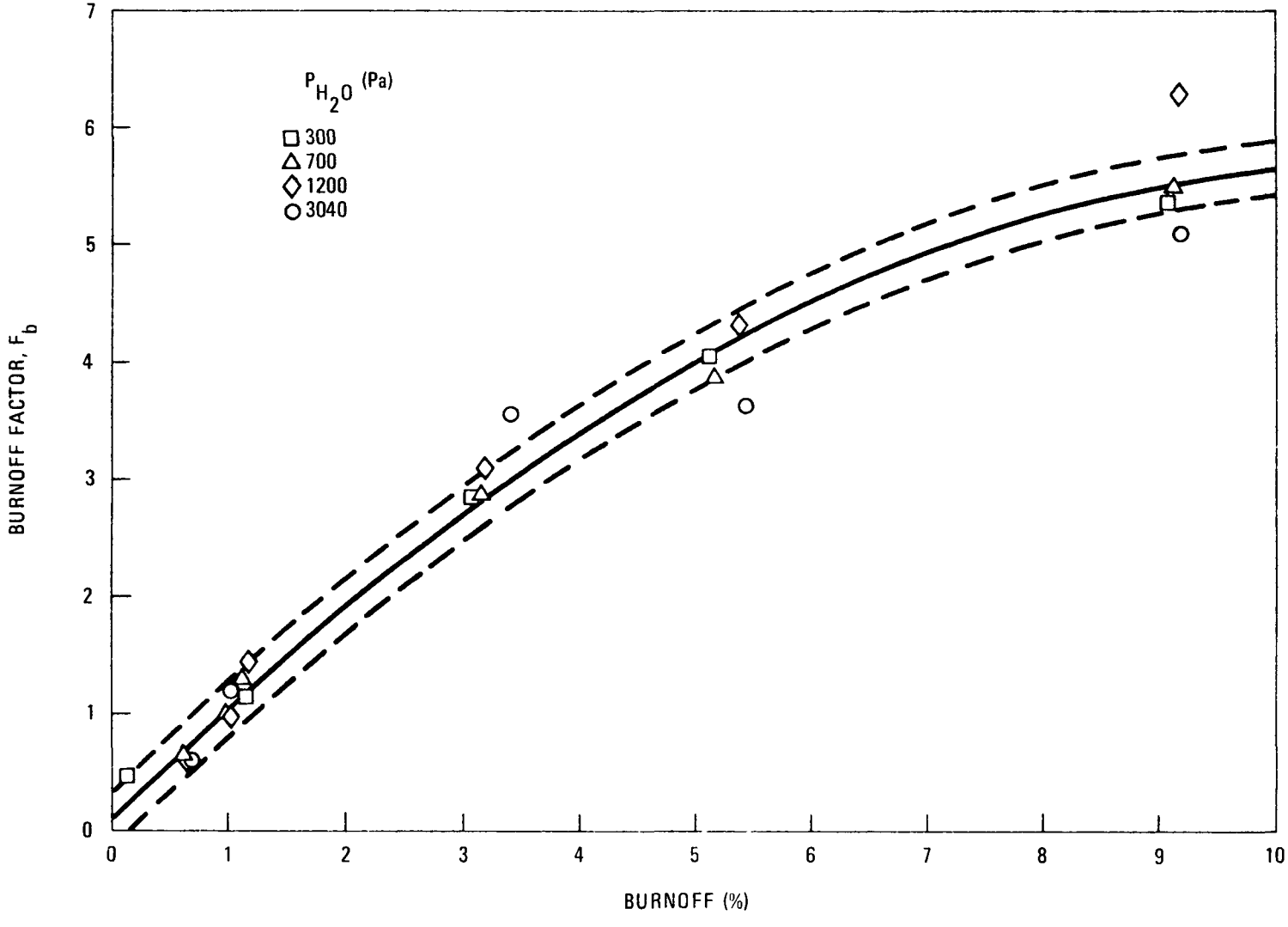

Fig. 4-8. Effect of burnoff on relative reaction rate (or burnoff factor F_b) at 1093 K

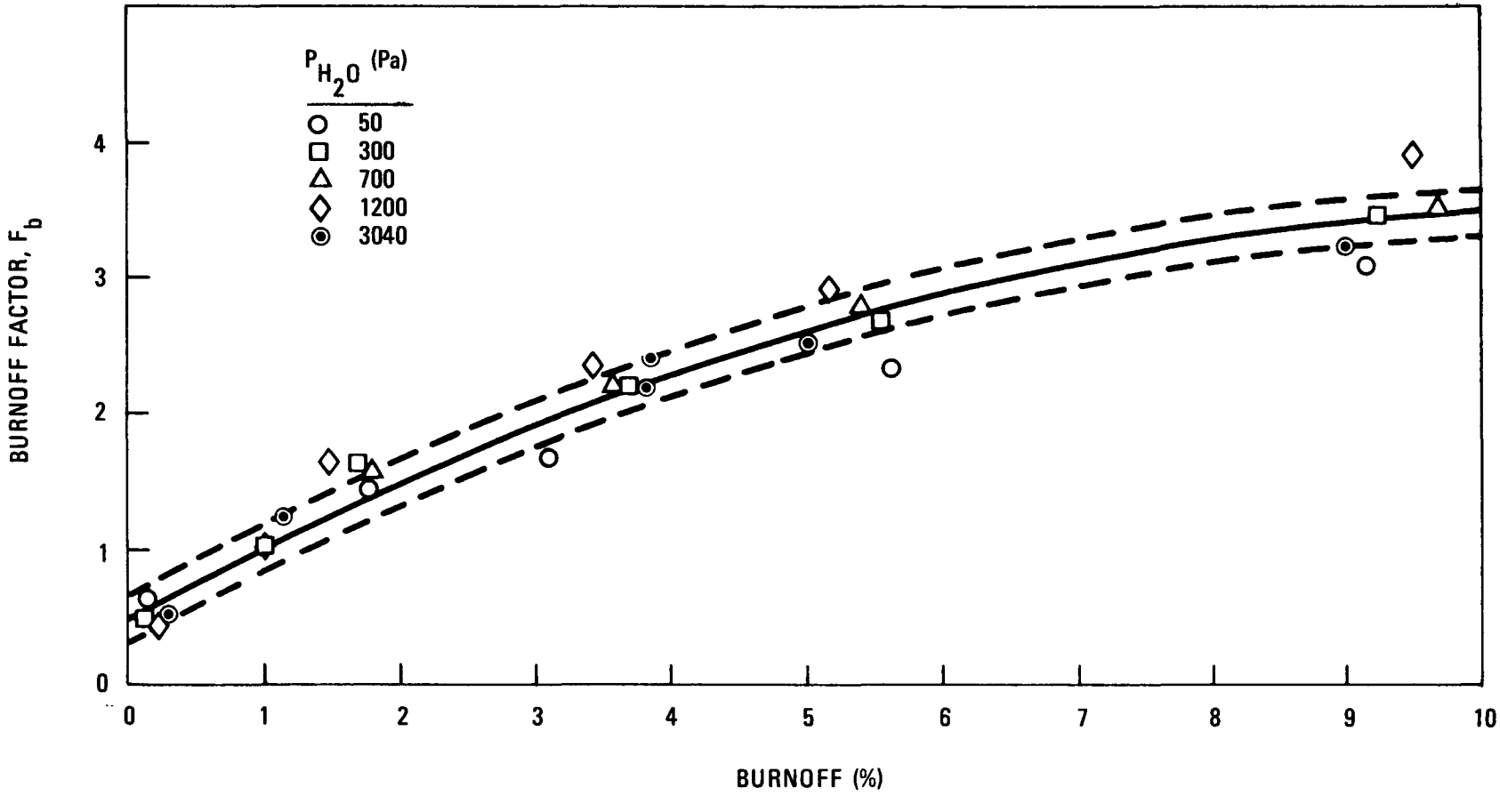

Fig. 4-9. Effect of burnoff on relative reaction rate (or burnoff factor F_b) at 1173 K

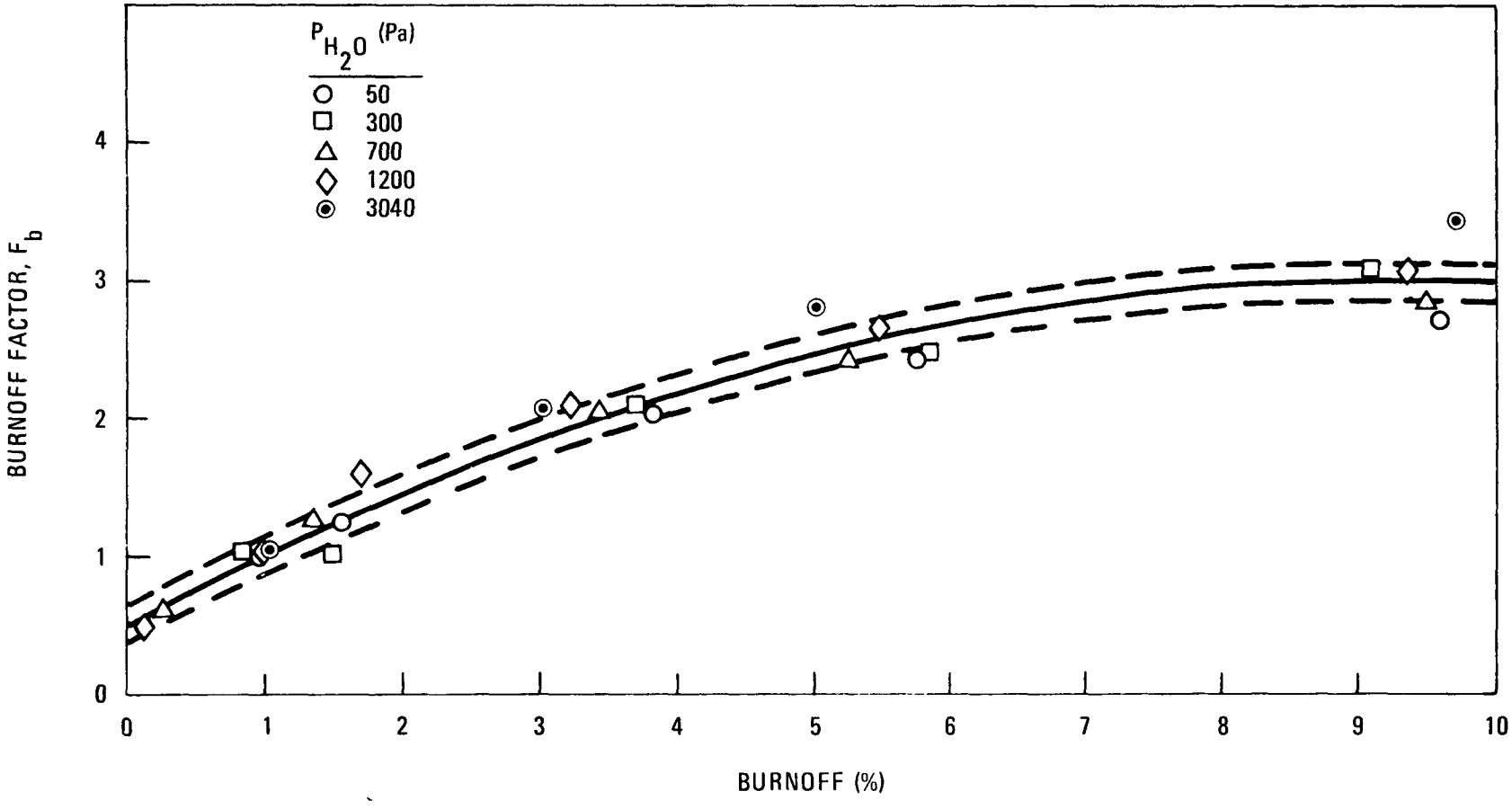

Fig. 4-10. Effect of burnoff on relative reaction rate (or burnoff factor F_b) at 1253 K

where R_{ss} = isothermal steady-state rate of reaction,

R_o = isothermal steady-state rate of reaction when $P_{H_2} = 0$.

Thus, a value of n can be obtained from the slope of a plot of $\ln(1/R_{ss} - 1/R_o)$ versus $\ln P_{H_2}$. Figure 4-11 shows such a plot, and Table 4-4 gives the experimental data, conditions, and the calculated n (slope) values. The determined value of n is 0.695 ± 0.179, and this value is in accord with n = 0.75 used in the OXIDE-3 code (Ref. 4-14); therefore, no change in the value of n is recommended.

Determination of K_1. To determine values of K_1, Eq. 4-8 is rearranged to give

$$1/R = \frac{1}{K_1 P_{H_2O}} + \frac{K_2 P_{H_2}^n}{K_1 P_{H_2O}} + \frac{K_3}{K_1} \qquad (4\text{-}14)$$

where under conditions in which $P_{H_2}^n = 0$, Eq. 4-14 reduces to:

$$1/R = 1/K_1 \left(\frac{1}{P_{H_2O}}\right) + \frac{K_3}{K_1} \quad . \qquad (4\text{-}15)$$

Accordingly, a value of K_1 can be derived from the slope of a plot of 1/R versus $1/P_{H_2O}$ in the absence of hydrogen inhibition (i.e., $P_{H_2} = 0$).

Plots of 1/R versus $1/P_{H_2O}$ for $P_{H_2} = 0$ are shown in Figs. 4-12 through 4-14. These plots were obtained from reaction rate data obtained using disk samples. Similar plots (not shown) were obtained using a cylindrical sample. It is apparent that two regimes for the dependence of 1/R on $1/P_{H_2O}$ exist, each yielding different slopes and intercepts and therefore different values of K_1 (and also K_3, as discussed in a later section). The values of K_1, associated apparent activation energies, and frequency factors obtained are given in Table 4-5. Since a profound transition in slope occurs at water vapor concentrations of about 300 Pa (3000 ppmv), the data

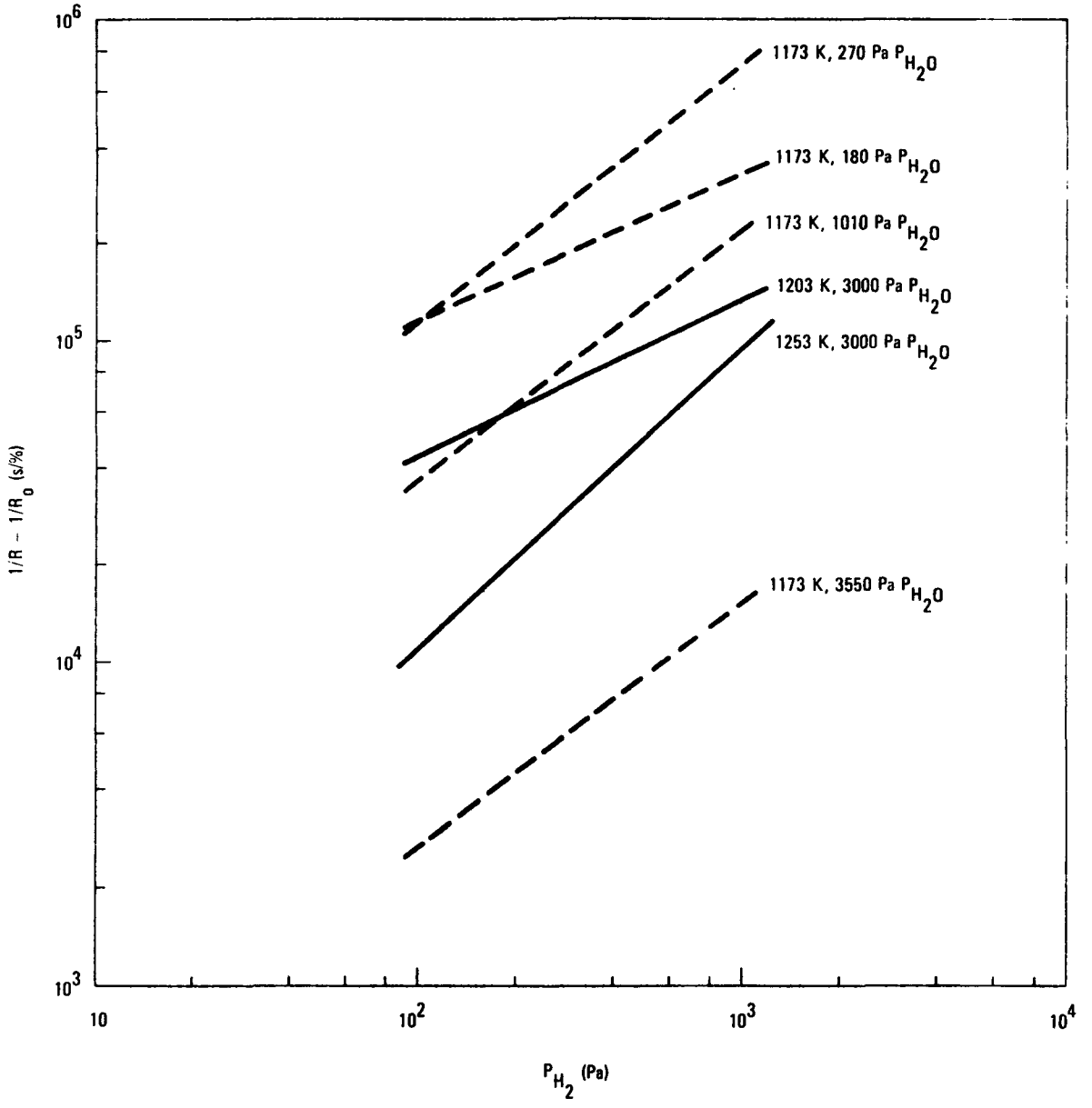

Fig. 4-11. Plot of $\ln(1/R - 1/R_O)$ versus $\ln P_{H_2}$ for the purpose of determining the coefficient of hydrogen sorption, n

TABLE 4-4
DETERMINATION OF n USING DATA FROM 12.7-mm-DIAMETER CYLINDERS

T (K)	$1/R - 1/R_o$ (s/%)	P_{H_2} (Pa)	P_{H_2O} (Pa)	Slope
1173	0.28×10^4	103	3550	
1173	1.52×10^4	1010	3550	0.732
1173	11.4×10^4	102	274	
1173	69.3×10^4	1010	274	0.782
1173	3.70×10^4	102	1010	
1173	21.9×10^4	1010	1010	0.769
1173	11.3×10^4	102	182	
1173	33.8×10^4	1010	182	0.484
1203	4.36×10^4	102	304	
1203	13.3×10^4	1010	304	0.448
1253	1.10×10^4	104	304	
1253	9.50×10^4	1010	304	0.926
				Average = 0.695
				Variance = 0.032
				Std. Dev. = 0.179

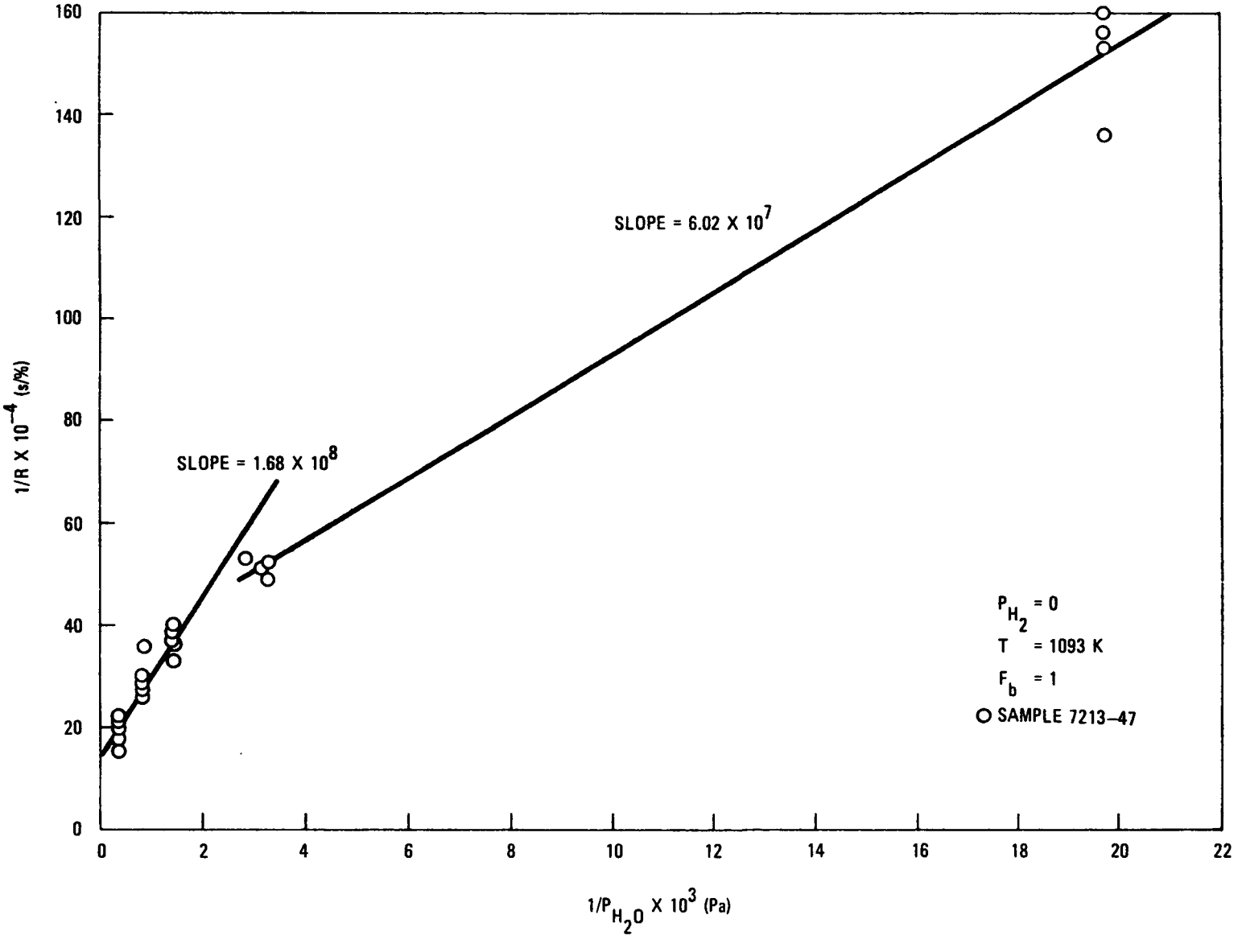

Fig. 4-12. Plot to determine values of K_1, T = 1093 K

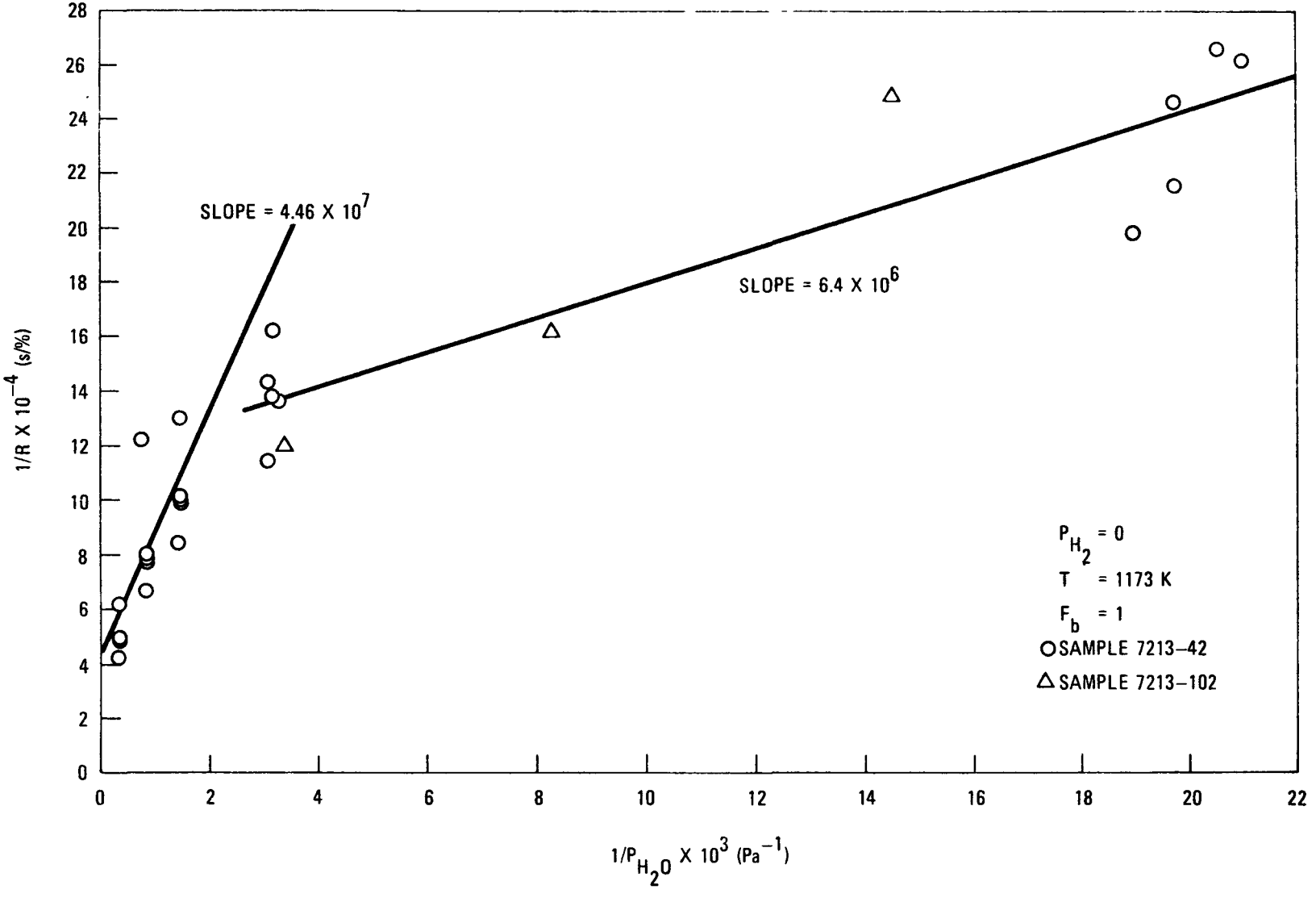

Fig. 4-13. Plot to determine value of K_1, T = 1173 K

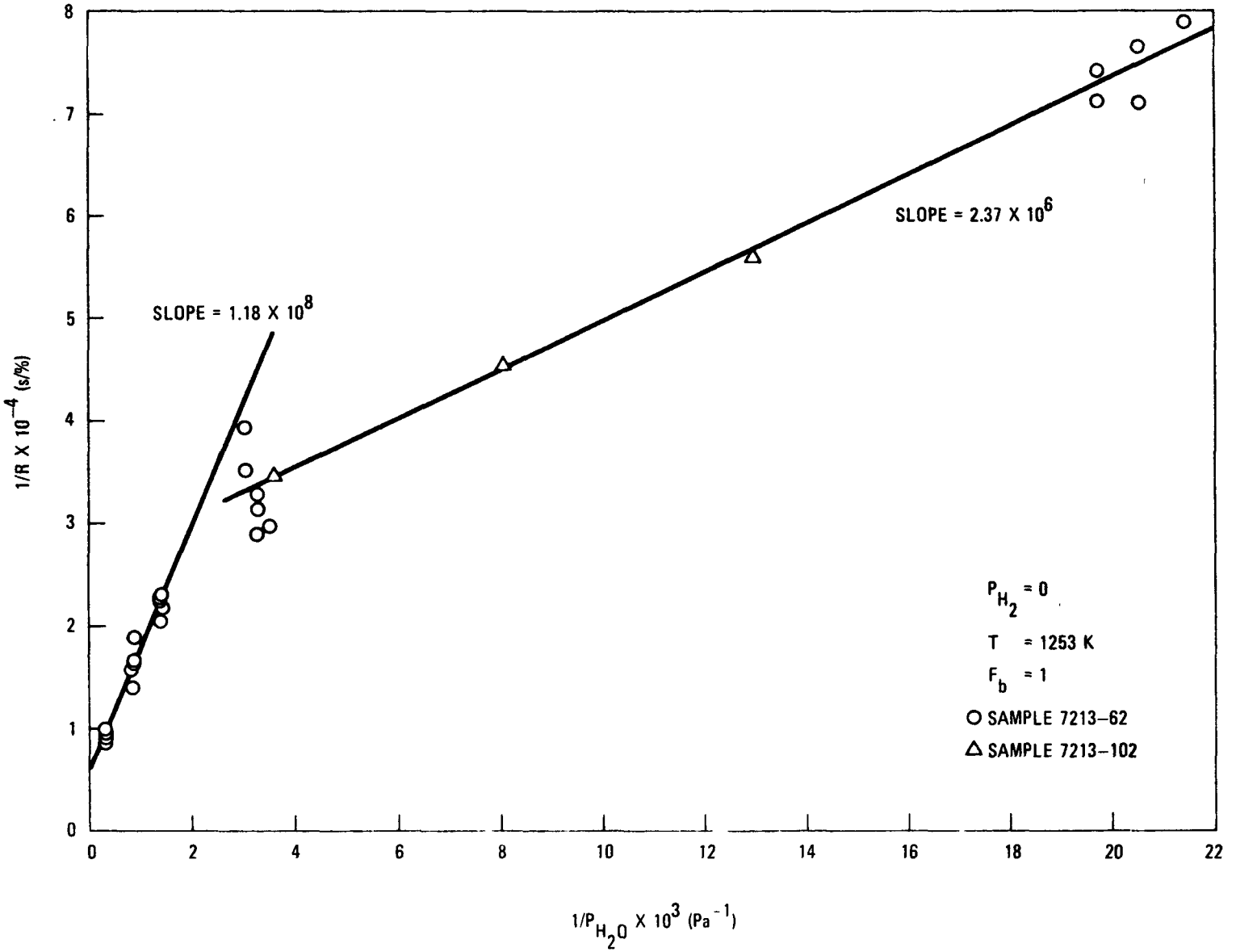

Fig. 4-14. Plot to determine value of K_1, T = 1253 K

TABLE 4-5
VALUES OF K_1, ACTIVATION ENERGIES, AND FREQUENCY FACTORS
DETERMINED FROM PLOTS OF 1/R VERSUS $1/P_{H_2O}$

Geometry	T (K)	P_{H_2O} (Pa)	$K_1 \times 10^8$ (%/s·Pa)	E_a (J/mol·K)	Frequency Factor
Cylinder	1153	>300	1.42		
Cylinder	1173		1.82		
Cylinder	1203		3.59		
Cylinder	1253		6.93	-195,000	11.0
Disk	1093	>330	0.594		
Disk	1173		2.24		
Disk	1253		8.49		
Disk	1093	50 to 330	1.66		
Disk	1173		15.7	-173,000	7.0
Disk	1253		42.2		

are presented in two sets in Table 4-5. This transition may reflect the effects on K_1 from the j_1 contribution, the rate of evaporation of water molecules from the substrate surface (see Eq. 4-9). At low water vapor concentrations, j_1 is assumed to be negligible. This may not be true at high water concentrations where fractional coverage of the active sites may approach unity.

The experimentally obtained activation energy of -172 kJ/mol·K (-41.2 kcal/mole·K) at lower partial pressures of water vapor agrees quite well with the value -171 kJ/mol·K (-40.9 kcal/mole·K) given in the OXIDE-3 code (Ref. 4-14). On the other hand, the activation energy of -195 kJ/mol·K (-46.7 kcal/mole·K) obtained at high water partial pressures is appreciably higher than the OXIDE-3 value.

Figure 4-15 is a plot of the K_1 values versus 1/T. Included is a curve representing the K_1 values used in the OXIDE-3 code (Ref. 4-14). It can be seen that the new K_1 values are appreciably lower than the OXIDE-3 values.

A fit to the K_1 values at high water vapor concentrations in Fig. 4-15 was accomplished by first using the POLFIT computer code to calculate parent standard deviations from the 1/R versus $1/P_{H_2O}$ plots. The variance associated with each slope was determined by use of the relationship

$$\sigma^2_{slope} = \frac{N\sigma_i^2}{N\Sigma x_i^2 - (\Sigma x_i)^2} \quad , \tag{4-16}$$

where N = number of data points,

σ_i = parent standard deviation of the dependent variable (1/R),

x_i = input independent variable $(1/P_{H_2O})$,

σ^2_{slope} = variance of the slope used in Eq. 4-15.

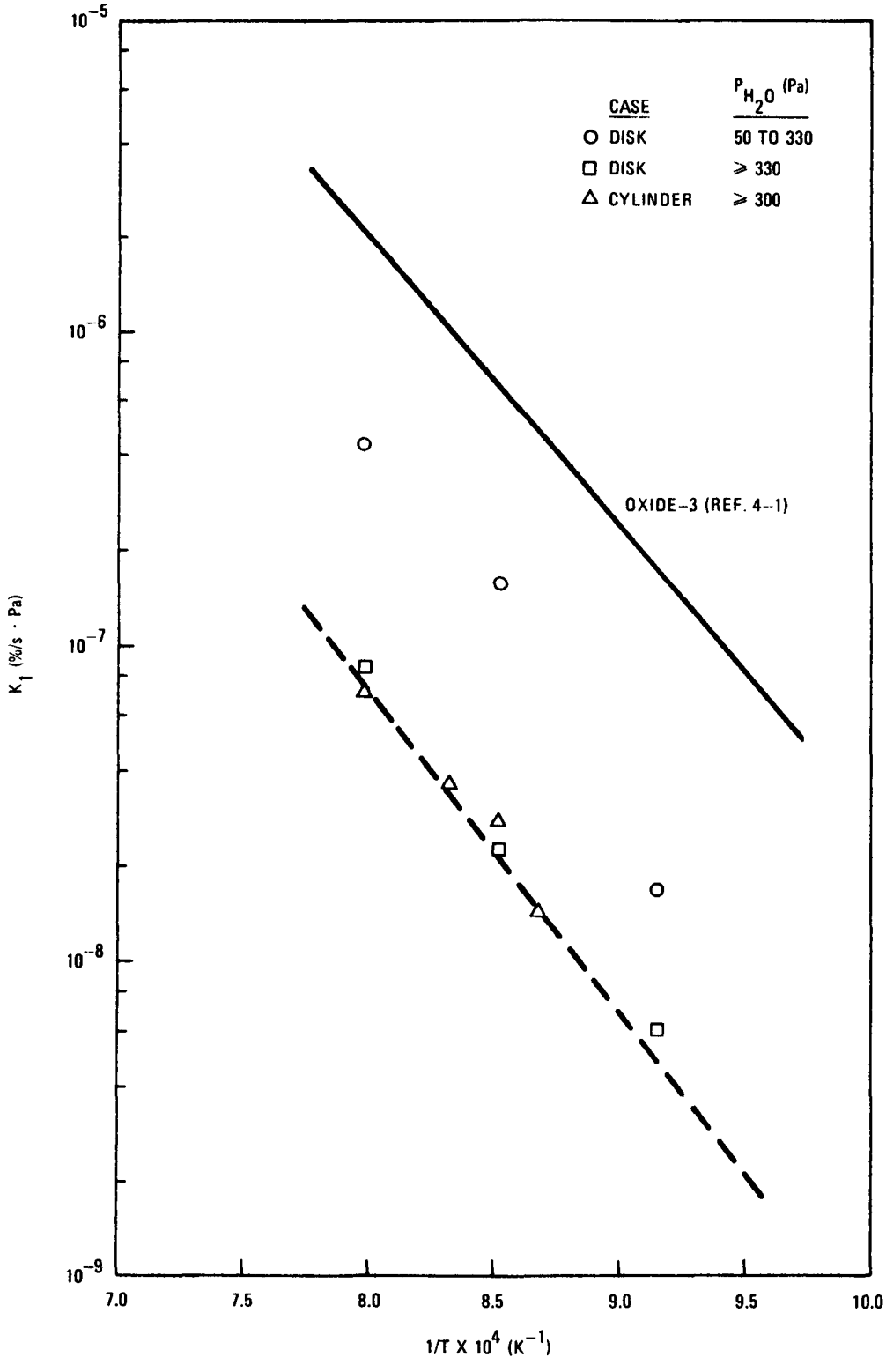

Fig. 4-15. Temperature dependence of the rate constant K_1 for the reaction of water vapor with H-451 graphite

POLFIT was then used to calculate the activation energy and frequency factor from the K_1 values (in Fig. 4-15), where the values were inversely weighed by the calculated variance associated with each value.

The resulting line (solid line in Fig. 4-15) is represented by

$$K_1(\%\ hr^{-1}\ atm^{-1}) = 4.0 \times 10^9 \exp(-46{,}700/RT) \quad ,$$

where R = 1.987 cal/deg·mole, or

$$K_1(\%/s{\cdot}Pa) = 11.0 \exp(-195{,}000/R'T) \quad ,$$

where R' = 8.314 J/K·mole. Values of K_1, as defined by this expression for 1% burnoff and $P_{H_2O} > 300$ Pa, are recommended for use in code calculations.

A recommendation for K_1 at $P_{H_2O} < 300$ Pa is not justified because of the meagre amount of data at low water vapor concentrations.

Determination of K_2. To determine values of K_2, Eq. 4-8 is rearranged to give

$$1/R = \frac{K_2}{K_1 P_{H_2O}} P_{H_2}^n + \frac{1 + K_3 P_{H_2O}}{K_1 P_{H_2O}} \quad . \tag{4-17}$$

Accordingly, a plot of 1/R versus $P_{H_2}^n$ should yield a straight line of slope $K_2/K_1P_{H_2O}$. A complication is that K_2 requires a prior knowledge of K_1, and any errors associated with K_1 would be propagated into the determination of K_2. Another possible source of error in K_2 is the fact that hydrogen sorption on graphite is a relatively slow process. This gives rise to a decreasing apparent oxidation rate with time up to about 20 hours, after which the oxidation rate is relatively constant. This phenomenon is illustrated in Figs. 4-16 and 4-17.

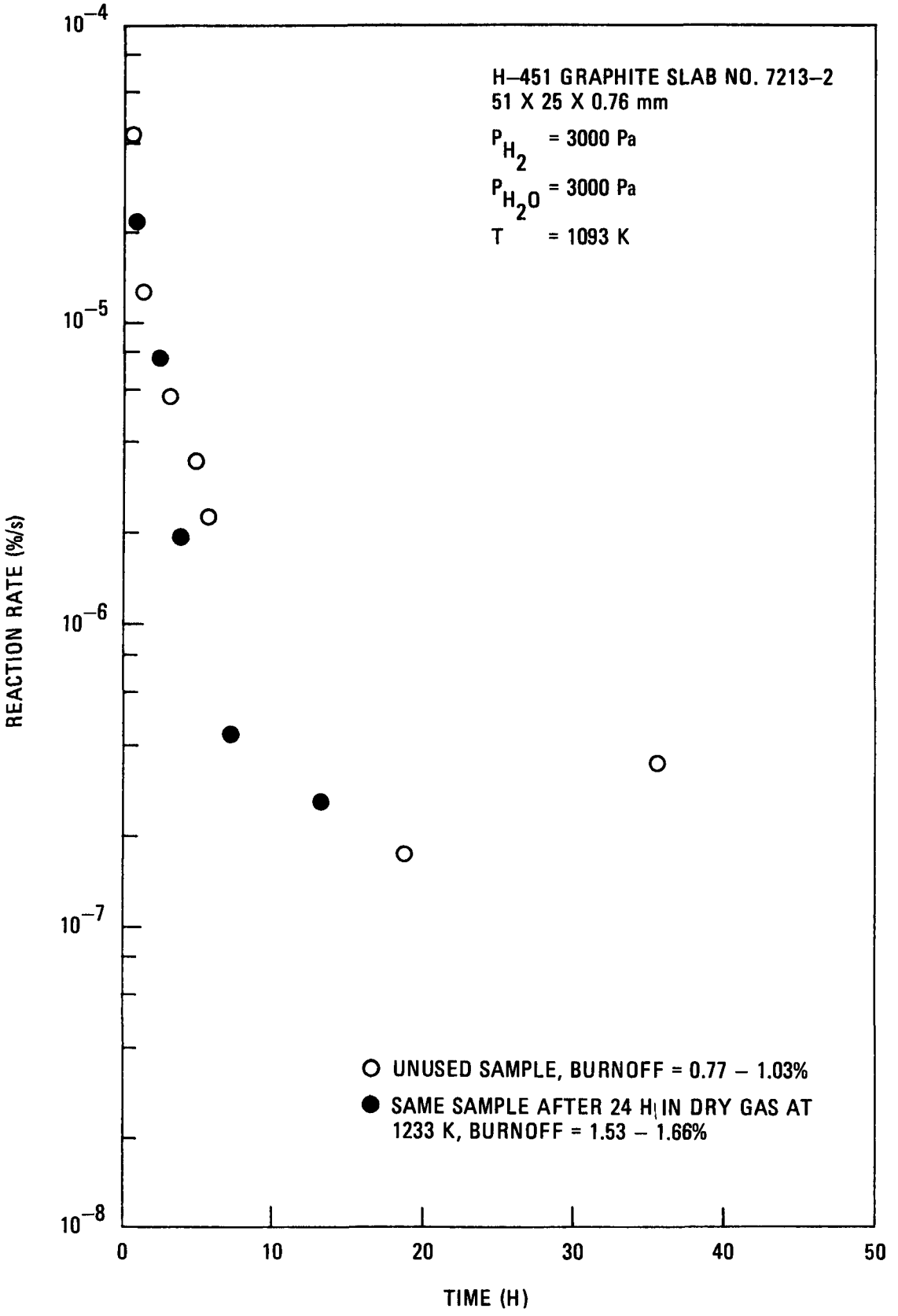

Fig. 4-16. Effect of slow hydrogen sorption on apparent oxidation rate

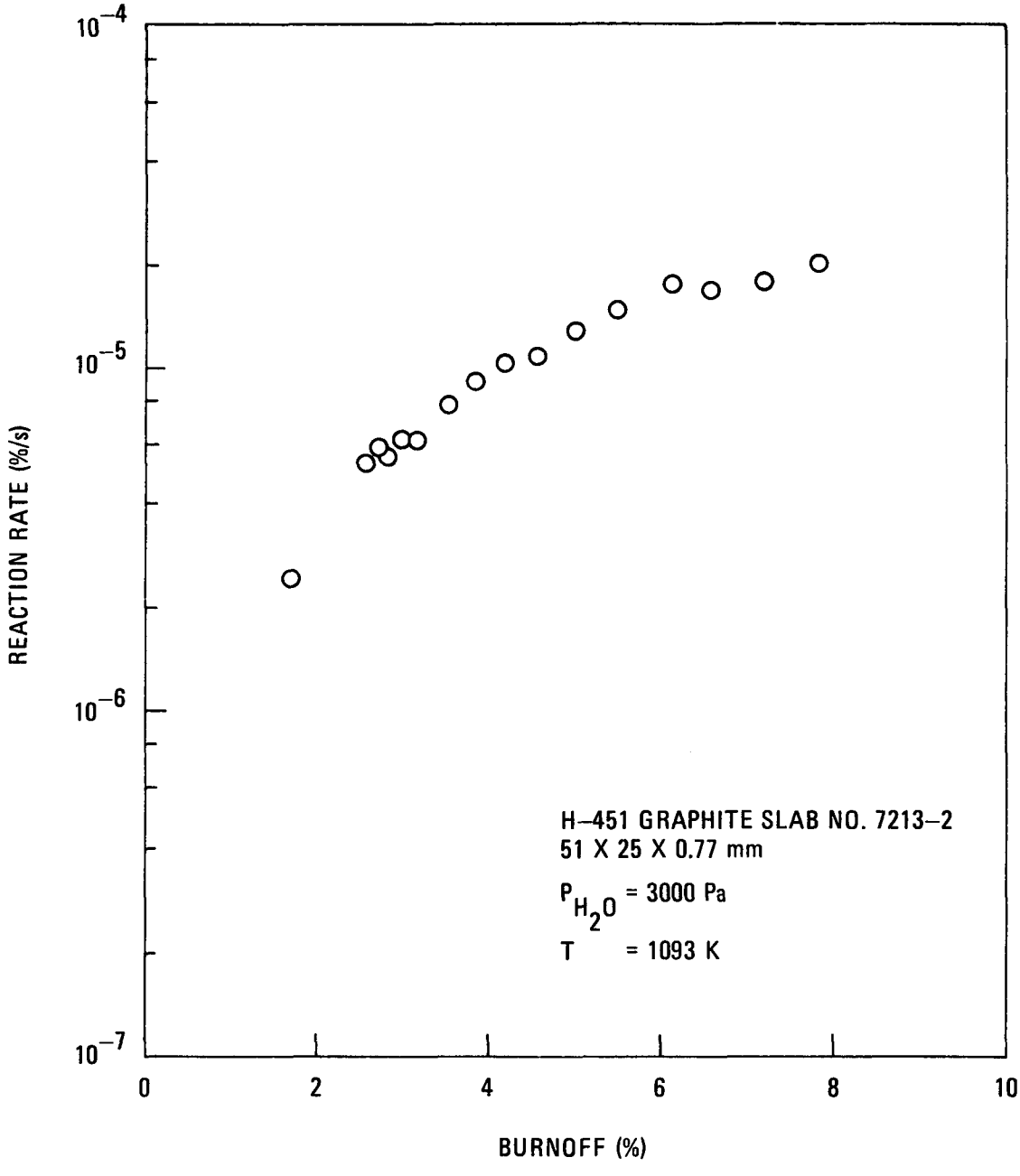

Fig. 4-17. Oxidation rate in the absence of hydrogen

To obtain the data in Fig. 4-16, a thin slab sample of H-451 graphite was first heated to 1093 K and then exposed to a gaseous mixture of 3% H_2 and 3% H_2O in helium (open circles). The reaction decreased continuously for up to about 20 hours. The same sample was then heated to 1233 K in dry gas for 24 hours to desorb hydrogen. The experiment was then exposed to the same gas mixture at 1093 K (closed circles); the reaction rate decreased as before. The sample was then oxidized in the absence of hydrogen, resulting in a more typical burnoff behavior (see Fig. 4-17); i.e., the reaction rate characteristically increased with time (or burnoff).

This phenomenon has dictated an experimental approach in which neither hydrogen partial pressure nor temperature is varied on a single sample in the course of a run. Moreover, data are taken only after at least 24 hours of equilibration with the process gas.

Table 4-6 and Fig. 4-18 present the experimentally determined values of K_2. The data exhibit considerable scatter, apparently due to the transient hydrogen phenomenon mentioned above, even though precautions were taken to minimize the effect of the phenomenon. Included in Fig. 4-18 is a line representing values of K_2 given in the OXIDE-3 report (Ref. 4-14); it can be seen that the new data lie appreciably below the OXIDE-3 line. The line through the data in Fig. 4-18 is an empirical fit, drawn with the same slope (i.e., same activation energy) as the line representing the OXIDE-3 data.

An attempt was made to fit the data points in Fig. 4-18 utilizing a statistical (least squares) method. The POLFIT computer code was used. For the determination of the activation energy and the frequency factor, least-squares determined slopes ($K_2/K_1P_{H_2O}$) were weighted inversely by their respective calculated variances. The resulting line did not fit the data as well as the empirical line.

The line through the data in Fig. 4-18 (i.e., the empirical line) is represented by

TABLE 4-6
VALUES OF THE RATE CONSTANT K_2 DETERMINED FROM REACTION RATE DATA FOR THE REACTION OF WATER VAPOR WITH H-451 GRAPHITE

Geometry	T (K)	$\frac{K_2}{K_1 P_{H_2O}}$	P_{H_2O} (Pa)	$K_1 \times 10^8$ (%/s·Pa)	$K_2 \times 10^3$ ($Pa^{-0.75}$)
Cylinder	1173	8.45×10^1	3650	2.04	6.29
Cylinder	1173	6.41×10^2	1010	2.04	13.2
Cylinder	1203	1.80×10^2	3140	3.36	19.0
Cylinder	1203	7.03×10^2	304	3.36	7.18
Cylinder	1253	5.46×10^2	304	7.35	12.2
Cylinder	1253	1.49×10^1	3240	7.35	3.54
Disk	1173	4.31×10^3	314	2.04	27.6
Disk	1173	2.38×10^3	709	2.04	34.4
Disk	1173	5.87×10^2	1220	2.04	14.6
Disk	1173	3.08×10^2	2940	2.04	18.5
Disk	1253	3.33×10^2	304	7.35	7.43
Disk	1253	1.33×10^1	719	7.35	1.23
Disk	1253	9.42×10^0	1220	7.35	0.845
Disk	1173	2.10×10^4	49	13.6	140
Cylinder	1173	1.73×10^3	182	13.6	42.8

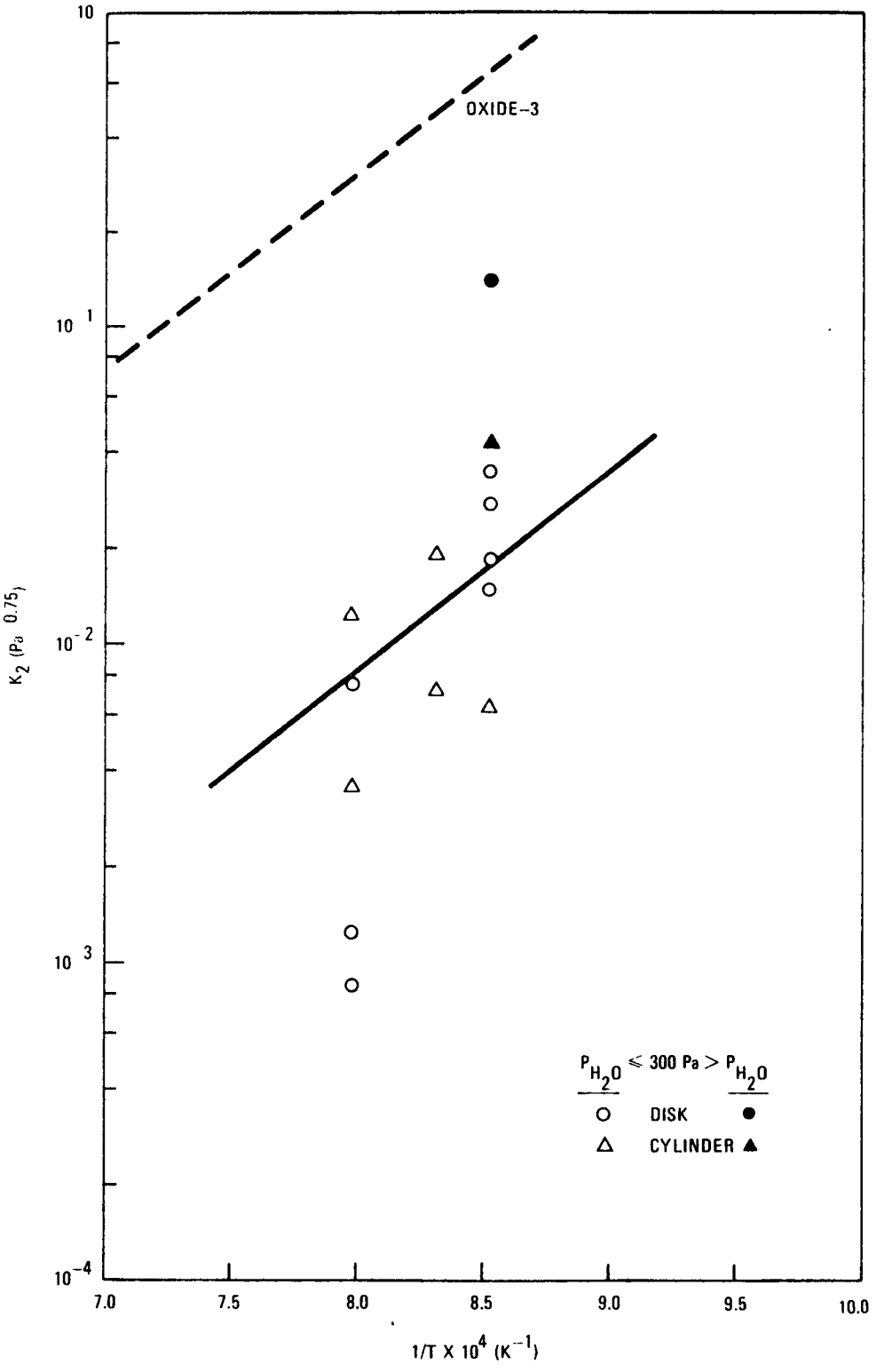

Fig. 4-18. Temperature dependence of rate constant K_2

$$K_2 \ (atm^{-0.75}) = 4.6 \times 10^{-4} \exp(28{,}600/RT)$$

or

$$K_2 \ (Pa^{-0.75}) = 8.2 \times 10^{-8} \exp(119{,}700/R'T)$$

for $P_{H_2O} \geq 300$ Pa. Values of K_2 defined by this expression are recommended for use in code calculations. (Note that the frequency factor was changed relative to the OXIDE-3 value; however, in view of the data scatter, the activation energy was not changed. It is of interest that the actual calculated activation energy using the weighting technique described above was 117 kJ/mole (or 28.0 kcal/mole).

Determination of K_3. According to Eq. 4-17, the intercept of a plot of 1/R versus $P_{H_2}^n$ is $(1 + P_{H_2O} K_3)/P_{H_2O} K_1$. Thus, values of K_3 can be obtained if values of K_1 are known. In determining values of K_3, the intercept data were partitioned into four near-isobaric ranges as shown in Table 4-7: in set 1, $P_{H_2O} \simeq 3000$ Pa; in set 2, $P_{H_2O} \simeq 710$ to 1200 Pa; in set 3, $P_{H_2O} \approx 300$ Pa; and in set 4, $P_{H_2O} \gtrsim 180$ Pa. The calculated values of K_3 are given in Table 4-7 and plotted versus 1/T in Fig. 4-19. It is apparent that the K_3 values in the high range of water vapor concentration (300 to 3000 Pa) are grouped together rather closely; however, the K_3 values at lower water concentration are significantly higher. This phenomenon is similar to the previous observations of K_1 and K_2, namely, that an apparent transition in rate constant values occurs at around 300 Pa H_2O. It can be seen in Fig. 4-19 that the K_3 values found lie appreciably below the line representing the K_3 values used in OXIDE-3 (Ref. 4-14).

The weighted line shown in Fig. 4-19 was calculated using the computer code POLFIT. Each intercept point was weighted according to the inverse of its variance. The variance of each intercept obtained from plots of 1/R versus $P_{H_2}^n$ was calculated using

$$\sigma_I^2 = \frac{\sigma^2 \Sigma x_i^2}{N\Sigma x_1^2 - (\Sigma x_i)^2} \quad , \tag{4-18}$$

TABLE 4-7
VALUES OF RATE CONSTANT K_3 DERIVED FROM REACTION RATE DATA
FOR REACTION OF WATER VAPOR WITH H-451 GRAPHITE

Geometry	T (K)	$\frac{K_3 P_{H_2O} + 1}{K_1 P_{H_2O}}$	P_{H_2O} (Pa)	$K_1 \times 10^8$ (%/s·Pa)	$K_3 \times 10^3$ (Pa^{-1})
Set 1					
Cylinder	1153	1.25×10^5	3170	1.43	1.47
Cylinder	1173	7.48×10^4	3620	2.04	1.25
Cylinder	1203	1.23×10^4	3140	3.39	0.98
Cylinder	1253	1.22×10^4	3270	7.37	0.59
Disk	1173	5.13×10^4	2970	2.04	0.71
Disk	1253	9.03×10^3	3190	7.35	0.35
Set 2					
Cylinder	1173	1.38×10^5	1040	2.04	1.86
Disk	1173	7.20×10^4	704	2.04	0.22
Disk	1173	9.69×10^4	1180	2.04	1.13
Disk	1253	1.55×10^4	1220	7.35	0.32
Disk	1253	2.30×10^4	719	7.35	0.30
Set 3					
Cylinder	1153	3.51×10^5	304	1.44	1.76
Cylinder	1173	3.30×10^5	271	2.04	3.04
Cylinder	1203	1.37×10^5	304	3.39	1.37
Cylinder	1253	7.28×10^4	304	7.35	0.57
Set 4					
Cylinder	1173	3.72×10^5	177	13.6	44.9
Disk	1173	2.63×10^5	49	13.6	15.4

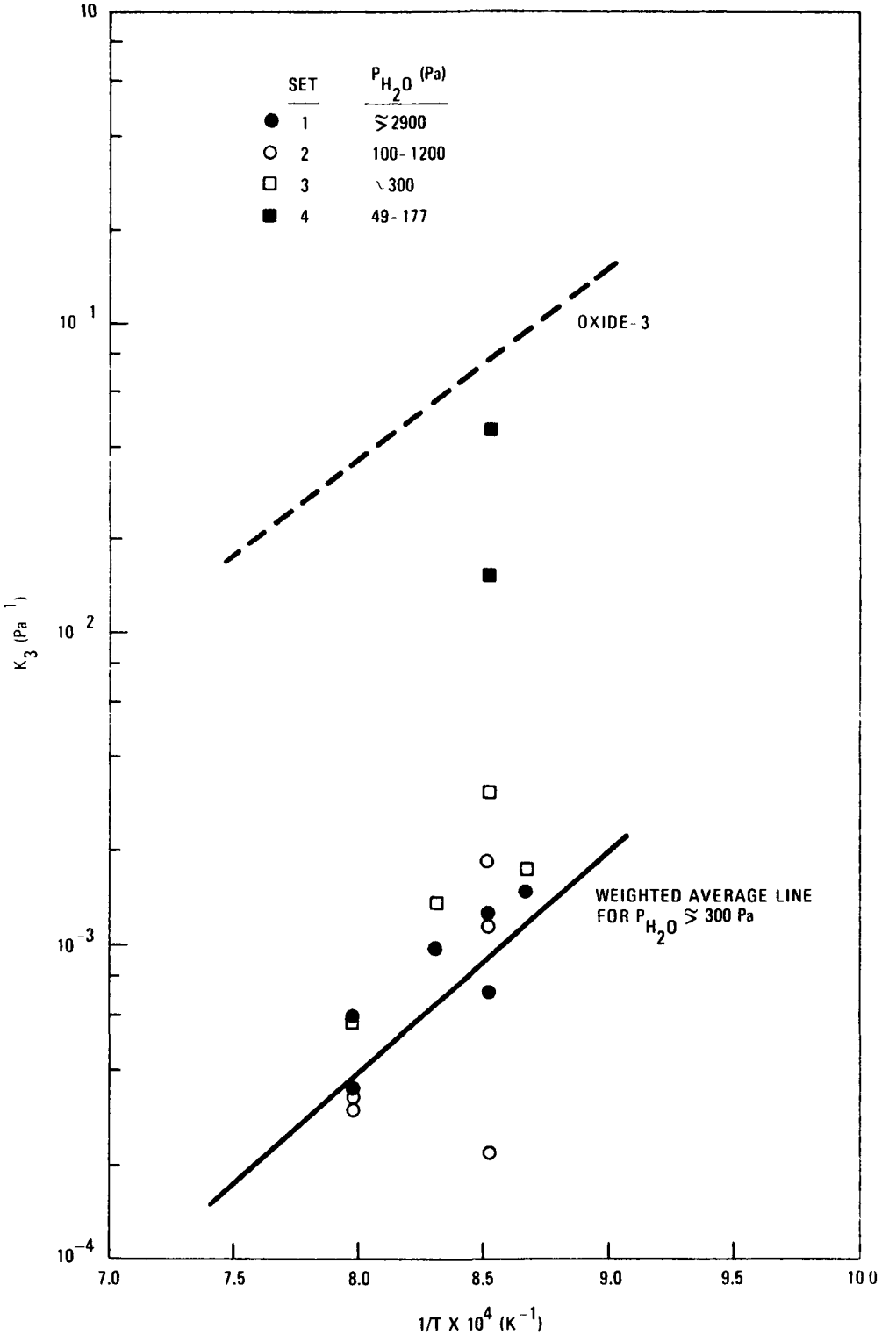

Fig. 4-19. Temperature dependence of K_3

where σ^2 = variance calculated for y_i (1/R), x_i^2 = input data of independent variable $(P_{H_2}^n)^2$, n = number of data points, and σ_I^2 = variance of the intercept.

Recommended values for K_3 at water vapor concentrations above 300 Pa are given by the expression

$$K_3 \ (atm^{-1}) = 1.3 \times 10^{-4} \exp(31,400/RT)$$

or

$$K_3 \ (Pa^{-1}) = 1.3 \times 10^{-9} \exp(131,400/R'T),$$

which corresponds to the line through the data in Fig. 4-19.

Discussion. The data obtained in this study clearly show that a single set of rate constants is not valid over the wide range of water concentration which could be encountered under normal and accident conditions in HTGR systems. The rate constants show a significant change at about 300 Pa H_2O. This apparent change may be due to the assumptions inherent in the Langmuir-Hinshelwood equation, in particular that the reaction rates represented by each constant (see previous section on theory) vary linearly with water vapor pressure.

The observation that hydrogen sorption on graphite is relatively slow and has a profound effect on the apparent oxidation rate (see Fig. 4-16) further suggests that different sets of constants should be used for normal and accident conditions in the reactor. In the case of normal reactor operation, water vapor concentrations up to 10 Pa and hydrogen concentrations up to 500 Pa are anticipated, and equilibration of hydrogen sorption is expected due to the long times involved. Under these conditions, one would expect relatively low oxidation rates. On the other hand, in the case of a major steam-leak accident, the core is rapidly subjected to high water concentrations and the hydrogen pressure increases as the water reacts with graphite. Under these conditions, one would expect the

graphite oxidation rate to start off relatively high and then decrease as hydrogen sorption occurs. Neglecting the effects of transient hydrogen sorption in either case should result in conservatively high estimates of the extent of graphite oxidation.

Table 4-8 summarizes values of the constant n and expressions for the rate constants K_1, K_2, and K_3 as recommended for H-451 graphite on the basis of the present study and as given in the OXIDE-3 report (Ref. 4-14). The recommended rate constants are for the range of high water vapor concentrations where the most reliable data were obtained. Further research is required to obtain rate constants for H-451 at low water vapor concentrations.

Calculated rates of graphite oxidation are compared with experimental rates in Figs. 4-20 and 4-21. The calculated rates, which are in the form of curves, were calculated using values of the constants from Table 4-8 in the Langmuir-Hinshelwood equation. The experimental rates are measured values for H-451 graphite samples. It can be seen that curves calculated with the new constants fit the experimental data more closely than curves calculated using the OXIDE-3 constants, particularly for $P_{H_2O} > 300$ Pa.

Subtask 640: Carbon Deposition Studies

Summary

Laboratory studies of the carbon deposition process are being performed to establish the magnitude of carbon deposition to be expected in the HTGR. The results show that T-22 steel, used in the steam generator, is an active catalyst; higher Cr- and Ni-containing alloys are less reactive. The apparent net reaction is $2CO = C + CO_2$; therefore, recycling of H_2O may not occur. An incubation period is always observed prior to the onset of visible carbon during which catalyst formation is presumed to occur. The most active catalyst appears to be in the deposit itself, in the form of iron crystals attached to the ends of the carbon filaments.

TABLE 4-8
SUMMARY OF CONSTANTS FOR USE IN THE LANGMUIR-HINSHELWOOD EQUATION

Constant	Units	Recommended for H-451 Graphite (Burnoff = 1%, $P_{H_2O} \geq 300$ Pa)	Former (OXIDE-3) (Burnoff = 1%)
n	--	0.75	0.75
K_1	%/h·atm	$4.0 \times 10^{9} \exp(-46{,}700/RT)$ [a]	$1.069 \times 10^{10} \exp(-40{,}900/RT)$
	%/s·Pa	$11.0 \exp(-195{,}400/R'T)$ [b]	
K_2	$atm^{-0.75}$	$4.6 \times 10^{-4} \exp(28{,}600/RT)$	$1.66 \times 10^{-2} \exp(28{,}600/RT)$
	$Pa^{-0.75}$	$8.2 \times 10^{-8} \exp(119{,}700/R'T)$	
K_3	atm^{-1}	$1.3 \times 10^{-4} \exp(31{,}400/RT)$	$5.31 \times 10^{-2} \exp(27{,}500/RT)$
	Pa^{-1}	$1.3 \times 10^{-9} \exp(131{,}400/R'T)$	

[a] $R = 1.987$ cal/deg·mole.

[b] $R' = 9.314$ J/K·mol.

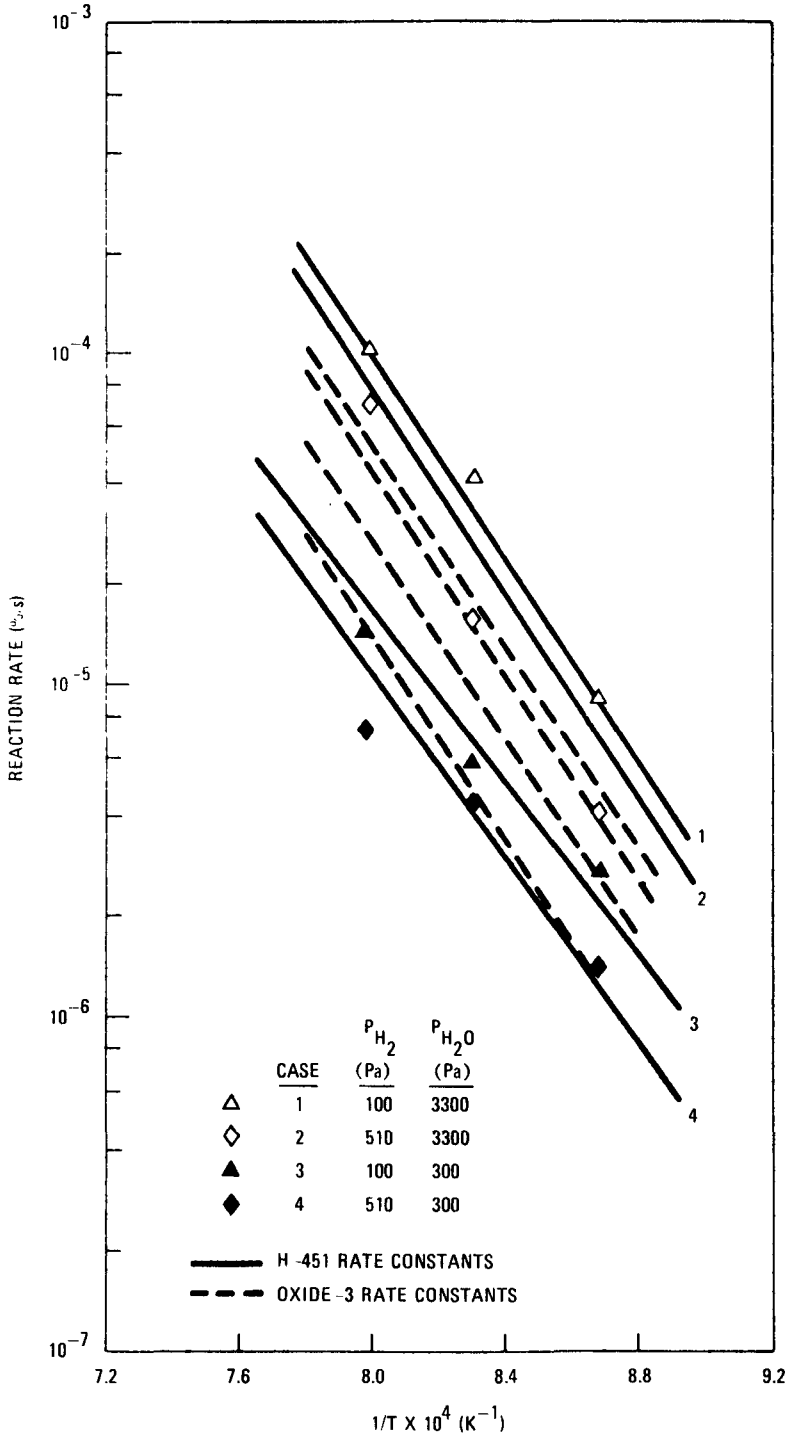

Fig. 4-20. Comparison of experimental data with curves calculated using new rate constants (for H-451 graphite) and rate constants reported in OXIDE-3 report (Ref. 4-1), P_{H_2} = 100 and 510 Pa

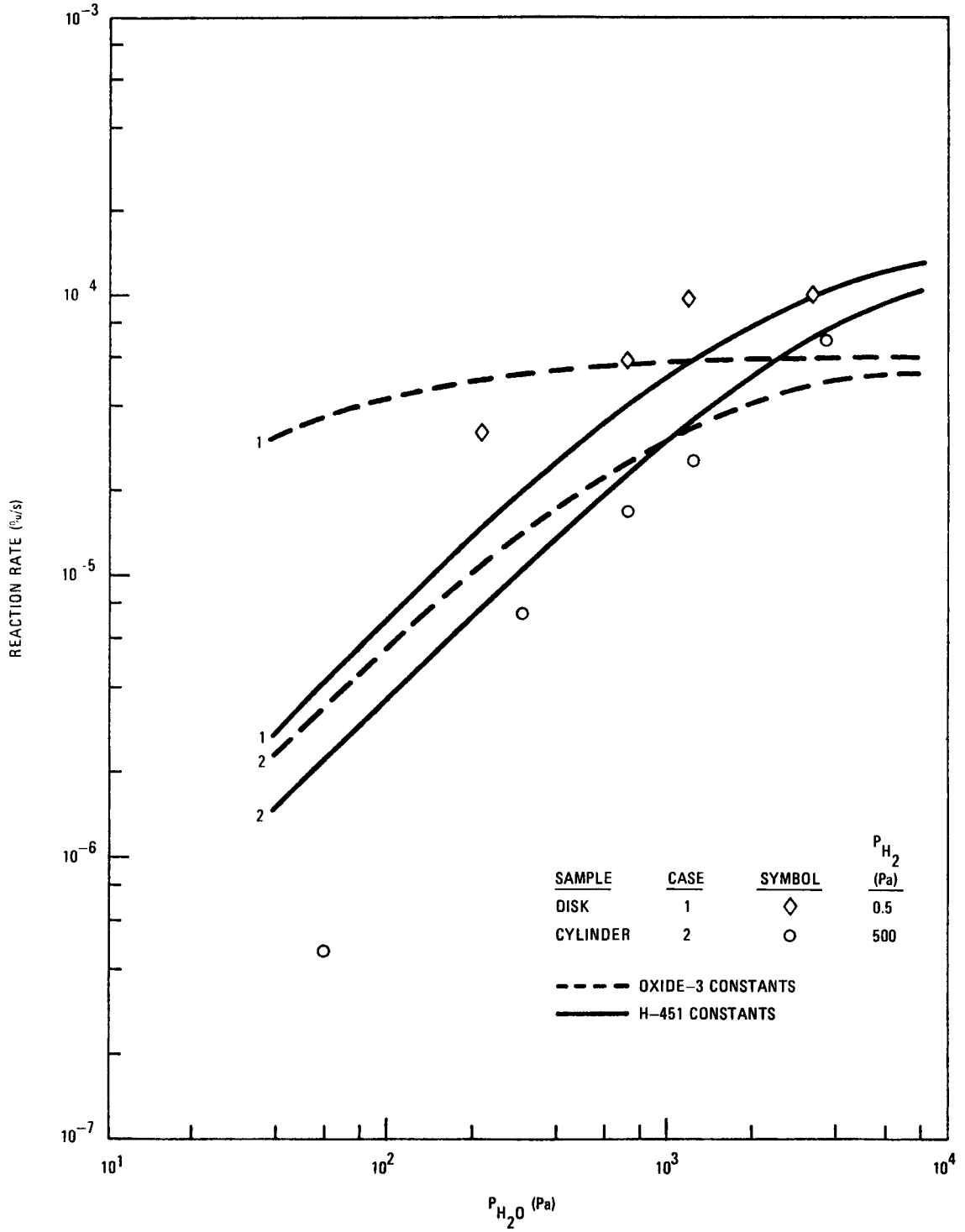

Fig. 4-21. Comparison of experimental data with curves calculated using new rate constants (for H-451 graphite) and rate constants reported in OXIDE-3 report (Ref. 4-1), P_{H_2} = 0.5 and 500

The process appears to be self-limiting in the high-concentration region due to eventual encapsulation of the catalyst crystal with carbon; however, the catalyst can be reactivated by exposure to oxidizing gas conditions.

Introduction

In the HTGR a carbon transfer may occur through the water gas (Eq. 4-19) and Boudouard (Eq. 4-20) reactions acting in one direction to oxidize the core graphite and then reversing their direction to deposit carbon under conditions found elsewhere in the primary circuit, notably the steam generator

$$\text{Water gas:}\quad C + H_2O \underset{\text{C deposition}}{\overset{\text{oxidation of core}}{\rightleftharpoons}} H_2 + CO \qquad (4\text{-}19)$$

$$\text{Boudouard:}\quad C + CO_2 \underset{\text{C deposition}}{\overset{\text{oxidation of core}}{\rightleftharpoons}} 2\,CO \qquad (4\text{-}20)$$

Other reactions which affect reactions 4-19 and 4-20 are oxidation of metals, particularly Fe by H_2O or CO_2 and the water shift reaction:

$$\text{Water shift:}\quad CO + H_2O \rightleftharpoons CO_2 + H_2 \quad . \qquad (4\text{-}21)$$

The reverse of reactions 4-19 and 4-20 is known to occur significantly only in the presence of suitable catalysts, the active ones being Fe and Ni, which occur abundantly in the steam generator tubing.

The H_2O in reaction 4-19 could initially come from steam inleakage, as from steam generator leaks. Moreover, it is possible that the occurrence of reaction 4-19 would recycle water and cause further oxidation of the core. This cyclic feature of carbon transport could cause an acceleration of the core corrosion rate for a given steam inleakage term. It is therefore important to determine the rates of these two reactions on steam generator materials. Because of water recycling, the case of reaction 4-19 predominating is more severe.

The goals of the study are:

1. Establish the magnitude of carbon deposition expected in HTGRs.

2. Determine the rate of carbon deposition on alloys of technical interest as a function of the following parameters:

   a. Alloy type.
   b. Surface condition: milled, polished, oxidized, etc.
   c. Temperature.
   d. Gas mixture: P_{H_2}, P_{CO}, P_{CO_2}, P_{H_2O}, and P_{H_2}/P_{H_2O}.

3. Investigate simple ways of mitigating carbon deposition reactions if it should prove necessary or desirable.

It is expected that this study will close the gaps in existing information.

Experimental Procedure and Apparatus

Comparative Tests. A qualitative screening test was set up in which several samples of different candidate steam generator alloys were tested together to determine their relative reaction rates.

The apparatus consisted of a controllable Lindberg furnace fitted with a 7-cm-diameter quartz tube containing the specimens, a regulated manifold to deliver the chosen gas mixture, an ice saturator maintained at constant temperature to inject a specified concentration of H_2O, a flowmeter to control inlet flow, a molecular sieve trap at the furnace outlet to capture H_2O, and a $Ba(OH)_2$ bubbler to capture any CO_2 produced by precipitation as $BaCO_3$. This equipment is shown schematically in Fig. 4-22.

The samples were small flat rectangular plates (approximately 20 cm^2) of 410 SS, 304 SS, Inconel 600, and T-22. The compositions of these alloys

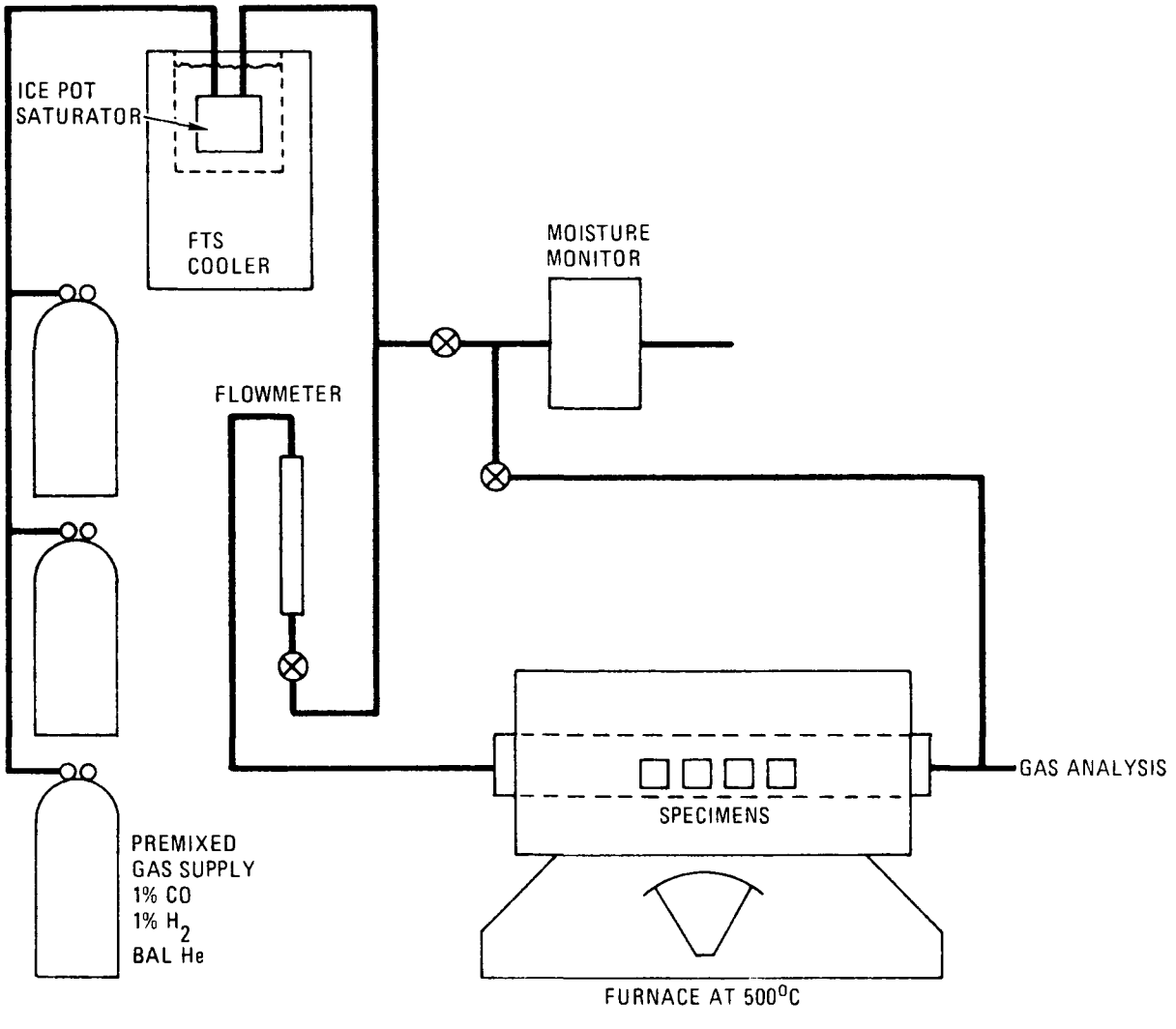

Fig. 4-22. Apparatus for carbon deposition comparative tests

are given in Table 4-9. The gas mixture used was 1.0 kPa CO and 1.0 kPa H_2 in He with either <5.0 Pa H_2O ($H_2/H_2O \geq 200$) or 30 Pa H_2O ($H_2/H_2O \simeq 33$).

Microbalance Rate Tests. The second type of test utilized automatic recording Cahn microbalances to obtain instantaneous reaction rate data. The apparatus is shown in Fig. 4-23. Small rectangular plates or disks of T-22 stock were polished on a diamond wheel and then washed in H_2O, alcohol, and acetone before being suspended from the balance beam by a platinum wire. After leak checking, the apparatus was evacuated and backfilled several times to flush out the system with the prescribed gas mixture. The desired flow was initiated through the apparatus, and the temperature was raised to the level of interest.

For two microbalances, the correct H_2O concentration was introduced via the bypass flow system shown in Fig. 4-23. The gas flow containing all the required components (except water) was split into two paths; one path was through a tube containing oxalic acid immersed in an ice bath (273 K), with the other bypassing the saturator. Later the two streams were reunited, passed through a large-volume chamber for homogeneous mixing, and then split to proceed to the microbalances and gas testing equipment. By controlling the proportion of gas flow bypassed, the water concentration in the gas could be adjusted to the desired level.

For the third microbalance, an FTS refrigeration unit with methanol in the cold-well controlled the temperature of ice in a high-mass copper saturator block through which the gas mixture flowed. Different water vapor concentrations were obtained by adjusting the ice temperature.

Experimental Results

Results of Comparative Tests. Three separate tests were performed, all at 773 K using He gas containing 1 kPa CO, 1 kPa H_2. The first run contained nine samples of 410 SS plate material and one of Inconel 600. The 410 SS samples were either as-received or were pretreated with grit

TABLE 4-9
COMPOSITION OF SPECIMENS ANALYZED IN COMPARATIVE TESTING

Alloy	Cr	Ni	Mo	Fe	Mn	C max	S max	Cu
Inconel 600	14.0-17.0	72 min	--	6.0-10.0	1.0 max	0.15	0.015	0.5 max
410 SS	11.5-13.5	--	--	Bal	--	0.15	--	--
304 SS	18.0-20.0	8.0-10.0	--	Bal	--	0.08	--	--
T-22 Std	2.25	--	1.0	Bal	0.3-0.6	0.15	0.035	--

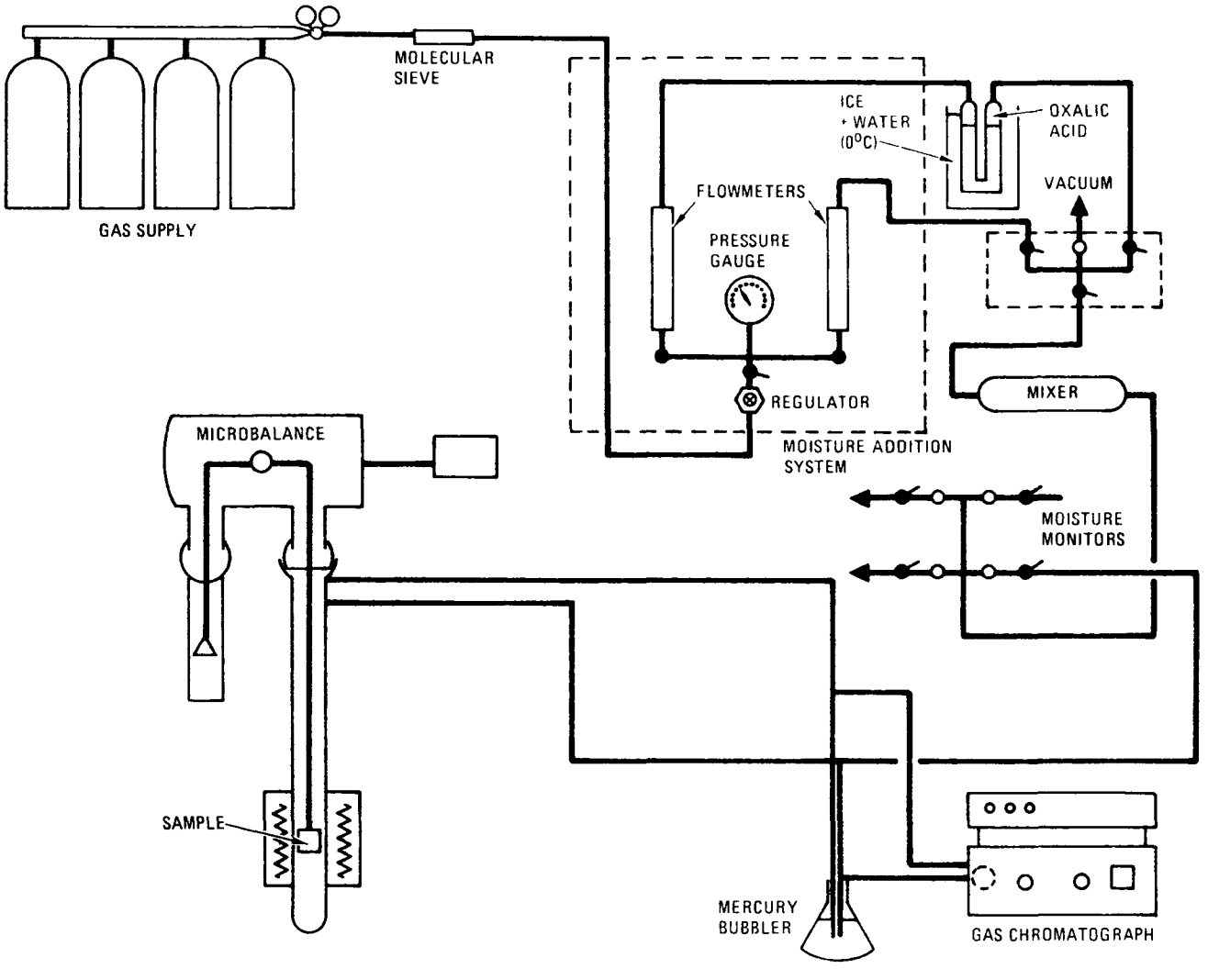

Fig. 4-23. Microbalance apparatus for carbon deposition studies

blasting or passivation, whereas the Inconel specimen was as-received. The moisture level was maintained at <5.0 Pa ($H_2/H_2O \geq 200$) and the gas flow was 50 cm^3/sec. The duration of this test was 167 hours.

In the second test the previously mentioned specimens were retained, and samples of 304 SS and T-22 were added. The test conditions remained the same. The duration of this run was 245 hours.

In the third run new samples were exchanged for those from the previous tests. The new specimens included 410 SS, 304 SS, Inconel 600, and T-22; the duration of the test was 1870 hours at a water level of 30 Pa H_2O ($H_2/H_2O = 33$).

The results of the comparative tests are summarized as follows:

1. An incubation period occurred before the visible onset of carbon deposition. In run 1, where H_2/H_2O was ≥ 200, the incubation period was 130 hours for the 410 SS sample furthest upstream. In run 3, where H_2/H_2O was ≈ 33, the incubation period of another 410 SS sample in the same position was 240 hours. The other downstream samples in all the tests exhibited longer periods of dormancy. The incubation period, therefore, is dependent on substrate and on gas content, particularly the H_2/H_2O ratio. The incubation period is believed to be due to formation of active catalysts, which cause an acceleration in reaction rate.

2. No visible difference in quantity of carbon formed was apparent in the oxidized, grit-blasted, or passivated 410 SS samples.

3. The order of reactivity for T-22 and 410 SS was approximately the same. The higher Cr content of the 410 SS was apparently not protective. 304 SS showed only minor deposition and Inconel 600 was virtually nonreactive. The following order of catalytic activity was observed:

T-22 ≥ 410 SS >> 304 SS > Inconel 600 .

4. Gas analysis of these qualitative runs revealed that CO_2 was a reaction product in addition to the carbon being deposited; CO was being consumed whereas the H_2 was unaffected, and the H_2O level was somewhat reduced. This indicated that the net reaction was the Bouduourd reaction (4-20). This is discussed in more detail in the following section.

Results of Microbalance Rate Studies. The results of the carbon deposition rate studies using automatic recording microbalances are shown in Figs. 4-24 through 4-26. In Fig. 4-24 reaction rates versus exposure time are shown for polished and preoxidized T-22 samples. These specimens were otherwise identical and were run under the same conditions of 773 K and 50 Pa H_2O, 1.0 kPa H_2, and 1.0 kPa CO in He. Both specimens exhibited long dormant incubation periods prior to the onset of carbon deposition. This period was 385 hours for the oxidized sample and 535 hours for the highly polished sample. The preoxidation accelerated the onset of carbon deposition, possibly by providing an iron-rich oxide layer on the surface that, when subsequently reduced by H_2, formed high surface area iron available for catalyst production.

The onset of carbon deposition was quite rapid following the incubation period. In many cases, as shown in Fig. 4-24, the observed rate exhibited step-like discontinuities between lengthy plateaus of constant rate, despite a concerted effort to maintain constant conditions of temperature, gas mixture, and flow rate. This phenomenon was observed in all tests (in three separate microbalances) and was confirmed by gas analysis for CO_2. The initial rate for the preoxidized specimen was about five times that of the polished T-22 samples. Another interesting feature of these data is the apparent step-like decay in reaction rate for the preoxidized sample. This type of phenomenon was observed in later tests, particularly where high deposition rates were involved. Postulated reasons for this apparent poisoning effect are discussed later.

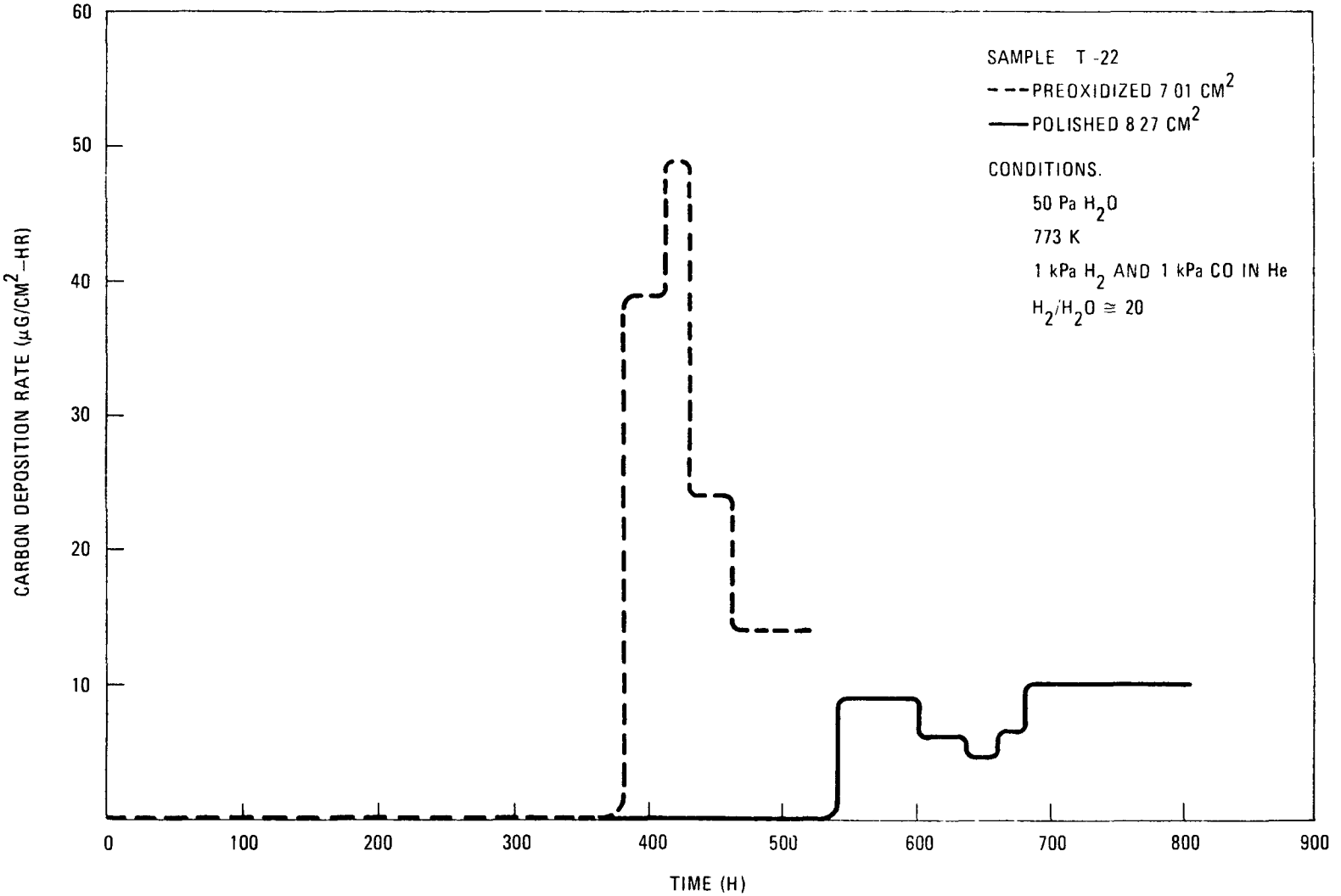

Fig. 4-24. Carbon deposition rate versus time

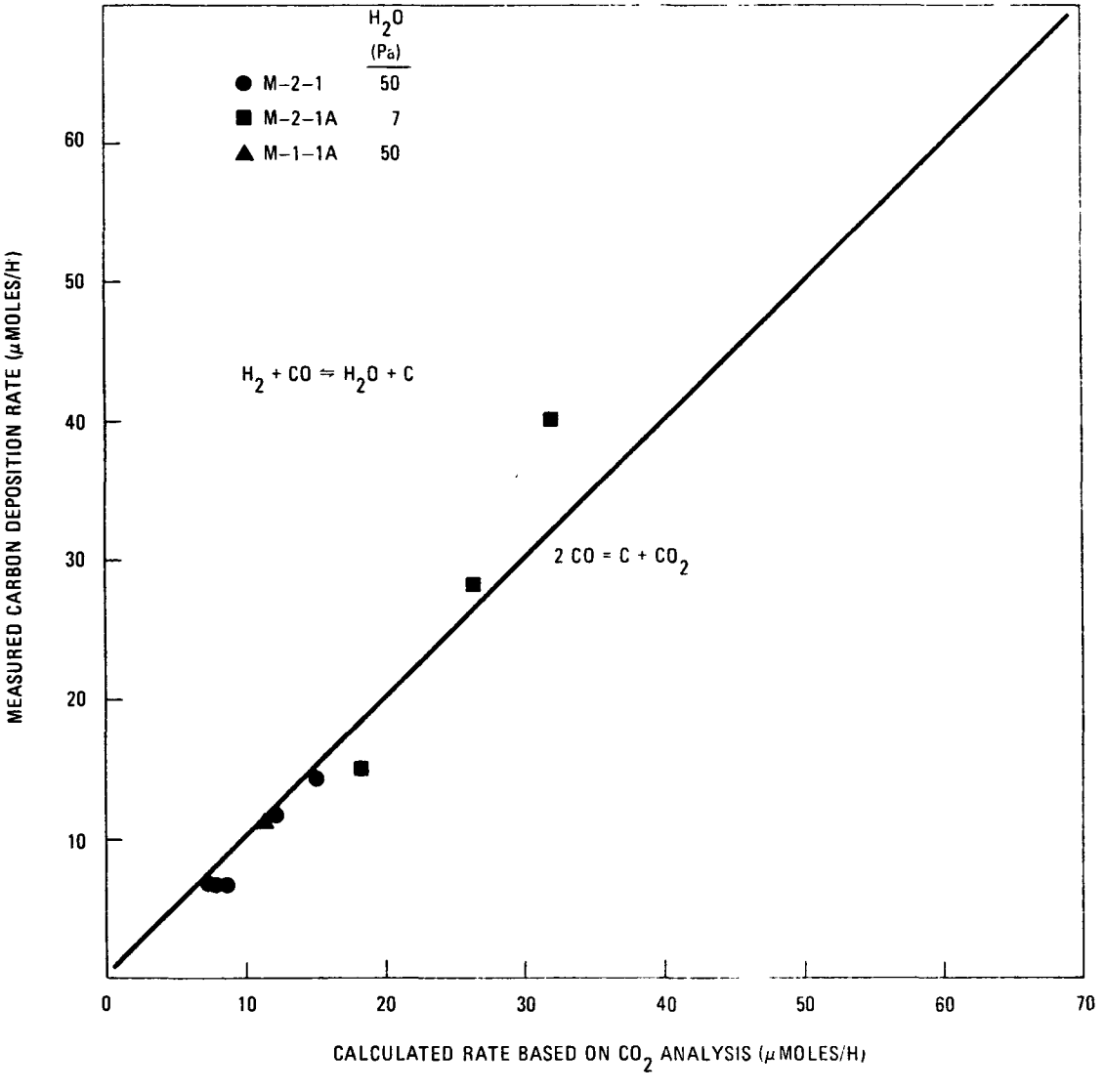

Fig. 4-25. Comparison of CO_2 production with weight gain

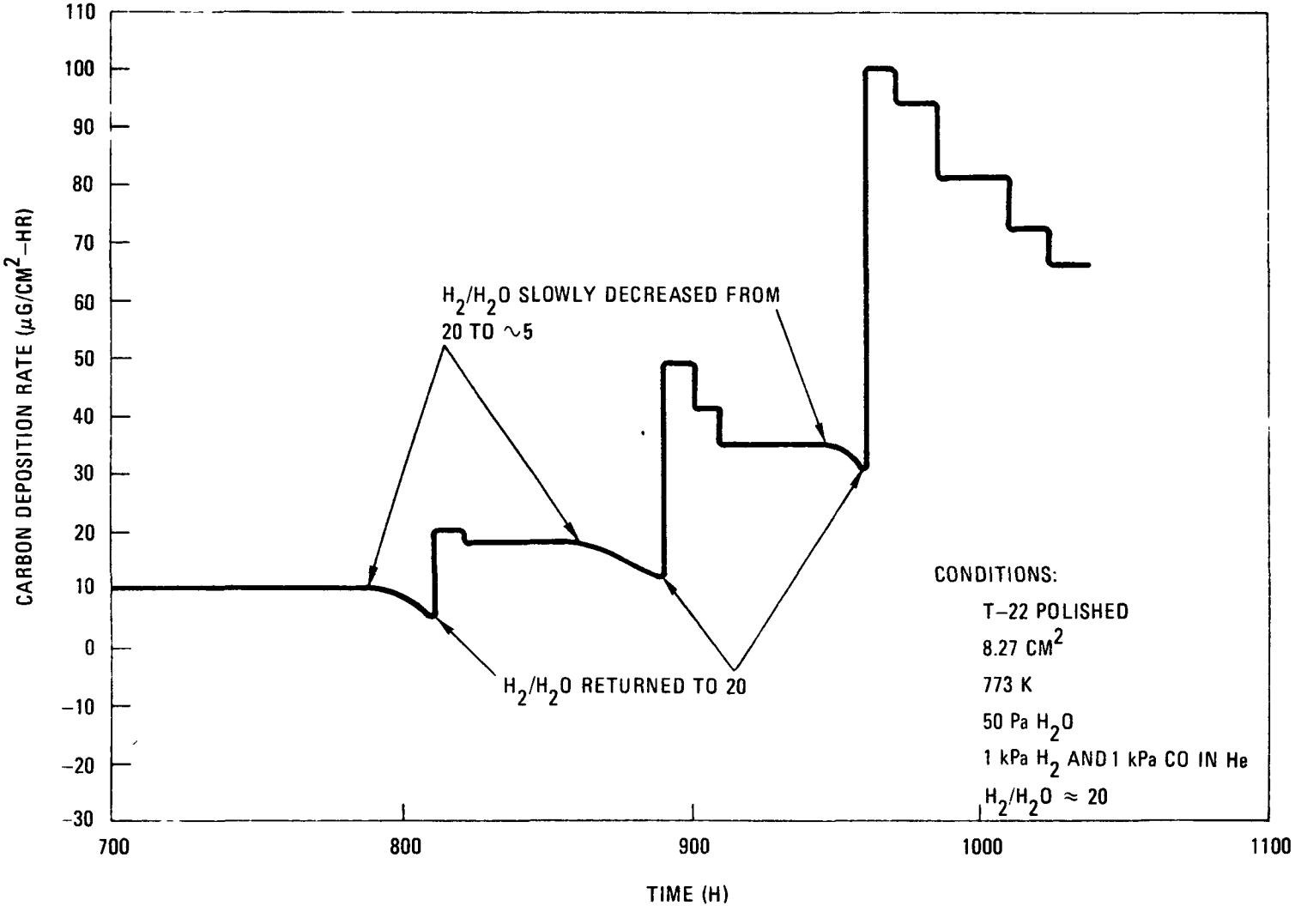

Fig. 4-26. Effect of H_2/H_2O cycling on carbon deposition rate

Analysis of inlet and outlet gas composition in both the comparative tests and the microbalance tests indicated that the net reaction occurring was the Boudouard (i.e., $2CO \rightarrow C + CO_2$). Moreover, the entire rate of weight gain observed on the microbalance could be accounted for by the rate of CO_2 production, as shown in Fig. 4-25. In Fig. 4-25 the solid line of unit slope through the origin is the predicted result if the net reaction is the Boudouard. Experimental points to the left of the line indicate some contribution of the water gas reaction (4-19).

It is emphasized that the data in Fig. 4-25 do not prove that the only reaction occurring is the Boudouard, but that the net effect of the reactions occurring is consistent with the equation $2CO = C + CO_2$.

It is possible that the following mechanism occurs: the reverse water gas reaction (4-19) deposits carbon, and H_2O formed in situ on the catalyst reacts quantitatively with CO (which is adsorbed on adjacent sites) via the water shift reaction (4-21) to replenish the H_2 and produce the CO_2 observed. The net effect of the combined reactions would be identical to the Boudouard reaction: no hydrogen would appear to be consumed (only CO) and no water would appear to be produced, the only visible products being C and CO_2.

To verify this proposed mechanism, H_2 was removed from the gas mixture in both the comparative and microbalance tests. The mass spectrographic analysis (Table 4-10) from the comparative tests indicated the occurrence of the water shift reaction (4-21). Note the reduction in water level and CO concentration and the production of both hydrogen and carbon dioxide, consistent with reaction 4-21. When H_2 was removed from the process stream of the microbalance tests, the reaction rate as measured by weight gain dropped to zero.

The complementary test of omitting the CO entirely from the inlet gas was also performed. A significant weight loss rate was observed with the inlet gas mixture 1 kPa H_2, 50 Pa H_2O. In addition, CO was measured in the

TABLE 4-10
RESULTS OF MASS SPECTROGRAPHIC ANALYSIS

	H_2O (ppm)	H_2 (%)	CO (%)	CO_2 (%)
Gas inlet	290	--	1.65	--
Gas outlet	21	0.041	1.52	0.054

outlet gas. These results are consistent with oxidation of the deposited carbon, since when the original CO-H_2 gas mixture was resumed, a dramatic increase in rate of weight gain was observed.

Yet another interesting observation is the phenomenon depicted in Fig. 4-26, where increased deposition rates occurred following periods where H_2/H_2O ratios were deliberately lowered from $\geq$20 to $\lesssim$5. At this temperature, 673 K, $H_2/H_2O \geq 20$ is definitely reducing to both carbon and iron which is conducive to carbon deposition. At $H_2/H_2O \leq 5$, the gas conditions are oxidizing and carbon deposition ceases. During this latter period, however, the catalysts were apparently being reactivated since when the higher H_2/H_2O ratios were resumed, the carbon deposition rates were higher than before the change (Fig. 4-26).

A possible explanation for this "cycling" phenomenon became apparent as a result of microscopic analysis of the carbon deposits. The carbon material deposited on the T-22 specimens was examined by scanning electron microscopy (SEM) and transmission electron microscopy (TEM). At the highest resolvable SEM magnification (20,000X), the outer surface of the deposit was seen to be composed of a tangled mass of filaments. Almost without exception, the filaments were terminated by dense Fe crystal heads. Moreover, filaments taken from T-22 samples which exhibited the apparent self-poisoning had Fe heads that were completely encapsulated by carbon.

It is postulated that the active catalyst is the Fe crystal head at the tip of each filament and that high rates of carbon deposition are eventually self-poisoning because of encapsulation of the crystal by carbon.

Lowering the H_2/H_2O ratio would cause oxidation of the carbon on the iron crystal as well as oxidation of iron on the substrate surface. Cycling the H_2/H_2O ratio back to the reducing regime would then cause resumption of carbon deposition at an increased rate as observed in Fig. 4-26.

To test whether the active catalyst is associated with the carbon (i.e., the iron crystal) or the metal substrate, the carbon deposited on one of the T-22 specimens was removed and a portion placed in a clear quartz boat. This specimen was then exposed to the same conditions as the cleaned T-22 specimen from which it had been removed. High rates of carbon deposition were observed on both the metal substrate and on the carbon deposit with no incubation period, consistent with an existing catalyst. The combined rate on the carbon and metal specimens was almost identical with that of the specimen before the carbon was removed. Moreover, about two-thirds of the total rate was observed on the carbon deposit and only one-third on the metal substrate.

The carbon material supported carbon deposition for a total of 540 hours. However, shortly after the rate was temporarily accelerated by cycling the H_2/H_2O ratio, the rate decayed and finally dropped to zero and could not be reactivated by further H_2/H_2O cycling.

Summary of Results

In summary, these results have the following specific features:

1. The order of reactivity of alloys tested is T-22 $\geq$ 410 SS >> 304 SS > Inconel 600.

2. An incubation period occurs which is dependent on surface conditions, temperature, and impurity concentration. Oxidized specimens exhibit shorter incubation periods than polished specimens.

3. Consistent with prior work, the overall reaction rate was found to be dependent on gas impurity concentration, temperature, H_2/H_2O, and surface conditions. Preoxidized samples had higher rates than polished samples, presumably because of the difference in specific surface area.

4. Cycling of the H_2/H_2O ratio causes step function increases in reaction rate, possibly due to oxidation of both carbon and iron during periods of low H_2/H_2O.

5. Although the metal substrate is catalytic, the main catalyst appears to be iron crystals at the tips of carbon filaments. The catalyst crystals can be poisoned by encapsulation with carbon at high rates of deposition.

6. According to gas analysis the net reaction is Boudouard; $2CO = C + CO_2$. In the absence of H_2, carbon deposition ceased while CO_2 production continued, indicating the occurrence of the shift reaction. The postulated mechanism therefore involves the coupled reactions: $H_2 + CO = C + H_2O$ (water gas) and $H_2O + CO = CO_2 + H_2$ (shift).

Conclusions

These tests have indicated that the catalysis of carbon deposition reactions is quite complex. As a result, the data are presently so imprecise as to preclude accurate prediction of the magnitude of carbon deposition in the reactor. Two encouraging results have emerged, however. First, the most active catalyst is in the carbon deposit itself, i.e., the iron crystals. This means that in the reactor the reaction rate will be limited because the carbon filaments and therefore the most active catalysts will be continuously scoured from the surface by the turbulent helium stream. The second significant finding is that the net reaction is Boudouard, or CO_2 production. This means that enhancement of core oxidation by recycling of water vapor will not occur.

TASK 900: FORT ST. VRAIN CHEMISTRY SURVEILLANCE

The rise-to-power program for the Fort St. Vrain HTGR was initiated on July 3, 1976. After reaching a power level of 26%* on August 2, 1976, the rise-to-power was interrupted because of a technical difficulty with one of the primary coolant circulators. During the rise to 26% power, steady-state operating conditions were attained at 2, 5, 8, 11, and 18% power in accordance with the rise-to-power schedule.

Gaseous radioactive levels and coolant impurity levels were measured at each steady-state power level. These measurements initiate a long-range surveillance program to study the transport behavior of fission products in the reactor and the interaction of coolant impurities with primary circuit materials. Information on fission product behavior is important for use in evaluating reactor performance (in particular fuel performance) and validating fission product transport codes such as TRAFIC, RANDI, and related codes. Information on coolant impurities is important for use in evaluating the extent of interaction of coolant impurities with primary circuit materials (in particular with core materials) and validating computer codes such as OXIDE and GOP. This surveillance program is conducted in cooperation with the Public Service Company of Colorado. A participant in the work to evaluate the interaction of coolant impurities with core materials is G. L. Tingey of Battelle Pacific Northwest Laboratories, under contract with Oak Ridge National Laboratory.

Results of the measurements of gaseous radioactive levels and coolant impurity levels during the rise to 26% power are presented below.

Subtask 920: Fort St. Vrain Fission Product Surveillance

Gaseous radioactivity levels for various noble gas isotopes were measured at each power level; the results are given in Table 4-11. These

*Percent of rated power.

TABLE 4-11
MEASURED STEADY-STATE ACTIVITIES FOR NOBLE GAS ISOTOPES AT VARIOUS POWER LEVELS DURING FSV RISE-TO-POWER

Date	Power (%)	Gross Circulating Activity (Ci)	Activity in the Primary Coolant by Isotope[a] ($\mu Ci/cm^3 \times 10^{-5}$ at STP)						
			Kr-85m	Kr-87	Kr-88	Kr-89	Xe-135	Xe-137	Xe-138
7/4/76	2.0	4.4	3.0	5.6	4.2	ND[b]	6.1	ND	4.5
		6.5	3.0	5.6	4.6	ND	6.8	8.2	6.3
Average		5.5	3.0	5.6	4.4		6.5	8.2	5.4
7/8/76	5.1	14.1	7.7	14.4	12.2	ND	20	6.1	15.1
		13.8	7.2	14.2	10.8	ND	19	8.0	14.9
Average		14.0	7.4	14.3	11.5		19	7.0	15.0
7/13/76	7.5	24	11.2	23	19.3	7.3	31	9.0	28
		25	12.1	23	20	7.8	35	10.2	25
Average		24	11.7	23	20	7.6	33	9.6	26
7/26/76	11.0	34	11.2	29	22	23	34	24	38
		29	11.2	26	22	17	32	14	34
Average		32	11.2	28	22	20	33	19	36
7/29/76	17.9	52	22	50	42	23	57	24	59
		57	21	50	44	41	54	32	59
Average		54	22	50	43	32	56	28	59
8/2/76	26.6[c]	71	30	63	55	40	89	31	71
		71	31	64	59	20	91	39	77
Average		71	31	64	57	30	90	35	74

[a] Data corrected for 2.5-min delay time between primary coolant and sampling point.

[b] Not determined.

[c] Steady-state condition probably not attained because of relatively short time at this power level.

data were used to calculate R/B* values given in Table 4-12. Estimated average fuel temperatures at the steady-state power levels are 483 K (410°F) at 2.0%, 508 K (455°F) at 5.1%, 573 K (570°F) at 7.5% (before adjusting orifices), 639 K (690°F) at 11.0%, and 683 K (770°F) at 17.9%. Predicted (calculated) gaseous radioactivity levels and R/B values, as reported by Dunn and Haire (Ref. 4-19) are given in Tables 4-13 and 4-14, respectively.

The measured and predicted activity and R/B values show good agreement with the measured values being slightly lower than the predicted values. This good agreement is pleasing considering the complexity of the calculations and the uncertainties involved in both the measurements and the calculations. The measured R/B values are low (in the 10^{-6} range) indicating satisfactory retention of fission gases by the fuel and thus satisfactory performance of the fuel.

Examination of the data in Table 4-12 shows that the R/B values generally decreased after the rise from 7.5 to 11.0% power. This decrease is attributed to a decrease in fuel temperature resulting from adjustment of the primary coolant flow orifices at 7.5% power. (The R/B values at 7.5% power were obtained prior to adjusting the orifices.) This suggests a significant decrease in fuel temperature for the regions of the core that dominated the fission gas release. The calculated decrease in R/B on adjusting the orifices was small (see Table 4-14), suggesting that the actual decrease in fuel temperature was greater than calculated.

The measured R/B values (Table 4-12) show a half-life dependence which is less than square root of half-life. This behavior is as expected considering the relatively low fuel temperatures involved (see Subtask 110).

The gaseous radioactivity levels given in Table 4-12 were measured from grab samples. In this measurement small glass vials (approximately 100 cm^3 in volume) are filled to a known pressure with primary coolant gas

*R/B is the ratio of release rate to birth rate at steady state.

TABLE 4-12
MEASURED R/B VALUES FOR NOBLE GAS ISOTOPES AT VARIOUS POWER LEVELS DURING FSV RISE-TO-POWER(a)

Date	Power (%)	R/B x 10^5						
		Kr-85m	Kr-87	Kr-88	Kr-89	Xe-135	Xe-137	Xe-138
7/4/76	2.0	0.52	0.38	0.22	--	0.30	--	0.12
		0.52	0.38	0.24	--	0.32	--	0.14
Average		0.52	0.38	0.23	--	0.31	--	0.13
7/8/76	5.1	0.47	0.36	0.23	--	0.34	0.05	0.12
		0.48	0.38	0.22	--	0.35	0.07	0.13
Average		0.48	0.37	0.22	--	0.34	0.06	0.13
7/13/76	7.5	0.49	0.41	0.26	0.06	0.39	0.05	0.15
		0.53	0.42	0.28	0.06	0.43	0.06	0.14
Average		0.51	0.42	0.27	0.06	0.41	0.06	0.15
7/26/76	11.0	0.33	0.34	0.20	0.12	0.27	0.10	0.15
		0.33	0.31	0.20	0.09	0.26	0.06	0.13
Average		0.33	0.32	0.20	0.10	0.26	0.08	0.14
7/29/76	17.9	0.46	0.38	0.26	0.07	0.35	0.06	0.14
		0.43	0.39	0.27	0.13	0.33	0.08	0.15
Average		0.44	0.38	0.26	0.10	0.34	0.07	0.14
8/2/76	26.6(b)	0.45	0.34	0.24	0.09	0.40	0.05	0.12
		0.46	0.34	0.26	--	0.41	0.06	0.13
Average		0.46	0.34	0.25	0.09	0.40	0.06	0.12

(a) Data corrected for 2.5-min delay time between primary coolant and sampling point.

(b) Steady-state condition probably not attained because of relatively short time at this power level

TABLE 4-13
PREDICTED STEADY-STATE ACTIVITIES FOR NOBLE GAS ISOTOPES AT VARIOUS POWER LEVELS DURING FSV RISE-TO-POWER[a]

Power (%)	Predicted Primary Coolant Activities[a] ($\mu Ci/cm^3 \times 10^{-5}$ at STP)					
	Kr-85m	Kr-88	Kr-89	Xe-135	Xe-137	Xe-138
2	4.1	9.4	2.2	40	5.1	10
5	10	23	5.6	99	13	25
8	17	39	9.4	160	21	41
8[b]	17	38	9.1	160	21	41
11	23	54	13	220	29	58
18	40	94	24	340	50	98
26.8	66	160	41	520	79	160

[a] From Ref. 4-19.

[b] After orifice adjustment

TABLE 4-14
PREDICTED R/B VALUES FOR NOBLE GAS ISOTOPES AT VARIOUS POWER LEVELS DURING FSV RISE-TO-POWER

Power (%)	Predicted R/B x 10^5[a]					
	Kr-85m	Kr-88	Kr-89	Xe-135	Xe-137	Xe-138
2	0.58	0.46	0.06	0.66	0.11	0.22
5	0.57	0.46	0.06	0.65	0.11	0.22
8	0.60	0.48	0.07	0.67	0.12	0.22
8[b]	0.59	0.47	0.06	0.66	0.11	0.22
11	0.62	0.49	0.07	0.68	0.12	0.23
18	0.69	0.55	0.07	0.71	0.12	0.24
26.8	0.79	0.63	0.09	0.76	0.13	0.25

[a] From Ref. 4-19.

[b] After orifice adjustment.

and gamma-counted using a Ge(Li) scintillation detector in conjunction with a multichannel pulse-height analyzer and associated instrumentation.

Other measurements used for evaluating fission product behavior in the Fort St. Vrain reactor are:

1. Circulating activity in the primary coolant. A continuous record (on a chart recorder) of the primary circuit fission product activity is provided by a scintillation detector. This instrument is calibrated using grab sample data.

2. R/B for noble gas isotopes of half-life <3 minutes. A fast gas sampler has been installed in the reactor to provide R/B data for krypton and xenon isotopes (including 32-s Kr-90, 10-s Kr-91, 41-s Xe-139, and 16-s Xe-140) with half-lives <3 minutes. The helium coolant is sampled through a short purge line. The gaseous isotopes are collected in a dry-ice - alcohol-cooled charcoal trap. The trap is gamma-counted, and the count data are analyzed as with the grab samples.

3. Circulating iodine activity. An iodine monitor has been installed in the reactor for measuring the quantity of gaseous radioactive iodine circulating in the primary coolant during steady-state reactor operation. These data will aid in evaluating (1) fuel performance, (2) holdup of iodine in the fuel element graphite, and (3) the fraction of iodine plated out per pass through the steam generator. The data are thus important in validating design methods. The iodine monitor consists of a tube-within-a-tube arrangement through which a hot helium coolant sample is drawn. A small charcoal trap at the inlet orifice of the inner tube provides for sorption of 6.7-h I-135 and 21-h I-133. The outer tube provides a means of purging iodine daughter product xenon isotopes to a fast gas sampling station with purified helium. The design is such that during the

measurement only xenon produced from the deposited iodine will be collected for gamma counting as per the fast gas analysis.

4. Plateout activity. Two replaceable plateout probes are installed in the Fort St. Vrain reactor primary coolant circuit, one in each loop. The probes will be analyzed periodically for Sr-90, I-131, and other nuclides of interest, and the results will be used to determine the total inventory of these nuclides in the primary circuit. The probe design is such that both the core inlet and outlet coolant streams will be continuously purged through the individual probe diffusion tubes in each loop. During the first core refueling operation and subsequent refueling operations, the plateout probes will be removed and subjected to gamma spectroscopy and radiochemical analysis. Activity profiles for isotopes such as Sr-90, I-131, Cs-137, and Ba-140 will be determined along the length of the diffusion tubes located within the plateout probe. Analysis of the plateout data should provide information concerning the amount, distribution, and chemical form of the metallic radionuclides released from the fuel into the coolant circuit during the sampling period. This information is very important for evaluating fuel performance and for validating design methods.

Fast gas samples were obtained at each power level where steady state was attained during the rise to 26% power. However, the activity levels were so low that no meaningful data were obtained. Samples with the iodine monitor were taken at 8 and 11% power, and the data are being processed.

The predicted gaseous radioactivity levels and R/B values given in Tables 4-13 and 4-14 were calculated using various computer codes as described in Ref. 4-19. Account was taken of (1) the nominal steady-state reactor operating characteristics (including helium flow, control rod positions, and reactor power level), (2) the core distribution of the various service limit fuel types, (3) the as-manufactured R/B for the

various fuel types, and (4) fuel deterioration factors determined for storage, fuel rod handling, and moisture exposure.

Subtask 940: Fort St. Vrain Coolant Impurity Surveillance

Primary coolant impurities were monitored during the rise to 26% power. Instruments used were a Varian gas chromatograph with helium ionization detectors and EG&G dew point moisture monitors. The gas chromatograph was set up to automatically sample the primary coolant every half hour.

It was observed that whenever the reactor power (i.e., temperature) was increased, the gaseous impurity levels increased, due to outgassing of core and primary circuit materials, but then declined (with the exception of hydrogen) due to removal by the purification system. Hydrogen did not follow this pattern because the titanium metal hydrogen getter units were out of service during this period except on the last day. Hydrogen, therefore, continuously increased throughout most of this startup period. When the getter unit was put in service 1 day before shutdown, the hydrogen concentration decreased significantly.

The data showing the behavior of the coolant impurities during the rise to 26% power are given in Table 4-15; two values of impurity concentrations are listed at each power level. The upper values are the peak concentrations observed shortly after each power increase. The lower values are the concentrations observed at the end of operation at the particular power level. Peaking of impurity concentration following a temperature rise is consistent with outgassing behavior.

The total quantities of gases removed from the primary circuit via the purification system are given in Table 4-16. Included in the table are predicted total quantities based on known graphite outgassing behavior (Ref. 4-20).

TABLE 4-15
PRIMARY COOLANT IMPURITY LEVELS DURING FSV
RISE-TO-POWER

Power Level[a] (%)	Time at Power Level (h)	Avg He Outlet Temp (K)	Coolant Impurity Level (ppmv)[b]						
			H_2	O_2	N_2	CH_4	CO	CO_2	H_2O
2.0	48	490	ND[c]	ND	117	0.7	0.3	2.4	240
					42	0.6	<0.1	1.8	72
5.2	48	520	12	1.0	120	0.5	0.4	5.5	75
			17	0.5	45	1.0	<0.1	2.3	57
7.8	72	590	46	2.6	85	5.6	3.4	6.9	65
			40	5.2	27	2.4	1.8	4.2	29
11.4	48	660	46	6.5	9	4.6	3.4	3.9	41
			48	6.2	7.5	3.6	2.7	3.2	26
18.5	42	700	75	6.0	8.0	9.0	7.8	15	97
			97	5.4	8.0	6.0	4.5	10	82

[a] Approximate power level during the steady-state period.

[b] The first value given is the peak value and the second is the final value.

[c] ND = not determined.

TABLE 4-16
EXPECTED AND MEASURED QUANTITIES OF IMPURITY GASES
REMOVED FROM PRIMARY COOLANT DURING FSV RISE-TO-POWER

Impurity	Quantity of Impurities Removed (kg)			
	Expected[a]			Measured[b]
	Blower Heatup T ≈ 640 K	Power 0-26% T ≈ 920 K	Total	Power 0-26%
H_2	--	5	5	(c)
N_2	1	4	5	25
CH_4	2	5	7	3
CO	--	3	3	4
CO_2	2	7	9	8
H_2O	4-16	0.5-2	5-19	68

[a] Expected values based on graphite outgassing.

[b] Measured value is amount removed by the purification system.

[c] Hydrogen getter not operating.

As shown by Table 4-16, the measured values agree quite well with the predicted values, with the exception of water and nitrogen. It is postulated that the extra quantity of water removed from the system is due to outgassing of the fibrous blanket insulation materials which were exposed to high moisture levels for rather long periods prior to startup. The extra nitrogen could have come from residual air in the system prior to charging with He.

REFERENCES

4-1. Myers, B. F., et al., "The Behavior of Fission Product Gases in HTGR Fuel Material," ERDA Report GA-A13723, General Atomic, to be published.

4-2. Guggenheim, E. A., Elements of the Kinetic Theory of Gases, Pergamon Press, New York, 1960.

4-3. "HTGR Fuels and Core Development Program Quarterly Progress Report for the Period Ending May 31, 1975," ERDA Report GA-A13444, General Atomic, June 30, 1975.

4-4. Crank, J., The Mathematics of Diffusion, Oxford University Press, London, 1970.

4-5. Goodknight, R. C., and I. Fatt, J. Phys. Chem. 65, 1709 (1961).

4-6. "HTGR Fuels and Core Development Program Quarterly Progress Report for the Period Ending May 31, 1976," ERDA Report GA-A13941, General Atomic, June 30, 1976.

4-7. Smith, P. D., and R. G. Steinke, "The Release of Metallic Fission Products from Multi-Layered Coated Particles, Part I - Theory," ERDA Report GA-A14033, General Atomic, to be published.

4-8. Jensen, D. D., and T. Hama, "The Release of Metallic Fission Products from Multilayered Coated Particles, Part II - Comparisons of Predictions and Measurements," ERDA Report GA-A14073, General Atomic, to be published.

4-9. "HTGR Base Program Quarterly Progress Report for the Period Ending February 28, 1974," USAEC Report GA-A12916, General Atomic, March 29, 1974.

4-10. "HTGR Fuels and Core Development Program Quarterly Progress Report for Period Ending November 30, 1975," ERDA Report GA-A13737, General Atomic, December 31, 1975.

4-11. Myers, B. F., and W. E. Bell, "Cesium Transport Data for HTGR Systems," ERDA Report GA-A13990, General Atomic, to be published.

4-12. "HTGR Accident Initiation and Progression Analysis Status Report, Volume V, Phase I Analyses and R&D Recommendations," ERDA Report GA-A13617, General Atomic, February 1976.

4-13. "HTGR Accident Initiation and Progression Analysis Status Report, Volume VI, Event Consequences and Uncertainties Demonstrating Safety R&D Importance of Fission Product Transport Mechanisms," ERDA Report GA-A13617, January 1976.

4-14. Peroomian, M. B., A. W. Barsell, and J. C. Saeger, "OXIDE-3: A Computer Code for Analysis of HTGR Steam or Air Ingress Accidents," General Atomic Report GA-A12493 (GA-LTR-7), January 15, 1972, pp. 3-30.

4-15. Giberson, R. C., and G. L. Tingey, "Reactions of Gaseous Impurities in a High-Temperature Gas Cooled Reactor," Battelle Northwest Laboratories Report BNWL-974, 1968.

4-16. Johnstone, H. F., C. Y. Chen, and D. S. Scott, "Kinetics of the Steam-Carbon Reaction in Porous Graphite Tubes," Ind. Eng. Chem. 44, 1568 (1952).

4-17. Walker, P. L., Jr., F. Rusinko, Jr., and L. G. Austin, "Gas Reactions of Carbon," Advan. Catalysis 11, 149 (1959).

4-18. Ergun, S., and M. Mentser, "Reactions of Carbon with CO_2 and Steam," Chemistry and Physics of Carbon, Vol. 1, P. L. Walker (ed.), Marcel Dekker, New York (1965), p. 229.

4-19. Dunn, T. D., and M. J. Haire, "Predictions of the Gaseous Radioactivity Level in the Primary Coolant of Fort St. Vrain During Initial Rise to Power," General Atomic unpublished data, April 1976.

4-20. Burnette, R. D., General Atomic unpublished data.

6. HTGR ALTERNATIVE FUEL SYSTEMS STUDIES
189a NO. SU047

Work under this task has been completed.

8. REACTOR PHYSICS
189a NO. SU002

FSV OPERATING DATA ANALYSIS

A final report (GA-A14007) describing a comparison of calculational results with the experimental data obtained during the initial stages of the FSV rise to power program has been completed and is in the final stages of formal review.

9. HTGR FUEL DEVELOPMENT AND ENGINEERING
189a NO. SU003

TASK 200: ACCELERATED IRRADIATION TESTS

Subtask 210: Fresh Fuel Qualification

Summary and Conclusions

Capsule P13T completed its scheduled irradiation on July 6, 1976. The test reached an estimated peak fast fluence of 8.8×10^{25} n/m^2 (E > 29 fJ)$_{HTGR}$. End-of-life fission gas release values were below predicted values for both cells. The final values for cells 1 and 2 were 1.6×10^{-5} and 2.8×10^{-6} R/B for Kr-85m, respectively. Postirradiation examination of the fuel samples is scheduled to begin at GA around September 1, 1976.

Capsule P13V has now reached an exposure of 6×10^{25} n/m^2 (E > 29 fJ)$_{HTGR}$, which is approximately 67% of its design exposure of 9×10^{25} n/m^2. Because of the current GETR mode of operation, the three cells toward the top of the reactor (4, 5, and 6) are below temperature during a portion of each cycle; the bottom three cells (1, 2, and 3) are operating at design values. Fission gas release values for all cells are in the range of 1 to 3×10^{-5} R/B Kr-85m.

Assembly of capsule P13U(R) has been stopped as a result of recent budgetary restrictions. All components are being stored, along with the design and assembly records for resumption of work at a later time.

Capsule HT-31, containing TRISO particles with 450-μm ThO_2 kernels, completed its irradiation in the High-Flux Isotope Reactor (HFIR) on June 16, 1976. Visual examination of the particles was conducted at ORNL. There was no apparent pressure vessel failure in any of the seven batches

irradiated at 1250°C. However, between 0 and 4% of the outer pyrocarbon coatings failed. These same batches irradiated in a companion test at 1500°C showed much higher failure fractions (generally 11 to 100%). The conditions of this latter test were very severe relative to reactor design conditions.

Capsule HT-33, containing ThO_2 TRISO and ThO_2 BISO particles coated in the 240-mm coater, began its irradiation in the HFIR during June 1976. HT-33 is scheduled to be discharged in October after receiving five cycles of irradiation.

Capsule P13T

Capsule P13T is the ninth in a GA series of LHTGR fuel irradiation tests conducted under the HTGR Fuels and Core Development Program. P13T is a large-diameter capsule containing two cells. Cell 1 is a qualification test of reference fresh fuel [TRISO UC_2 (VSM) and BISO ThO_2 particles] irradiated at 1300°C. Cell 2 is an evaluation test of reference fresh fuel and recycle fissile fuel [TRISO UC_xO_y (WAR) particles] irradiated at 1100°C. The capsule was inserted in the ORR reactor in May 1975. The capsule was discharged from the core on July 6, 1976 after being irradiated to a peak fast fluence of 8.8×10^{25} n/m^2 $(E > 29\ fJ)_{HTGR}$. A detailed description of the capsule is given in Ref. 9-1.

After completion of the irradiation, capsule P13T was removed from the reactor and transferred to the storage pool, where it will remain until it is prepared for shipment to GA, which is scheduled for August. The PIE of P13T is scheduled to begin in September 1976.

The fission gas release values at end-of-life were 1.6×10^{-5} and 2.8×10^{-6} R/B (Kr-85m) for cells 1 and 2, respectively. Figures 9-1 and 9-2 show the complete operating curves for cells 1 and 2. The predicted and measured R/B curves indicate that the fuel performed well during irradiation. The two curves are not in complete agreement, indicating the fuel

performed somewhat better than expected based on current design calculations. The results of the postirradiation analysis of capsule P13T should help clarify the differences between the measured and predicted fission gas release data.

Capsules P13U(R) and P13V

Capsule P13V is a constant-temperature and thermal cycle qualification test of WAR TRISO and ThO_2 BISO cured-in-place fuel. Peak exposure on this capsule has now reached 6×10^{25} n/m^2 $(E > 29 \text{ fJ})_{HTGR}$, which is approximately 67% of the peak design exposure of 9×10^{25} n/m^2.

Because of the frequent GETR shutdowns which result in generally low rod bank positions, the flux experienced by P13V has been generally skewed from design conditions toward the bottom of the core. This has resulted in the top cells (cells 4, 5, and 6) reaching design temperature only 50 to 75% of the time. Temperatures average 50° to 75°C below design. It has also become evident that the cell 1 peak thermal cycle design temperature cannot generally be reached, even with the use of 100% neon in the primary and secondary containments. Peak thermal cycling temperatures have generally averaged ∿1400°C.

Argon is currently being used without difficulty in both cell 3 and cell 6 to achieve the desired operating set point. Neon is being used in the secondary containment to raise the general P13V operating temperatures so that the control set point can be reached as often as possible.

Also, as a result of the GETR method of operation, the operating set point for cell 5 was changed from 1500° to 1350°C in order to minimize temperature changes during irradiation. At the time of the change, it was intended that cell 5 of capsule P13U(R) would operate at 1500°C through the use of argon in the primary containment.

The current (8/10/76) steady-state operating conditions for P13V are shown in Table 9-1 and in Figs. 9-3 through 9-9.

Flow checks on P13V during a recent shutdown have revealed that cells 1, 2, and 4 have developed primary to secondary containment leaks. Cells 3, 5, and 6 are currently leak-tight. The R/B results from cells 1, 2, and 4 do not appear to be currently affected.

Work on the construction and safety analysis of P13U(R) has been stopped because of recent budget restrictions on the HTGR Fuels and Core Development Program. The capsule will be stored for future irradiation and all pertinent data are being documented for future reference should funding for the capsule be restored in FY-78.

Capsules HT-31 and HT-33

Capsule and Test Description. The HT-31 and HT-33 irradiation capsules are part of a continued cooperative effort between GA and ORNL and are funded by the ERDA-sponsored HTGR Fuels and Core Development Program. Specifically, these two capsules are designed to characterize the irradiation behavior of unbonded BISO (HT-33 only) and TRISO coated ThO_2 fertile fuel particles. A detailed description of the capsule fuel is given in Ref. 9-2. The experiments are designated to be conducted in the target position of the HFIR at ORNL. The experimental design and operation are similar to the HT-12 through HT-15 and HT-17 through HT-19 series. Experiments of this type are conducted in the HT (target) position of the HFIR because the high fluxes in the reactor allow the accumulation of high fast neutron doses and high thorium burnups in a short time.

HFIR target (HT) experiments provide a rapid means of evaluating and screening fuel materials and material variables which are being considered for use in HTGRs. The materials being evaluated in capsules HT-31 and HT-33 are coatings which have been deposited in the GA pilot plant 240-mm-diameter Freon-cooled coater. The coater design and coater charge sizes represent a significant change in process conditions in comparison with conditions used to fabricate previous irradiation capsule samples. The experimental test matrix for unbonded particles is directed toward defining

relationships between OPyC density, anisotropy, and coating rate and fuel particle performance for materials produced in this new coater.

The objectives of capsules HT-31 and HT-33 are as follows:

1. Coater size effects. Evaluate the irradiation performance of unbonded particles fabricated in the 240-mm-diameter pilot plant coater and establish performance criteria equivalent to those for particles of similar designs and coating properties fabricated in the prototype 127-mm-diameter coater. Fabricating fuel particles in the large coater is part of the planned processing scale-up and verification of applicability of previous specifications to the scaled-up process is desirable. The samples will be irradiated at nominal temperatures of 1200° and 1500°C over an estimated fast neutron exposure $(E > 29\ fJ)_{HTGR}$ between 3.9 and 9.7 x 10^{25} n/m^2. Tables 9-2 and 9-3 give the design test conditions and a general description of fuel particle attributes. The exposure corresponds to an estimated fuel burnup between 4.5 and 12.5% FIMA.*

2. TRISO designs. An equally important objective is to evaluate TRISO coated 450-μm-diameter ThO_2 particles as a potential backup design for BISO coated ThO_2 particles. The TRISO coated particle offers a design option which at high reactor temperatures is expected to be more retentive of fission products than BISO particles. The TRISO coated ThO_2 particle has an added degree of conservatism in that the mean kernel diameter is reduced by nominally 10% in comparison with the standard 500-μm-diameter BISO coated particle. A comparative evaluation between 500-μm-diameter TRISO coated ThO_2 particles tested in capsules HT-28 and HT-29 and the HT-31 and HT-33 tests should serve to establish anticipated performance benefits in the TRISO coated 450-μm-diameter ThO_2 design. Capsules HT-31 and HT-33 will both include

*Fissions per initial metal atom.

a sample from a batch of TRISO coated 500-μm-diameter ThO_2 particles (Batch 6252-05-0160) irradiated in capsules HT-28 and HT-29, which will provide a basis for comparing results.

3. OPyC properties. A secondary set of objectives is to define empirical relationships between fuel performance and OPyC property variables: density, anisotropy, coating rate, and oriented porosity (TRISO only). Figure 9-10 is a schematic diagram of the variable test matrix for TRISO coated fuel tested in capsules HT-31 and HT-33. Seven separate batches are grouped into two sets of coating rates and a subgrouping of different bulk densities. A further subdivision (different coater bed sizes) exists for two sets of batches in order to characterize the degree of oriented porosity, which generally increases with the coater bed surface area. Figure 9-11 is the test matrix for the BISO coated particles tested in capsule HT-33. Two bulk densities, two coating rates, a range of optical anisotropies, and one heat treatment condition will be evaluated.

Capsules HT-31 and HT-33 each contain a total of 32 different positions. Gneeral Atomic will occupy 16 positions in HT-31 and 32 positions in HT-33. The unbonded particle locations in each capsule are divided into two sections: eight positions at 1500°C and eight positions at 1200°C. The design fast fluence for positions operating at 1200°C will be from 3.9 to 7.6 x 10^{25} n/m^2 $(E > 29\ fJ)_{HTGR}$ while positions at 1500°C will operate from 7.0 to 9.7 x 10^{25} n/m^2 $(E > 29\ fJ)_{HTGR}$.

The irradiation positions in HT-31 and HT-33 are uninstrumented, and the designated temperatures in these capsules are particle surface temperatures based on design graphite magazine temperatures. A thermal history study comparable to the analysis of HT-17, -18, and -19 will be provided by ORNL to specify and control the operating conditions of HT-31 and HT-33. Particle loadings were determined by defining design values for power densities through an appropriate thermal analysis and specifying the necessary thorium loadings to maintain the required temperatures in HT-31 and HT-33.

Correspondingly, the total number of particles per position was determined by dividing the thorium weight per particle and the total allowable thorium weight for a designated position. Irradiation exposure for these capsules began March 14, 1976.

The particle batches were selected so that the combined influence of coating rate and coating density on coating integrity and fission gas retention (BISO) can be determined. To aid in postirradiation analysis, the particles irradiated in HT-31 and HT-33 were chosen so that the particles within each individual batch had a constant total coated particle density and a narrow distribution of kernel and total coated particle diameters. Briefly, coated particles were sieved to plus or minus one standard deviation in particle diameter. They were further separated by selecting, via constant density columns, only those particles having the batch-average total coated particle density. Following density separation, the particles were radiographed individually to characterize each sample. Particles were heated in vacuum for 1 hour at 1400°C to ensure volatilization of any of the fluids used for density separation. Both TRISO and BISO coated batches were heat treated to simulate the fuel rod heat treatment cycle. The TRISO batches were heated to 1800°C for 30 minutes in Ar, while the BISO ThO_2 batches were heat treated to 1650°C for 90 minutes in Ar. The 1650°C heat treatment rather than 1800°C was employed in order to determine if a lower fuel rod heat treatment would produce equivalent or improved performance. A few BISO samples which were not heat treated will also be tested. Preparing samples by these techniques also facilitates measuring particle dimensional changes during the irradiation since the density, and hence volume, can easily be determined after irradiation.

TRISO Coated ThO_2 Particles. Figure 9-10 is a schematic diagram of the test matrix for TRISO coated ThO_2 particles. The test matrix depicts a systematic variation for three independent variables, viz, OPyC coating rate and bulk density as primary variables with coater bed size being a secondary effect probably related to oriented porosity. Tables 9-2 and 9-3 are a general description of TRISO coated ThO_2 particles tested in capsules HT-31 and HT-33, respectively.

BISO Coated ThO_2 Particles. Six ThO_2 batches containing 500-μm kernels are being tested in the HT-33 capsule. The particles in all batches have similar dimensions. Five of the batches were fabricated in the large coater with different OPyC coating rates, diluent gases, and temperatures to obtain the desired OPyC coating densities and optical anisotropies (BAF_o values). Two OPyC coating rates (4 and 6 μm/min), two bulk densities (1.68 and 1.90 Mg/m^3), and a range of BAF_o values (1.04 to 1.08) are being tested in the five batches fabricated in the large coater. The diluent coating gas was N_2 for three of the batches and H_2 for other two batches. The H_2 dilution, which is a new coating development, appears to improve certain OPyC coating properties.

The sixth batch, previously irradiated in capsules HT-28 and HT-29, was manufactured in the 127-mm-diameter coater and will be used as a comparison sample. Most of the present irradiation data are from batches coated in these smaller coaters. One sample from each batch was heat treated to 1650°C for 90 minutes in Ar to simulate the fuel rod heat-treatment cycle, which affects important coating parameters. Two of the large-coater samples were not heat treated; these will be used as comparison samples. The test matrix for the larger-coater ThO_2 BISO batches is shown in Fig. 9-11. A general description of the samples is given in Table 9-4.

PIE of HT-31. The GA HT-31 capsule specimens occupied two graphite magazines, each containing eight samples. The samples in the high-temperature magazine were irradiated at 1500°C to a fluence of 8.2 to 9.0 x 10^{25} n/m^2 $(E > 29\ fJ)_{HTGR}$ and a burnup of 8.2 to 8.9% FIMA. The low-temperature magazine specimens were tested at 1200°C to a fluence of 4.6 to 7.2 x 10^{25} n/m^2 $(E > 29\ fJ)_{HTGR}$ and a burnup of 4.9 to 7.2% FIMA. HT-31 was discharged from the HFIR on June 16, 1976. The capsule was disassembled and the samples were examined at ORNL.

Each sample was examined visually under the stereomicroscope. A description of the samples and the results of the visual examination are presented in Table 9-5. The samples irradiated at ∿1200°C had a range of

OPyC coating failure of 0 to 3.6% and no pressure vessel failures (failure of SiC). The 1500°C samples had pressure vessel failures of 0 to 94.9% and no OPyC failure by itself. All the kernels from broken particles were in a fine powder form.

Two main problems were encountered during the visual examination. The three samples with the highest failure had so much kernel powder that it was impossible to observe the particles. These specimens were sieved using a 355-μm screen to remove the fine powder so that the visual examination could be completed. The other problem was that the total number of particles for three of the nine samples for which the total number of particles could be counted did not agree with the original sample size reported. Two of the samples (43 and 46) had one extra particle; it is unlikely that the source of the extra particles was unloading of a previous sample. The final sample to be unloaded had four missing particles. There is the slight possibility that four particles could have been lost while unloading. The difficulty in pinpointing the cause of the differences lies in the fact that when ORNL loaded the GA samples into the graphite crucibles, the number of particles was not counted.

The general conclusion from the visual examination is that the samples irradiated at 1200°C performed well while most of the 1500°C samples did not. No total particle failure occurred in the low-temperature samples and the OPyC coating failure was low. All failures in the high-temperature specimens were of the pressure-vessel type. The two samples which performed the best had the lowest bulk ($\leq$1.59 Mg/m^3) and liquid gradient ($\leq$1.74 Mg/m^3) OPyC densities and the low coating rate ($\sim$5 μm/min). No other correlations of particle failure with the coating parameters were obvious. A more detailed analysis will be made after completion of the PIE.

The postirradiation examination plan for capsule HT-31 has been issued (Ref. 9-3). Analysis of the samples will begin in September 1976 at the GA hot cell and the PIE work is scheduled to be completed in December 1976.

The following properties will be measured: particle dimensions (radiography), fission gas release, fission product retention (gamma-ray spectrometry), OPyC coating density, microstructure, and optical anisotropy (BAF_o).

TASK 300: INTEGRAL FUEL SYSTEM TESTING

Subtask 310: Peach Bottom Fuel Test Elements

Fuel Test Element FTE-15

Conclusion. The general performance of the full-size HTGR fuel rods and candidate fuel types in FTE-15 was good at estimated peak exposures of 2.0×10^{25} n/m^2 $(E > 29\ fJ)_{HTGR}$ at ∿1520°C. The thermal analysis for this test element is not complete and therefore comparison of fuel failure measurements with predictions have not been made. Some of the general conclusions of this fuel examination were as follows:

1. The structural integrity of most of the fuel rods was good after exposures of 2.0×10^{25} n/m^2 $(E > 29\ fJ)_{HTGR}$ at ∿1520°C. Several fuel stacks had poor structural integrity after irradiation because of a below-normal matrix loading.

2. Fission gas release measurements of Kr-85m at 1100°C showed fuel failure between 0 and 10% at the peak irradiation conditions. The highest gaseous release was from a fuel blend containing a ThC_2 TRISO batch which had high failure. The lowest release was from the fuel rods containing TRISO UO_2 and BISO or TRISO ThO_2 fuel blends.

3. The UC_2 TRISO particles all showed SiC attack at peak temperatures of ∿1520°C. In some cases this attack extended half-way through the SiC coating.

4. Kernel migration of ThC_2 fuel kernels was also observed. The maximum migration was 10 to 20 μm into the buffer at peak irradiation conditions.

5. A ThC_2 TRISO fuel particle batch showed ∿50% OPyC failure and ∿20% pressure vessel failure at peak irradiation conditions.

6. Fuel rod gamma scanning showed good fuel homogeneity in all cases and low volatile fission product release.

7. Graphite fuel body gamma scanning showed insignificant plateout of cesium from fuel failure.

8. A BISO ThO_2 particle batch irradiated in a thermal stability spine sample to 2.0×10^{25} n/m^2 $(E > 29\ fJ)_{HTGR}$ at ∿1550°C showed good irradiation performance.

9. SiC attack in UC_2 TRISO fissile particles irradiated in thermal stability spine samples from ∿1230° to 1640°C was similar to that observed in the fuel rods.

10. A $UC_{4.3}O_{1.3}$ TRISO (WAR) particle showed good thermal stability and no SiC attack in thermal stability spine samples irradiated to conditions similar to those where SiC attack was observed in the UC_2 (VSM) particles.

11. A high OPyC failure on the $UC_{4.3}O_{1.3}$ (WAR) particle batch was correlated to the size of the fuel particle. Measured and predicted failures using Weibull statistics showed good agreement.

Experiment Description. FTE-15 was the second of two nearly identical test elements irradiated in the Peach Bottom reactor facility. FTE-14, the companion test element, was irradiated to 317 EFPD; the FTE-14 fuel performance was reported in Ref. 9-4.

The major objective of these test elements was to evaluate HTGR fuel types and materials in a representative HTGR environment. The postirradiation data were a direct comparison and verification source for the following HTGR design codes: (1) fluence and depletion, (2) thermal performance, (3) thermal and Wigner strain and stress, and (4) fission product behavior.

Under Phase III of the Peach Bottom Test Element Program, FTE-15 was inserted in core position A03-03 on July 6, 1972 and irradiated for 315.8 EFPD. It was then switched to core position A14-08 and irradiated for an additional 196.1 EFPD. The total irradiation of FTE-15 was 512.1 EFPD in Core 2. The average radial power factor for FTE-15 in Core 2 was 0.98 and the energy production was 7.3×10^4 kW/day. The maximum EOL fuel temperature was ~1520°C and the peak fluence was 2.0×10^{25} n/m^2 $(E > 29\ fJ)_{HTGR}$.

The design of FTE-15 was three identical teledial fuel bodies in a standard Peach Bottom driver containment; 198 fuel rods and 19 centrally located spine samples were tested in the element. FTE-15 was assembled with two thermocouples at 1917.7 mm (75.5 in.) total core height [i.e., 1257.3 mm (49.5 in.) active core height]. Thermocouple A was a W/Re type thermocouple located near the spine samples and thermocouple B was a C/A type thermocouple located near the outer sleeve.

The assembly of FTE-15 is shown in Fig. 9-12. A list of the detailed drawings for all the test element components is given in Table 9-6. The sleeve and upper and lower reflectors were standard Peach Bottom driver element designs; the materials used in these components are listed in Table 9-7. The purge flow in this element was down the center of the top reflector, through the upper porous plug, down the gap between the sleeve inside diameter and the fuel body outside diameter, through the internal trap in the bottom reflector and the standoff pin, and into the main manifold of the Peach Bottom reactor. No individual fission gas release measurements were taken.

The fuel zone consisted of three teledial 787.4 mm (31 in.) long fuel bodies (Fig. 9-13) stacked one on top of another. Bodies 1 and 2 were radially oriented to one another by means of two thermocouples, which are shown in the cross section of the fuel body in Fig. 9-14. Body 3 was not positioned via any thermocouples and therefore was subject to azimuthal movement. Eleven fuel rods were loaded into each of the six teledial holes. Spine samples were loaded into the 19.1 mm (0.75 in.) diameter hole in the center of the bodies. Body 2 had a stepped outside diameter to vary the temperature. A detailed drawing of body 2 is shown in Fig. 9-15.

FTE-15 contained 198 fuel rods that were carbonized in Al_2O_3 beds. These rods consisted of a closely packed bed of blended fissile and fertile coated fuel particles bonded together in a carbonaceous matrix. The matrix was a blend of 27 to 30% natural-flake graphite flour and 70 to 73% coal tar pitch. The matrix was prepared by hot-mixing the ingredients to form a homogeneous blend, followed by cooling to room temperature and then grinding the solid matrix into granules suitable for use in the fuel rod injection equipment. The impurities in the matrix were kept in the low ppm range.

Both the fuel particles and the fuel rods were made in production equipment using the then-available production processes and quality control techniques. The hot matrix was injected into the particle bed with a prototype injection machine similar to that built for manufacturing Fort St. Vrain fuel. After cooling, the fuel rods were removed from the injection die; at this point, the rods were referred to as "green" rods. The green rods were then packed into Al_2O_3 beds and subjected to a carbonization treatment.

The carbonization cycle consisted of heating the fuel rods in a flowing nitrogen atmosphere for 2 hr to 750°C and holding at that temperature for 0.5 hr. The fuel rods were then heat treated by passing them through a furnace, which had a hot zone 1814.4 mm (72 in.) long, at 1800°C and at a rate of 25.4 mm (1 in.) per min. The atmosphere in the furnace was argon. The cured rods were measured for length and diameter and loaded into the three graphite fuel bodies.

The fuel bodies contained a variety of fuel blends. Table 9-8 gives the location of the various fuel blends and Table 9-9 shows the preirradiation attributes of the fuel particles. The fuel rod preirradiation quality control attributes are shown in Table 9-10. The spine samples and their location in the test element are given in Table 9-11.

Visual Examination. During unloading of the fuel rods from the graphite bodies, extensive fuel rod failure was observed in stacks 4 and 5 of body 2. Composite photographs of these stacks and a description of the unloading is given in Ref. 9-5. The other fuel rods showed some matrix end cap cracking and some surface crazing. In some cases, there were also striations down the length of the fuel rod, which were caused by debris caught in the gap between the fuel rod and fuel body during unloading.

Fuel rods that were chosen for fission gas release measurements were first examined with the Bausch and Lomb stereomicroscope. Photomicrographs of these fuel rods are shown in Figs. 9-16 through 9-34. Examination of these rods showed clearer evidence of the surface and matrix end cap cracking observed during the unloading. Unloading damage was high in some cases; the number of surface failures is tabulated in Table 9-12. Some particles showed black soot marks on the surface; these were caused by in-service surface fuel failure.

The high fuel rod failure in stacks 4 and 5 was found by metallography to be caused by a below-specified matrix loading. The lack of matrix caused lower fuel rod strength and subsequent fuel rod cracking.

Fission Gas Release Measurements. Fourteen fuel rods of representative fuel in FTE-15 were chosen for fission gas release measurements for Kr-85m at 1100°C in the TRIGA irradiation facility. A comparison of fission gas release measurements and fuel failure measured by metallography is shown in Table 9-12. The correction for nominal preirradiation contamination and defective particle fuel failure to the postirradiation fission gas release measurements is shown in Table 9-13. From this correction, a predicted postirradiation fission gas release value can be used to calculate a

corrected fuel failure. This failure fraction is defined as the amount of U-235 normalized fissionable material that has been exposed because of irradiation-induced failure. This technique is outlined in Ref. 9-6. In all the fuel rods the failure fraction was between 0 and 5% except for rods in stacks 2 and 5 of body 2. The fuel failure of 9 to 13% calculated from fission gas release from fuel rods from stack 2 were due to the high ThC_2 TRISO fuel failure observed during metallography. The high failure in rod 2-5-2 was most likely due to low matrix content, which possibly caused both fissile and fertile failure. Metallography will be done on some of the fuel rod fragments in the high-temperature region of this stack to substantiate this hypothesis. The fuel stacks with the lowest corrected fuel failure were in stacks 3 and 6 of body 2, which contained UO_2 TRISO - ThO_2 TRISO/UO_2 TRISO - ThO_2 BISO.

Fuel Rod Metallography. Six fuel rods from the center of body 2, which had the highest fast neutron fluence and temperature [2.0×10^{25} n/m^2 $(E > 29\ fJ)_{HTGR}$ and 1516°C], were selected for metallography. These fuel rods represented each fuel blend tested in FTE-15 (Table 9-8). A summary of the postirradiation examination of these fuel rods is given in Table 9-12. A radial metallographic cross section and a representative photomicrograph of the matrix of each of these fuel rods are shown in Figs. 9-35 through 9-40. Representative photomicrographs of the fuel particles in each of these fuel rods are shown in Figs. 9-41 through 9-48. A single-channel gamma scan plot of most of the fuel rods examined is shown in Fig. 9-49.

The UC_2 TRISO fissile particles examined showed SiC attack up to 10 to 15 μm through the coating. UO_2 TRISO and $(Th,U)O_2$ TRISO fissile, ThO_2 BISO and TRISO fertile, and ThC_2 BISO fertile fuel showed good irradiation performance at these severe high-temperature conditions. Several cases of ThC_2 kernel migration were observed up to 10 to 20 μm into the buffer. Structural failure of two of the fuel rod types resulted from lack of matrix material. The final thermal analysis on this element is not complete and thus the irradiation effects on the FTE-15 fuel could not be compared to predictions at the time of this report.

Fuel rods 2-1-5 and 2-2-5 both contained a UC_2 TRISO fissile particle. In each case there was buffer densification and debonding in this particle type and measurable SiC attack. There was observable SiC attack in 15 to 60% of the particles in fuel rods 2-1-5 and 2-2-5. Figures 9-41 and 9-43 show the degree of this attack, which in rod 2-2-5 extended half-way through the SiC coating in one case. Because the SiC failure in both of these rods was hairline, it was difficult to determine if it was an irradiation effect or polishing damage. Fission gas release measurements (Table 9-13) of rods 2-1-4 and 2-1-5 were low, which indicates polishing damage. Because of the high fission gas release and the high ThC_2 failure of fuel rod 2-2-5, it could not be determined if the UC_2 particle failure was irradiation induced.

Rods 2-3-9, 2-5-2, and 2-6-5 contained UO_2 TRISO fissile particles. This fissile fuel type had buffer densification and debonding, but in all cases the thermal stability of the kernel was good (Figs. 9-45, 9-47, and 9-48). A $(Th,U)O_2$ TRISO fissile particle in fuel rod 2-4-3 was examined (Fig. 9-46); its performance was also considered good at these peak exposures.

A ThO_2 BISO batch and a TRISO fertile batch were examined in fuel rods 2-3-9 and 2-6-5, respectively. Both of these particle batches looked good after irradiation (Figs. 9-45 and 9-48). The high SiC failure in the TRISO batch was considered to be the result of polishing because of the low fission gas release measurement of fuel rod 2-6-5.

The ThC_2 kernel in fuel rod 2-1-5 was the only case of kernel migration observed in FTE-15. Figure 9-42 shows one case of ThC_2 kernel migration that extended 10 to 20 μm in the buffer coating toward the center of the fuel rod. BISO ThC_2 fertile particles were also tested in fuel rods 2-4-3 and 2-5-2. No ThC_2 kernel migration was observed in either of these fuel rods.

The high OPyC coating failure of the ThC_2 BISO fuel in fuel rod 2-4-3 was considered to be due to the hydrolysis of the fuel kernels during the

metallographic examination since no metallographic mounting resin was observed in the large cracks. The two OPyC failures of the ThC_2 BISO particles in fuel rod 2-5-2 were due to production defects (see Fig. 9-47). The ThC_2 kernel was also tested with a TRISO coating in fuel rod 2-2-5 (Fig. 9-44) where ∿50% OPyC failure was observed. The observed failure was not inconsistent with failure levels observed during irradiation of similar fuel in capsule F-30 (Ref. 9-6). Fission gas release from fuel rod 2-2-5 indicated that about 13% of fissionable material in fertile and fissile fuel was exposed by failed coatings, which shows that high failure of OPyC on fertile fuel was not associated with an equal total coating failure.

The other significant metallographic finding was the reason for the high structural failure of the fuel rods in stacks 4 and 5 of body 2. Study of the radial cross sections of the fuel rods in Figs. 9-35 through 9-40 shows that fuel rods 2-4-3 and 2-5-2 both had significantly less matrix phase than the other rods examined. The failure of these rods was simply due to not enough bonding material to keep them together. The high OPyC failure in the TRISO UO_2 fissile particles in fuel rod 2-5-2 was unexplained. There is a possible correlation of the lack of matrix and the high OPyC failure. Additional metallography would be necessary to prove this point.

Fuel Rod Gamma Scanning. All of the fuel rods used in the postirradiation examination or stored as historical specimens were gamma scanned with the Ge(Li) detector in the GA hot cell. The technique for scanning has been described earlier in Ref. 9-7. Briefly it consists of passing the fuel rods slowly past a collimator which has its long axis perpendicular to the length of the rods. During the scanning operation both single-channel and multichannel scans are collected.

Cs-137 single-channel scans of five representative fuel rods used in the postirradiation examination are shown in Fig. 9-49. These plots show that the relative fuel homogeneity is good in all cases.

The results of the multichannel scans of the various fuel rods is shown in Table 9-14. From the Cs-137 inventory a composite burnup value was calculated, which is also tabulated in Table 9-14 and shown in Figs. 9-50 through 9-52. These data were plotted in three sets for convenience because of the wide variety of fuel loadings. Theoretically fuel rods with fuel loadings having the same Th/U ratio should be comparable. Therefore, the three plots represent narrow ranges of Th/U ratios, which allows a meaningful comparison. When the GAUGE/FEVER-calculated and chemistry-measured burnups have been completed, they will be compared to these data.

The Cs-137/Zr-95 ratio can be used as a fuel failure monitor. If there is no Cs-137 loss due to fuel failure or diffusive release, this ratio should be the same for fuel rods with similar Th/U loading ratios. Figures 9-53 through 9-55 show the Cs-137/Zr-95 ratio of fuel rods plotted for the same three groupings of Th/U ratios discussed in the burnup analysis above. It is obvious that in all cases the measured values are within a narrow band, which indicates that the Cs-137 loss was low (i.e., <10%) in all cases. This is substantiated by metallography, fission gas release, and graphite gamma scanning.

Graphite Fuel Body Gamma Scanning. The graphite fuel bodies were axially gamma scanned using the same scanning geometry as was used for the fuel rods. Two scans were done on each fuel body. One axial scan was centered on holes 1 and 2 and the other was centered on holes 4 and 5. The area scanned in each of these scans is shown in Fig. 9-56. In no case was there any significant cesium plateout on the fuel bodies, which indicates low fissile fuel failure; this is substantiated by fission gas release measurements and metallography.

Thermal Stability Spine Samples. A variety of particle types were tested in the thermal stability type II spine samples. The location of the spine samples is shown in Table 9-11 and a description of the crucible is given in Fig. 9-57. The purpose of these crucibles was to irradiate different fuel types in a relatively isothermal environment to a variety of temperatures and burnups. ThO_2 BISO fertile, UC_2 TRISO fissile, and UC_xO_y

TRISO (WAR) fissile particle batches were chosen for analysis from both FTE-14 and FTE-15, which had identical spine sample experiments. A description of these particles is given in Table 9-15. The irradiation exposures of the particles in FTE-15 were between 1.8×10^{25} n/m^2 and 2.0×10^{25} n/m^2 $(E > 29 \text{ fJ})_{HTGR}$ at 1200° to 1600°C. FTE-14 spine samples were described earlier in Ref. 9-4 but are included here to show the effect of irradiation exposure on the performance of these particles.

All the spine sample batches were examined with the Bausch and Lomb stereomicroscope after unloading. Stereophotographs of the FTE-15 spine samples are shown in Figs. 9-58 through 9-60. A summary of the failure fraction of the OPyC coatings observed during stereoexamination is tabulated in Table 9-16. All the fuel particle types showed good exterior appearances except for UC_xO_y (WAR) particle batch OR-1694. In the four experiments where this particle batch was tested in FTE-14 and FTE-15, a 6 to 8% OPyC failure fraction was observed. From the stereophotograph of the WAR particles in Fig. 9-59, it is obvious that larger particles failed more frequently than the smaller particles. This particular particle batch was unusual because it had a wide range of particle diameters.

The effect of OPyC coating failure in TRISO particles has been observed and discussed by Kaae and Harmon in Refs. 9-8 and 9-9. The basis of these discussions is from Weibull statistics. The general mathematical formulation is shown in Eq. 9-1. The basis for this equation is that the probability of finding a critical flaw in a brittle material is proportional to the volume of the material under stress:

$$F = 1 - \exp\left[-\int_v \left(\frac{\sigma}{\sigma_o}\right)^M dV\right] \quad , \tag{9-1}$$

where F = failure probability,

v = volume under stress,

σ = uniaxial stress,

σ_o = normalizing material property parameter,

M = Weibull modulus.

For comparison purposes, in this particular case the stresses in the OPyC layer are assumed to be constant in all of the particles because of similar coating conditions and irradiation exposures. With this assumption and the fact that the volume of the OPyC and the difference between the outside and inside OPyC diameters cubed are proportional, Eq. 9-1 reduces to Eq. 9-2:

$$\log(1 - F) = C_1 \left[d^3 - (d - 2t)^3\right] + C_2 \quad , \tag{9-2}$$

where C_1 and C_2 = constants,

d = particle diameter,

$1 - F$ = survival fraction,

t = OPyC coating thickness = 40 μm.

If $d^3 - (d - 2t)^3$ and $\log(1 - F)$ are plotted, the least-squares fit of the data should be a straight line with slope C_1 and intercept C_2. Taking the four particle batches of OR-1694 particles tested, a survival fraction $(1 - F)$ was determined for particle sizes in 25-μm-diameter increments. These data are plotted in Fig. 9-61 and a least-squares fit of the data is shown. The good correlation in this particular case shows that when the irradiation conditions and outer pyrocarbon stresses are constant, the particle size is a critical factor in determining the OPyC failure level. This analysis indicates the need of applying Weibull statistics to present HTGR OPyC failure prediction models.

A summary of the metallographic examination of both the FTE-14 and FTE-15 spine samples is shown in Table 9-16. Photomicrographs of the FTE-15 spine samples are shown in Figs. 9-62 through 9-66. Results of the metallographic examination of FTE-14 spine samples were reported in Ref. 9-4. The ThO_2 BISO fertile particle batch 4252-02-070 showed good thermal stability at a peak exposure of 2.0×10^{25} n/m^2 $(E > 29\ fJ)_{HTGR}$ at ∿1350°C. The fissile particles allowed an excellent comparison between the UC_2 (VSM) and UC_xO_y (WAR) fuel kernel types.

The UC_2 (VSM) batch 4161-01-030 showed both increasing SiC attack by lanthanide fission products and SiC failure with higher temperatures and irradiation exposures. No SiC attack was seen in spine sample TS 3-6 at ∿1230°C. Figures 9-63 and 9-64 show the increasing SiC attack in samples TS 4-6 and TS 5-6 with respective temperatures of ∿1540° and 1610°C. Because the temperatures of these spine samples are still preliminary, no conclusions can be drawn regarding the kinetics of this attack. When the thermal analysis has been completed, the rate of SiC attack can be compared to work outlined in Ref. 9-7.

In comparison to the performance of the UC_2 (VSM) particles, the $UC_{4.3}O_{1.3}$ (WAR) TRISO fissile particles showed good kernel and fission product performance. Photomicrographs of the two batches of OR-1694 particles are shown in Figs. 9-65 and 9-66. Because of the shrinkage of the low-density kernel, the WAR particles have a large void in the center. The dark field photomicrographs in Figs. 9-65 and 9-66 show that no significant metallic fission products have migrated out of the kernel and, subsequently, no SiC attack was observed. This is due to the fact that the O_2-doped kernels retain the metallic fission products as oxides and inhibit their diffusion to the SiC interface.

REFERENCES

9-1. Young, C. A., and D. P. Harmon, "Preirradiation Report of Fuel Materials for P13T Capsule Irradiation," ERDA Report GA-A13343, General Atomic, April 1976.

9-2. Kovacs, W. J., C. A. Young, and D. P. Harmon, "Preirradiation Report for TRISO and BISO ThO_2 Particles in Irradiation Capsules HT-31 and HT-33," ERDA Report GA-A13923, to be published.

9-3. Young, C. A., "Capsule HT-31 Postirradiation Examination Plan," General Atomic unpublished data, July 20, 1976.

9-4. "HTGR Fuels and Core Development Program, Quarterly Progress Report for the Period Ending November 30, 1974," USAEC Report GA-A13253, General Atomic, January 21, 1975.

9-5. "HTGR Fuels and Core Development Program, Quarterly Progress Report for the Period Ending May 31, 1975," ERDA Report GA-A13444, General Atomic, June 30, 1975.

9-6. Scott, C. B., and D. P. Harmon, "Postirradiation Examination of Capsule F-30," General Atomic Report GA-A13208, April 1, 1975.

9-7. "HTGR Fuels and Core Development Program, Quarterly Progress Report for the Period Ending February 21, 1976," ERDA Report GA-A13804, General Atomic, March 31, 1976.

9-8. Kaae, J. L., "Application of Weibull Statistics to the Strength of Pyrolytic Carbon," General Atomic Report GA-A13869, March 1976.

9-9. Kaae, J. L., and D. P. Harmon, General Atomic unpublished data, April 15, 1976.

TABLE 9-1
CURRENT STEADY-STATE P13V OPERATING CONDITIONS[a]

Cell No.	Control Temp. (°C)		Cell Contents	Fast Fluence ($X\ 10^{25}\ n/m^2$) $(E > 29\ fJ)_{HTGR}$	R/B Kr-85m
	Design	Actual Decalibrated			
1	1250	1262	WAR TRISO/ThO_2 BISO	4	3×10^{-5}
2	1150	1172	WAR TRISO/ThO_2 BISO	6	1×10^{-5}
3	1175	1201	ThO_2 BISO only	6	3×10^{-5}
4	1250	1131	Unbonded reference particles	5.5	2×10^{-5}
5	1375	1415	WAR TRISO/ThO_2 BISO	4	3×10^{-5}
6	1250	1257	WAR TRISO only	2.6	3×10^{-5}

[a] Rod Bank = 26.1 in.

TABLE 9-2
GENERAL DESCRIPTION OF TRISO COATED PARTICLES TESTED IN CAPSULE HT-31

Particle Batch Data Retrieval Number	Kernel Mean Diameter (μm)	Coating Phases												Total Coated Particle						Test Conditions					
		Buffer		IPyC				SiC		OPyC															
		Thickness (μm)	Density[a] (Mg/m^3)	Thickness (μm)	Density[a] (Mg/m^3)	Coating Rate (μm/min)	BAF_o[b]	Thickness (μm)	Density[a] (Mg/m^3)	Thickness (μm)	Density[a] (Mg/m^3)	Coating Rate (μm/min)	BAF_o[b]	Coating Thickness (μm)	Mean Diameter (μm)	Mean Density[c] (Mg/m^3)	Th-232 Particle Loading[d] (μg/particle)	Exposed Heavy Metal ($\frac{\mu g \text{ heavy metal}}{g \text{ heavy metal}}$)[e]	Defective SiC Fraction[f] ($\frac{\mu g \text{ Th leached}}{\text{total g Th}}$)	X-ray Plate I.D.	Number of Particles Tested	Sample Position	Design Test Temperature (°C)	Design Peak Fast Fluence ($E > 29$ fJ)$_{HTGR}$ (10^{25} n/m^2)	Design Burnup (% FIMA)
6252-05-0160-005	511	69	1.04	30	1.84	3.93	ND[g]	35	3.20	48	1.85	4.40	ND	176	873	3.59	654	2	36	LB341	34	43	1200	5.6	6.2
6252-05-0160-006	509	68	1.04	30	1.84	3.93	ND	34	3.20	50	1.85	4.58	ND	176	872	3.59	654	2	36	LB342	51	27	1500	7.7	8.4
6252-06-0161-001	449	69	1.07	34	1.90	4.09	1.076	41	3.22	45	1.74	5.00	1.022	181	819	3.39	429	8.3	2.7	LB346	53	49	1200	4.4	5.0
6252-06-0161-002	448	68	1.07	34	1.90	4.09	1.076	41	3.22	44	1.74	4.89	1.022	181	823	3.39	429	8.3	2.7	LB347	78	38	1500	7.0	7.7
6252-06-0261-001	448	60	1.12	39	1.93	4.43	1.088	39	3.21	47	1.70	5.34	1.028	190	813	3.26	424	0.8	120	LB361	52	48	1200	4.7	5.2
6252-06-0261-002	448	59	1.12	39	1.93	4.43	1.088	39	3.21	46	1.70	5.23	1.028	190	812	3.26	424	0.8	120	LB362	77	36	1500	7.3	7.9
6252-07-0161-001	448	57	1.12	39	1.93	4.43	1.079	39	3.20	50	1.81	5.56	1.027	191	816	3.23	415	9.2	10.6	LB366	54	46	1200	5.0	5.6
6252-07-0161-002	448	58	1.12	39	1.93	4.43	1.079	40	3.20	52	1.81	5.78	1.027	191	823	3.23	415	9.2	10.6	LB367	80	35	1500	7.4	8.0
6252-07-0261-001	447	63	1.12	39	1.93	4.43	1.098	39	3.21	46	1.80	5.11	1.030	187	820	3.32	423	0.8	3.5	LB371	53	45	1200	5.2	5.8
6252-07-0261-002	446	62	1.12	39	1.93	4.43	1.098	39	3.21	47	1.80	5.22	1.030	187	821	3.32	423	0.8	3.5	LB372	78	33	1500	7.5	8.2
6252-08-0161-001	447	60	1.12	39	1.93	4.43	1.065	39	3.20	49	1.89	5.44	1.034	194	836	3.30	414	1	18	LB336	54	51	1200	3.9	4.5
6252-08-0161-002	447	60	1.12	39	1.93	4.43	1.065	39	3.20	50	1.89	5.56	1.034	194	836	3.30	414	1	18	LB337	80	29	1500	7.7	8.4
6252-09-0161-001	447	66	1.07	34	1.90	4.09	1.095	41	3.22	47	1.78	7.23	1.018	185	823	3.34	426	1	7.2	LB356	53	42	1200	5.9	6.4
6252-09-0161-002	447	63	1.07	34	1.90	4.09	1.095	42	3.22	48	1.78	7.38	1.018	185	819	3.34	426	1	7.2	LB357	78	32	1500	7.6	8.2
6252-10-0161-001	447	63	1.07	34	1.90	4.09	1.074	42	3.22	53	1.98	8.15	1.036	189	829	3.31	421	2	8.4	LB351	53	40	1200	6.2	6.8
6252-10-0161-002	446	62	1.07	34	1.90	4.09	1.074	42	3.22	51	1.98	7.85	1.036	189	824	3.31	421	2	8.4	LB352	79	30	1500	7.6	8.3

[a] Measured on parent batch prior to density separation.
[b] Measured on nonheat-treated parent batch using Seibersdorf optical anisotropy unit (24-μm diameter spot).
[c] Determined by Hg porosimeter.
[d] Calculated from density and thickness of parent batch coating phases and ThO_2 stoichiometry.
[e] Determined by hydrolysis test on parent batch and indicates total amount of exposed heavy metal; not corrected for partial conversion of oxide to carbide.
[f] Determined by burn and 24-hr ultraleach on parent batch.
[g] ND = not determined.

TABLE 9-3
GENERAL DESCRIPTION OF TRISO COATED PARTICLES TESTED IN CAPSULE HT-33

Particle Batch Data Retrieval Number	Kernel Mean Diameter (μm)	Coating Phases												Total Coated Particle						Test Conditions					
		Buffer		IPyC				SiC		OPyC															
		Thickness (μm)	Density[a] (Mg/m^3)	Thickness (μm)	Density[a] (Mg/m^3)	Coating Rate (μm/min)	BAF_o[b]	Thickness (μm)	Density[a] (Mg/m^3)	Thickness (μm)	Density[a] (Mg/m^3)	Coating Rate (μm/min)	BAF_o[b]	Coating Thickness (μm)	Mean Diameter (μm)	Mean Density[c] (Mg/m^3)	Th-232 Particle Loading[d] (μg/particle)	Exposed Heavy Metal[e] (μg heavy metal / g heavy metal)	Defective SiC Fraction[f] (μg Th leached / total g Th)	X-ray Plate I.D.	Number Of Particles Tested	Sample Position	Design Test Temperature (°C)	Design Peak Fast Fluence (E > 29 fJ)HTGR (10^{25} n/m^2)	Design Burnup (% FIMA)
6252-05-0160-007	509	68	1.04	30	1.84	3.93	ND[g]	35	3.20	50	1.85	4.58	ND	176	872	3.59	654	2	36	LB343	34	45	1200	6.5	9.4
6252-05-0160-008	510	68	1.04	30	1.84	3.93	ND	34	3.20	48	1.85	4.40	ND	176	870	3.59	654	2	36	LB344	51	30	1500	9.6	12.4
6252-06-0161-003	448	64	1.07	34	1.90	4.09	1.076	41	3.22	44	1.74	4.89	1.022	181	818	3.39	429	8.3	2.7	LB348	53	48	1200	5.9	8.0
6252-06-0161-004	450	68	1.07	34	1.90	4.09	1.076	41	3.22	46	1.74	5.11	1.022	181	824	3.39	429	8.3	2.7	LB349	78	33	1500	9.3	12.1
6252-06-0261-003	448	60	1.12	39	1.93	4.43	1.088	38	3.21	47	1.70	5.34	1.028	190	812	3.26	424	0.8	120	LB363	52	46	1200	6.3	8.6
6252-06-0261-004	449	59	1.12	39	1.93	4.43	1.088	39	3.21	48	1.70	5.45	1.028	190	816	3.26	424	0.8	120	LB364	77	32	1500	9.5	12.2
6252-07-0161-003	448	58	1.12	39	1.93	4.43	1.079	39	3.20	51	1.81	5.67	1.027	191	826	3.23	415	9.2	10.6	LB368	54	43	1200	6.9	9.5
6252-07-0161-004	447	58	1.12	39	1.93	4.43	1.079	38	3.20	52	1.81	5.78	1.027	191	821	3.23	415	9.2	10.6	LB369	80	36	1500	9.1	11.8
6252-07-0261-003	446	61	1.12	39	1.93	4.43	1.098	39	3.21	46	1.80	5.11	1.030	187	813	3.32	423	0.8	3.5	LB373	53	42	1200	7.3	9.7
6252-07-0261-004	447	62	1.12	39	1.93	4.43	1.098	38	3.21	46	1.80	5.11	1.030	187	814	3.32	423	0.8	3.5	LB374	78	35	1500	9.2	11.9
6252-08-0161-003	447	61	1.12	39	1.93	4.43	1.065	38	3.20	47	1.89	5.22	1.034	194	836	3.30	414	1	18	LB338	54	49	1200	5.5	7.5
6252-08-0161-004	448	61	1.12	39	1.93	4.43	1.065	38	3.20	50	1.89	5.56	1.034	194	836	3.30	414	1	18	LB339	80	27	1500	9.6	12.5
6252-09-0161-003	448	65	1.07	34	1.90	4.09	1.095	42	3.22	47	1.78	7.23	1.018	185	824	3.34	426	1	7.2	LB358	53	40	1200	7.6	10.2
6252-09-0161-004	447	67	1.07	34	1.90	4.09	1.095	42	3.22	49	1.78	7.54	1.018	185	826	3.34	426	1	7.2	LB359	78	38	1500	8.7	11.5
6252-10-0161-003	447	63	1.07	34	1.90	4.09	1.074	42	3.22	51	1.98	7.85	1.036	189	826	3.31	421	2	8.4	LB353	53	51	1200	4.9	7.0
6252-10-0161-004	445	62	1.07	34	1.90	4.09	1.074	42	3.22	51	1.98	7.85	1.036	189	818	3.31	421	2	8.4	LB354	79	29	1500	9.6	12.5

[a] Measured on parent batch prior to density separation.
[b] Measured on nonheat-treated parent batch using Seibersdorf optical anisotropy unit (24-μm diameter spot).
[c] Determined by Hg porosimeter.
[d] Calculated from density and thickness of parent batch coating phases and ThO_2 stoichiometry.
[e] Determined by hydrolysis test on parent batch and indicates total amount of exposed heavy metal; not corrected for partial conversion of oxide to carbide.
[f] Determined by burn and 24-hr ultraleach on parent batch.
[g] ND = not determined.

TABLE 9-4
GENERAL DESCRIPTION OF BISO COATED PARTICLES FOR HT-33 CAPSULE

Sample Batch Number	Heat Treatment	Kernel Diameter[a] (μm)	Coatings										Total Coated Particle					Capsule Description		Design Irradiation Parameters		
			Coater Size (mm)	Buffer		Outer Isotropic						Total Coating Thickness[a] (μm)	Diameter[a] (μm)	Density[h] (Mg/m^3)	Th Content[i] (wt %)	Exposed Th[c,j] (kg Th/kg Th)	Fission Gas Release[d,k]	Position No.	Number of Particles	Fuel Temperature (°C)	Fast Fluence ($\times 10^{25}$ n/m^2) ($E > 29$ fJ)$_{HTGR}$	Burnup (% FIMA)
				Thickness[a] (μm)	Density[b,c] (Mg/m^3)	Thickness[a] (μm)	Density[d] (Mg/m^3) Sink Float[e]	Density[d] (Mg/m^3) Bulk[f]	Coating Rate[d] (μm/min)	BAF_o[d,g]	Fabrication Diluent Gas											
6542-27-0161-001	Yes	500	127	87	1.09	75	1.86[1]	1.78[1]	4.2	1.041[m]	Ar	162	823	3.45	56.8	3.7×10^{-6}	3.4×10^{-6}[1]	8	40	1200	6.8	9.1
6542-27-0161-002	Yes	503	127	88	1.09	75	1.86[1]	1.78[1]	4.2	1.041[m]	Ar	164	829	3.45	56.8	3.7×10^{-6}	3.4×10^{-6}[1]	17	57	1500	9.5	11.7
6542-29-0261-001	Yes	504	240	94	1.13	76	1.96	1.89	4.4	1.081	N_2	170	843	3.45	54.9	6.1×10^{-7}	6.1×10^{-5}	10	39	1200	7.4	9.6
6542-29-0261-002	Yes	503	240	93	1.13	72	1.96	1.89	4.2	1.081	N_2	166	833	3.45	54.9	6.1×10^{-7}	6.1×10^{-5}	15	55	1500	9.2	11.4
6542-39-0161-001	Yes	508	240	86	1.13	71	1.98	1.92	3.9	1.079	N_2	156	821	3.61	58.9	4.5×10^{-7}	6.2×10^{-6}	2	38	1200	5.1	7.2
6542-39-0161-002	Yes	508	240	86	1.13	74	1.98	1.92	4.1	1.079	N_2	161	826	3.61	58.9	4.5×10^{-7}	6.2×10^{-6}	21	54	1500	9.9	12.1
6542-40-0161-001	Yes	500	240	91	1.10	73	1.74	1.67	5.8	1.042	H_2	164	828	3.35	57.1	5.1×10^{-4}	$<1.4 \times 10^{-6}$	4	41	1200	5.8	7.8
6542-40-0161-002	Yes	502	240	93	1.10	71	1.74	1.67	5.7	1.042	H_2	164	827	3.35	57.1	5.1×10^{-4}	$<1.4 \times 10^{-6}$	23	58	1500	10.0	12.2
6542-40-0260-001	No	503	240	85	1.10	76	1.77	1.69	5.6	1.038	H_2	161	829	3.36	57.0	2.2×10^{-5}	3.6×10^{-6}	7	41	1200	6.6	8.8
6542-40-0260-002	No	500	240	88	1.10	77	1.77	1.69	5.7	1.038	H_2	164	826	3.36	57.0	2.2×10^{-5}	3.6×10^{-6}	26	58	1500	10.2	12.4
6542-40-0261-001	Yes	500	240	89	1.10	78	1.77	1.70	5.8	1.038	H_2	168	832	3.39	57.0	2.2×10^{-5}	$<1.4 \times 10^{-6}$	5	41	1200	6.0	8.2
6542-40-0261-002	Yes	501	240	87	1.10	76	1.77	1.70	5.6	1.038	H_2	164	828	3.39	57.0	2.2×10^{-5}	$<1.4 \times 10^{-6}$	24	58	1500	10.1	12.3
6542-41-0160-001	No	507	240	91	1.13	70	2.00	1.93	5.6	1.060	N_2	160	827	3.51	56.0	1.5×10^{-5}	4.2×10^{-5}	13	40	1200	8.1	10.3
6542-41-0160-002	No	505	240	88	1.13	68	2.00	1.93	5.4	1.060	N_2	155	817	3.51	56.0	1.5×10^{-5}	4.2×10^{-5}	20	56	1500	9.8	12.0
6542-41-0161-001	Yes	503	240	92	1.13	69	2.02	1.93	5.5	1.081	N_2	161	825	3.54	56.0	1.5×10^{-5}	5.6×10^{-5}	11	40	1200	7.6	9.6
6542-41-0161-002	Yes	503	240	92	1.13	69	2.02	1.93	5.5	1.081	N_2	161	823	3.54	56.0	1.5×10^{-5}	5.6×10^{-5}	18	56	1500	9.6	11.8

[a] Measured or calculated on capsule test samples.
[b] Determined by a mathematical calculation.
[c] Measured on as-coated parent batch.
[d] Measured on heat-treated parent batches, except where noted, for the heat-treated capsule test samples; otherwise the as-coated parent batches were measured.
[e] Measured by a liquid-gradient technique.
[f] Calculated from the equation: $1/\rho_B = 1/\rho_{SF} + K(AP)$, where: ρ_B = bulk density, ρ_{SF} = sink float density, K = constant, and AP = accessible porosity.
[g] Optical anisotropy measured using the Seibersdorf optical unit at GA.
[h] Density of density-separated fraction measured by liquid-gradient technique.
[i] Calculated from parent batch densities and dimensions of density-separated fraction for particle components and the kernel composition.
[j] Determined by acid-leach test.
[k] Release rate/birth rate for Kr-85m at 1100°C; activated in linear accelerator.
[l] Values for as-coated parent batch; data not available for heat-treated parent batch.
[m] Sample heat treated at 1800°C for 1 hr in He.

TABLE 9-5

DESCRIPTION AND RESULTS OF VISUAL EXAMINATION OF TRISO ThO_2 SPECIMENS IRRADIATED IN HT 31 CAPSULE

Specimen Particle Number	Particle Properties[a]							Irradiation Conditions			Results of Visual Exam			Primary Particle Design Variables[d]		
	Kernel Diameter (μm)	Coater Size (mm)	Charge Size for OPyC Coating (kg of Heavy metal)	OPyC Coating Density (Mg/m^3) Liquid Gradient	OPyC Coating Density (Mg/m^3) Bulk	OPyC Coating Rate (μm/min)	BAF_o[b]	Capsule Position[c]	Fast Fluence (10^{25} n/m^2) (E > 29 fJ)$_{HTGR}$	Burnup (% FIMA)	Number of Particles Examined	OPyC Coating Failure (%)	Pressure Vessel Failure (%)	Coating Rate	Bulk Density	OPyC Charge Size
1200°C Magazine (900°C Graphite Crucible Temperature)																
6252-08-0161-001	447	240	6.6	1.89	1.73	5.4	1.034	51	4.6	4.9	50[e]	0	0	Low	High	Small
6252-06-0161-001	449	240	11.0	1.74	1.59	5.0	1.022	49	5.1	5.4	53	0	0	Low	Low	Large
6252-06-0261-001	448	240	6.6	1.70	1.57	5.3	1.028	48	5.4	5.6	52	0	0	Low	Low	Small
6252-07-0161-001	448	240	13.2	1.81	1.59	5.6	1.027	46	5.9	6.1	55[g]	3 6	0[f]	Low	Low	Large
6252-07-0261-001	447	240	6.6	1.80	1.65	5.1	1.030	45	6.1	6.3	53	1 9	0[f]	Low	Medium	Small
6252-05-0160-005	511	125	1.8	1.85	(h)	4.4	(h)	43	6.6	6.7	35[i]	0	0	(j)	(j)	(j)
6252-09-0161-001	447	240	5.5	1.78	1.59	7.2	1.018	42	6.8	6.9	53	1.9	0[f]	High	Low	Small
6252-10-0161-001	447	240	5.5	1.98	1.75	8.2	1.036	40	7.2	7.2	53	1.9	0[f]	High	High	Small
1500°C Magazine (1250°C Graphite Crucible Temperature)																
6252-06-0161-002	448	240	11.0	1.74	1.59	4.9	1.022	38	8.2	8.2	78	0	0	Low	Low	Large
6252-06-0261 002	448	240	6.6	1.70	1.57	5.2	1.028	36	8.5	8.4	77[1]	(k)	11.7	Low	Low	Small
6252-07-0161-002	448	240	13.2	1.81	1.59	5.8	1.027	35	8.6	8.5	80[1]	(k)	52.5	Low	Low	Large
6252-07-0261-002	446	240	6.6	1.80	1.65	5.2	1.030	33	8.7	8.6	78[1]	(k)	38 5	Low	Medium	Small
6252-09-0161-002	447	240	5.5	1.78	1.59	7.4	1.018	32	8.8	8.7	78[1,m]	(k)	94.9	High	Low	Small
6252-10-0161-002	446	240	5.5	1.98	1.75	7.8	1.036	30	8.9	8 8	79[1]	(k)	53 2	High	High	Small
6252-08-0161-002	447	240	6.6	1.89	1.73	5.6	1.034	29	9.0	8.8	80[1,m]	(k)	80.0	Low	High	Small
6252-05-0160-006	509	125	1.8	1.85	(h)	4 6	(h)	27	9.0	8.9	51[1,m]	(k)	94.1	(j)	(j)	(j)

(a) All specimens were screened, density separated to parent batch average, and heat treated at 1800°C for 30 minutes in Ar.

(b) Measured with Seibersdorf optical anisotropy unit using 24-μm circle.

(c) The number designates the axial position in capsule, the numbers increase consecutively towards the bottom of the capsule (relative to the reactor core)

(d) Word descriptions are relative to the HT-31 particle batches only.

(e) Does not agree with design number of particles (54 reported).

(f) The OPyC coatings did not usually come off the failed coating and, therefore, it is not conclusive that the SiC is intact.

(g) Does not agree with design number of particles (54 reported).

(h) Not determined.

(i) Does not agree with design number of particles (34 reported).

(j) This sample previously tested in HT-28 and -29 has a 500-μm diameter kernel and was coated in the 127-mm coater.

(k) OPyC coating failure without pressure vessel failure was not observed.

(l) Total number of particles could not be counted due to high failure, value given is the design number of particles for specimen

(m) Sample was screened using a 355-μm screen with a 3" diameter to remove the kernel powder

TABLE 9-6
DRAWING/PARTS LIST FOR FTE-15

Dwg./Part No.	Issue	Title	Dwg./Part No.	Issue	Title
11891-1,-2	C	Assembly	12800-1	A	Plug
11666-1	B	Sleeve	11952-1	D	Fuel body assembly, 15-2
11668-1	B	Brazing ring	12791-1	A	Fuel stack assembly
11669-6	B	Upper reflector	12792-1	A	Fuel stack assembly
11670-2	B	Bottom connector	12793-1	B	Fuel stack assembly
11671-1	B	Screen	12880-1	A	Fuel stack assembly
11672-1,-2	B	W/Re, C/A thermocouples	11865-1	B	Fuel stack assembly
11673-1	B	Upper contacts	11871-1	C	Fuel stack assembly
11674-1	A	Thermocouple mounting ring	11885-1	C	Fuel body
11675-1	A	Contact spring	11916-1	B	Compact pusher
11676-1	A	Insulator	11917-1	B	Fuel hole plug
11677-1	A	Nut	11918-1	B	Sample hole plug
1804-00		Washer	12840-3,-4	A	Spines
11541-1	B	Spacer	12798-4,-5,-6	A	Thermal stability sample
11958-1	A	Lower reflector	12799-4,-5,-6	A	Body
11542-1	B	Internal trap assembly	127300-1	A	Plug
11550-1	B	Trap	11954-1	C	Fuel body assembly 15-3
11662-3,-4	B	Filter, pin	11859-1	B	Fuel stack assembly
11552-1	A	Nut	11862-1	B	Fuel stack assembly
11551-1	A	Disk	11865-1	B	Fuel stack assembly
11952-1	E	Fuel body assembly 15-1	12880-1	B	Fuel stack assembly
11859-1	B	Fuel stack assembly	11871-1	C	Fuel stack assembly
11862-1	B	Fuel stack assembly	12793-1	B	Fuel stack assembly
11865-1	B	Fuel stack assembly	11886-1	C	Fuel body
12880-1	B	Fuel stack assembly	11916-1	B	Compact pusher
11871-1	C	Fuel stack assembly	11917-1	B	Fuel hole plug
12793-1	B	Fuel stack assembly	11918-1	B	Sample hole plug
11884-1	C	Fuel body	12840-1,-2	A	Spines
11916-1	B	Compact pusher	12798-7,-8,-9	A	Thermal stability sample
11917-1	B	Fuel hole plug	12799-7,-8,-9	A	Body
11918-1	B	Sample hole plug	127800-1	A	Plug
12870-5,-6	A	Spines			
12793-1,-2,-3	A	Thermal stability sample			
12799-1,-2,-3	A	Body			

TABLE 9-7
GRAPHITE MATERIALS USED IN PEACH BOTTOM FUEL ELEMENTS

Fuel Element Component	Core 1 Driver Graphite Type		Core 2 Driver Graphite Type		FTE-3, -4, -5, -6 Graphite Type	
	Base Stock	Manufacturer	Base Stock	Manufacturer	Base Stock	Manufacturer
Top reflector	H-253[a]	GLCC	H-381[b]	GLCC	H-381[b]	GLCC
Top spine	711-GSXY	Speer	711-T	Speer	H-327	GLCC
Lower two spines (with T/L slots)	711-GSXY	Speer	711-GSXY	Speer	H-327	GLCC
Fuel compact or rod						
Filler	GP-38 flour	UCC	GP-38 flour	UCC	6353	Ashbury
Binder	Barrett No. 30	Allied Chemical	Barrett No. 30	Allied Chemical	15V	Allied Chemical
Graphite fuel body	NA[c]		NA		H-327	GLCC
Sleeve	H-253[a]	GLCC	H-382[b]	GLCC	H-382[b]	GLCC
Internal trap	806 RL	Speer	580	Speer	580	Speer
Lower reflector	806 RL	Speer	580	Speer	H-327	GLCC
Bottom connector	H-253[a]	GLCC	H-381	GLCC	H-253[a]	GLCC

[a] Also referred to as HLM-85-10, made with Texas Lockport coke.

[b] Also referred to as HLM-85-10, made with "Y" coke. Discrimination into H-381 and H-382 lacks explanation. It should be noted that most of the Core 1 and all Core 2 HLM-85-10 material was graphitized in a standard Acheson-type furnace for about 28 days with temperatures up to 2800°C. However, some of the Core 1 material went through a rapid graphitization process in a tube furnace for about 1 hr at 2800°C (which also has been used for impregnation purposes of Core 1 and 2 sleeves after machining). About 40 elements in Core 2 were made out of leftover Core 1 rapid graphitized material. This material happened to shrink more than the Core 2 standard material, as realized during the Core 2 unloading exercise.

[c] NA = not applicable.

TABLE 9-8
FUEL ROD PARTICLE LOADING COMBINATIONS FOR FTE-15

Upper End

	Fuel Hole No.	Item No.	Fissile Particle	Item No.	Fertile Particle
Body No. 3	**Body No. 3**				
	1	21	(200μm)UC_2 TRISO	17	(400μm)ThC_2 BISO
	2	21	(200μm)UC_2 TRISO	15	(400μm)ThC_2 TRISO
	3	12	(200μm)UO_2 TRISO	13	(400μm)ThO_2 BISO
	4	23	(250μm)$(Th,U)O_2$ TRISO	24	(450μm)ThC_2 BISO
	5	16	(150μm)UO_2 TRISO	24	(450μm)ThC_2 BISO
	6	12	(200μm)UO_2 TRISO	15	(400μm)ThC_2 TRISO
Body No. 2	**Body No. 2**				
	1	21	(200μm)UC_2 TRISO	17	(400μm)ThC_2 BISO
	2	21	(200μm)UC_2 TRISO	15	(400μm)ThC_2 TRISO
	3	12	(200μm)UO_2 TRISO	13	(400μm)ThO_2 BISO
	4	23	(250μm)$(Th,U)O_2$ TRISO	24	(450μm)ThC_2 BISO
	5	16	(150μm)UO_2 TRISO	24	(450μm)ThC_2 BISO
	6	12	(200μm)UO_2 TRISO	18	(400μm)ThO_2 TRISO
Body No. 1	**Body No. 1**				
	1, 2, 3 4, 5, 6	14	(150μm)UC_2 TRISO	24	(450μm)ThC_2 BISO

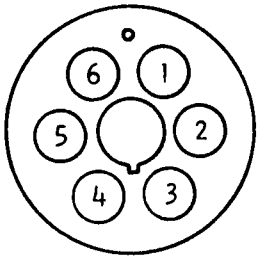

Fuel hole identification

TABLE 9-9
FTE-15 FUEL ROD PARTICLE SPECIFICATIONS

Item No.	FMB No.[a]	Kernel		Particle Type	As-Manufactured Coating Parameters							
					Mean Thickness (μm)					OPyC Density (Mg/m^3)	OPyC OPTAF	Sic Density (Mg/m^3)
		Type	Nominal Diameter (μm)		Buffer	IPyC	SiC	OPyC	Total			
12	4162-00-031	UO_2	200	TRISO	92	26	26	37	175	1.83	1.07	3.18
13	4252-00-011	ThO_2	400	BISO	73	--	--	70	156	2.00	1.14	--
14	4161-00-011	UC_2	145	TRISO	47	23	22	25	112	1.82	1.09	3.20
15	4261-00-011	ThC_2	358	TRISO	54	35	25	38	135	1.81	1.14	3.19
16	4162-01-021	UO_2	150	TRISO	51	24	26	25	123	1.86	1.09	3.19
17	4251-00-031	ThC_2	368	BISO	68	--	--	54	122	1.98	1.16	--
18	4262-00-051	ThO_2	400	TRISO	71	16	35	25	138	1.81	1.08	3.21
21	4161-01-031	UC_2	200	TRISO	87	28	29	38	162	1.80	1.11	3.20
23	4163-00-011	$(Th,U)O_2$[b]	250	TRISO	69	32	36	72	218	1.77	1.09	3.20
24	4251-01-021	ThC_2	433	BISO	82	--	--	64	133	1.96	1.13	--

[a] Fuel Materials Branch data retrieval number.

[b] Th/U ratio = 1.0.

TABLE 9-10
FTE-15 FUEL ROD PREIRRADIATION ATTRIBUTES

Body	Hole	Fuel Blend	Preirradiation Fission Gas Release[a] Kr-85m at 1100°C	Exposed Heavy Metal[b] (kg Th/kg Th)	Heavy Metal Loadings[c]		Impurities								
					Th ($\times 10^{-3}$ kg)	U ($\times 10^{-3}$ kg)	B (ppm)	Fe (ppm)	S (ppm)	Ti (ppm)	V (ppm)	Residual Hydrogen (ppm)	Residual Ash (ppm)	H_2O (ppm)	Cl (ppm)
1	1-2	150-μm UC_2 TRISO 450-μm ThC_2 BISO	6.8×10^{-6}	6.7×10^{-7}	13.28	0.961	<1	<40	340	<40	<40	290	938	<1	46
1	3-4	150-μm UC_2 TRISO 450-μm ThC_2 BISO	4.5×10^{-6}	1.5×10^{-6}	10.526	0.956	3	80	340	<40	<40	290	600	<1	46
1	5	150-μm UC_2 TRISO 450-μm ThC_2 BISO	1.7×10^{-6}	2.5×10^{-4}	12.18	0.961	3	<40	280	<40	<40	560	550	<1	16
1	6	150-μm UC_2 TRISO 450-μm ThC_2 BISO	4.6×10^{-6}	8.2×10^{-7}	10.58	0.945	3	80	340	<40	<40	290	1350	<1	30
2	1	200-μm UC_2 TRISO 400-μm ThC_2 BISO	7.3×10^{-7}	3.7×10^{-5}	6.483	0.992	4	80	1190	<40	<40	200	1500	4	NA[d]
2	2	200-μm UC_2 TRISO 400-μm ThC_2 TRISO	3.6×10^{-6}	5.0×10^{-5}	7.791	0.996	4	<200	1020	<40	<40	<1	250	6	NA
2	3	200-μm UO_2 TRISO 400-μm ThO_2 BISO	5.0×10^{-6}	1.7×10^{-4}	8.776	0.982	8	<40	1180	<40	<40	700	600	3	NA
2	4	250-μm $(Th,U)O_2$ TRISO 450-μm ThC_2 BISO	2.8×10^{-7}	7.8×10^{-5}	6.349	0.962	8	<40	1180	<40	<40	700	600	3	NA
2	5	150-μm UO_2 TRISO 450-μm ThC_2 BISO	1.4×10^{-6}	5.3×10^{-6}	10.998	0.914	4	80	1180	<40	<40	700	600	3	NA
2	6	200-μm UO_2 TRISO 400-μm ThO_2 TRISO	3.3×10^{-6}	1.8×10^{-3}	8.400	0.940	8	<40	1180	<40	<40	700	600	3	NA
3	1	200-μm UC_2 TRISO 400-μm ThC_2 BISO	8.2×10^{-7}	1.5×10^{-5}	6.434	1.016	4	<200	1020	<40	<40	<1	250	6	NA
3	2	200-μm UC_2 TRISO 400-μm ThC_2 TRISO	2.0×10^{-6}	5.3×10^{-6}	7.930	0.969	4	<200	1020	<40	<40	<1	250	6	NA
3	3	200-μm UO_2 TRISO 400-μm ThO_2 BISO	5.0×10^{-6}	1.7×10^{-4}	8.776	0.982	8	<40	1180	<40	<40	700	600	3	NA
3	4	250-μm $(Th,U)O_2$ TRISO 450-μm ThC_2 BISO	2.8×10^{-7}	7.8×10^{-5}	6.349	0.962	8	<40	1180	<40	<40	700	600	3	NA
3	5	150-μm UO_2 TRISO 450-μm ThC_2 BISO	1.4×10^{-6}	5.3×10^{-6}	10.998	0.914	4	80	1180	<40	<40	700	600	3	NA
3	6	200-μm UO_2 TRISO 400-μm ThC_2 TRISO	8.4×10^{-6}	7.1×10^{-5}	8.571	0.962	8	<40	1180	<40	<40	700	600	3	NA

[a] Corrected for steady state.

[b] Hydrolysis measurement.

[c] Target uranium loading was 0.962 g.

[d] NA = not available.

TABLE 9-11
SPINE SAMPLES IN FTE-15
(ACCURACY: ±0.001 IN.)

Position	Preirrad. Length (in.)	Preirrad. Weight (g)	Mean Active Core Height[a] (in.)	Sample Type	Ident. No.	Composite Spine Length [mm (in.)] Preirrad.	Composite Spine Length [mm (in.)] Postirrad.	ΔL/L (%)	Gamma Activity Reading[b]
Bottom Body 1									
Δ	0.380								
1	18.849	210.3	8.654	Graphite	10				100 mr - c 50 mr - 1 ft
2	1.188	14.683	18.673	Thermal stability	TS-1-15				∞ - c 16.5r - 1 ft
3	1.250	14.623	19.892	Thermal stability	TS-2-15				∞ - c 16.5r - 1 ft
4	1.250	14.580	21.142	Thermal stability	TS-3-15	786.88 (30.192)	765.91 (30.154)	-0.13±0.003	∞ - c 19.5r - 1 ft
5	6.500	72.35	25.017	Tensile sample	11959-19				5.5 mr - c 500 mr - 1 ft
6	1.155	12.91	28.844	Graphite	8				75 mr - c 25 mr - 1 ft
d[c]	0.533								
Σ	31.105								
Body 2									
Δ	0.380								
1	7.787	87.49	34.228	Graphite	2				50 mr - c 0 - 1 ft
2	1.250	14.650	38.747	Thermal stability	TS-4				∞ - c 20r - 1 ft
3	0.500	5.583	39.622	Pyrocarbon	11953-20				100 mr - c 0 - 1 ft
4	6.50	72.275	43.122	Tensile sample.	11953-22				50 mr - c 0 - 1 ft
5	1.250	14.660	46.997	Thermal stability	TS-5				∞ - c 19.5r - 1 ft
6	0.500	5.529	47.872	Pyrocarbon	11953-19	753.62 (29.670)	745.11 (29.335)	-1.13±0.003	50 mr - c 0 - 1 ft
7	1.500	17.066	48.872	Creep sample	11953-23-4C				200 mr - c 50 mr - 1 ft
8	1.250	14.588	50.247	Thermal stability	TS-6				∞ - c 20r - 1 ft
9	1.500	17.761	51.622	Creep sample	11953-24-9C				100 mr - c 0 - 1 ft
10	1.438	18.478	53.091	Creep sample	11953-25-14C				100 mr -c 0 - 1 ft
11	0.562	5.519	54.091	Pyrocarbon	11953-21				50 mr - c 0 - 1 ft
12	5.633	64.68	57.188	Graphite	4				100 mr - c 0 - 1 ft
d[c]	1.055								
Σ	31.105								
Body 3									
Δ	0.380								
1	4.103	45.77	63.492	Graphite	7				75 mr - c 10 mr - 1 ft
2	0.500	5.578	65.793	Pyrocarbon	11954-20				100 mr - c 0 - 1 ft
3	1.500	18.478	66.793	Creep sample	11954-19-(1K)				50 mr - c 0 - 1 ft
4	1.250	13.988	68.168	Thermal stability	TS-7	753.19 (29.653)	747.45 (29.427)	-0.76±0.003	∞ - c 15r - 1 ft
5	1.250	14.691	69.418	Thermal stability	TS-8				∞ - c 15r - 1 ft
6	1.250	14.608	70.668	Thermal stability	TS-9				∞ - c 15r - 1 ft
7	19.800	224.50	81.193	Graphite	12				100 mr - c 50 mr - 1 ft
d[c]	1.075								
Σ	31.108								
Top									

[a] Active core height starts at 26.00 in. from Ref. 0. Experimental fuel height: specified 26.15 in. and measured 26.215 in. from Ref. 0. Body 1, bottom line, is 1.15 in. under active core height.

[b] Indicates reading distance; c = contact.

[c] Plenum d.

TABLE 9-12
SUMMARY OF POSTIRRADIATION EXAMINATION OF FTE-15 FUEL RODS

Fuel Rod Ident.(a)	Fuel Types		Irradiation Conditions			Fission Gas Release(c) R/B Kr-85m	Dimensional Change		Broken Particles on Surface(d)	Metallographic Examination										
										Fissile Particle						Fertile Particle				
	Fissile Particle	Fertile Particle	Avg Fuel Temp(b) (°C)	Fast Fluence ($E > 29$ fJ)$_{HTGR}$ ($\times 10^{25}$ n/m^2)	FIMA Fissile (%)		Diameter (%)	Length (%)		OPyC Failure (%)	95% Confidence Limits P (%)	SiC Failure (%)	95% Confidence Limits P (%)	Pressure Vessel Failure (%)	95% Confidence Limits P (%)	OPyC Failure (%)	95% Confidence Limits P (%)	SiC Failure (%)	95% Confidence Limits P (%)	Pressure Vessel Failure (%)	95% Confidence Limits P (%)
2-1-4	UC_2 TRISO	ThC_2 BISO	1467	(e)	(e)	9.6×10^{-5}	-2.65	-2.37	3											
2-1-5	UC_2 TRISO	ThC_2 BISO	1516	(e)	(e)	2.3×10^{-4}	-2.66	-2.60	0	1.6	$0 \le P \le 8.6$	15.6(f)	$7.5 \le P \le 26.5$	0.0	$0 \le P \le 5.5$	0.0	$0 \le P \le 1.6$	--		--	
2-2-4	UC_2 TRISO	ThC_2 TRISO	1467	(e)	(e)	4.6×10^{-4}	-1.17	-0.82	16												
2-2-5	UC_2 TRISO	ThC_2 TRISO	1516	(e)	(e)	6.7×10^{-4}	-1.57	-1.90	14	4.4	$0.1 \le P \le 12.1$	14.7(f)	$7.1 \le P \le 25.3$	1.5	$0 \le P \le 8.1$	47.9	$32.0 \le P \le 68$	23.9	$14.2 \le P \le 35.5$	19.7	$10.6 \le P \le 29.8$
2-3-4	UO_2 TRISO	ThO_2 BISO	1467	(e)	(e)	1.3×10^{-4}	-2.08	-2.02	26												
2-3-5	UO_2 TRISO	ThO_2 BISO	1516	(e)	(e)	4.6×10^{-5}	-2.09	-2.27	3												
2-3-9	UO_2 TRISO	ThO_2 BISO	1408	(e)	(e)	2.7×10^{-4}	-2.13	-2.20	5	1.8(g)	$0 \le P \le 10.1$	1.8(g)	$0 \le P \le 10.1$	1.8(g)	$0 \le P \le 10.1$	0.0	$0 \le P \le 1.6$	--		--	
2-4-3	$(Th,U)O_2$ TRISO(h)	ThC_2 BISO	1373	(e)	(e)	2.7×10^{-4}	-1.85	-2.40	3	1.6	$0.4 \le P \le 5.6$	1.6	$0.4 \le P \le 5.6$	1.6	$0.4 \le P \le 5.6$	8.3(i)	$4.7 \le P \le 14.2$	--		7.5(i)	$4.1 \le P \le 13.3$
2-5-2	UO_2 TRISO	ThC_2 BISO	1339	(e)	(e)	4.7×10^{-4}	-2.63	-2.54	2	27.9	$21.3 \le P \le 35.6$	2.7	$1.1 \le P \le 6.8$	1.4	$0.4 \le P \le 4.8$	1.6(j)	$0.3 \le P \le 4.4$	--		--	
2-6-4	UO_2 TRISO	ThO_2 TRISO	1467	(e)	(e)	3.0×10^{-4}	-0.86	-1.20	2												
2-6-5	UO_2 TRISO	ThO_2 TRISO	1516	(e)	(e)	6.5×10^{-5}	-0.63	-1.56	4	0.0	$0 \le P \le 4.3$	1.1	$0 \le P \le 4.3$	0.0	$0 \le P \le 4.3$	1.3	$0.4 \le P \le 3.8$	8.3	$5.4 \le P \le 12.6$	0.9	$0.2 \le P \le 3.1$
3-2-3	UC_2 TRISO	ThC_2 TRISO	1294	(e)	(e)	3.3×10^{-4}	-0.74	-1.02	51												
3-3-3	UO_2 TRISO	ThO_2 TRISO	1294	(e)	(e)	5.8×10^{-5}	NA(k)	NA	19												
3-3-10	UO_2 TRISO	ThO_2 BISO	1252	(e)	(e)	1.7×10^{-5}	NA	NA	NA												

(a) Fuel body - fuel hole - fuel rod.
(b) Preliminary temperature.
(c) At 1100°C in TRIGA.
(d) From stereo examination.
(e) GAUGE/FEVER calculations not complete.
(f) Polishing damage.
(g) One particle on surface.
(h) Th/U = 1.01.
(i) One production failure; 10 hydrolysis failures during examination.
(j) Two production failures.
(k) NA = not available.

TABLE 9- 13
FTE-15 FISSION GAS RELEASE SUMMARY

Fuel Rod Ident (a)	Fraction of Total Thorium		Fraction of Defective SiC Coatings(b)		Fraction of Fissions(c)		Thorium Contamination(d) ($\times 10^{-4}$ g Th/g Th)	Calculated Fission Gas Release(e) R/B Kr-85m				Expected Fission Gas Release R/B Kr-85m	EOL TRIGA R/B Kr-85m(g)	R/B	Pressure Vessel Failure(e)	
								Defective Fissile		Fertile						
	Fissile A	Fertile B	Fissile C	Fertile D	U-235 E	U-233 F	G	U-235 $H = CE(R/B)_f$	Th $I = ACF(R/B)_f$	Defective $J = BDF(R/B)_f$	Th Cont (f) $K = FG(R/B)_{f_{cont}}$	$H + I + J + K = L$	M	$M - L = N$	Corrected $N/(R/B_f)$	Uncorrected $N/(R/B_f)$
2-1-4	0	1 0	$1\ 46 \times 10^{-4}$	0	0 38	0 62	0 37	$2\ 77 \times 10^{-7}$	0	0	$6\ 88 \times 10^{-6}$	$7\ 16 \times 10^{-6}$	$9\ 6 \times 10^{-5}$	8.88×10^{-5}	0 018	0 019
2 1-5	0	1 0	$1\ 46 \times 10^{-4}$	0	0 37	0 63	0 37	$2\ 70 \times 10^{-7}$	0	0	$6\ 89 \times 10^{-6}$	$7\ 16 \times 10^{-6}$	$2\ 3 \times 10^{-4}$	$2\ 23 \times 10^{-4}$	0 045	0 046
2 2-4	0	1 0	$5\ 8 \times 10^{-5}$	$1\ 0 \times 10^{-3}$	0 43	0 57	0 50	$1\ 24 \times 10^{-7}$	0	$2\ 85 \times 10^{-6}$	$8\ 55 \times 10^{-6}$	$1\ 15 \times 10^{-5}$	$4\ 6 \times 10^{-4}$	$4\ 49 \times 10^{-4}$	0 090	0 092
2 2-5	0	1 0	$5\ 8 \times 10^{-5}$	$1\ 0 \times 10^{-3}$	0 43	0 57	0 50	$1\ 24 \times 10^{-7}$	0	$2\ 85 \times 10^{-6}$	$8\ 55 \times 10^{-6}$	$1\ 15 \times 10^{-5}$	$6\ 7 \times 10^{-4}$	$6\ 58 \times 10^{-4}$	0 132	0 134
2 3-4	0	1 0	$1\ 0 \times 10^{-3}$	0	0 45	0 55	1 70	$2\ 25 \times 10^{-6}$	0	0	$2\ 81 \times 10^{-5}$	$3\ 04 \times 10^{-5}$	$1\ 3 \times 10^{-4}$	$9\ 97 \times 10^{-5}$	0 020	0 076
2-3-5	0	1 0	$1\ 0 \times 10^{-3}$	0	0 45	0 55	1 70	$2\ 25 \times 10^{-6}$	0	0	$2\ 81 \times 10^{-5}$	$3\ 04 \times 10^{-5}$	$4\ 6 \times 10^{-5}$	$1\ 57 \times 10^{-5}$	0 003	0 009
2-3-9	0	1 0	$1\ 0 \times 10^{-3}$	0	0 43	0 57	1 70	$2\ 25 \times 10^{-6}$	0	0	$2\ 90 \times 10^{-5}$	$3\ 13 \times 10^{-5}$	$2\ 7 \times 10^{-4}$	$2\ 39 \times 10^{-4}$	0 048	0 054
2-4-3	0 147	0 853	$5\ 6 \times 10^{-5}$	0	0 38	0 62	0 78	$1\ 06 \times 10^{-7}$	$2\ 55 \times 10^{-8}$	0	$1\ 45 \times 10^{-5}$	$1\ 46 \times 10^{-5}$	$2\ 7 \times 10^{-4}$	2.55×10^{-4}	0 051	0 054
2-5-2	0	1 0	$2\ 80 \times 10^{-4}$	0	0 49	0 51	0 05	$6\ 86 \times 10^{-7}$	0	0	$7\ 65 \times 10^{-7}$	$1\ 45 \times 10^{-6}$	$4\ 7 \times 10^{-4}$	$4\ 69 \times 10^{-4}$	0 094	0 094
2-6-4	0	1 0	$5\ 0 \times 10^{-3}$	$2\ 1 \times 10^{-3}$	0 49	0 51	18 0	$1\ 23 \times 10^{-5}$	0	$5\ 36 \times 10^{-5}$	$2\ 75 \times 10^{-4}$	$3\ 41 \times 10^{-4}$	$3\ 0 \times 10^{-5}$	$-3\ 11 \times 10^{-4}$	--	0 006
2-6-5	0	1 0	$5\ 0 \times 10^{-3}$	$2\ 1 \times 10^{-3}$	0 49	0 51	18 0	$1\ 23 \times 10^{-5}$	0	$5\ 36 \times 10^{-5}$	$2\ 75 \times 10^{-4}$	$3\ 41 \times 10^{-4}$	$6\ 5 \times 10^{-5}$	$-2\ 76 \times 10^{-4}$	--	0 013
3-2-3	0	1 0	$2\ 6 \times 10^{-4}$	$2\ 2 \times 10^{-3}$	0 32	0 68	0 05	$4\ 16 \times 10^{-7}$	0	$7\ 48 \times 10^{-6}$	$1\ 02 \times 10^{-6}$	$8\ 92 \times 10^{-6}$	$3\ 3 \times 10^{-4}$	$3\ 21 \times 10^{-4}$	0 064	0 066
3-3-3	0	1 0	$1\ 0 \times 10^{-3}$	0	0 34	0 66	1 70	$1\ 7 \times 10^{-6}$	0	0	$3\ 37 \times 10^{-5}$	$3\ 54 \times 10^{-5}$	$5\ 8 \times 10^{-5}$	$2\ 26 \times 10^{-5}$	0 005	0 012
3-3-10	0	1 0	$1\ 0 \times 10^{-3}$	0	0 20	0 80	1 70	$1\ 7 \times 10^{-6}$	0	0	$4\ 08 \times 10^{-5}$	$4\ 25 \times 10^{-5}$	$1\ 7 \times 10^{-5}$	$-2\ 55 \times 10^{-5}$	--	0 003

(a) Fuel body - fuel hole - fuel rod

(b) Calculated from burn-leach or nominal preirradiation fission gas release

(c) GAUCE/FEVER calculation

(d) Nominal preirradiation hydrolysis measurement

(e) Assume $R/B_f = 0\ 005$

(f) Assume $R/B_f = 0\ 30$

(g) At 1100°C

TABLE 9-14
FTE-15 FUEL ROD SUMMARY

FUEL ROD I.D.	MEAN CORE HT (MM)	PA-233 (311.9KEV) (CI)	RU-103 (497.1KEV) (CI)	RU-106 (511.9KEV) (CI)	CS-134 (604.7KEV) (CI)	CS-137 (661.6KEV) (CI)	CE-144 (695.6KEV) (CI)	ZR-95 (724.2KEV) (CI)	CS-137 /ZR-95 (CT/MIN)	TOTAL FIMA %
1-1-1	695.96	0.00000	0.00000	7.61078E-01	3.75959E-01	8.65946E-01	1.12915E+01	1.42785E+01	.13086	1.94762
	2SIG ERR	0.00000	0.00000	1.84411E-01	7.80209E-02	1.75149E-01	2.83807E+00	4.81312E+00	.03553	.40278
1-1-2	756.43	.00000	0.00000	8.50030E-01	4.52582E-01	9.23909E-01	1.17051E+01	1.84345E+01	.10815	2.07799
	2SIG ERR	0.00000	0.00000	2.04085E-01	9.33039E-02	1.86832E-01	3.00937E+00	5.28473E+00	.02223	.42965
1-1-3	822.96	0.00000	0.00000	8.82949E-01	5.35796E-01	9.57781E-01	1.30356E+01	1.92715E+01	.10724	2.15417
	2SIG ERR	0.00000	0.00000	2.11267E-01	1.09779E-01	1.93599E-01	3.32881E+00	5.33568E+00	.02055	.44523
1-1-4	886.46	0.00000	0.00000	8.76046E-01	5.60751E-01	9.12462E-01	1.17861E+01	1.61307E+01	.12206	2.05224
	2SIG ERR	0.00000	0.00000	2.19853E-01	1.14828E-01	1.84567E-01	3.12187E+00	4.89574E+00	.02789	.42443
1-1-5	946.96	0.00000	0.00000	8.77558E-01	6.56174E-01	9.91923E-01	1.22049E+01	1.95748E+01	.10934	2.23096
	2SIG ERR	0.00000	0.00000	2.01973E-01	1.33903E-01	2.00511E-01	3.10618E+00	5.77286E+00	.02371	.46112
1-1-6	1008.46	0.00000	0.00000	9.36762E-01	7.32272E-01	1.03127E+00	1.27098E+01	1.87117E+01	.11892	2.31946
	2SIG ERR	0.00000	0.00000	2.21292E-01	1.49234E-01	2.08465E-01	3.05290E+00	5.90818E+00	.02907	.47942
1-1-7	1076.96	0.00000	0.00000	1.08762E+00	9.25317E-01	1.18291E+00	1.44321E+01	2.42075E+01	.10544	2.66050
	2SIG ERR	0.00000	0.00000	2.60535E-01	1.88097E-01	2.38866E-01	3.54103E+00	6.65091E+00	.01985	.54939
1-1-8	1140.46	0.00000	0.00000	1.05269E+00	9.77425E-01	1.19068E+00	1.52691E+01	2.36031E+01	.10885	2.67798
	2SIG ERR	0.00000	0.00000	2.48677E-01	1.98353E-01	2.40436E-01	3.69547E+00	6.31382E+00	.01933	.55300
1-1-9	1203.96	0.00000	0.00000	1.15773E+00	1.09023E+00	1.28139E+00	1.71310E+01	2.72727E+01	.10138	2.88200
	2SIG ERR	0.00000	0.00000	2.75517E-01	2.21113E-01	2.58693E-01	4.22496E+00	7.27929E+00	.01790	.59500
1-1-10	1267.46	0.00000	0.00000	1.04866E+00	1.05947E+00	1.22676E+00	1.62041E+01	2.35796E+01	.11226	2.75913
	2SIG ERR	0.00000	0.00000	2.48723E-01	2.14735E-01	2.47675E-01	3.92717E+00	6.55934E+00	.02169	.56966
1-1-11	1330.96	0.00000	0.00000	1.23811E+00	1.25538E+00	1.39113E+00	1.77299E+01	2.80306E+01	.10709	3.12883
	2SIG ERR	0.00000	0.00000	2.90418E-01	2.54396E-01	2.80760E-01	4.18740E+00	7.69938E+00	.02014	.64577
2-1-1	1485.85	0.00000	0.00000	1.29820E+00	1.35203E+00	1.39498E+00	1.86028E+01	2.90995E+01	.10344	5.98234
	2SIG ERR	0.00000	0.00000	2.96938E-01	2.73542E-01	2.81498E-01	4.35877E+00	7.58413E+00	.01726	1.23457
2-1-2	1549.35	0.00000	0.00000	1.37180E+00	1.38480E+00	1.40964E+00	1.74439E+01	2.91499E+01	.10435	6.04525
	2SIG ERR	0.00000	0.00000	3.10086E-01	2.80063E-01	2.84508E-01	4.21118E+00	7.76881E+00	.01836	1.24776
2-1-3	1612.85	0.00000	0.00000	1.34575E+00	1.39043E+00	1.41404E+00	1.67993E+01	2.62702E+01	.11615	6.06410
	2SIG ERR	0.00000	0.00000	2.99426E-01	2.81249E-01	2.85345E-01	4.04258E+00	7.20690E+00	.02178	1.25145
2-1-4*	1676.35	0.00000	0.00000	1.75079E+00	1.73903E+00	1.76584E+00	2.41843E+01	3.60157E+01	.10580	7.57279
	2SIG ERR	0.00000	0.00000	3.96668E-01	3.51268E-01	3.56041E-01	5.45347E+00	8.66087E+00	.01406	1.56162
2-1-5*	1739.85	0.00000	0.00000	1.85857E+00	1.79612E+00	1.79057E+00	2.32292E+01	3.21521E+01	.12017	7.67883
	2SIG ERR	0.00000	0.00000	4.05182E-01	3.62728E-01	3.60972E-01	5.23076E+00	7.56506E+00	.01481	1.58327
2-1-6	1803.35	0.00000	0.00000	1.39496E+00	1.40792E+00	1.43168E+00	1.84369E+01	3.15671E+01	.09786	6.13974
	2SIG ERR	0.00000	0.00000	3.14623E-01	2.84849E-01	2.88879E-01	4.42352E+00	8.19521E+00	.01617	1.26696
2-1-7	1866.85	0.00000	0.00000	1.41742E+00	1.36393E+00	1.38994E+00	1.74282E+01	2.72189E+01	.11019	5.96074
	2SIG ERR	0.00000	0.00000	3.28244E-01	2.75873E-01	2.80469E-01	4.09524E+00	6.94734E+00	.01744	1.23007
2-1-8	1903.35	0.00000	0.00000	1.32419E+00	1.35765E+00	1.36426E+00	1.91781E+01	2.72625E+01	.10798	5.85060
	2SIG ERR	0.00000	0.00000	3.04832E-01	2.74617E-01	2.75347E-01	4.57947E+00	7.38520E+00	.01971	1.20758

TABLE 9-14 (Continued)

2-1-9	1993.85	0.000000	0.000000	1.38642+00	1.38636+00	1.37950+00	1.82770+01	3.03334+01	.09813	5.91599
	2SIG ERR	0.000000	0.000000	3.14991-01	2.80425-01	2.78412-01	4.27681+00	8.10818+00	.01738	1.22103
2-1-10	2057.35	0.000000	0.000000	1.33979+00	1.39981+00	1.42355+00	1.81557+01	2.92009+01	.10519	6.10491
	2SIG ERR	0.000000	0.000000	3.16357-01	2.83098-01	2.87240-01	4.25683+00	7.77282+00	.01845	1.25977
2-1-11	2120.81	0.000000	0.000000	1.39673+00	1.45694+00	1.44639+00	1.98758+01	2.86311+01	.10901	6.20282
	2SIG ERR	0.000000	0.000000	3.16880-01	2.94589-01	2.91872-01	4.60084+00	7.49129+00	.01836	1.28007
3-1-1	2276.21	0.000000	0.000000	1.37281+00	1.26536+00	1.32900+00	1.74942+01	2.95931+01	.09690	5.71879
	2SIG ERR	0.000000	0.000000	3.16225-01	2.56214-01	2.68255-01	4.06439+00	8.02646+00	.01774	1.18047
3-1-2	2339.71	0.000000	0.000000	1.05197+00	1.10711+00	1.24455+00	1.75329+01	2.52457+01	.10637	5.35542
	2SIG ERR	0.000000	0.000000	2.48215-01	2.24321-01	2.51351-01	4.09108+00	7.25718+00	.02196	1.10602
3-1-3	2403.21	0.000000	0.000000	1.14081+00	9.94001-01	1.17551+00	1.35332+01	2.43856+01	.10402	5.05834
	2SIG ERR	0.000000	0.000000	2.67360-01	2.01556-01	2.37374-01	3.38936+00	7.20413+00	.02261	1.04453
3-1-4	2466.21	0.000000	0.000000	1.09804+00	9.24975-01	1.13478+00	1.54260+01	2.11136+01	.11597	4.88306
	2SIG ERR	0.000000	0.000000	2.60367-01	1.87800-01	2.29237-01	3.82875+00	6.51474+00	.02725	1.00869
3-1-5	2530.21	0.000000	0.000000	1.01599+00	8.38100-01	1.07758+00	1.30437+01	2.38585+01	.09746	4.63693
	2SIG ERR	0.000000	0.000000	2.36094-01	1.70380-01	2.17693-01	3.31485+00	7.25010+00	.02230	.95789
3-1-6	2593.71	0.000000	0.000000	1.02031+00	7.44556-01	1.00308+00	1.33738+01	2.27372+01	.09519	4.31634
	2SIG ERR	0.000000	0.000000	2.44911-01	1.51570-01	2.02745-01	3.46356+00	6.86343+00	.02153	.89208
3-1-7	2657.21	0.000000	0.000000	9.12522-01	6.55905-01	9.47644-01	1.28256+01	1.89146+01	.10811	4.07780
	2SIG ERR	0.000000	0.000000	2.20041-01	1.33848-01	1.91621-01	3.19312+00	6.09561+00	.02734	.84310
3-1-8	2720.71	0.000000	0.000000	8.83159-01	5.72542-01	8.73620-01	4.41111+01	1.67429+01	.11259	3.75926
	2SIG ERR	0.000000	0.000000	2.13695-01	1.17242-01	1.76750-01	1.12264+01	5.96705+00	.03324	.77763
3-1-9	2784.21	0.000000	0.000000	8.18192-01	4.91977-01	8.36261-01	1.13833+01	1.80743+01	.09984	3.59850
	2SIG ERR	0.000000	0.000000	2.07107-01	1.01139-01	1.69220-01	3.10743+00	5.92420+00	.02595	.74449
3-1-10	2847.71	0.000000	0.000000	7.45377-01	4.13613-01	7.66964-01	9.70573+00	1.62927+01	.10158	3.30031
	2SIG ERR	0.000000	0.000000	1.83916-01	8.53631-02	1.55382-01	2.58415+00	5.47246+00	.02745	.68353
3-1-11	2911.21	0.000000	0.000000	7.15970-01	3.53420-01	7.37831-01	1.04726+01	1.54521+01	.10303	3.17482
	2SIG ERR	0.000000	0.000000	1.74852-01	7.34142-02	1.49446-01	2.80764+00	5.27220+00	.02852	.65743
2-2-4*	1676.35	0.000000	0.000000	1.62432+00	1.67600+00	1.72788+00	2.17439+01	3.56253+01	.10466	6.32697
	2SIG ERR	0.000000	0.000000	3.59141-01	3.38652-01	3.48458-01	4.95239+00	8.66803+00	.01445	1.30495
2-2-5	2911.21	0.000000	0.000000	1.61471+00	1.66073+00	1.71254+00	2.23327+01	3.64759+01	.10131	6.27080
	2SIG ERR	0.000000	0.000000	3.59200-01	3.35619-01	3.45364-01	5.05429+00	9.00438+00	.01461	1.29337
2-2-6	1803.85	0.000000	0.000000	1.22564+00	1.27745+00	1.32718+00	1.80831+01	2.83679+01	.10095	4.85973
	2SIG ERR	0.000000	0.000000	2.85120-01	2.58496-01	2.67913-01	4.22590+00	7.69035+00	.01846	1.00323
2-2-11	2120.81	0.000000	0.000000	1.30589+00	1.33022+00	1.35779+00	1.66026+01	3.03446+01	.09655	4.97181
	2SIG ERR	0.000000	0.000000	3.08491-01	2.69236-01	2.74817-01	4.00714+00	7.99233+00	.01659	1.02882
3-2-2	2339.71	0.000000	0.000000	1.23983+00	1.11319+00	1.24877+00	1.61672+01	2.90991+01	.09260	4.49704
	2SIG ERR	0.000000	0.000000	2.87180-01	2.25859-01	2.52328-01	4.00136+00	9.43702+00	.02364	.92916
3-2-3	2403.21	0.000000	0.000000	1.50991+00	1.33245+00	1.53394+00	2.00812+01	3.26806+01	.10128	5.52398
	2SIG ERR	0.000000	0.000000	3.35372-01	2.69610-01	3.10381-01	4.57936+00	8.04665+00	.01459	1.14279

TABLE 9-14 (Continued)

3-2-5	2530.21	[illegible]	[illegible]	1.00214+00	8.60502-01	1.06391+00	1.38828+01	2.38309+01	.09633	3.83130
	2SIG ERR	[illegible]	0.00000	2.41321-01	1.75078-01	2.15130-01	3.57792+00	8.41857+00	.02806	.79213
3-2-10	2847.71	[illegible]	[illegible]	7.40829-01	3.91636-01	7.85369-01	9.10588+00	1.19754+01	.14151	2.82824
	2SIG ERR	[illegible]	[illegible]	1.91115-01	8.12450-02	1.59150-01	2.78557+00	6.31811+00	.06913	.58589
2-3-1	1485.45	[illegible]	[illegible]	1.24051+00	1.24573+00	1.32292+00	1.75149+01	2.82505+01	.10105	4.34421
	2SIG ERR	[illegible]	[illegible]	2.92008-01	2.52092-01	2.67090-01	4.11744+00	7.57567+00	.01804	.89692
2-3-2	1549.35	[illegible]	[illegible]	1.17507+00	1.19342+00	1.32189+00	1.61310+01	2.89216+01	.09862	4.34082
	2SIG ERR	[illegible]	[illegible]	2.79017-01	2.41648-01	2.66845-01	3.85536+00	7.61567+00	.01688	.89610
2-3-3	1612.85	[illegible]	[illegible]	1.29441+00	1.25436+00	1.32601+00	1.69062+01	2.77169+01	.10323	4.35435
	2SIG ERR	[illegible]	[illegible]	3.07910-01	2.53988-01	2.67640-01	4.06457+00	7.65680+00	.01965	.89879
2-3-4*	1676.35	[illegible]	[illegible]	1.63958+00	1.58760+00	1.68633+00	2.05975+01	3.43244+01	.10601	5.53756
	2SIG ERR	[illegible]	[illegible]	3.75140-01	3.21024-01	3.40991-01	4.72958+00	8.18512+00	.01371	1.14218
2-3-5*	1739.85	[illegible]	[illegible]	1.53113+00	1.55353+00	1.64546+00	2.21514+01	3.38006+01	.10504	5.40338
	2SIG ERR	[illegible]	[illegible]	3.44573-01	3.14085-01	3.31849-01	4.96628+00	8.15799+00	.01414	1.11450
2-3-6	1803.35	0.00000	0.00000	1.27623+00	1.26816+00	1.31375+00	1.72103+01	2.78700+01	.10172	4.31409
	2SIG ERR	0.00000	0.00000	2.95042-01	2.56796-01	2.65177-01	4.18843+00	7.48287+00	.01820	.89051
2-3-9*	1993.85	[illegible]	0.00000	1.68378+00	1.60898+00	1.71182+00	2.19079+01	3.54518+01	.10419	5.62128
	2SIG ERR	[illegible]	0.00000	3.71798-01	3.25062-01	3.45177-01	4.92535+00	8.56831+00	.01408	1.15928
2-3-10	2057.35	[illegible]	[illegible]	1.47819+00	1.27881+00	1.36211+00	1.92237+01	2.78163+01	.10566	4.47289
	2SIG ERR	[illegible]	[illegible]	3.39491-01	2.58846-01	2.74938-01	4.50723+00	7.71486+00	.02029	.92329
2-3-11	2120.81	[illegible]	[illegible]	1.19583+00	1.20349+00	1.27945+00	1.70064+01	2.88500+01	.09569	4.20145
	2SIG ERR	[illegible]	[illegible]	2.80747-01	2.43671-01	2.58301-01	4.04629+00	7.52098+00	.01599	.86741
3-3-2	2339.71	[illegible]	0.00000	1.12405+00	1.10212+00	1.22895+00	1.59479+01	2.73363+01	.09701	4.03563
	2SIG ERR	[illegible]	[illegible]	2.67562-01	2.23598-01	2.48260-01	4.01996+00	1.02217+01	.03065	.83364
3-3-3	2403.21	[illegible]	0.00000	1.45346+00	1.32779+00	1.53444+00	1.93697+01	3.19101+01	.10376	5.03879
	2SIG ERR	0.00000	0.00000	3.24711-01	2.68652-01	3.09535-01	4.47985+00	8.03390+00	.01583	1.03953
3-3-5	2530.21	[illegible]	0.00000	9.94862-01	8.31570-01	1.02836+00	1.29738+01	2.07837+01	.10677	3.37694
	2SIG ERR	[illegible]	[illegible]	2.42173-01	1.69457-01	2.07954-01	3.21630+00	8.70952+00	.03933	.69823
3-3-11	2847.71	[illegible]	[illegible]	8.97069-01	5.13687-01	9.11799-01	1.20024+01	1.97084+01	.09983	2.99417
	2SIG ERR	0.00000	0.00000	2.10653-01	1.05453-01	1.84353-01	2.86343+00	5.69224+00	.02082	.61899
2-4-3	1612.85	[illegible]	[illegible]	1.22016+00	1.24585+00	1.32462+00	1.73515+01	2.56781+01	.11131	5.80798
	2SIG ERR	[illegible]	[illegible]	2.80112-01	2.52219-01	2.67397-01	4.03123+00	7.13600+00	.02146	1.19898
2-4-9	1993.85	0.00000	0.00000	1.25347+00	1.22335+00	1.28737+00	1.67602+01	2.82773+01	.09824	5.64465
	2SIG ERR	0.00000	0.00000	2.94538-01	2.47967-01	2.60024-01	4.16481+00	9.16161+00	.02504	1.16506
2-4-10	2057.35	0.00000	0.00000	1.30202+00	1.23664+00	1.29664+00	1.72565+01	2.54152+01	.11009	5.68529
	2SIG ERR	0.00000	0.00000	2.97223-01	2.50413-01	2.61712-01	4.11412+00	6.93956+00	.02044	1.17351
2-4-11	2057.35	0.00000	0.00000	1.24282+00	1.24494+00	1.31389+00	1.77769+01	2.69347+01	.10526	5.76098
	2SIG ERR	0.00000	0.00000	2.86038-01	2.51975-01	2.65171-01	4.08535+00	7.44996+00	.02009	1.18982
3-4-3	2403.21	0.00000	0.00000	1.08931+00	9.93142-01	1.13907+00	1.52466+01	2.33593+01	.10522	4.99438
	2SIG ERR	0.00000	0.00000	2.52208-01	2.01682-01	2.30183-01	3.92084+00	6.53072+00	.03216	1.03202

TABLE 9-14 (Continued)

3-4-4	2466.71	0.00000	0.00000	1.08407+00	9.13094-01	1.08106+00	1.44398+01	2.32111+01	.10050	4.74006
	2SIG ERR	0.00000	0.00000	2.61948-01	1.85599-01	2.18564-01	3.68116+00	9.49336+00	.03586	.97988
3-4-5	2530.21	0.00000	0.00000	1.09387+00	8.49144-01	1.05849+00	1.50177+01	1.69410+01	.13482	4.64109
	2SIG ERR	0.00000	0.00000	2.58004-01	1.72781-01	2.13944-01	3.75757+00	7.21094+00	.05067	.95919
2-5-2	1549.85	0.00000	0.00000	1.67120+00	1.61172+00	1.72365+00	2.24958+01	3.82866+01	.09714	4.63442
	2SIG ERR	0.00000	0.00000	3.70982-01	3.25748-01	3.47575-01	5.01786+00	9.15476+00	.01268	.95579
2-5-4	1676.35	0.00000	0.00000	1.13112+00	1.06661+00	1.17048+00	1.48854+01	2.68420+01	.09409	3.14711
	2SIG ERR	0.00000	0.00000	2.59891-01	2.16142-01	2.36437-01	3.59433+00	7.36741+00	.01769	.65007
3-5-2	2339.71	0.00000	0.00000	1.10833+00	9.79853-01	1.15510+00	1.56416+01	2.31187+01	.10781	3.10875
	2SIG ERR	0.00000	0.00000	2.59464-01	1.98714-01	2.33296-01	3.69584+00	6.80448+00	.02328	.64144
3-5-4	2466.71	0.00000	0.00000	9.15504-01	8.18162-01	1.02643+00	1.41685+01	2.14157+01	.10342	2.75980
	2SIG ERR	0.00000	0.00000	2.15552-01	1.66351-01	2.07444-01	3.50834+00	6.67154+00	.02471	.57033
3-5-9	2784.21	0.00000	0.00000	7.78717-01	4.67805-01	8.00024-01	9.36842+00	1.33210+01	.12959	2.15105
	2SIG ERR	0.00000	0.00000	1.88381-01	9.59779-02	1.61953-01	2.69172+00	4.92723+00	.04036	.44519
2-6-4*	1676.35	0.00000	0.00000	1.62322+00	1.63398+00	1.70511+00	2.09419+01	3.44063+01	.10694	5.84982
	2SIG ERR	0.00000	0.00000	3.62921-01	3.30213-01	3.43837-01	4.75599+00	8.38503+00	.01484	1.20645
2-6-5*	1739.85	0.00000	0.00000	1.65004+00	1.64851+00	1.69902+00	2.22131+01	3.25544+01	.11262	5.82893
	2SIG ERR	0.00000	0.00000	3.72154-01	3.33148-01	3.42636-01	5.05092+00	7.90072+00	.01543	1.20223
2-6-6	1803.35	0.00000	0.00000	1.26663+00	1.28353+00	1.35474+00	1.72472+01	2.53271+01	.11542	4.66780
	2SIG ERR	0.00000	0.00000	2.92075-01	2.59923-01	2.73464-01	4.15415+00	7.69256+00	.02637	.95944
2-6-7	1866.85	0.00000	0.00000	1.25704+00	1.29910+00	1.36400+00	1.81931+01	2.81340+01	.10461	4.67956
	2SIG ERR	0.00000	0.00000	2.92931-01	2.62998-01	2.75333-01	4.32376+00	7.80491+00	.02010	.96599
2-6-8	1930.35	0.00000	0.00000	1.27208+00	1.29683+00	1.36432+00	1.81095+01	3.06549+01	.09603	4.68065
	2SIG ERR	0.00000	0.00000	2.91419-01	2.62493-01	2.75409-01	4.30777+00	8.68158+00	.01924	.96686
2-6-9	1993.85	0.00000	0.00000	1.24672+00	1.28847+00	1.33504+00	1.80899+01	2.88568+01	.09983	4.58022
	2SIG ERR	0.00000	0.00000	2.85610-01	2.60817-01	2.69500-01	4.28482+00	7.95983+00	.01895	.94552
2-6-10	2057.35	0.00000	0.00000	1.30312+00	1.27931+00	1.33458+00	1.72306+01	2.85637+01	.10082	4.57864
	2SIG ERR	0.00000	0.00000	3.11310-01	2.59038-01	2.69444-01	4.11445+00	8.08331+00	.02017	.94532
2-6-11	2120.81	0.00000	0.00000	1.31912+00	1.31442+00	1.37326+00	1.70769+01	3.06199+01	.09677	4.71133
	2SIG ERR	0.00000	0.00000	3.05744-01	2.66054-01	2.77227-01	4.05849+00	8.69758+00	.01951	.97263
3-6-2	2339.71	0.00000	0.00000	1.10551+00	9.64399-01	1.12518+00	1.58761+01	2.50947+01	.09675	3.78208
	2SIG ERR	0.00000	0.00000	2.63328-01	1.95763-01	2.27274-01	3.76046+00	7.02084+00	.01893	.78119
3-6-3	2403.21	0.00000	0.00000	1.08162+00	9.17234-01	1.10432+00	1.46926+01	1.96617+01	.12120	3.71199
	2SIG ERR	0.00000	0.00000	2.52823-01	1.86189-01	2.23063-01	3.59906+00	6.01616+00	.02806	.76672
3-6-10	2847.71	0.00000	0.00000	6.28636-01	3.69151-01	7.12444-01	9.68834+00	1.48110+01	.10380	2.39475
	2SIG ERR	0.00000	0.00000	1.58649-01	7.65261-02	1.44310-01	2.65458+00	4.93100+00	.02767	.49590

*These rods were scanned at the same time. The data indicate these rods had a ~25% higher isotope inventory than neighboring fuel rods, which indicates a systematic counting error that has not been identified. These rods are not included in the burnup plots in Figs. 9-50 through 9-52.

TABLE 9-15
FUEL PARTICLE ATTRIBUTES OF REFERENCE AND TESTED DESIGNS

Ident Number[a]	Kernel			Coating Type[b]	As-Manufactured Coating Parameters								Total Particle Parameters			
					Nominal Thickness (μm)										Heavy Metal Content	
	Type	Density (Mg/m^3)	Nominal Diameter (μm)		Buffer (μm)	IPyC (μm)	SiC (μm)	OPyC (μm)	Total (μm)	OPyC Density (Mg/m^3)	OPyC OPTAF[c]	SiC Density (Mg/m^3)	Density (Mg/m^3)	Diam. (μm)	U (wt %)	Th (wt %)
Reference particles																
Fissile	UC_2	>10.3	200	TRISO	100	35	40	40	210	1.80	(d)	>3.18	2.26	570	NA[e]	--
	UC_xO_y	3.35	305	TRISO	60	35	35	40	170	1.80	(d)	>3.18	2.19	575	NA	--
Fertile	ThO_2	>9.5	500	BISO	85	--	--	75	160	1.85	(d)	--	3.35	820	--	--
FTE-14 and -15 Peach Bottom tested particles																
Fissile																
4161-01-030	UC_2	10.90	203	TRISO	87	28	29	32	170	1.80	1.11	3.20	2.41	540	20.35	--
OR-1694	$UC_{4.3}O_{1.3}$	3.3	394	TRISO	50	20	21	39	130	1.91	<1.2	3.24	2.24	566	22.2	--
Fertile																
4252-02-070	ThO_2	9.86	480	BISO	70	--	--	72	142	2.02	1.16	--	3.84	765	--	57.38

[a] Data retrieval number, Fuel Materials Branch.

[b] Relative number of coatings.

[c] Optical anisotropy.

[d] BAF_0 specified at ≤1.03.

[e] NA = not available

TABLE 9-16
SUMMARY OF FTE-14 AND -15 POSTIRRADIATION EXAMINATION OF THERMAL STABILITY SPINE SAMPLES

Fuel Test Element	FMB Particle Batch Number[a]	Particle Type	Location[b]	EOL Avg Fuel Temp[c] (°C)	Fast Fluence[d] (E > 29 fJ)$_{HTGR}$ (x10^{25} n/m^2)	FIMA[e] (%)	Fission Gas Release R/B Kr-85m	Number of Particles in Sample		Stereo Examination		Metallography Examination[f]								
								Stereo	Metallography	OPyC Failure (%)	SiC Failure (%)	OPyC Failure (%)	95% Confidence Limits P (%)	SiC Failure (%)	95% Confidence Limits P (%)	Pressure Vessel Failure (%)	95% Confidence Limits P (%)	Mixed Fission Products in IPyC	95% Confidence Limits P (%)	SiC Attack (%)	95% Confidence Limits P (%)
FTE-14	4161-01-030	TRISO UC_2 (VSM)	TS 3-6	1000	1.1	--	NA[g]	1056	86	0	0	0	$3.0 \le P \le 4.5$	0	$0 \le P \le 4.5$	0	$0 \le P \le 4.5$	19	$9.0 \le P \le 27.0$	0	$0 \le P \le 4.5$
	4161-01-030	TRISO UC_2 (VSM)	TS 5-6	1410	1.3	--	NA	1026	91	0	0	0	$0 \le P \le 4.2$	3.2	$1.0 \le P \le 8.5$	0	$0 \le P \le 4.2$	95	$85.0 \le P \le 100$	4.4	$1.0 \le P \le 10.0$
	4161-01-030	TRISO UC_2 (VSM)	TS 4-6	1300	1.3	24.8	NA	1049	19	0	0	0	$0 \le P \le 22.0$	5.3	$0 \le P \le 25.0$	0	$0 \le P \le 22.0$	100	$99.0 \le P \le 100$	47.0	$24.0 \le P \le 71.0$
	OR-1694	TRISO UC_2 (WAR)	TS 2-6	970	1.1	22.9	NA	883	286	7.3	0	8.7	$6.0 \le P \le 12.6$	1	$0.1 \le P \le 2.0$	0	$0 \le P \le 1.3$	0	$0 \le P \le 1.3$	0	$0 \le P \le 1.3$
	OR-1694	TRISO UC_2 (WAR)	TS 6-6	1290	1.2	--	NA	863	241	7.0	0.7	3.7	$2.0 \le P \le 6.9$	0	$0 \le P \le 1.6$	0	$0 \le P \le 1.6$	0	$0 \le P \le 1.6$	0	$0 \le P \le 1.6$
	4252-01-070	BISO ThO_2	TS 6-1	1290	1.2	--	NA	221	40	0	--	0	$0 \le P \le 9.0$	--	--	0	$0 \le P \le 9.0$	--	--	--	--
FTE-15	4161-01-030	TRISO UC_2 (VSM)	TS 3-6	1230	1.8	--	NA	1043	53	0	0	5.7	$1.0 \le P \le 16.0$	7.5	$4.0 \le P \le 18.0$	5.7	$1.0 \le P \le 16.0$	32.1	$20.0 \le P \le 46.0$	0	$0 \le P \le 6.5$
	4161-01-030	TRISO UC_2 (VSM)	TS 4-6	1540	2.0	--	NA	1048	42	0	0	4.8	$0.3 \le P \le 16.6$	21.4	$10.7 \le P \le 37.0$	4.8	$0.3 \le P \le 16.6$	100.0	$99.9 \le P \le 100$	21.2	$10.7 \le P \le 37.0$
	4161-21-030	TRISO UC_2 (VSM)	TS 5-6	1640	2.0	38.4	NA	1060	44	0	0	0	$0 \le P \le 7.9$	9.1	$2.5 \le P \le 23.0$	0	$0 \le P \le 7.9$	100.0	$99.9 \le P \le 100$	18.5	$8.4 \le P \le 33.0$
	OR-1694	TRISO UC_2 (WAR)	TS 2-6	1210	1.8	33.8	NA	844	59	7.4	0	13.6	$6.0 \le P \le 25.0$	0	$0 \le P \le 6.0$	0	$0 \le P \le 6.0$	0	$0 \le P \le 6.0$	0	$0 \le P \le 6.0$
	OR-1694	TRISO UC_2 (WAR)	TS 6-6	1550	2.0	--	NA	841	45	6.5	0	4.4	$0.2 \le P \le 15.2$	2.2	$0 \le P \le 12.0$	2.2	$0 \le P \le 12.0$	0	$0 \le P \le 7.7$	0	$0 \le P \le 7.7$
	4252-02-070	BISO ThO_2	TS 6-1	1550	2.0	--	NA	221	33	0	--	0	$0 \le P \le 10.7$	--	--	0	$0 \le P \le 10.7$	--	--	--	--

[a] Fuel Materials Branch data retrieval number.
[b] TS 15-6 (thermal stability type II, crucible No. 15 - hole No. 6).
[c] TREVER calculated.
[d] GAUGE/FEVER calculated.
[e] Mass spectroscopy measured.
[f] Approximately 10 to 20% of the sample is examined.
[g] NA = not available.

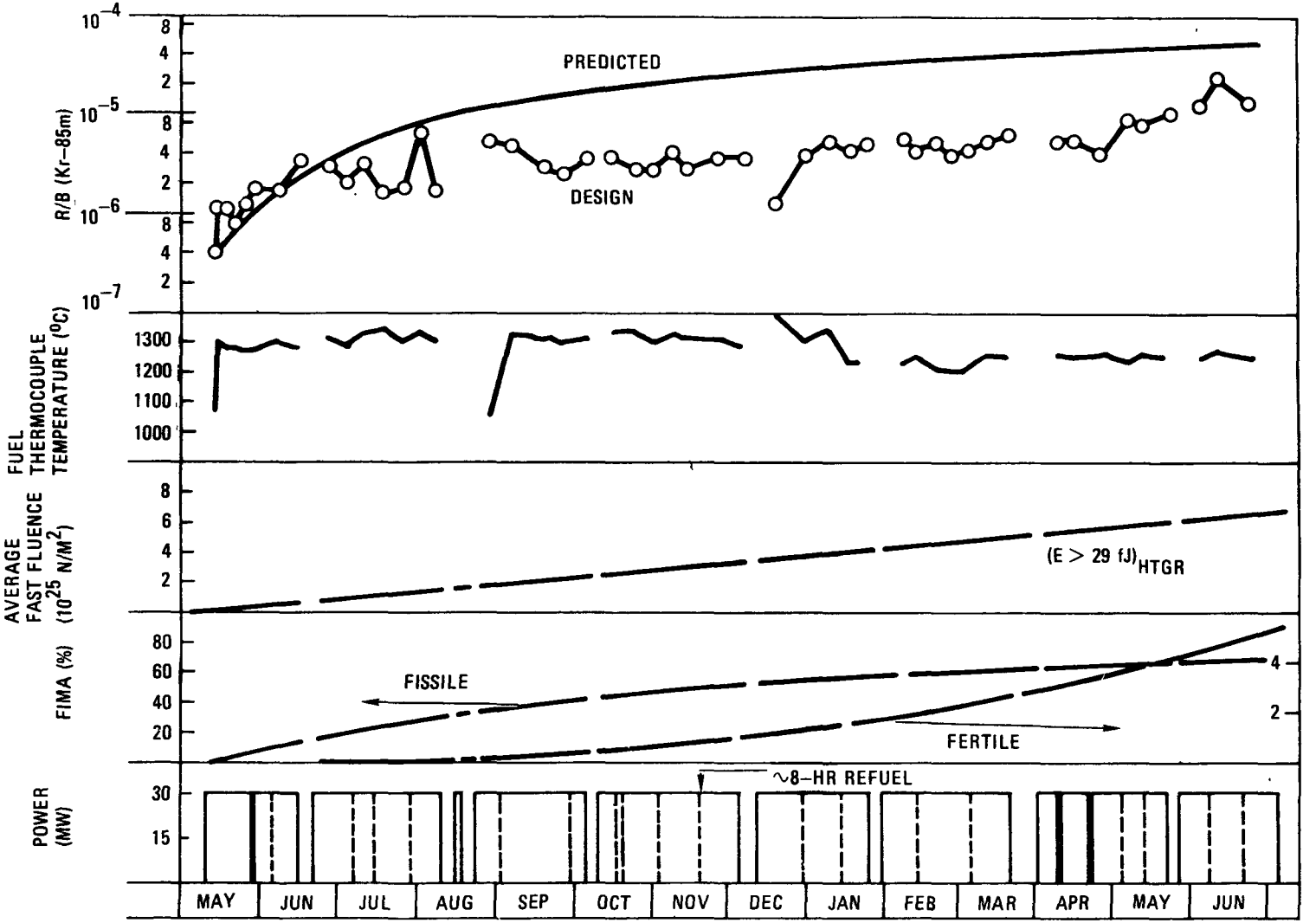

Fig. 9-1. Operation history for cell 1 of P13T

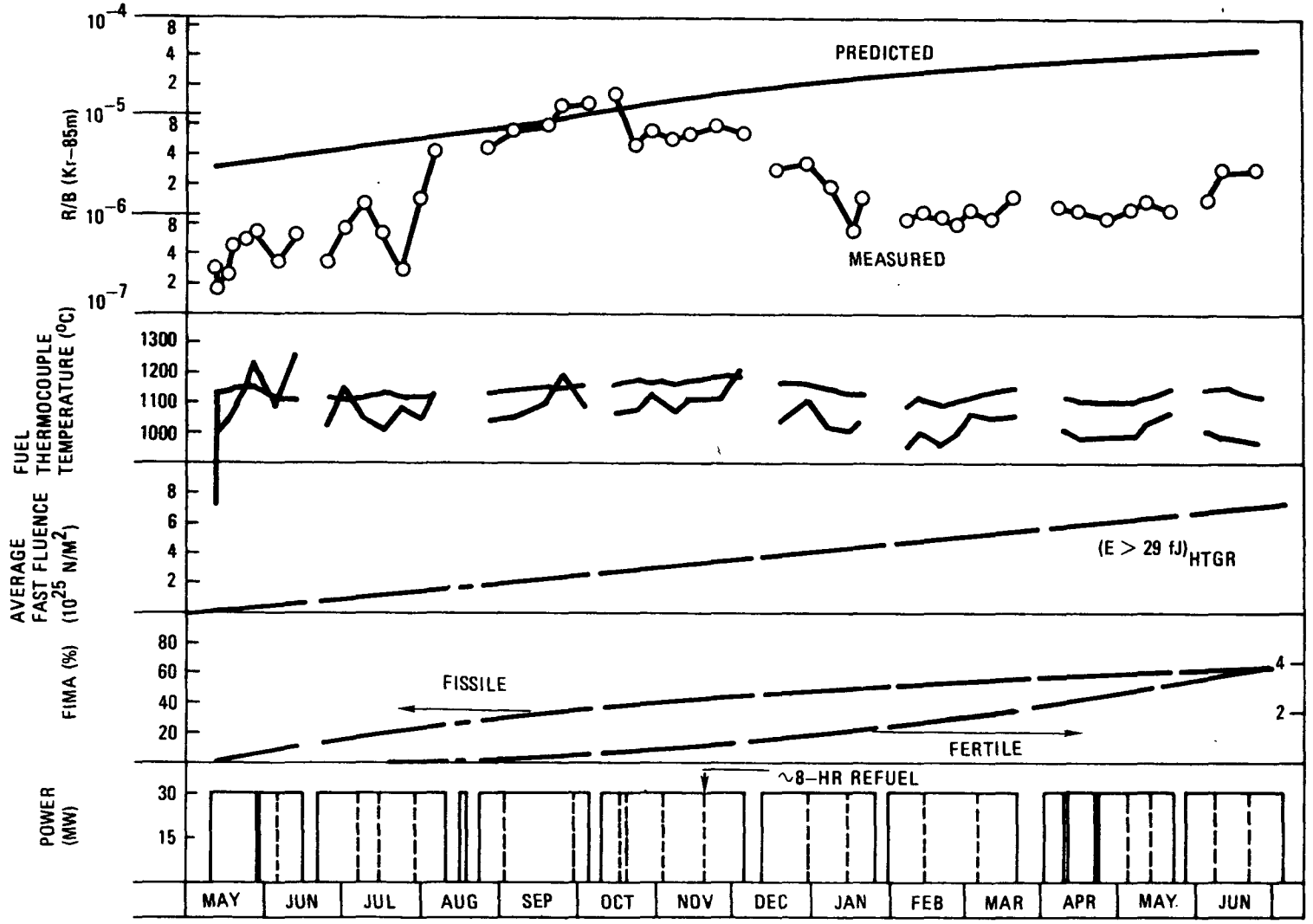

Fig. 9-2. Operation history for cell 2 of P13T

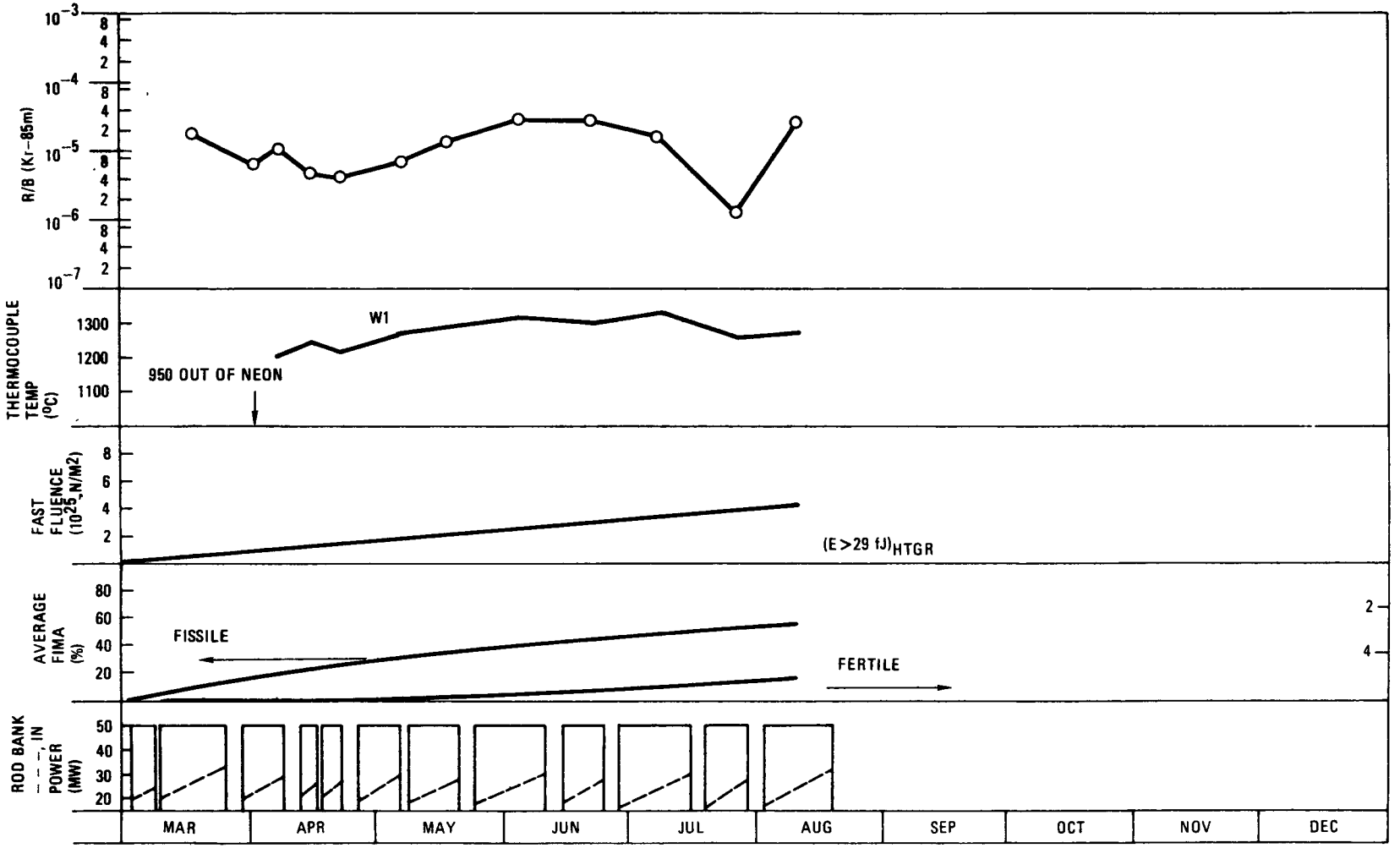

Fig. 9-3. Operation history for cell 1 of P13V to August 10, 1976

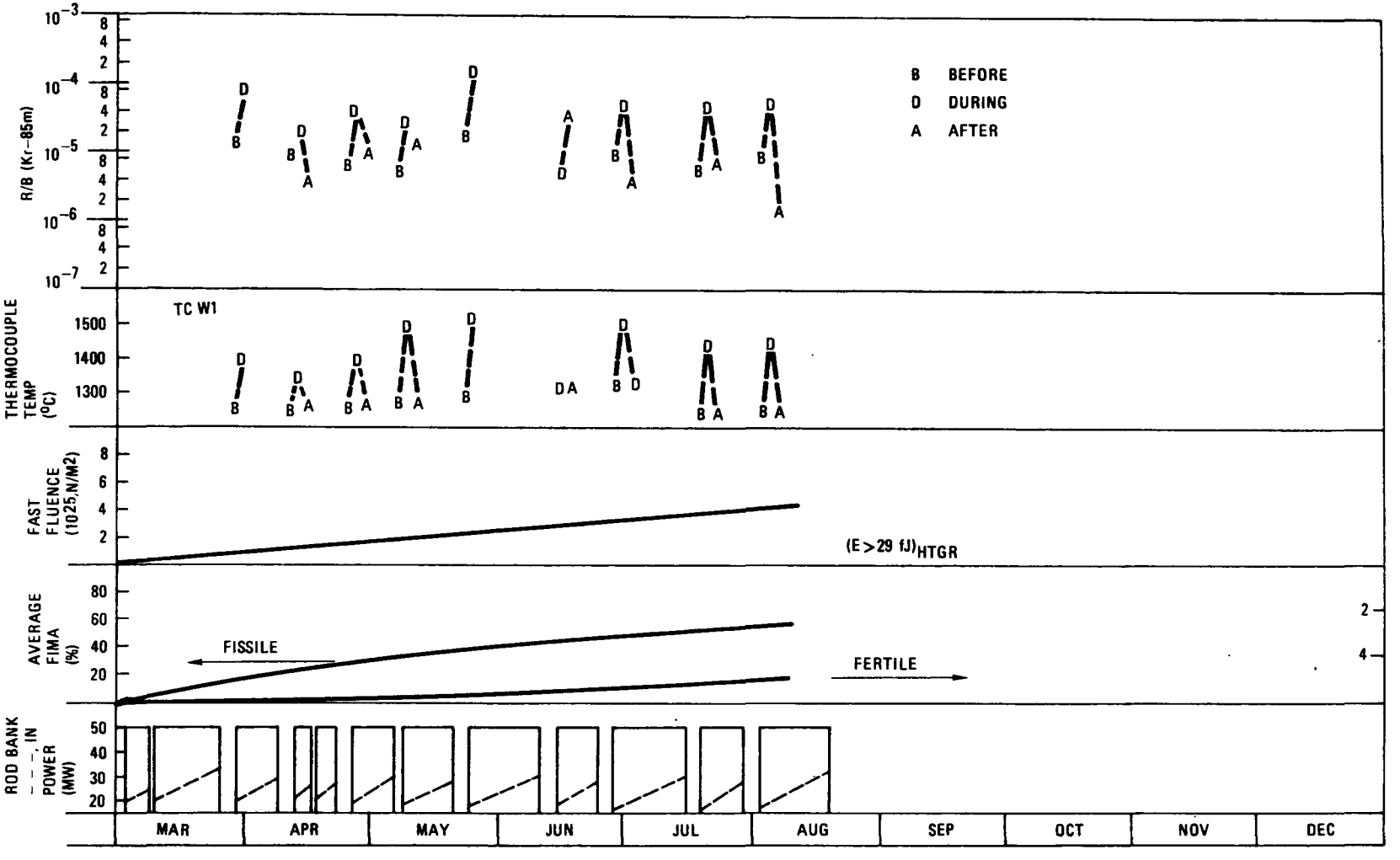

Fig. 9-4. Operation history for cell 1 of P13V thermal cycled to August 10, 1976

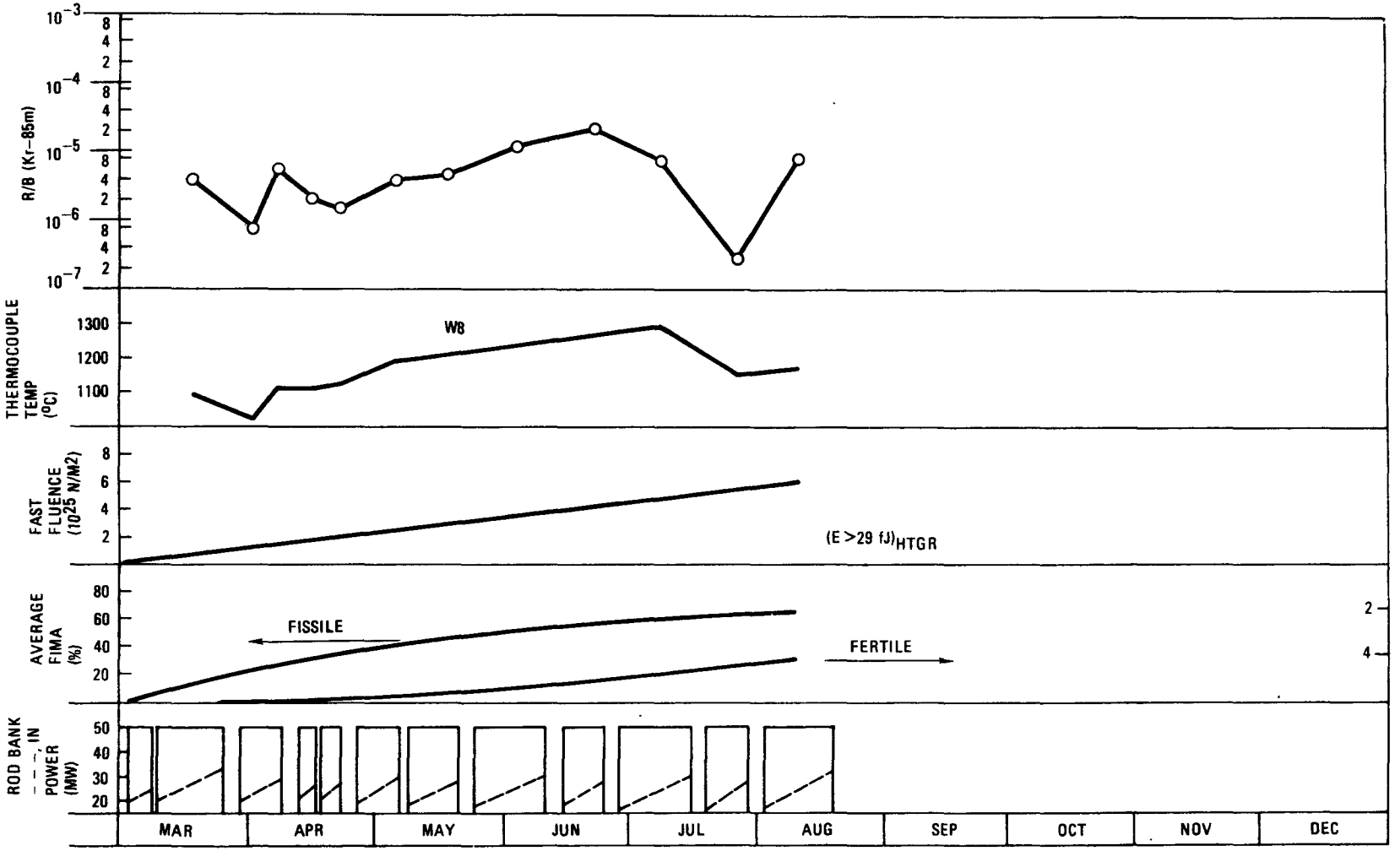

Fig. 9-5. Operation history for cell 2 of P13V to August 10, 1976

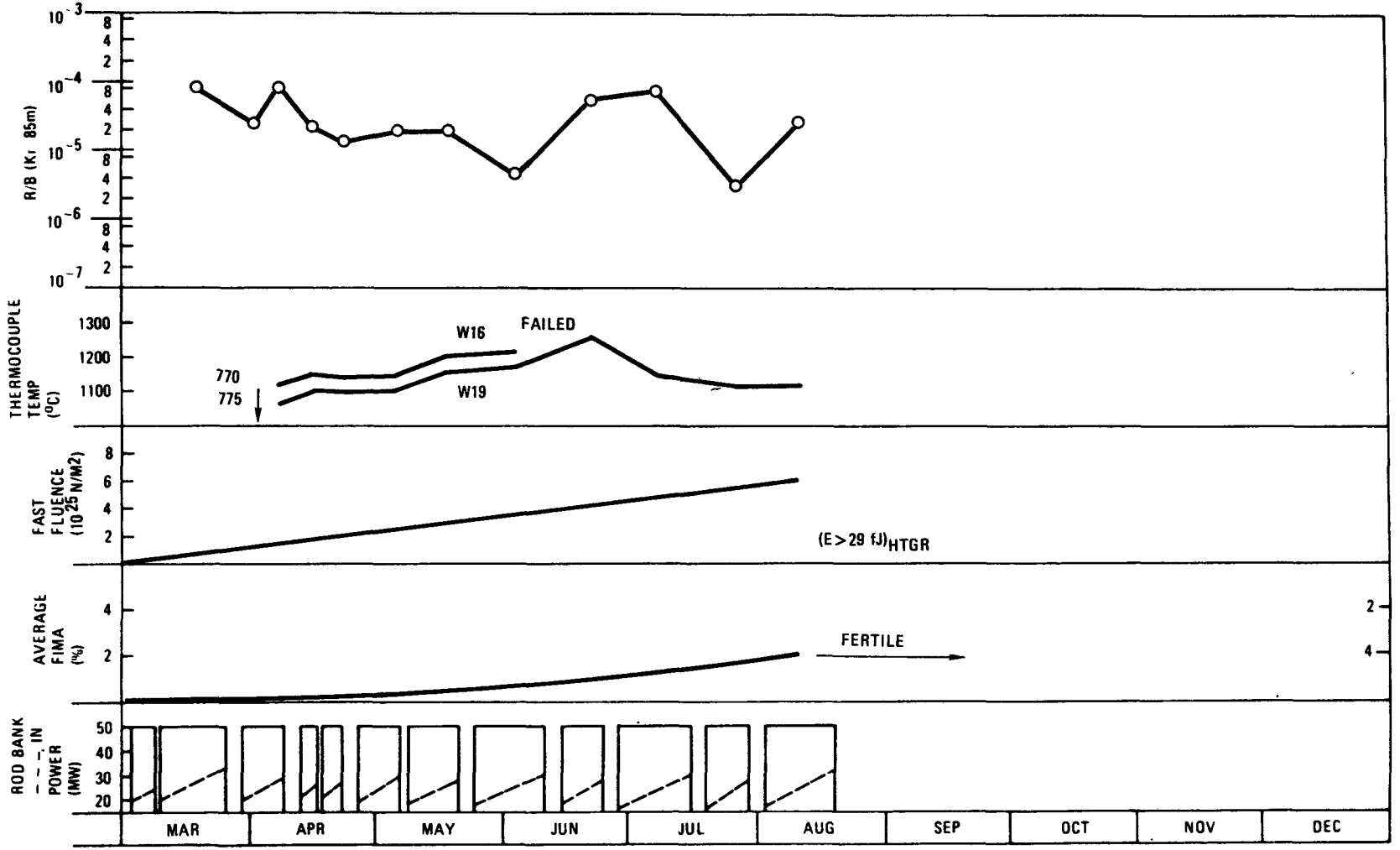

Fig. 9-6. Operation history for cell 3 of P13V to August 10, 1976

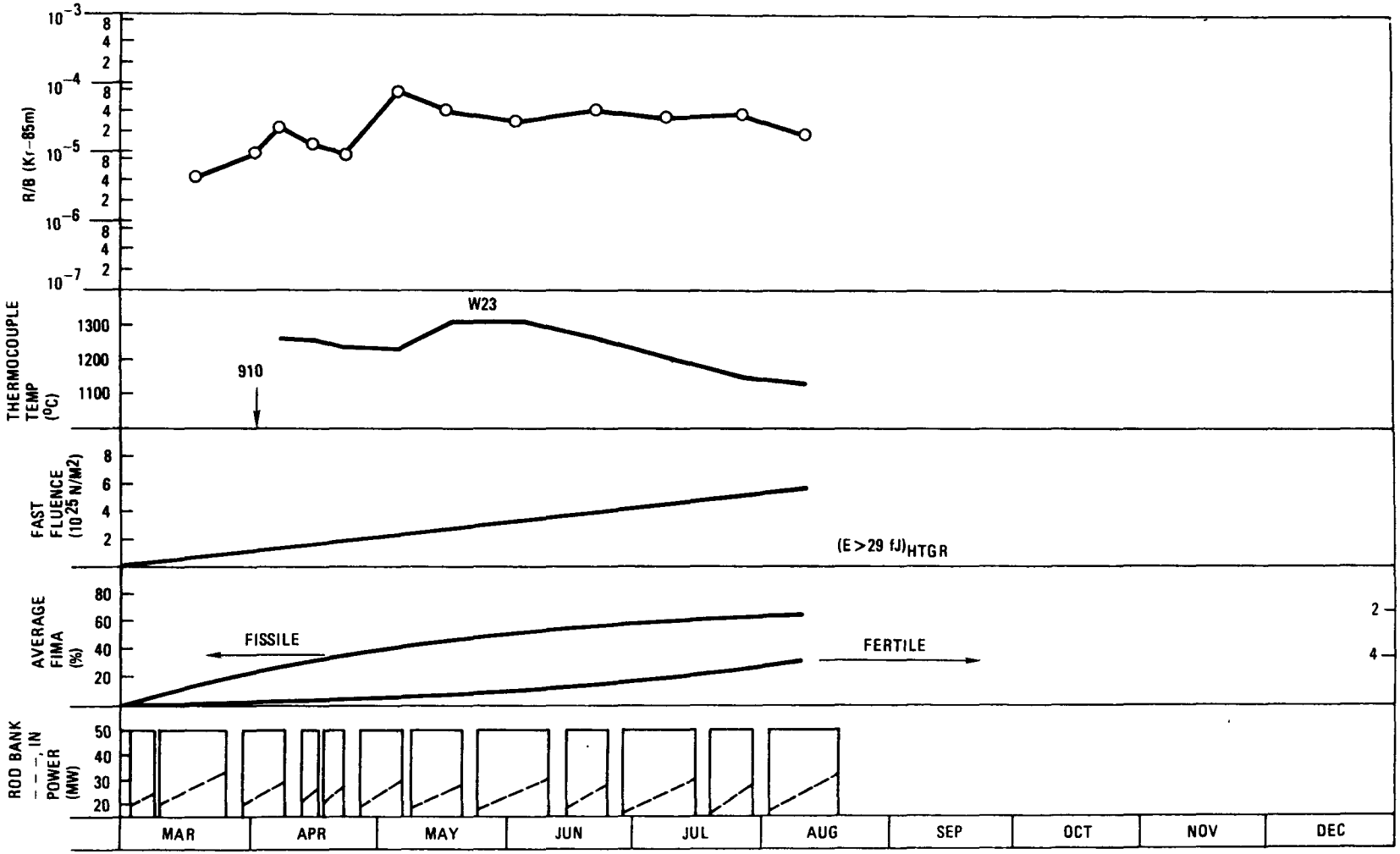

Fig. 9-7. Operation history for cell 4 of P13V to August 10, 1976

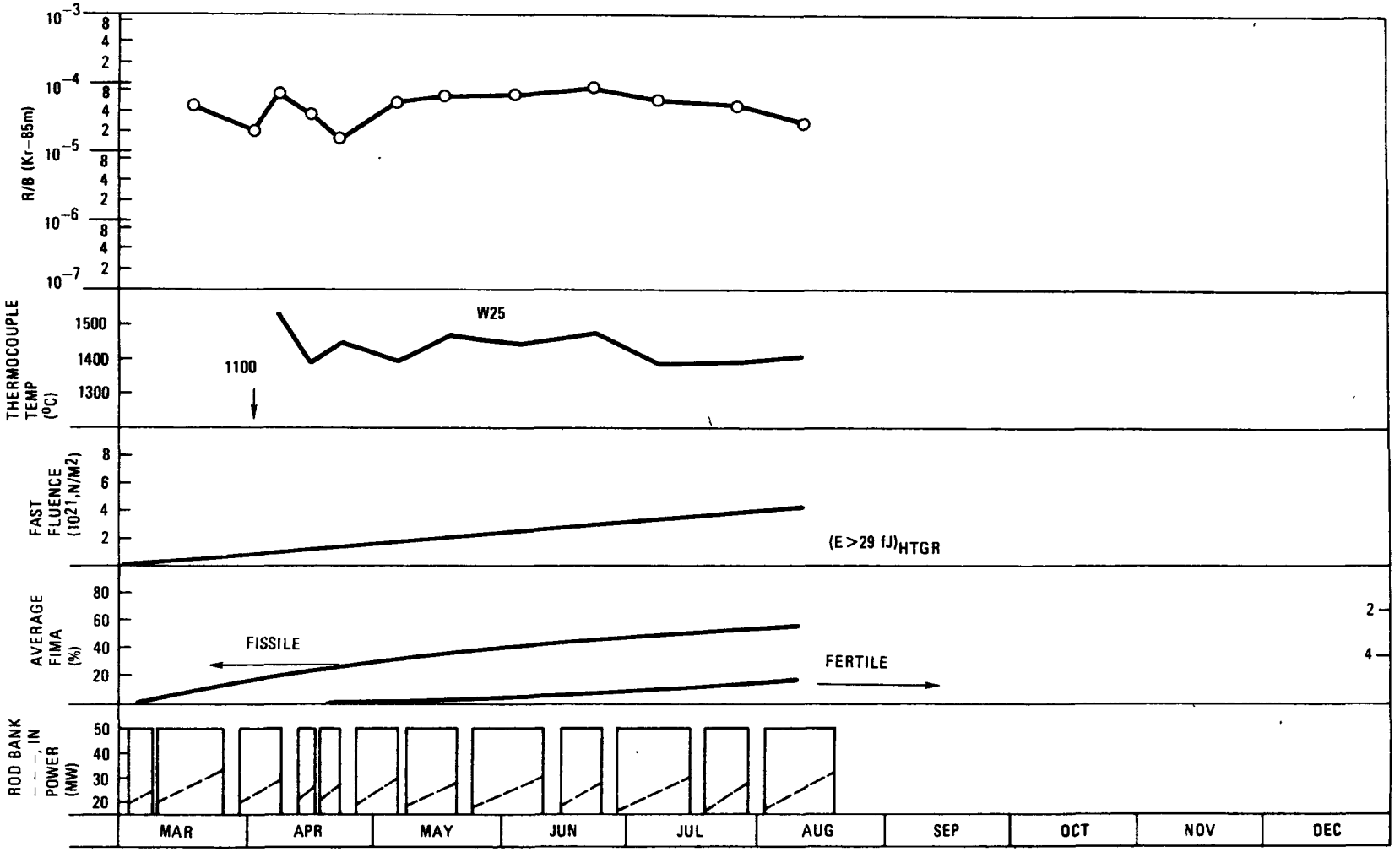

Fig. 9-8. Operation history for cell 5 of P13V to August 10, 1976

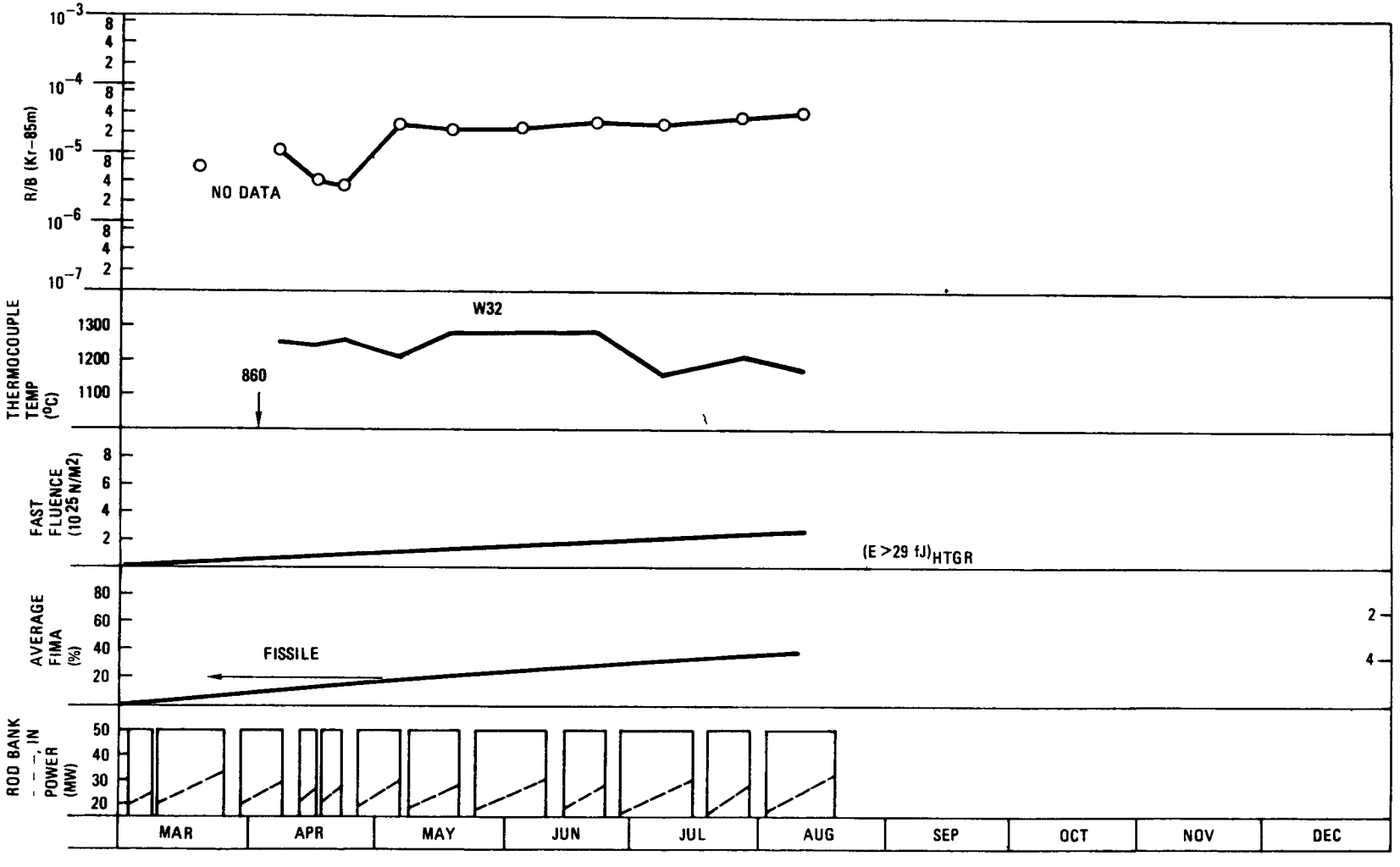

Fig. 9-9. Operation history for cell 6 of P13V to August 10, 1976

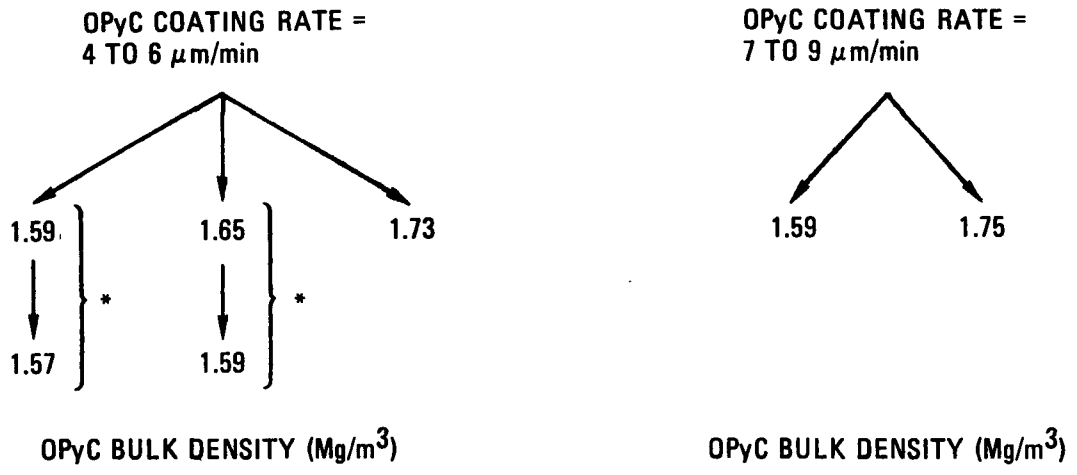

* DIFFERENCE BETWEEN BATCHES IN A SET IS THE INITIAL COATER BED SIZE; I.E., ONE BATCH WAS COATED WITH A Th CHARGE OF ~13 kg WHILE THE SECOND BATCH WAS COATED USING ~7 kg OF Th.

Fig. 9-10. Schematic diagram of test matrix for TRISO coated ThO_2 particles

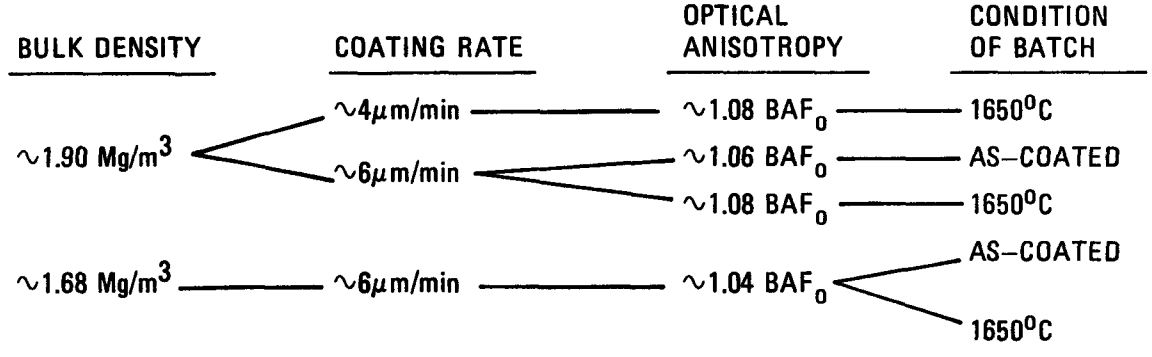

Fig. 9-11. Test matrix of primary OPyC coating variables of ThO_2 BISO batches made in the large coater for capsule HT-33

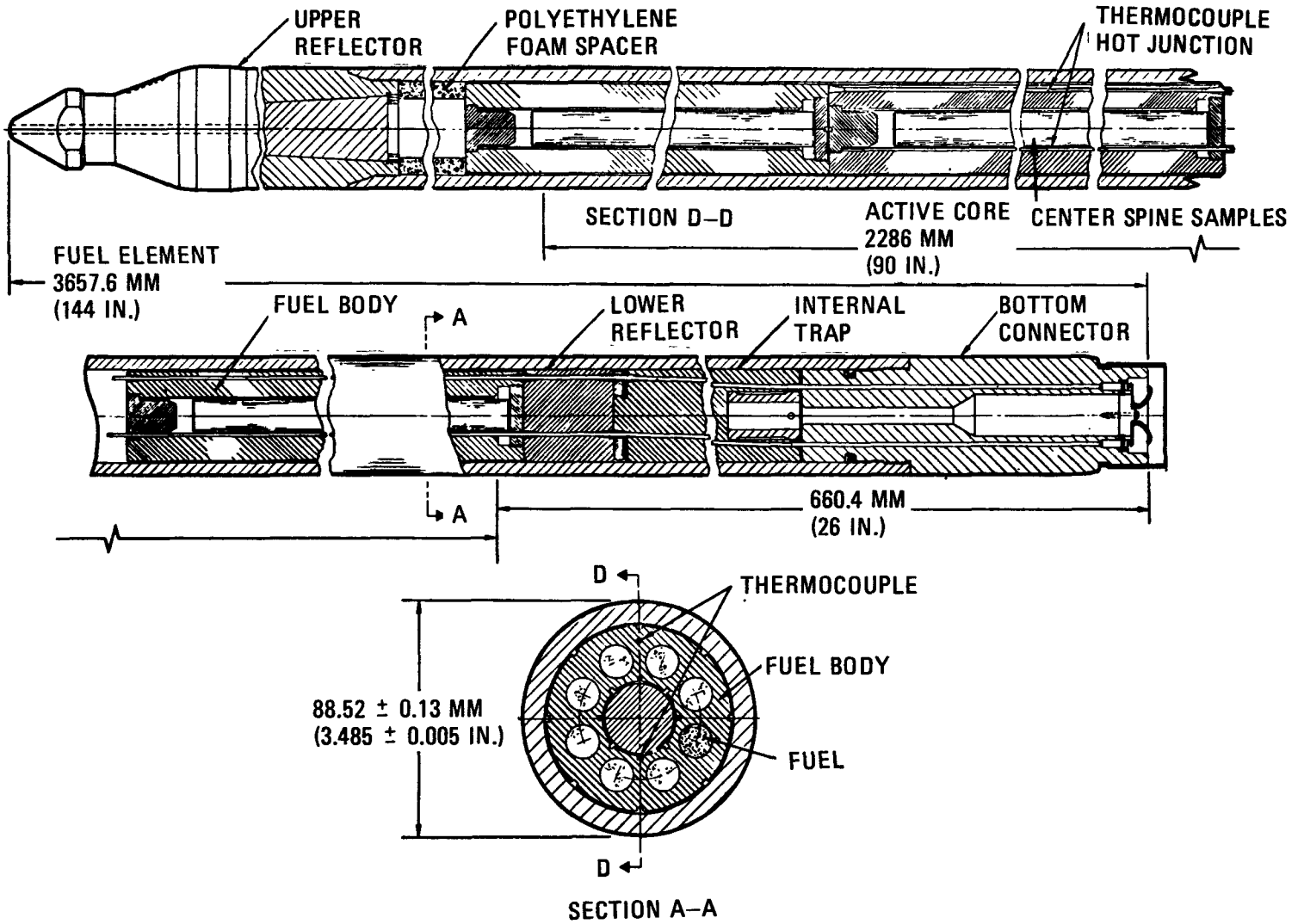

Fig. 9-12. FTE-15 assembly

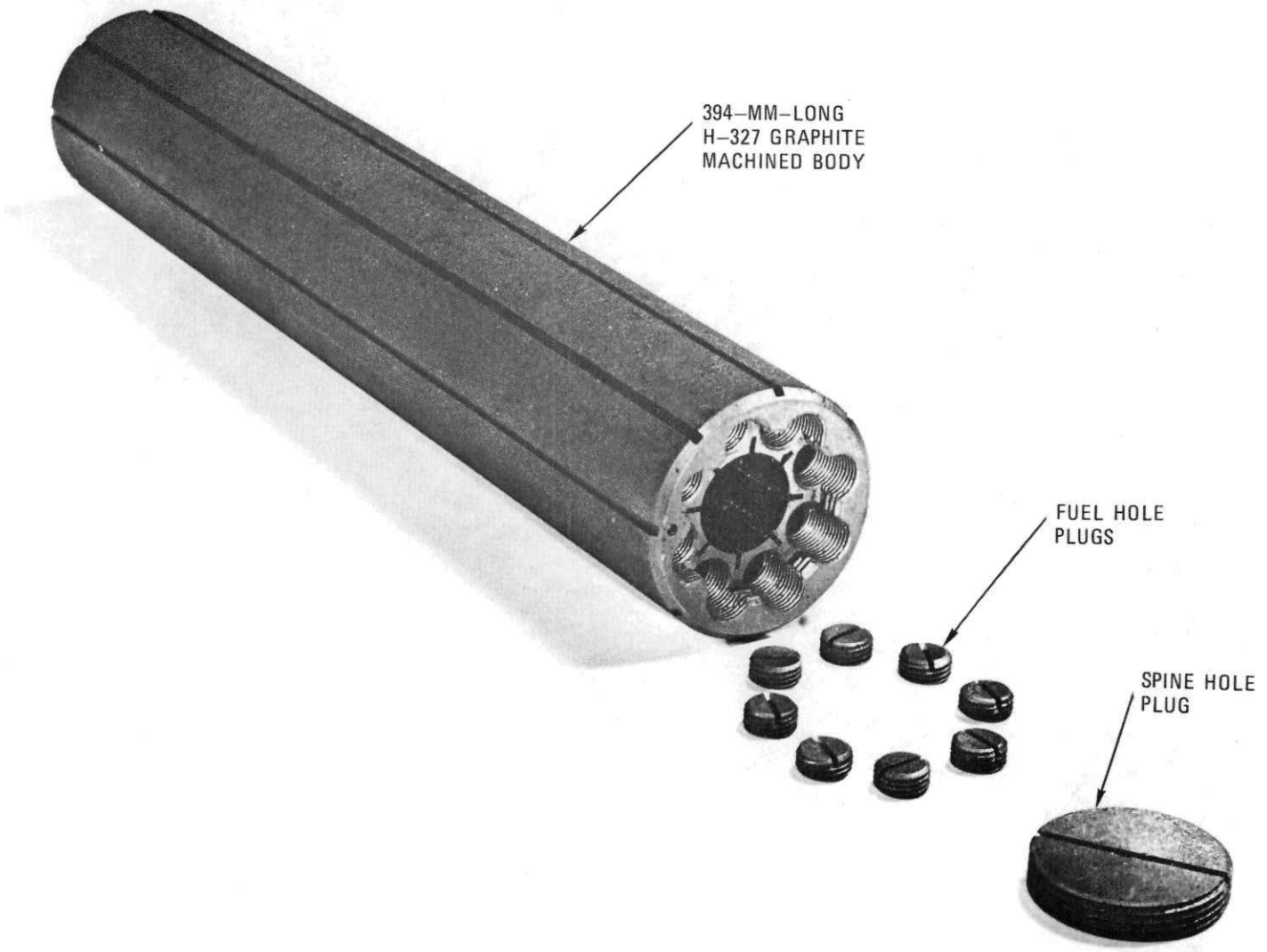

Fig. 9-13. Graphite fuel body for Peach Bottom fuel test elements

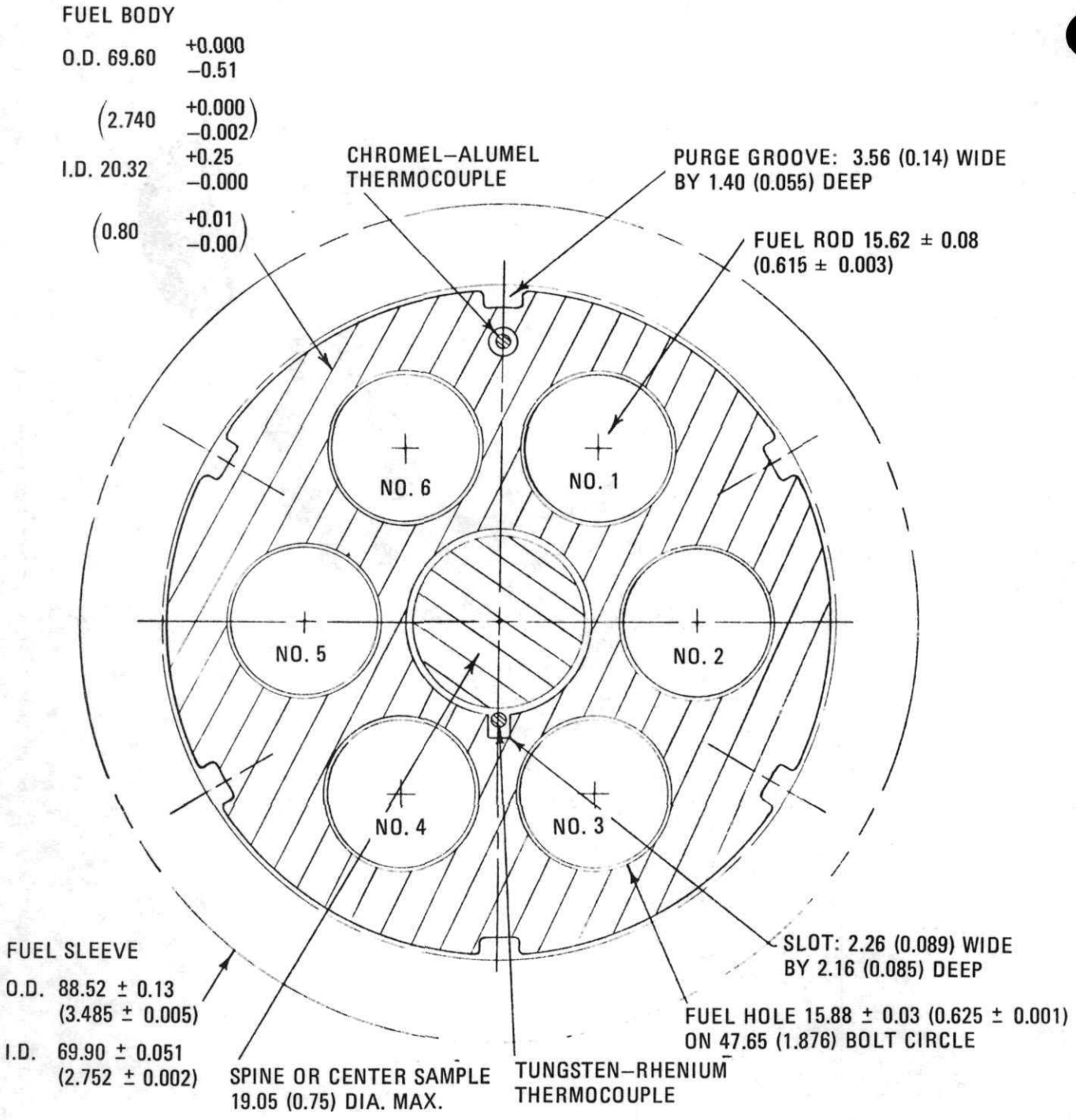

DIMENSIONS IN MM (IN.)

Fig. 9-14. Cross section of FTE-15

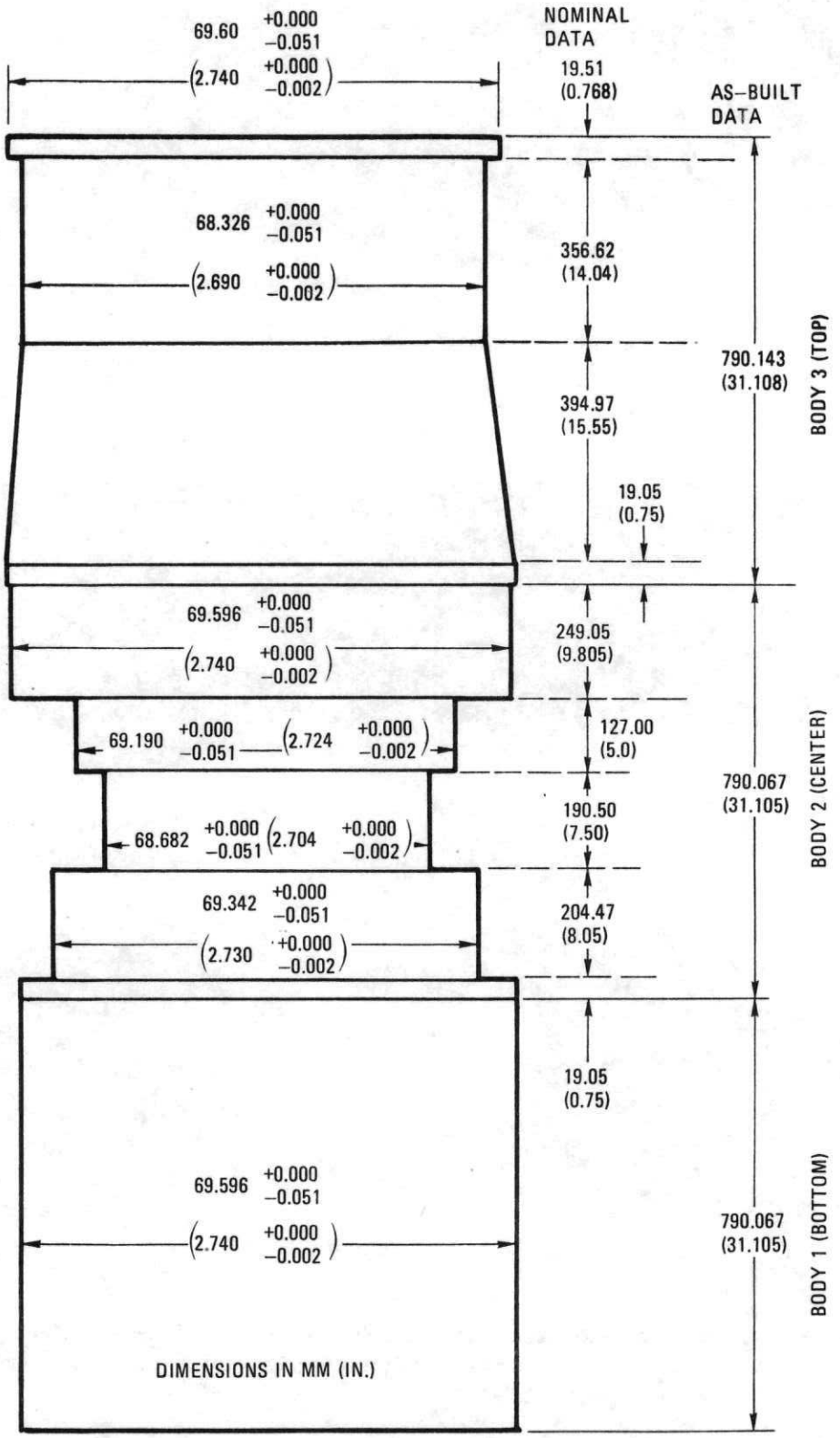

Fig. 9-15. Fuel body outside dimensions for FTE-15

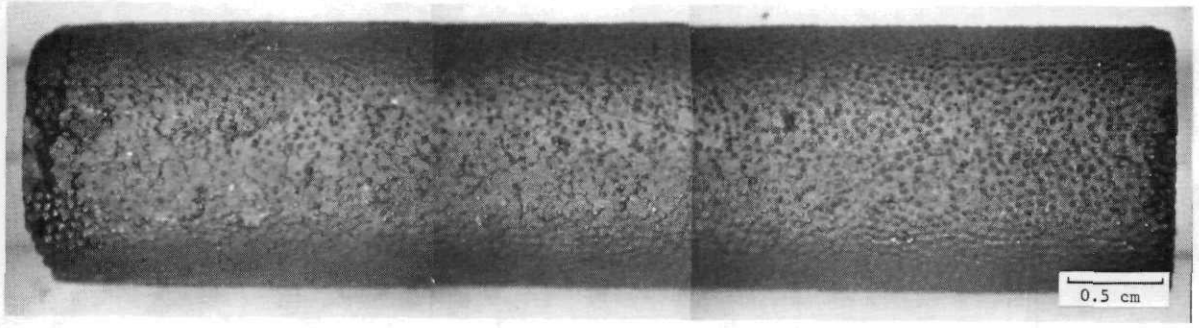

S7437 (123-125)

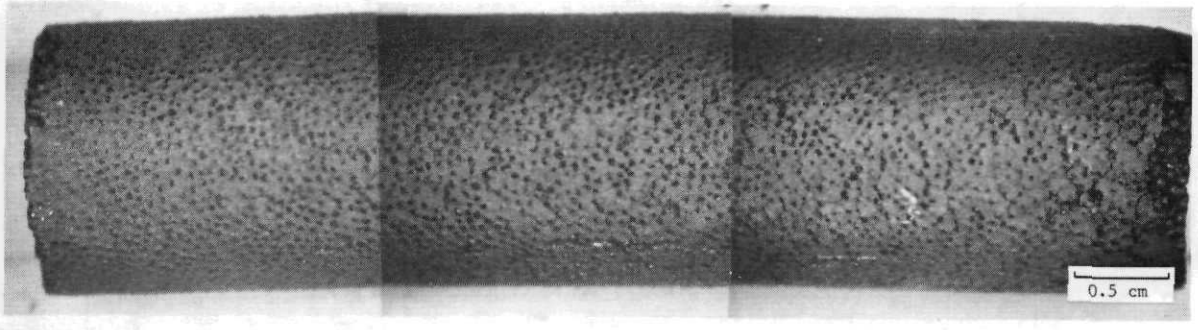

S7437 (127-129)

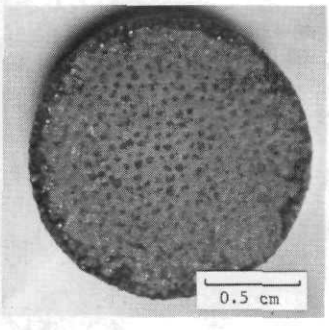

S7437-122

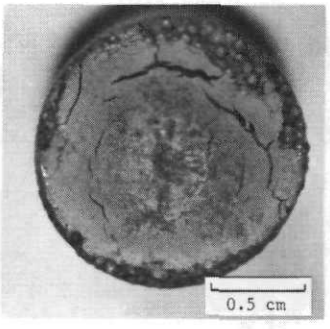

S7437-121

Fig. 9-16. Visual examination of FTE-15 fuel rod 2-1-4 (UC_2 TRISO - ThC_2 BISO). Irradiation conditions ∿2.5 x 25 n/m^2 ($E \geq 29$ fJ)$_{HTGR}$ at ∿1467°C

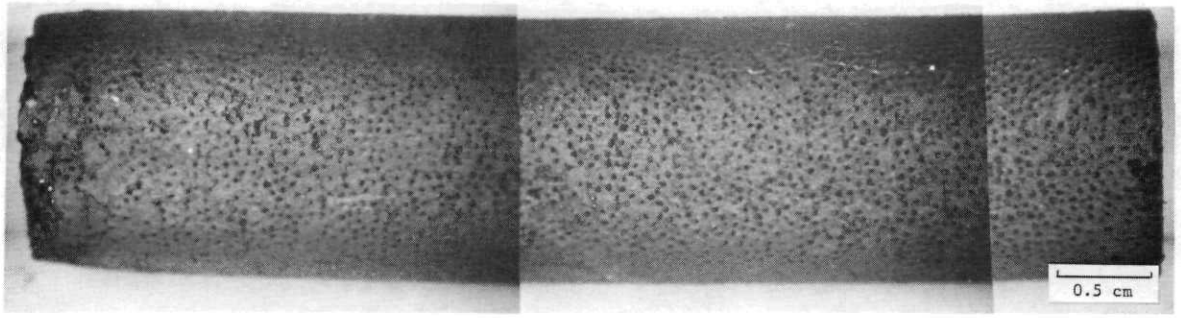

S7437 (132-134)

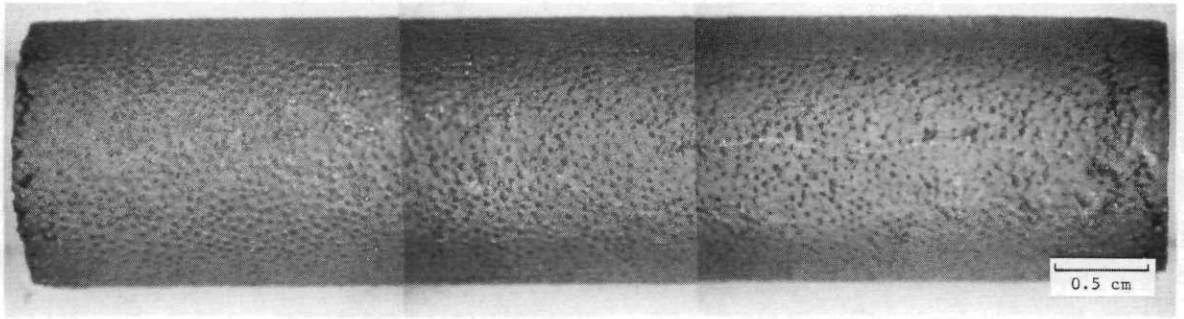

S7437 (135-137)

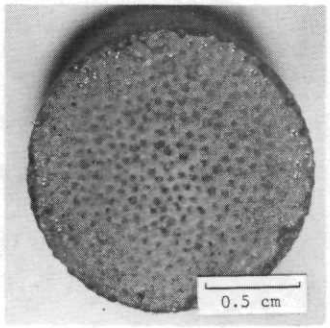

S7437-131

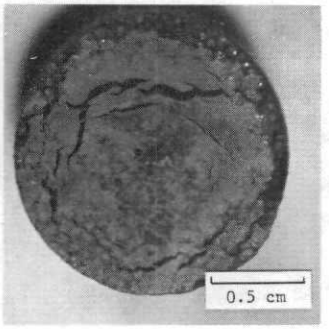

S7437-130

Fig. 9-17. Visual examination of FTE-15 fuel rod 2-1-5 (UC_2 TRISO - ThC_2 BISO). Irradiation conditions ~2.5 x 25 n/m^2 $(E \geq 29\ fJ)_{HTGR}$ at ~1516°C

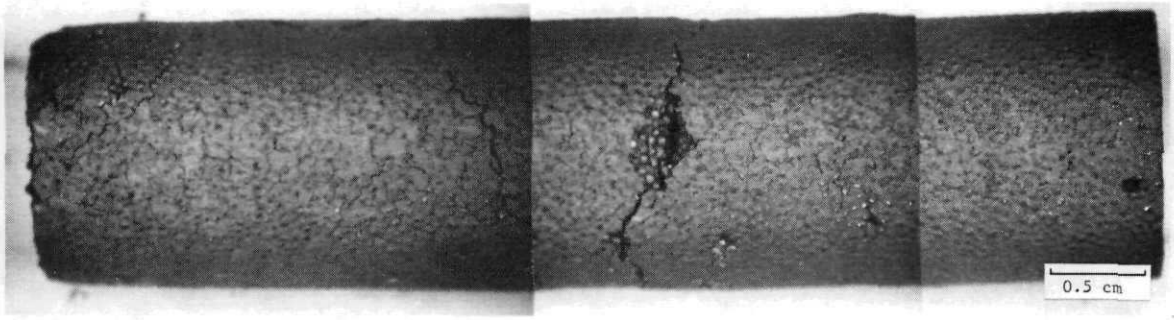

S7437 (73-75)

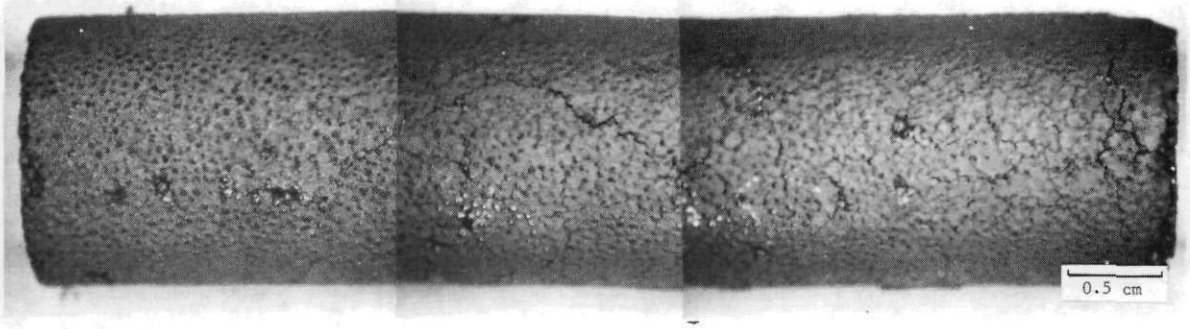

S7437 (76-78)

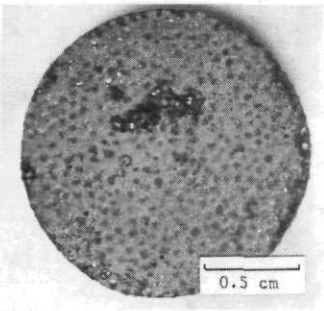

S7437-71

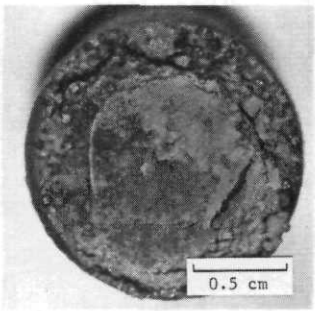

S7437-70

Fig. 9-18. Visual examination of FTE-15 fuel rod 2-2-4 (UC_2 TRISO - ThC_2 TRISO). Irradiation conditions ∿2.5 x 25 n/m^2 $(E \geq 29\ fJ)_{HTGR}$ at ∿1467°C

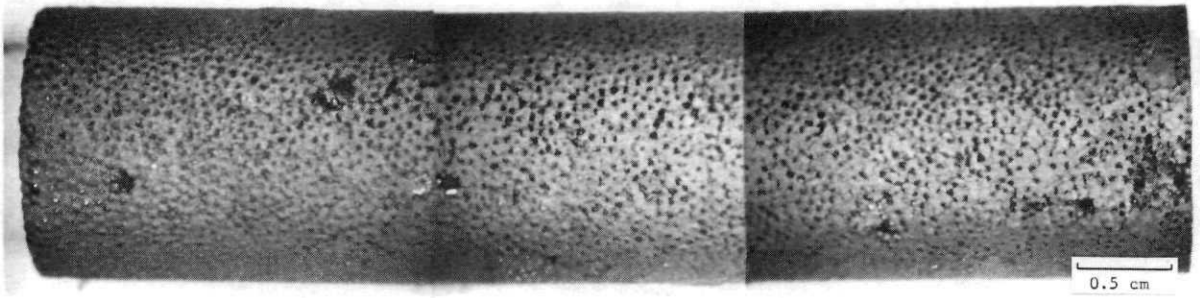

S7437 (81-83)

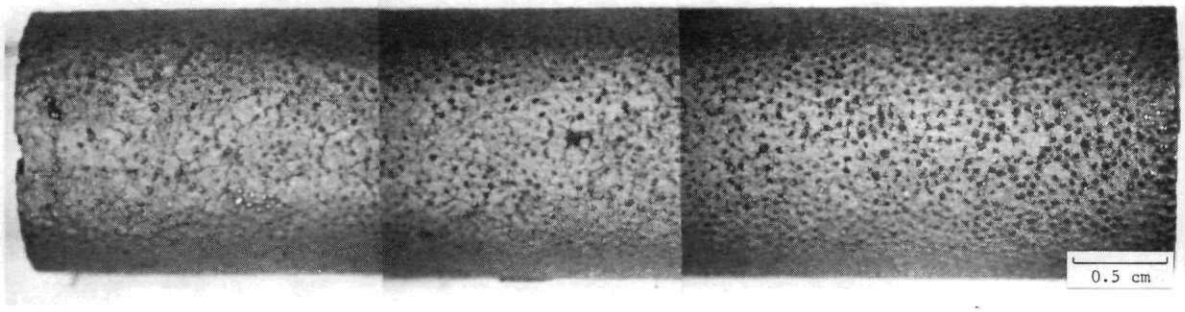

S7437 (84-86)

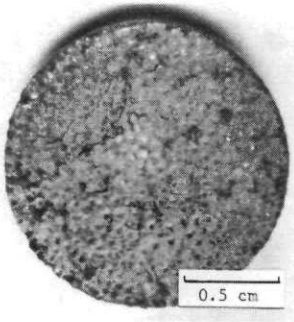

S7437-79

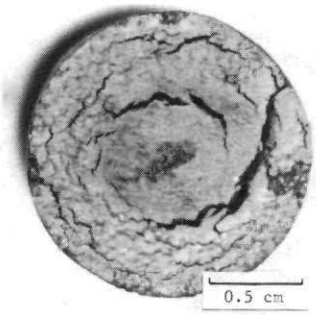

S7437-80

Fig. 9-19. Visual examination of FTE-15 fuel rod 2-2-5 (UC_2 TRISO - ThC_2 TRISO). Irradiation conditions ~2.5 x 25 n/m^2 ($E \geq 29$ fJ)$_{HTGR}$ at ~1516°C

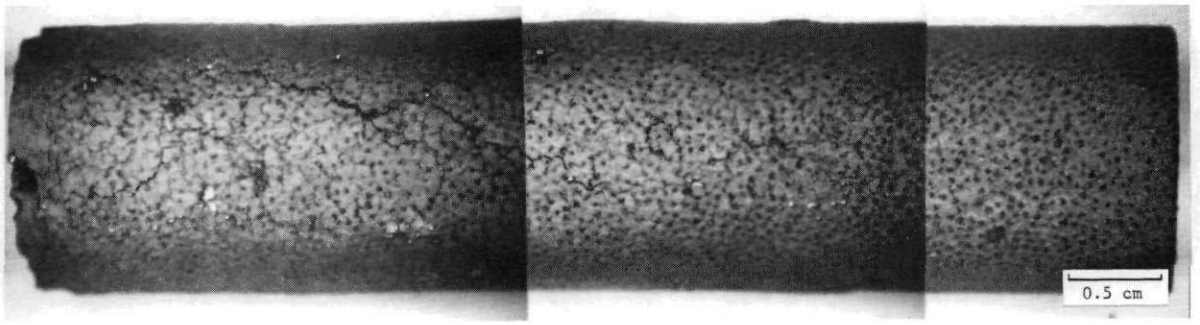

S7437 (51-53)

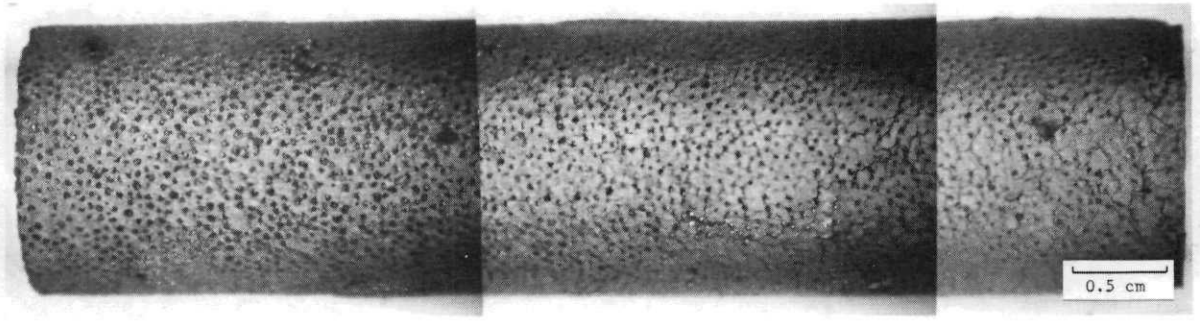

S7437 (56-58)

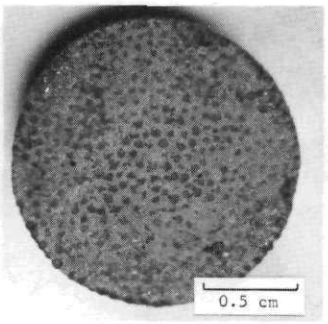

S7437-50

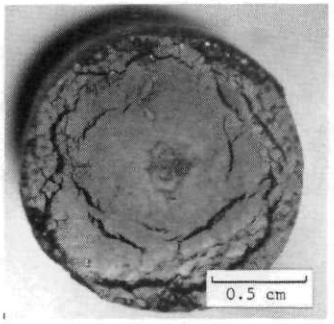

S7437-49

Fig. 9-20. Visual examination of FTE-15 fuel rod 2-2-7 (UC_2 TRISO - ThC_2 TRISO). Irradiation conditions ∿2.5 x 25 n/m^2 $(E \geq 29\ fJ)_{HTGR}$ at ∿1497°C

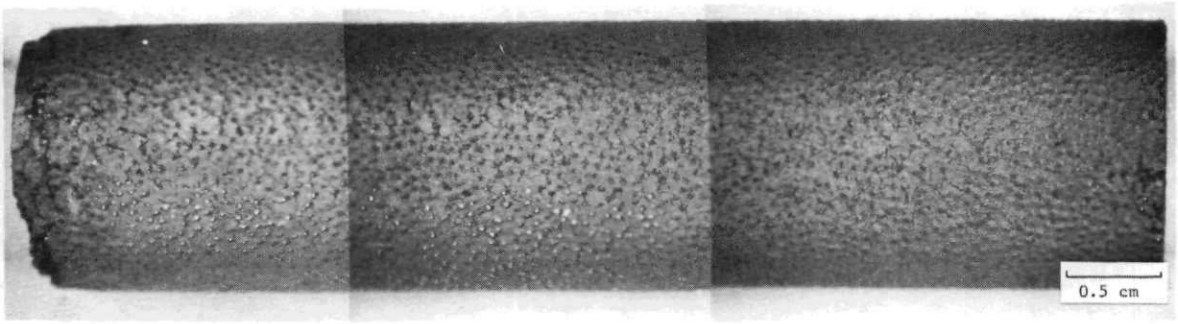

S7437 (150-152)

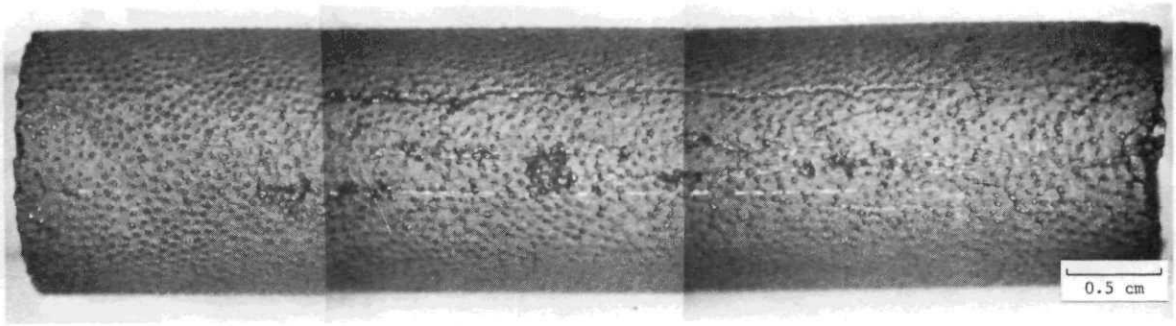

S7437 (153-155)

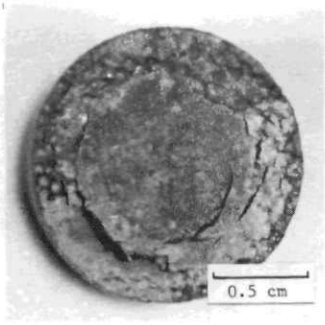

S7437-149

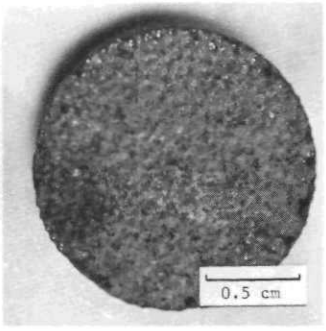

S7437-148

Fig. 9-21. Visual examination of FTE-15 fuel rod 2-3-4 (UO_2 TRISO - ThO_2 BISO). Irradiation conditions ∿2.5 x 25 n/m^2 ($E \geq 29$ fJ)$_{HTGR}$ at ∿1467°C

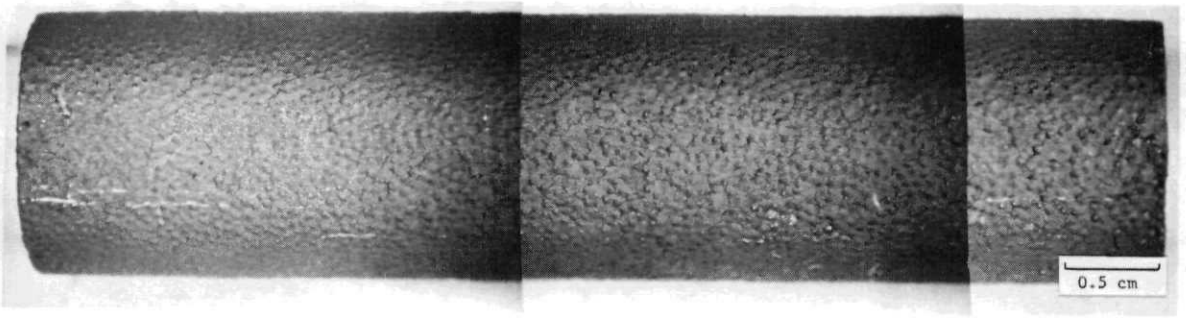

S7437 (140-142)

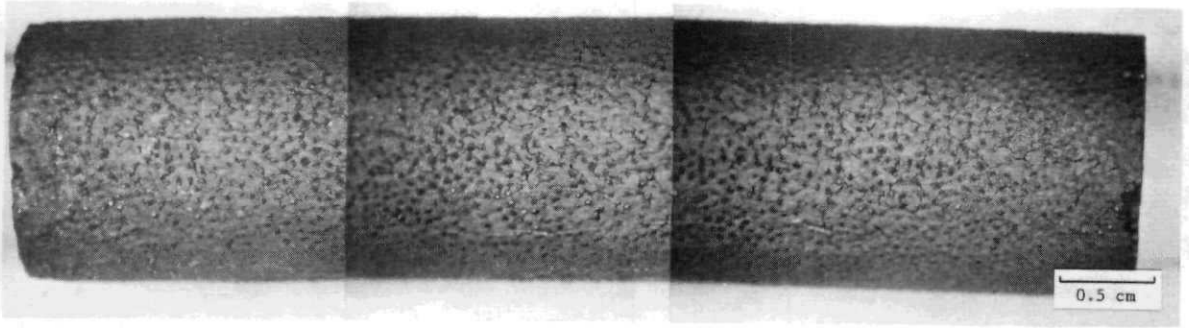

S7437 (143-145)

S7437-138

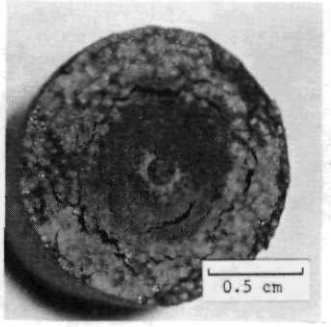

S7437-139

Fig. 9-22. Visual examination of FTE-15 fuel rod 2-3-5 (UO_2 TRISO - ThO_2 BISO). Irradiation conditions ∿2.5 x 25 n/m^2 ($E \geq 29$ fJ)$_{HTGR}$ at ∿1516°C.

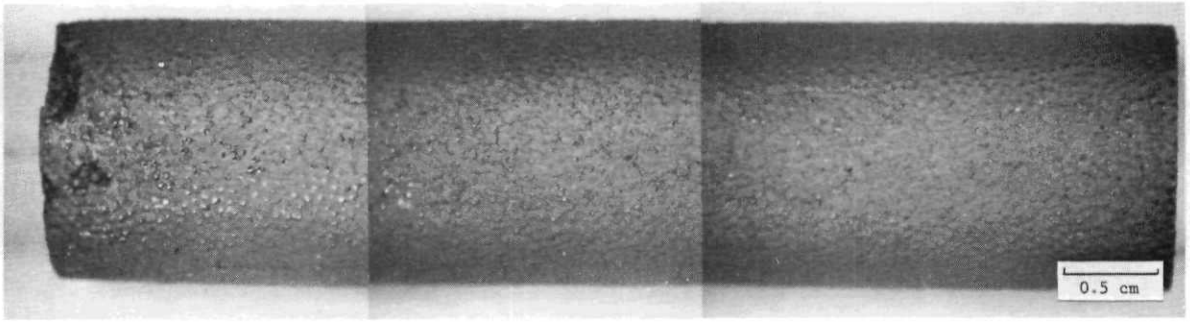

S7437 (61-63)

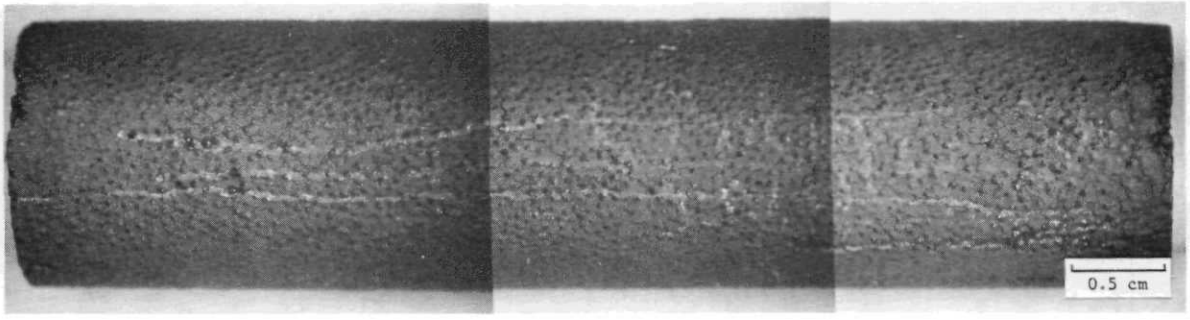

S7437 (64-66)

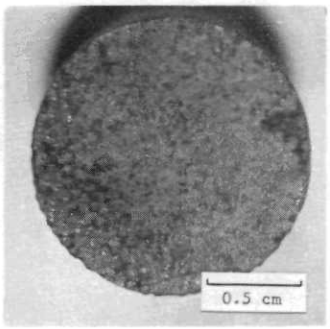

S7437-60

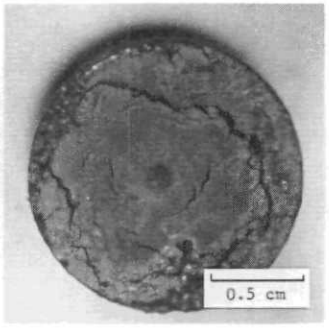

S7437-59

Fig. 9-23. Visual examination of FTE-15 fuel rod 2-3-7 (UO_2 TRISO - ThO_2 BISO). Irradiation conditions ∿2.5 x 25 n/m^2 $(E \geq 29\ fJ)_{HTGR}$ at ∿1497°C

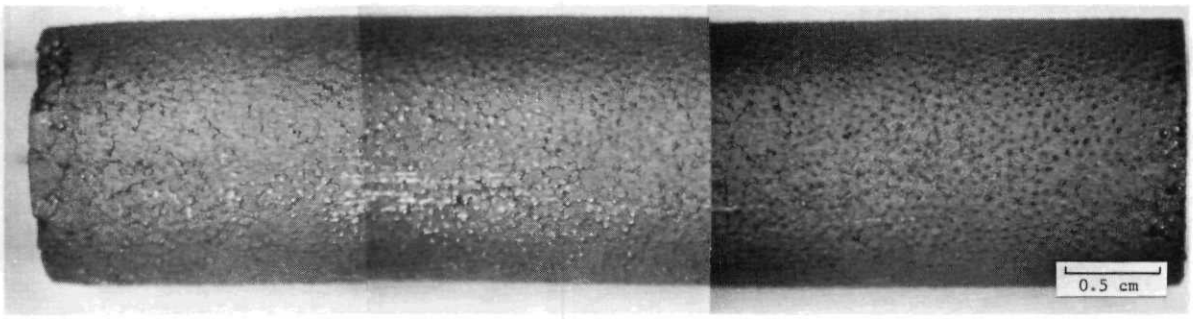

S7437 (43-45)

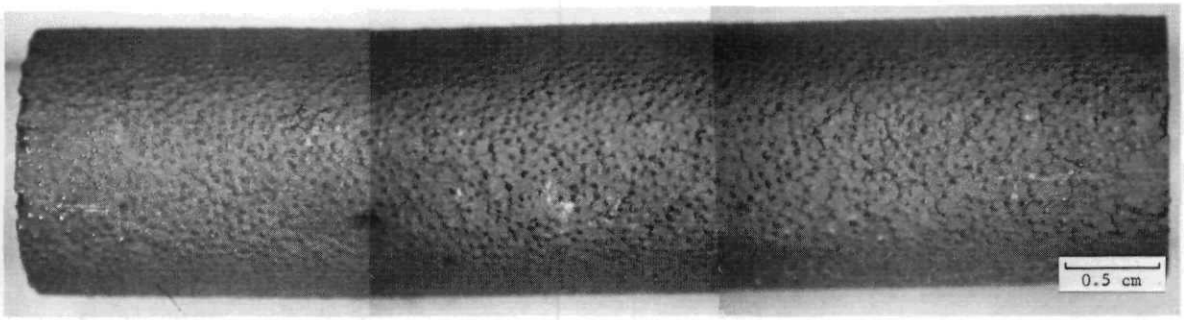

S7437 (46-48)

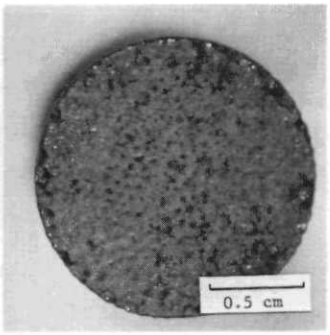

S7437-42

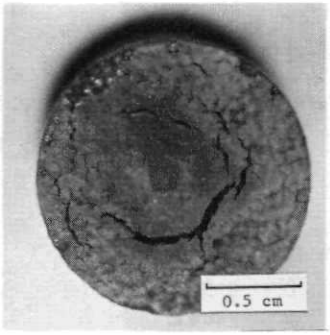

S7437-41

Fig. 9-24. Visual examination of FTE-15 fuel rod 2-3-8 (UO_2 TRISO - ThO_2 BISO). Irradiation conditions ∿2.5 x 25 n/m^2 $(E \geq 29\ fJ)_{HTGR}$ at ∿1448°C

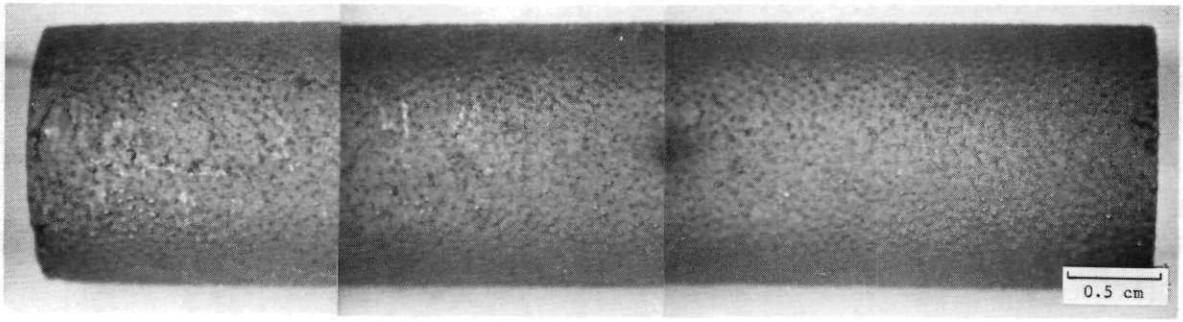

S7437 (34-36)

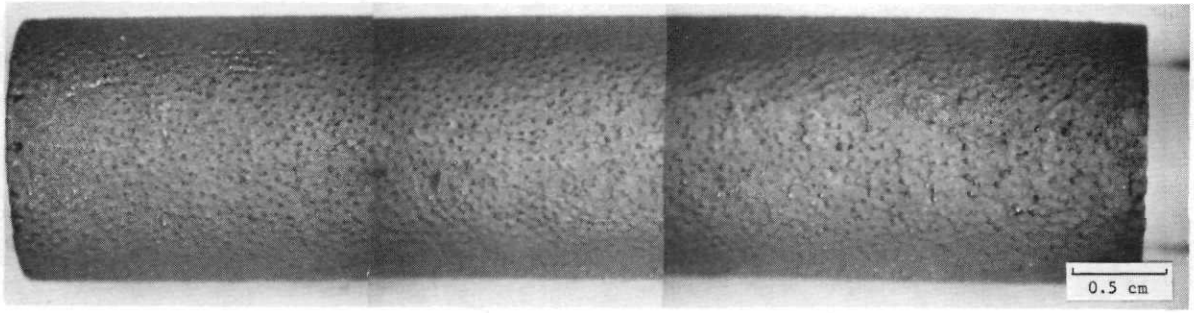

S7437 (38-40)

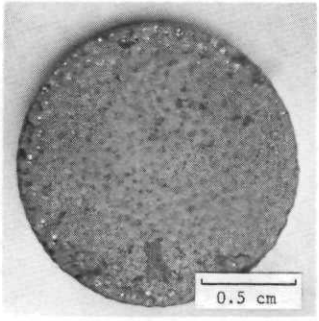

S7437-33

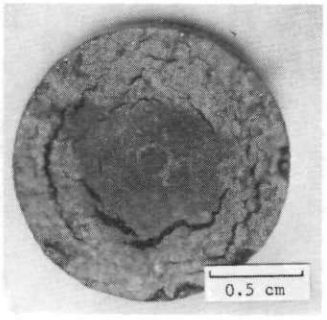

S7437-32

Fig. 9-25. Visual examination of FTE-15 fuel rod 2-3-9 (UO_2 TRISO - ThO_2 BISO). Irradiation conditions ∿2.3 x 25 n/m^2 $(E \geq 29\ fJ)_{HTGR}$ at ∿1408°C

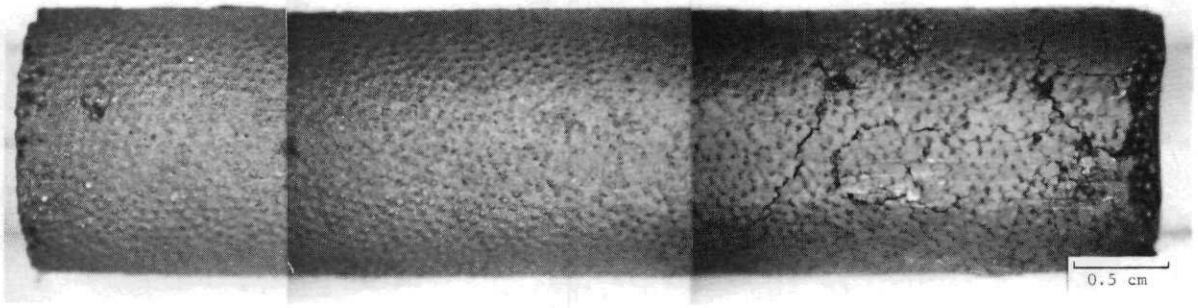

S7437 (99-101)

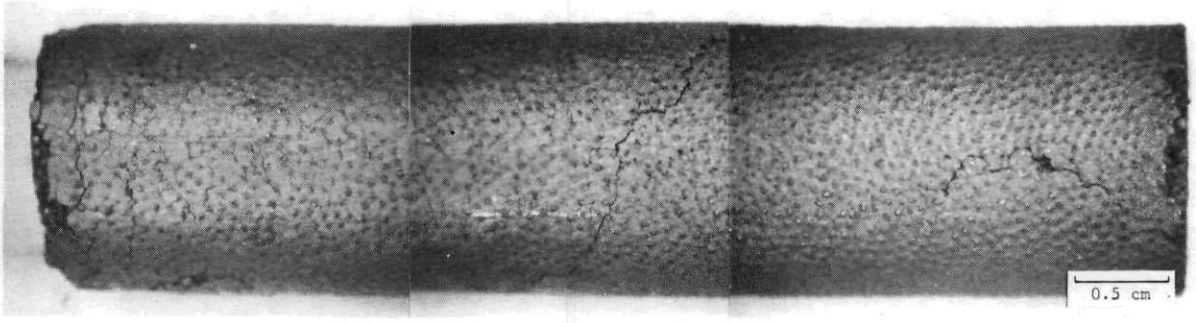

S7437 (102-104)

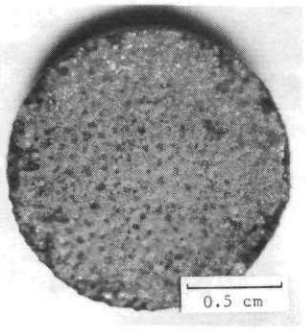

S7437-97

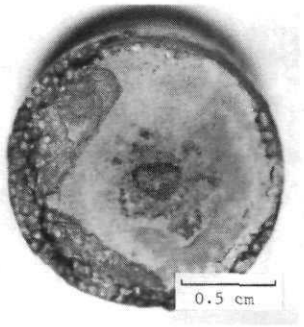

S7437-96

Fig. 9-26. Visual examination of FTE-15 fuel rod 2-4-3 ($(Th,U)O_2$ TRISO - ThC_2 BISO). Irradiation conditions $\sim$2.5 x 25n/m^2 $(E \geq 29\ fJ)_{HTGR}$ at $\sim$1373°C

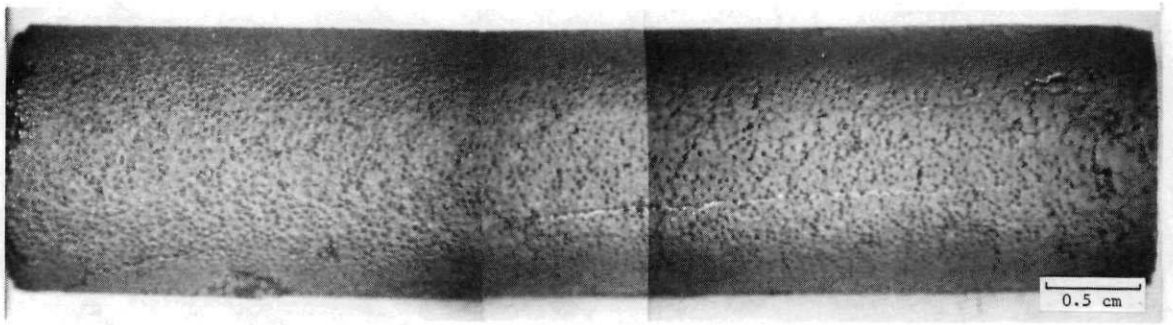

S7437 (8-10)

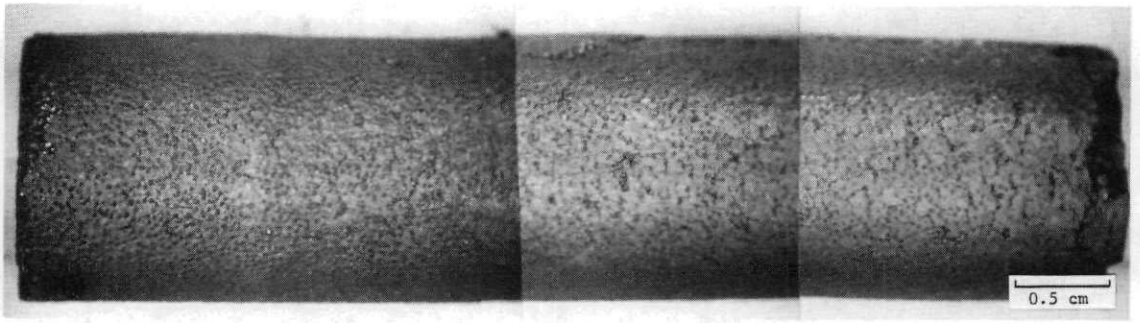

S7437 (11, 12A, 12)

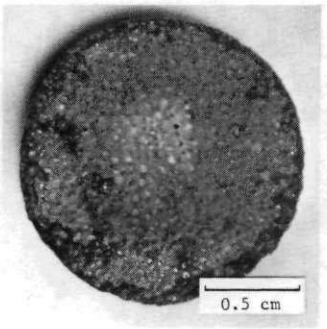

S7437-5

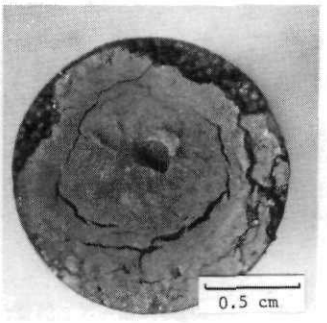

S7437-6

Fig. 9-27. Visual examination of FTE-15 fuel rod 2-5-2 (UO_2 TRISO - ThC_2 BISO). Irradiation conditions 2.3 x 25 n/m^2 $(E \geq 29\ fJ)_{HTGR}$ at ∿1339°C

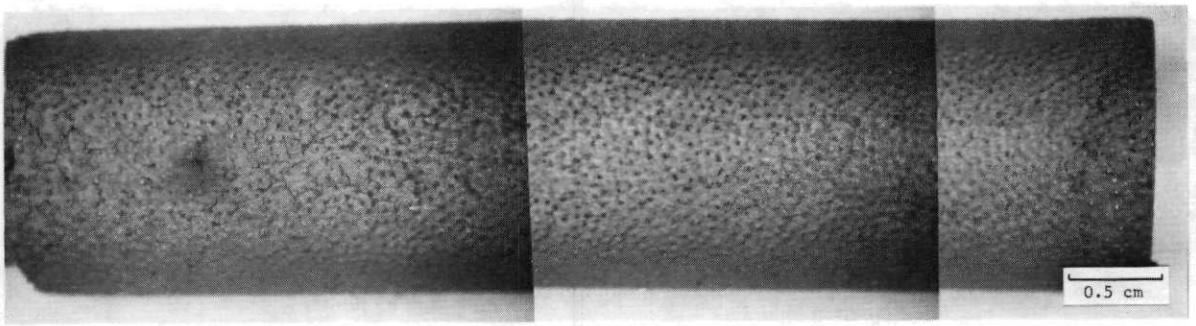

S7437 (15-17)

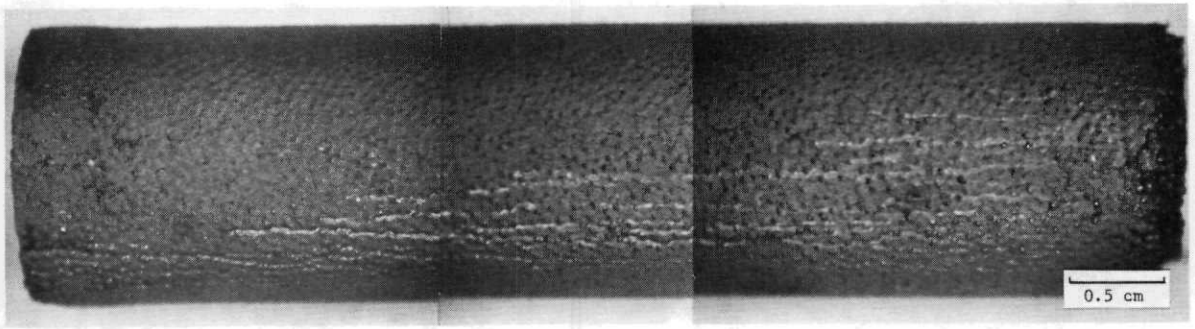

S7437 (19-21)

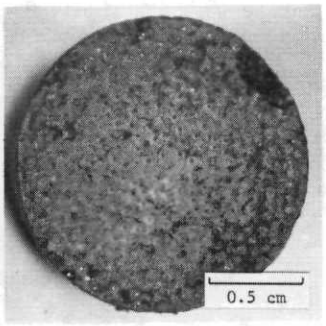

S7437-14

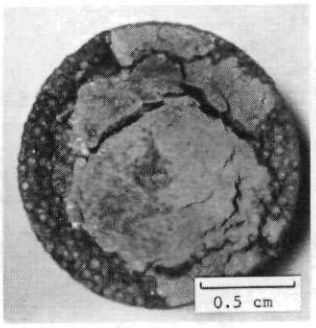

S7437-13

Fig. 9-28. Visual examination of FTE-15 fuel rod 2-6-4 (UO_2 TRISO - ThO_2 TRISO). Irradiation conditions ∿2.5 n/m^2 ($E \geq 29$ fJ)$_{HTGR}$ at ∿1467°C

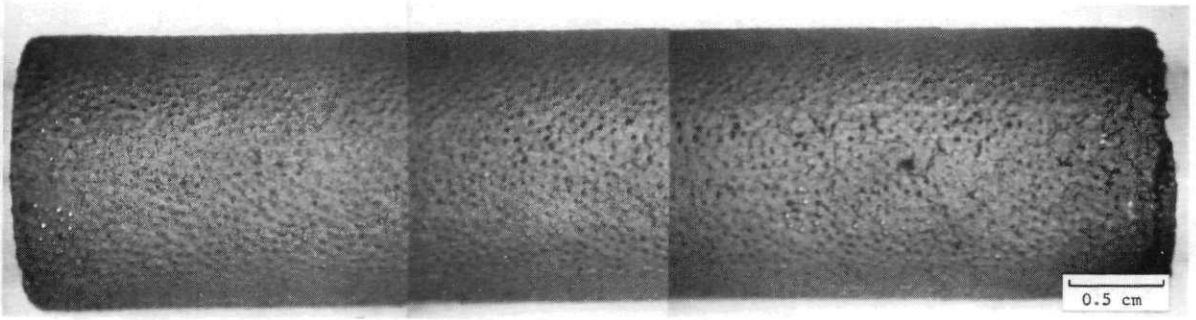

S7437 (24-26)

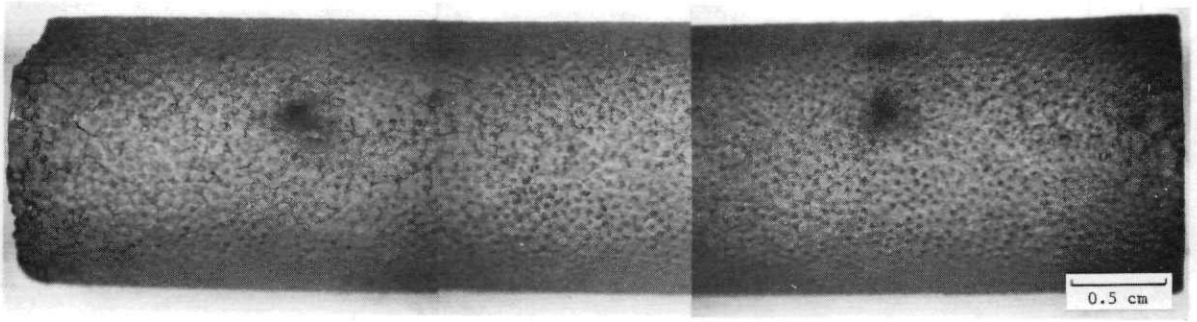

S7437 (27-29)

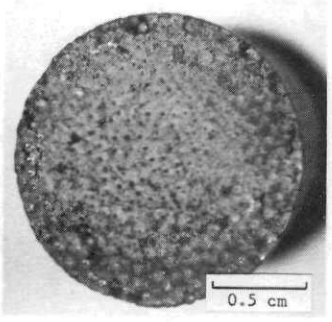

S7437-22

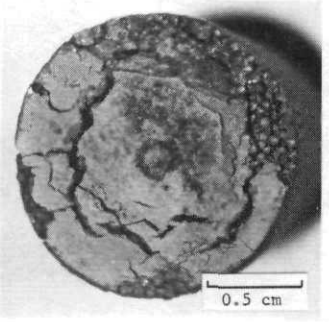

S7437-23

Fig. 9-29. Visual examination of FTE-15 fuel rod 2-6-5 (UO_2 TRISO - ThO_2 TRISO). Irradiation conditions ∿2.5 x 25 n/m^2 ($E \geq 29$ fJ)$_{HTGR}$ at ∿1516°C.

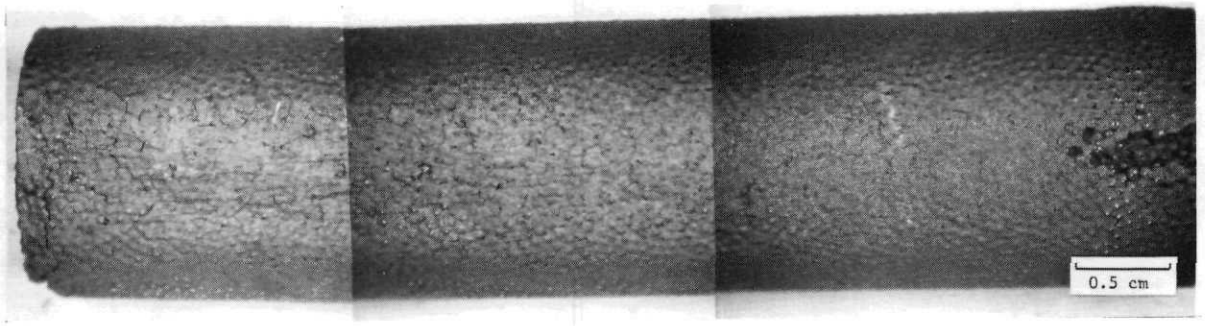

S7437 (89-91)

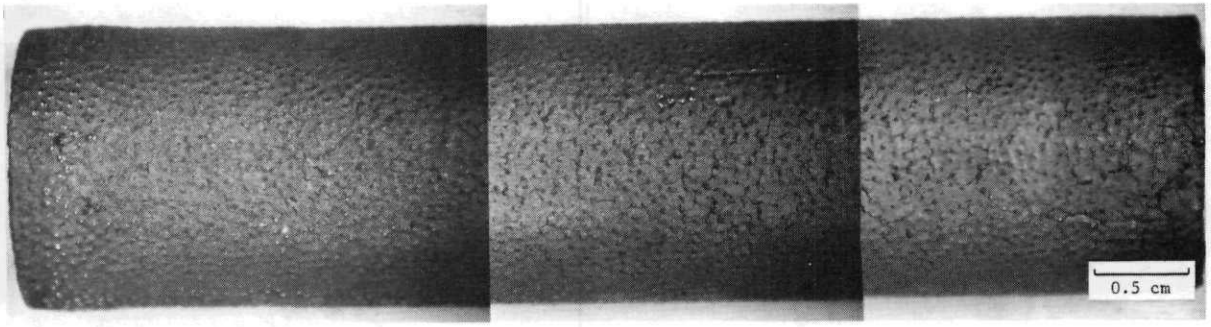

S7437 (93-95)

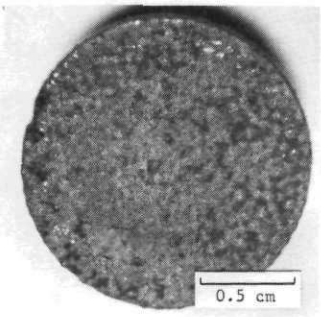

S7437-88

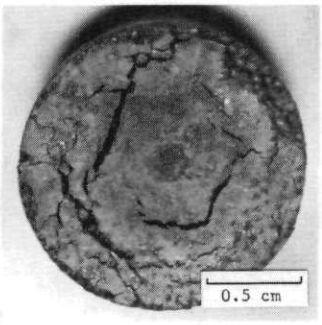

S7437-87

Fig. 9-30. Visual examination of FTE-15 fuel rod 2-6-11 (UO_2 TRISO - ThO_2 TRISO). Irradiation conditions ∿2.0 x 25 n/m^2 ($E \geq 29$ fJ)$_{HTGR}$ at ∿1217°C

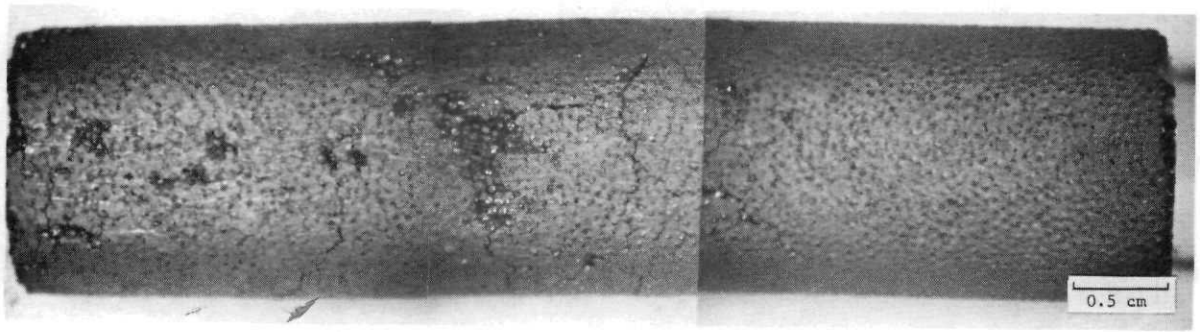

S7437 (178-180)

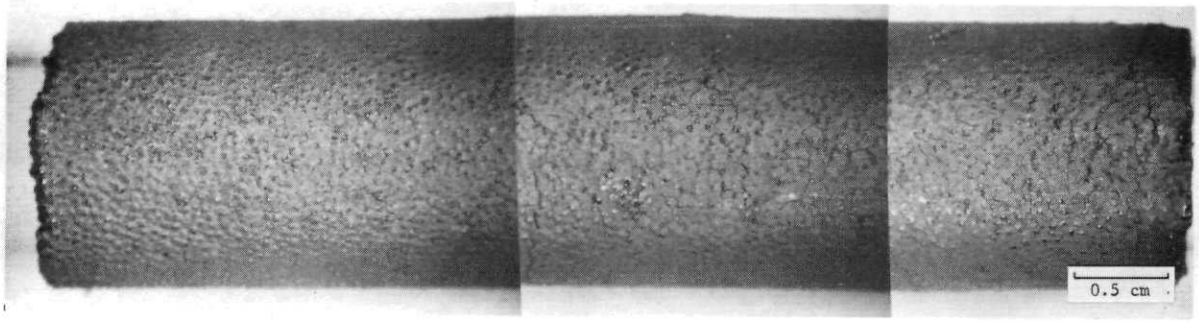

S7437 (181-183)

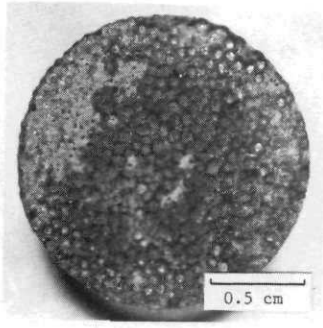

S7437-174

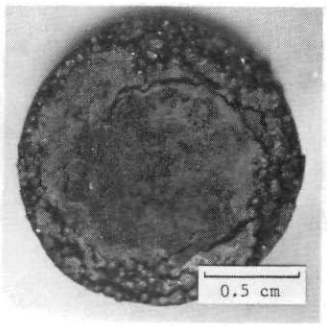

S7437-173

Fig. 9-31. Visual examination of FTE-15 fuel rod 3-2-3 (UC_2 TRISO - ThC_2 TRISO). Irradiation conditions ∿1.8 x 25 n/m^2 ($E \geq 29$ fJ)$_{HTGR}$ at ∿1294°C

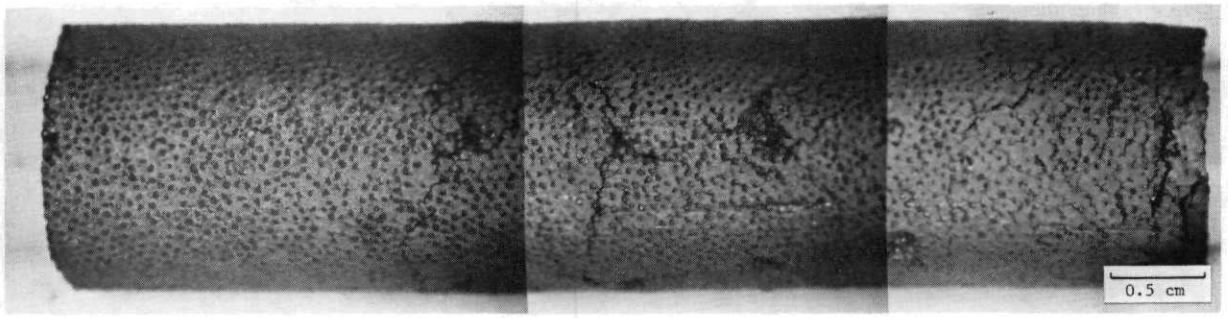

S7437 (159-161)

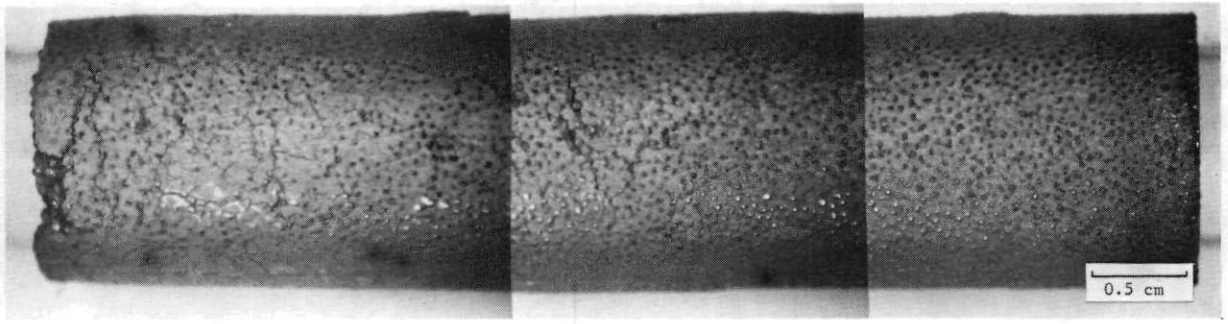

S7437 (162-164)

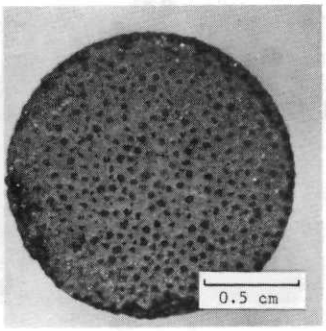

S7437-156

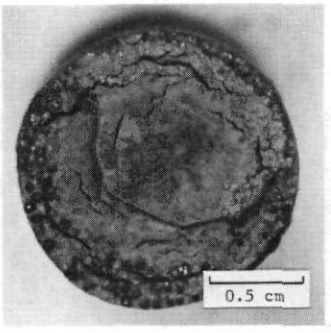

S7437-157

Fig. 9-32. Visual examination of FTE-15 fuel rod 3-2-4 (UC_2 TRISO - ThC_2 TRISO). Irradiation conditions ~1.8 x 25 n/m^2 ($E \geq 29$ fJ)$_{HTGR}$ at ~1287°C

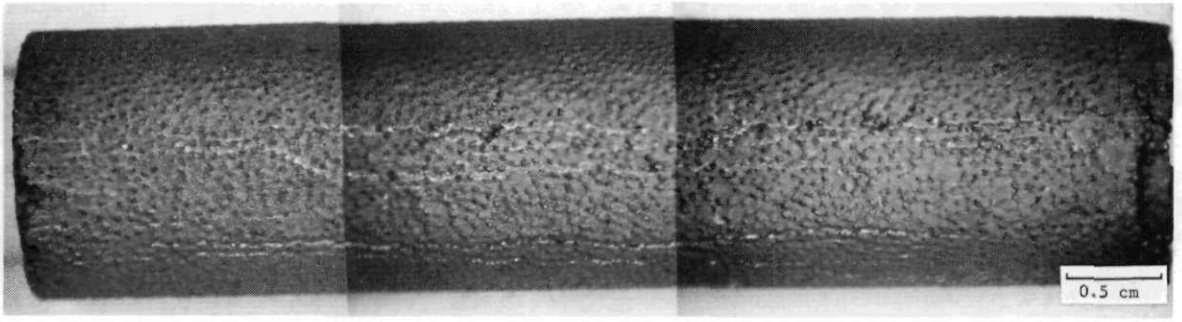

S7437 (187-189)

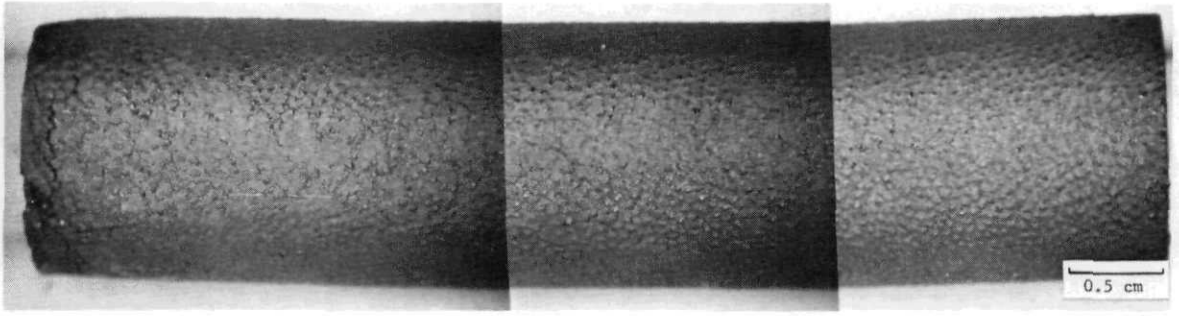

S7437 (190-192)

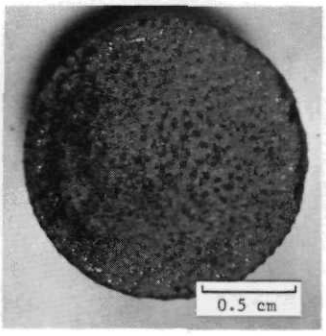

S7437-184

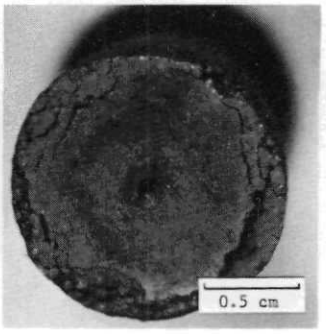

S7437-185

Fig. 9-33. Visual examination of FTE-15 fuel rod 3-3-3 (UO_2 TRISO - ThO_2 TRISO). Irradiation conditions ∿1.8 x 25 n/m^2 ($E \geq 29$ fJ)$_{HTGR}$ at ∿1294°C

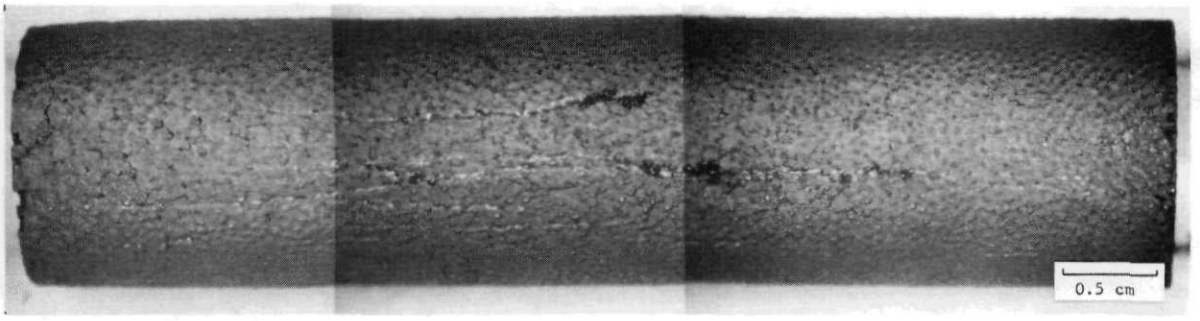

S7437 (167-169)

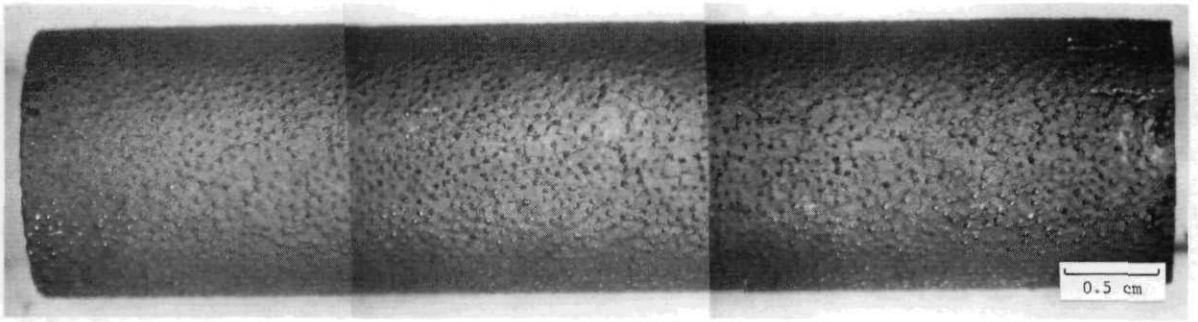

S7437 (170-172)

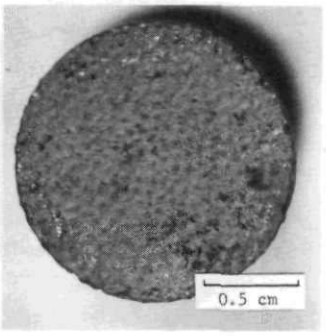

S7437-166

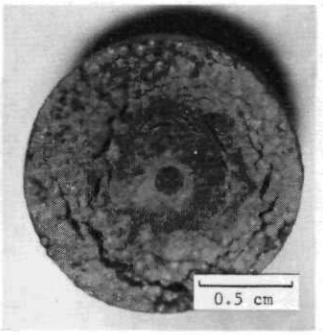

S7437-165

Fig. 9-34. Visual examination of FTE-15 fuel rod 3-3-4 (UO_2 TRISO - ThO_2 TRISO). Irradiation conditions ∿1.8 x 25 n/m^2 $(E \geq 29\ fJ)_{HTGR}$ at ∿1287°C

L7437-99 (a)

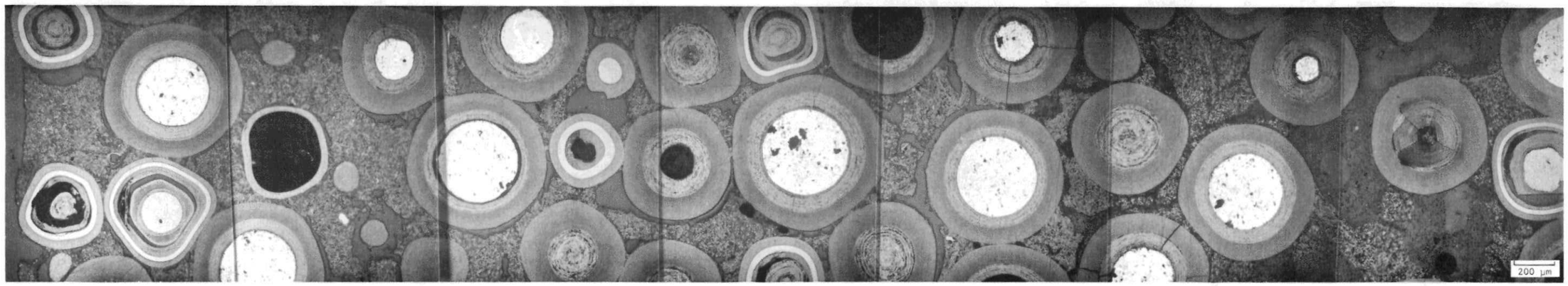

L7437 (87-93) (b)

Fig. 9-35. Photomicrograph of FTE-15 fuel rod 2-1-5 (UC_2 TRISO - ThC_2 BISO blend). Irradiation conditions $\sim 2.5 \times 10^{25}$ n/m^2 (E > 29 fJ)$_{HTGR}$ at 1516°C. (a) typical graphite matrix and (b) composite radial cross section.

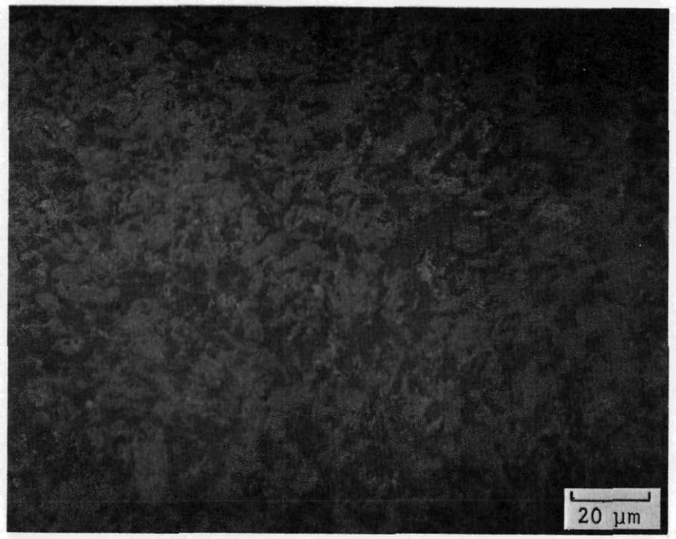

L7437-183 (a)

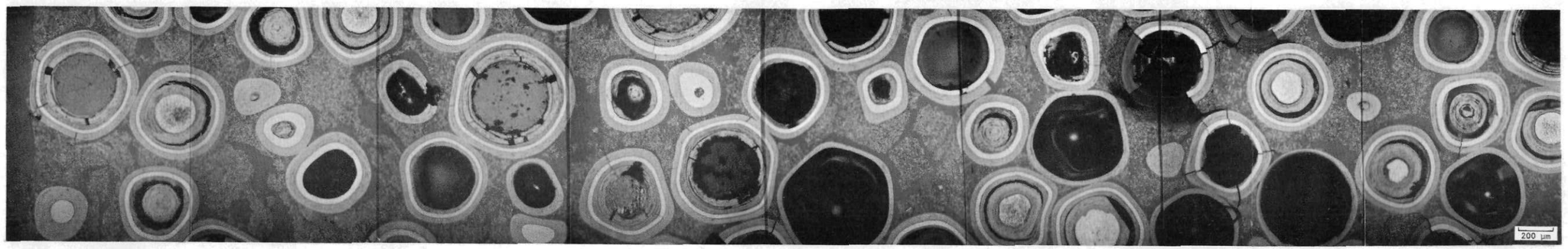

L7437 (174-181) (b)

Fig. 9-36. Photomicrograph of FTE-15 fuel rod 2-2-5 (UC_2 TRISO - ThC_2 TRISO blend). Irradiation conditions ∿2.5 x 10^{25} n/m^2 $(E > 29\ fJ)_{HTGR}$ at 1516°C. (a) typical graphite matrix and (b) composite radial cross section.

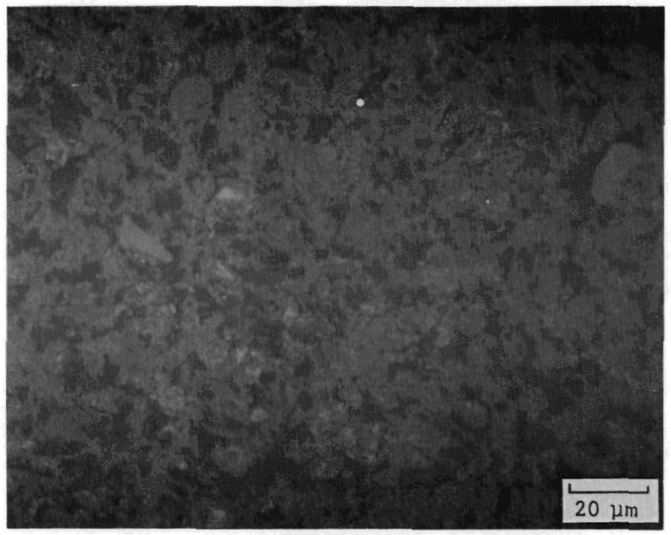

L7437-109 (a)

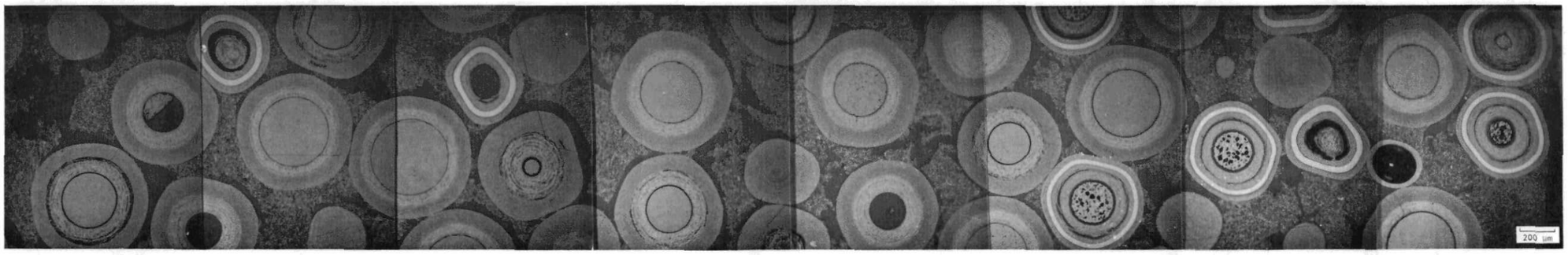

L7437 (110-117) (b)

Fig. 9-37. Photomicrograph of FTE-15 fuel rod 2-3-9 (UO_2 TRISO - ThO_2 BISO blend). Irradiation conditions $\sim 2.4 \times 10^{25}$ n/m^2 $(E > 29\ fJ)_{HTGR}$ at 1408°C. (a) typical graphite matrix and (b) composite radial cross section.

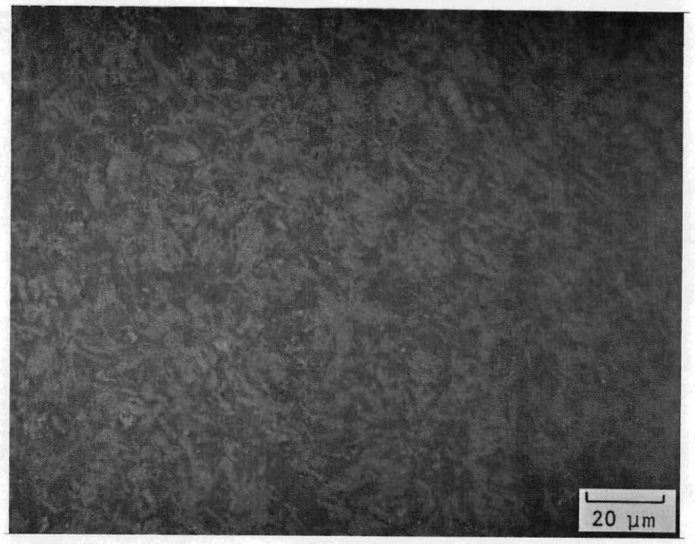

L7437-159

(a)

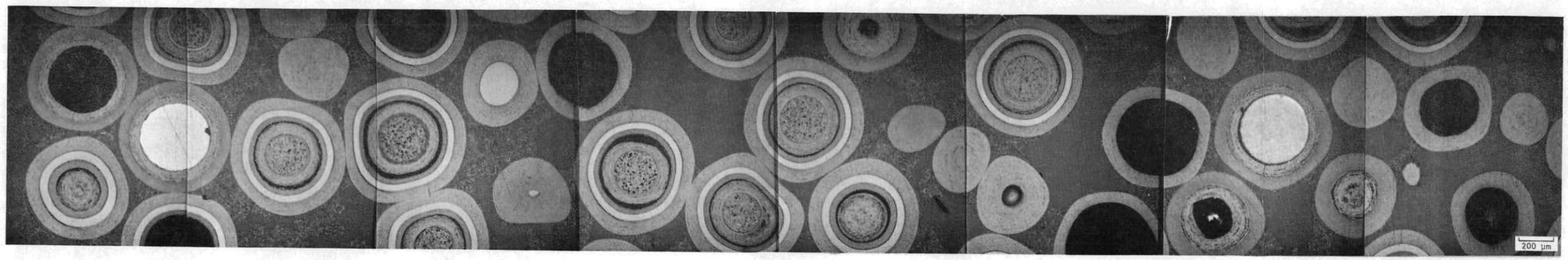

L7437 (148-155)

(b)

Fig. 9-38. Photomicrograph of FTE-15 fuel rod 2-4-3 $(Th,U)O_2$ TRISO - ThC_2 BISO blend). Irradiation conditions $\sim 2.4 \times 10^{25}$ n/m^2 (E > 29 fJ)$_{HTGR}$ at 1373°C. (a) typical graphite matrix and (b) composite radial cross section.

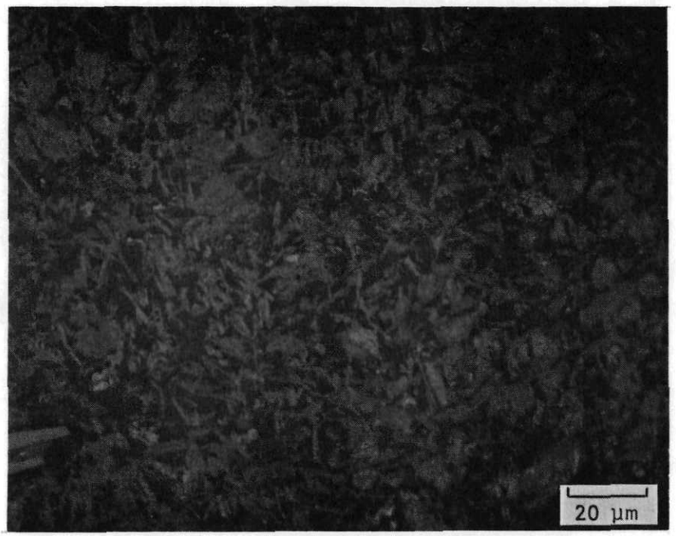

L7437-194 (a)

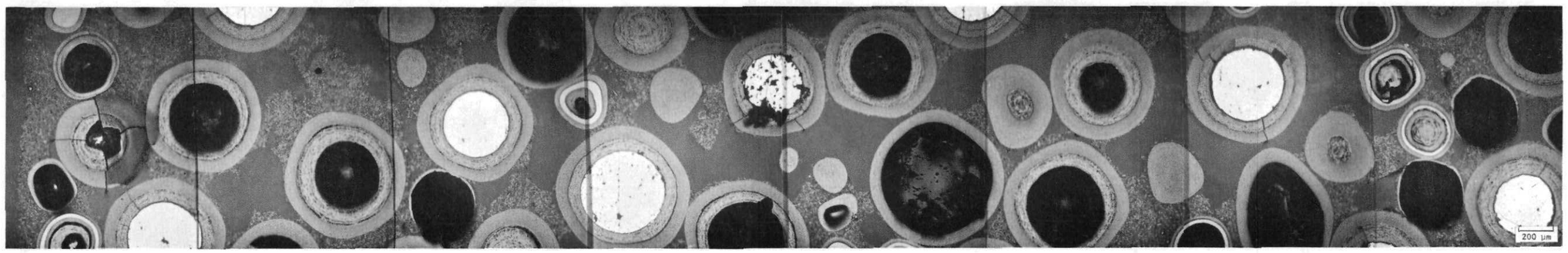

L7437 (197-204) (b)

Fig. 9-39. Photomicrograph of FTE-15 fuel rod 2-5-2 (UO_2 TRISO - ThC_2 BISO blend). Irradiation conditions $\sim 2.4 \times 10^{25}$ n/m^2 (E > 29 fJ)$_{HTGR}$ at 1339°C. (a) typical graphite matrix and (b) composite radial cross section.

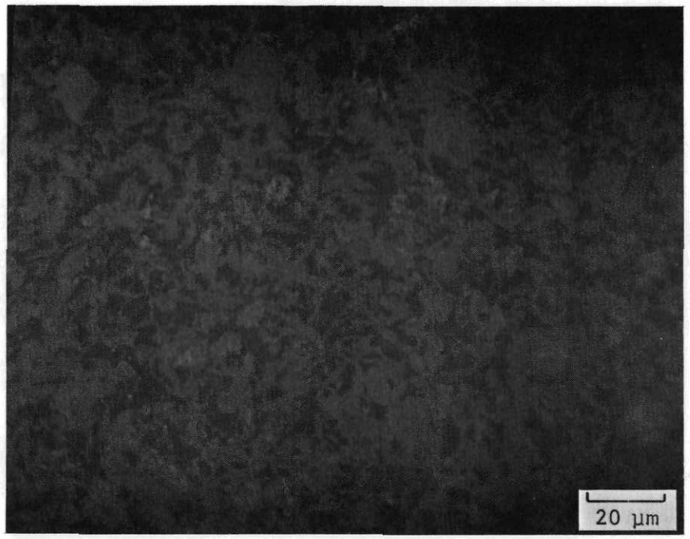

L7437-140 (a)

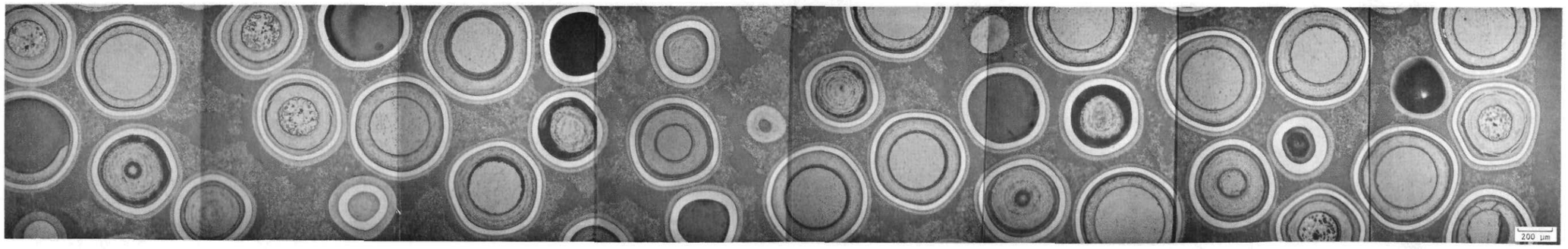

L7437 (127-134) (b)

Fig. 9-40. Photomicrograph of FTE-15 fuel rod 2-6-5 ($\overline{UO_2}$ TRISO - ThO_2 TRISO blend). Irradiation conditions $\sim 2.5 \times 10^{25}$ n/m^2 (E > 29 fJ)$_{HTGR}$ at 1516°C. (a) typical graphite matrix and (b) composite radial cross section.

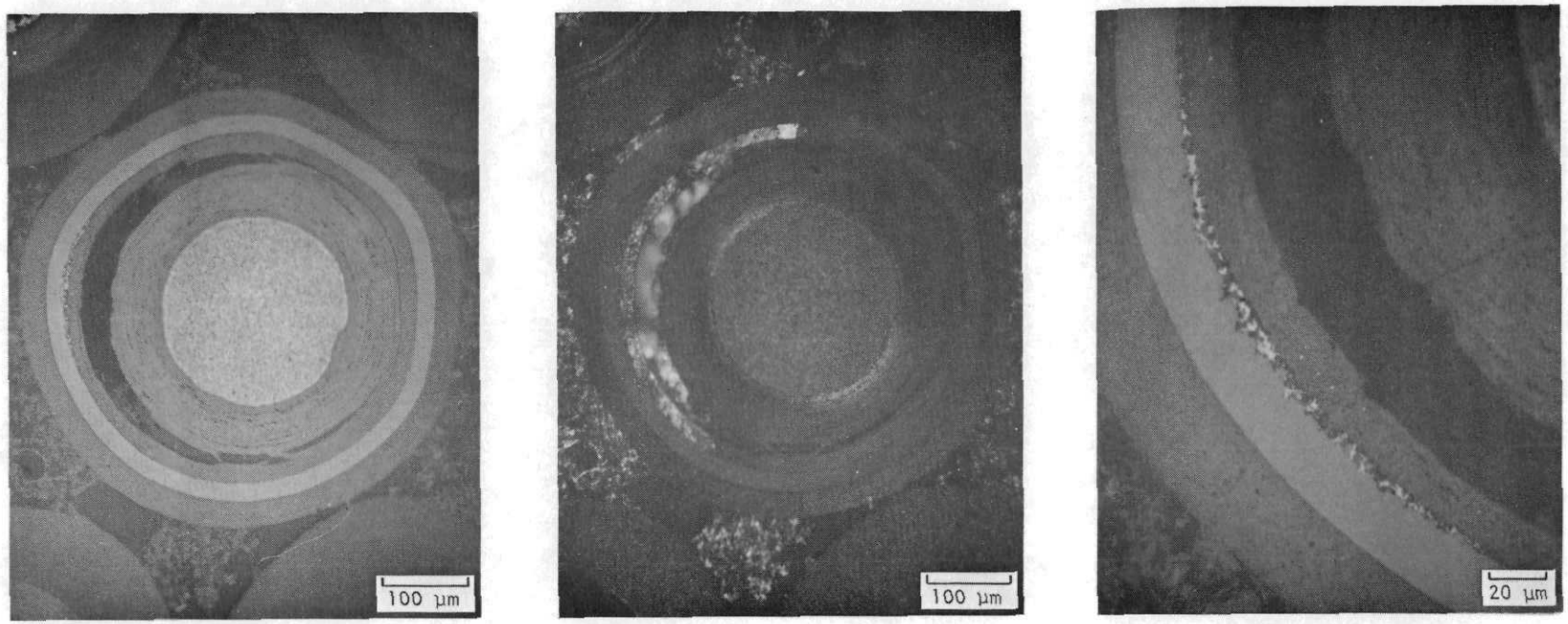

L7437-84 (a) L7437-85 (b) L7437-86 (c)

Fig. 9-41. Photomicrographs of representative fissile UC_2 particle from FTE-15 fuel rod 2-1-5 showing SiC attack. Irradiation conditions $\sim 2.5 \times 10^{25}$ n/m^2 $(E \geq 29 \text{ fJ})_{HTGR}$ at 1516°C. (a) bright field, (b) dark field showing concentration of metallic fission products at SiC - OPyC interface, and (c) high magnification of SiC attack.

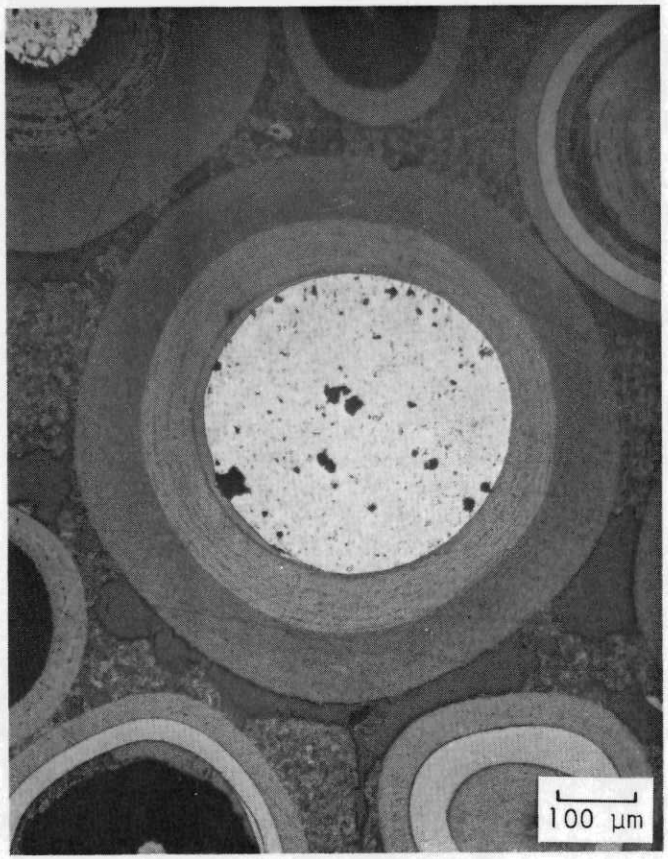

L7437-81 (a)

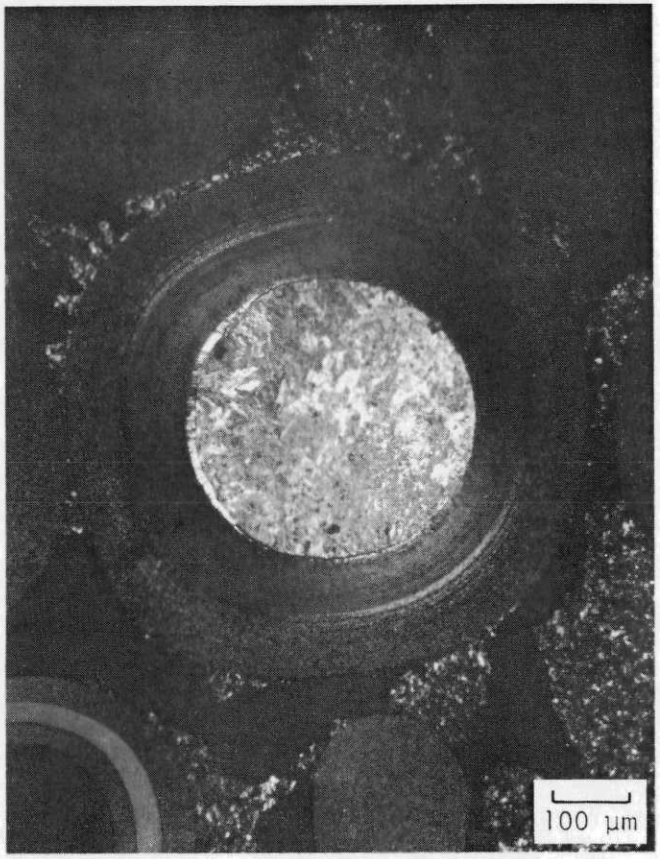

L7437-78 (b)

Fig. 9-42. Photomicrographs of representative fertile ThC_2 BISO particle from FTE-15 fuel rod 2-1-5 showing kernel migration. Irradiation conditions $\sim 2.5 \times 10^{25}$ n/m^2 $(E \geq 29 \text{ fJ})_{HTGR}$ at 1516°C. (a) light field, (b) dark field - kernel migrating twoard center of rod. Particle location ~5 particle diameters from side of rod.

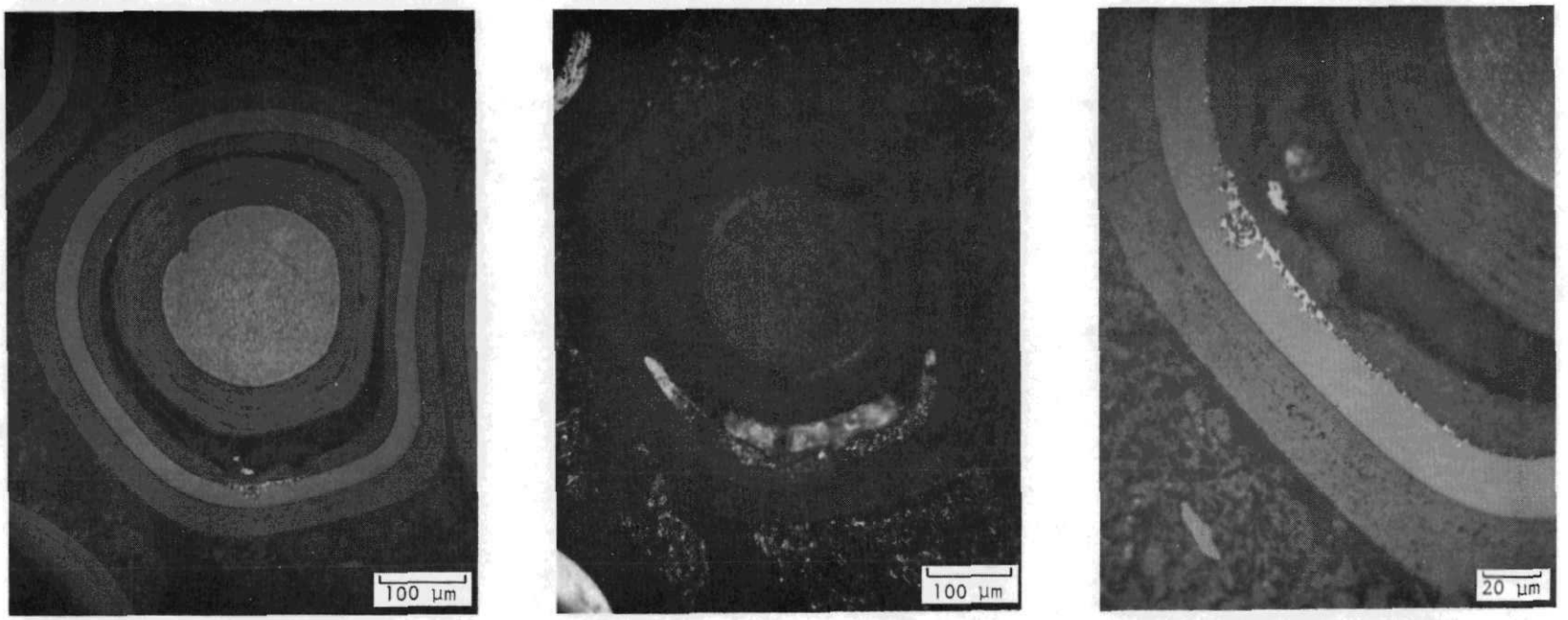

L7437-163 (a) L7437-164 (b) L7437-165 (c)

Fig. 9-43. Photomicrographs of representative fissile UC_2 TRISO particle in FTE-15 fuel rod 2-2-5 showing SiC attack. Irradiation conditions $\sim 2.5 \times 10^{25}$ n/m^2 $(E \geq 29 \text{ fJ})_{HTGR}$ at 1516°C. (a) bright field, (b) dark field showing metallic fission product concentration in IPyC, and (c) high magnification of SiC attack.

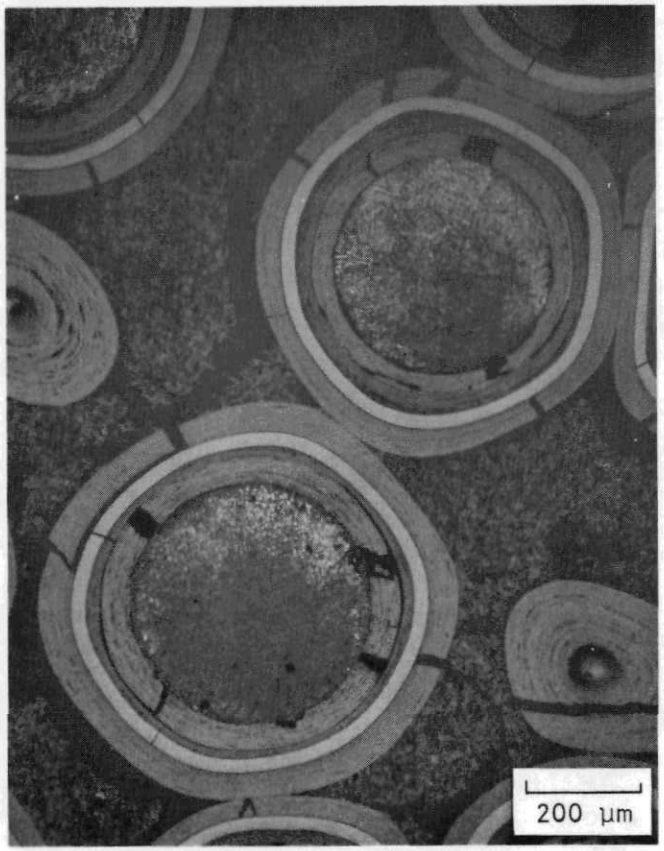

L7437-166 (a)

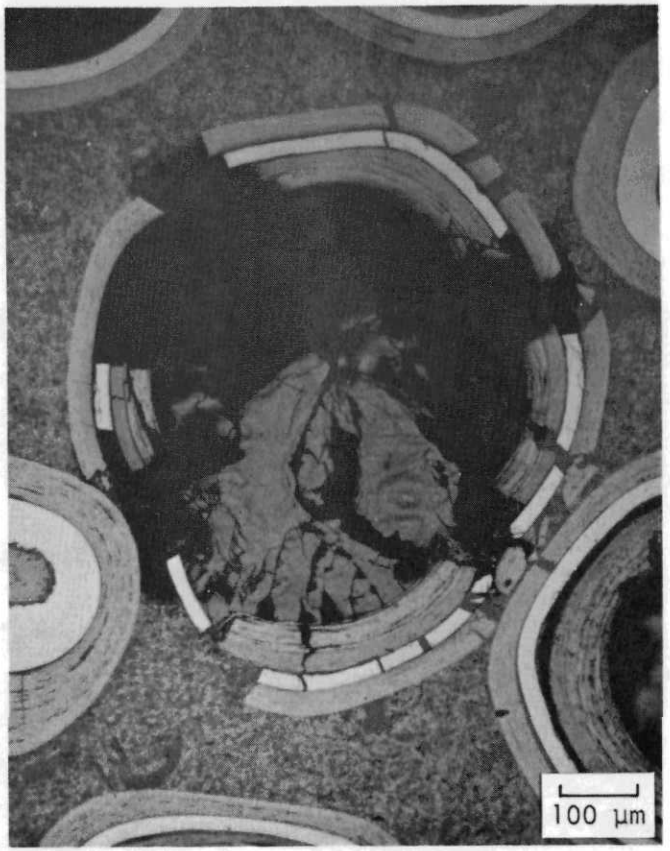

L7437-173 (b)

Fig. 9-44. Photomicrographs of fertile ThC_2 TRISO particles in FTE-15 fuel rod 2-2-5. Irradiation conditions $\sim 2.5 \times 10^{25}$ n/m^2 $(E \geq 29\ fJ)_{HTGR}$ at 1516°C. (a) ThC_2 TRISO pair showing OPyC failure and (b) production ThC_2 TRISO failure.

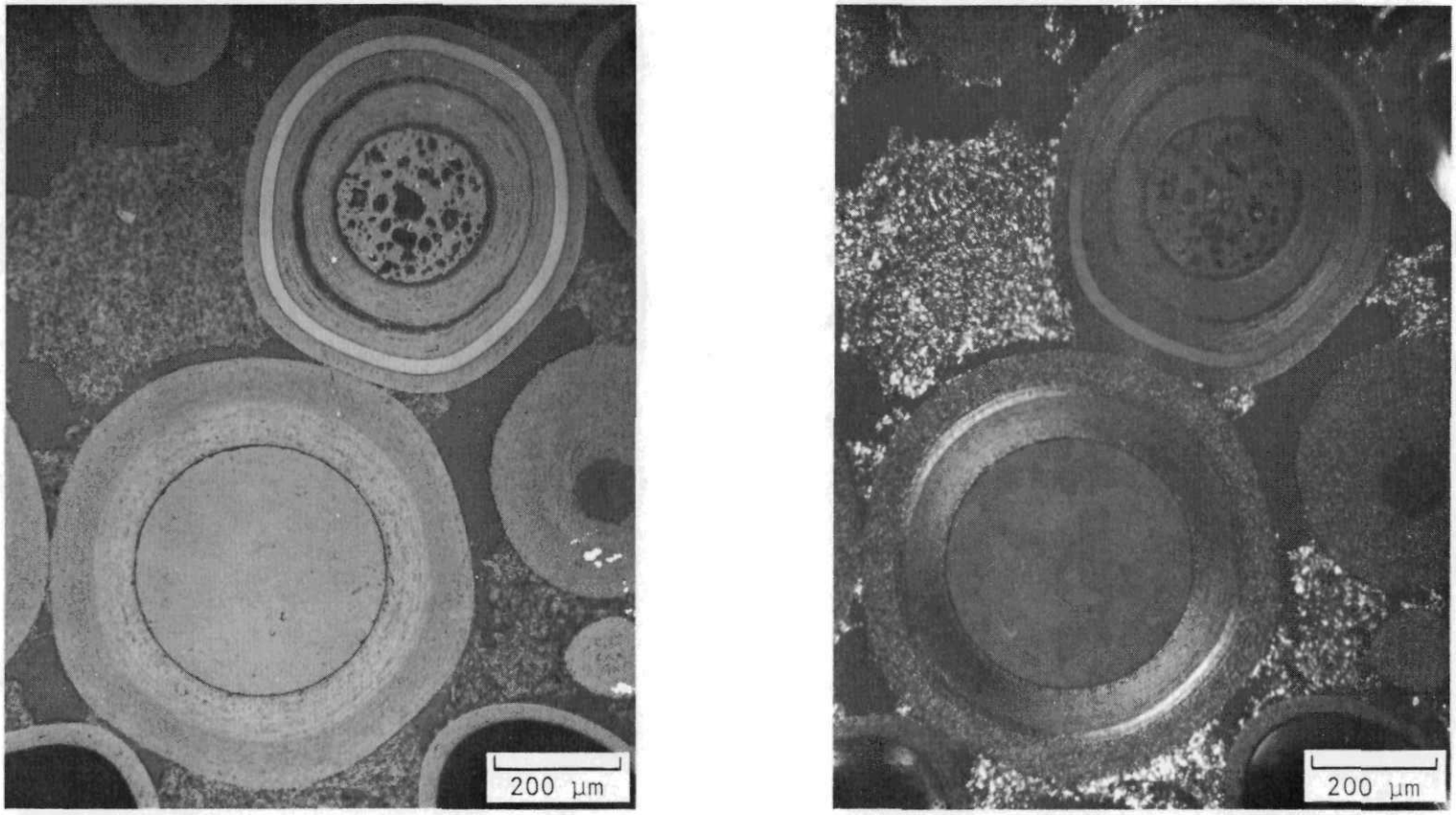

L7437-104 (a) L7437-105 (b)

Fig. 9-45. Photomicrographs of representative fissile UO_2 and fertile ThO_2 pair from FTE-15 fuel rod 2-3-9. Irradiation conditions $\sim 2.4 \times 10^{25}$ n/m^2 $(E \geq 29\ fJ)_{HTGR}$ at 1408°C. (a) bright field and (b) dark field.

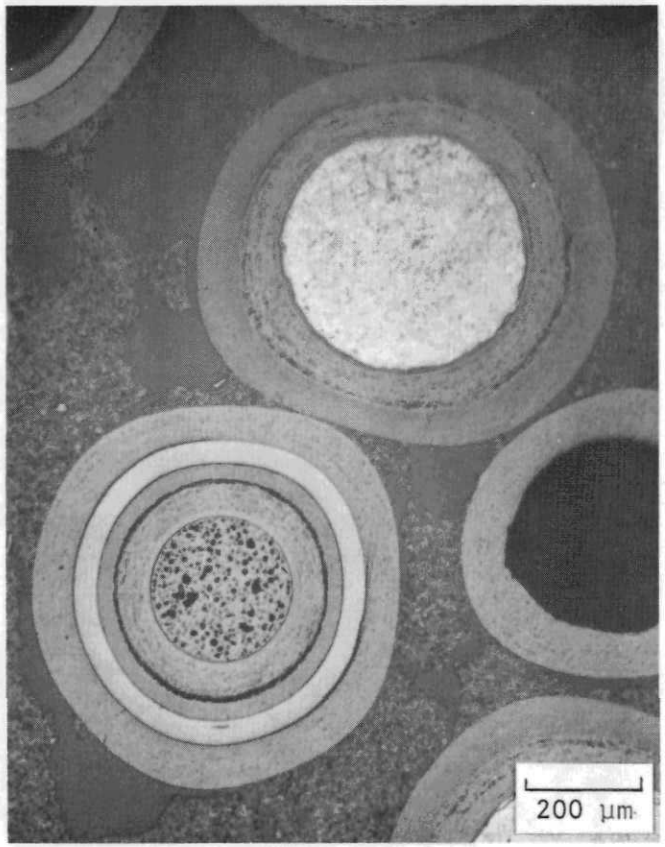

L7437-146 (a)

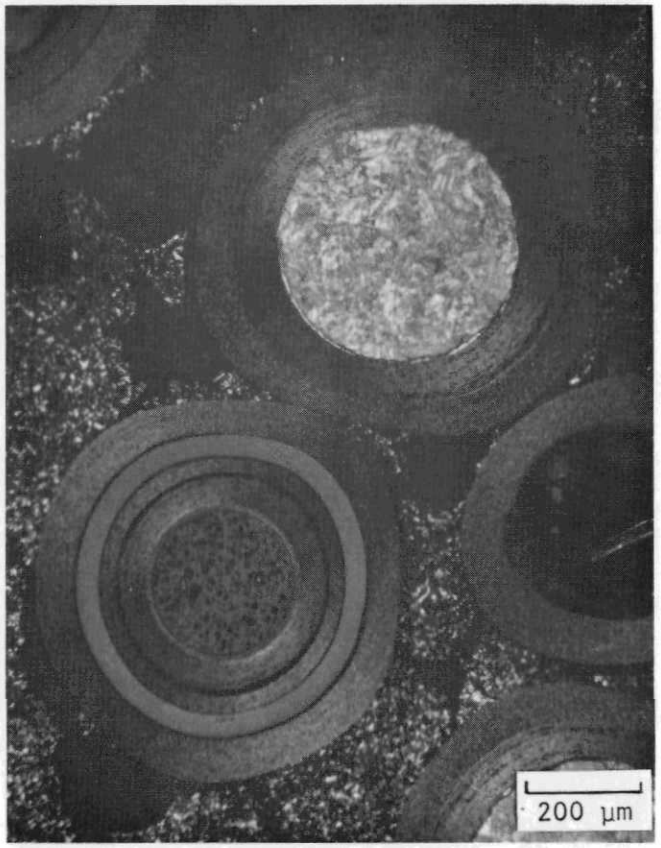

L7437-147 (b)

Fig. 9-46. Photomicrographs of representative $(Th,U)O_2$ TRISO fissile and ThC_2 BISO fuel particles from FTE-15 fuel rod 2-4-3. Irradiation conditions $\sim 2.4 \times 10^{25}$ n/m^2 $(E \geq 29 \text{ fJ})_{HTGR}$ at 1373°C. (a) bright field and (b) dark field.

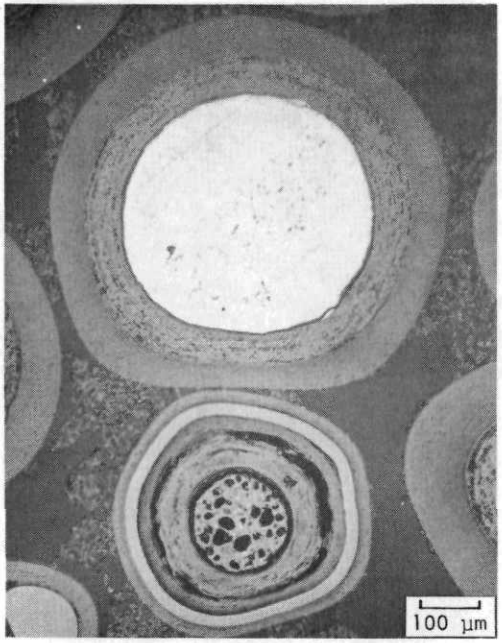

L7437-184 (a)

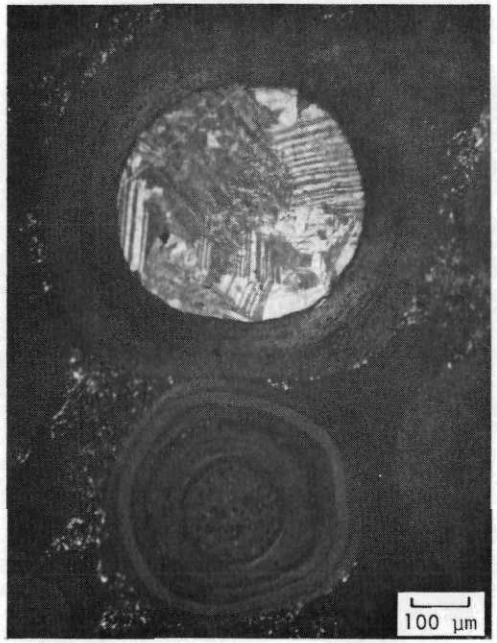

L7437-185 (b)

L7437-192 (c)

Fig. 9-47. Photomicrographs of representative UO_2 fissile and ThC_2 fertile particles from FTE-15 fuel rod 2-5-2. Irradiation conditions 2.4×10^{25} n/m^2 $(E \geq 29 \text{ fJ})_{HTGR}$ at 1339°C. (a) bright field, (b) dark field, and (c) ThC_2 production failure.

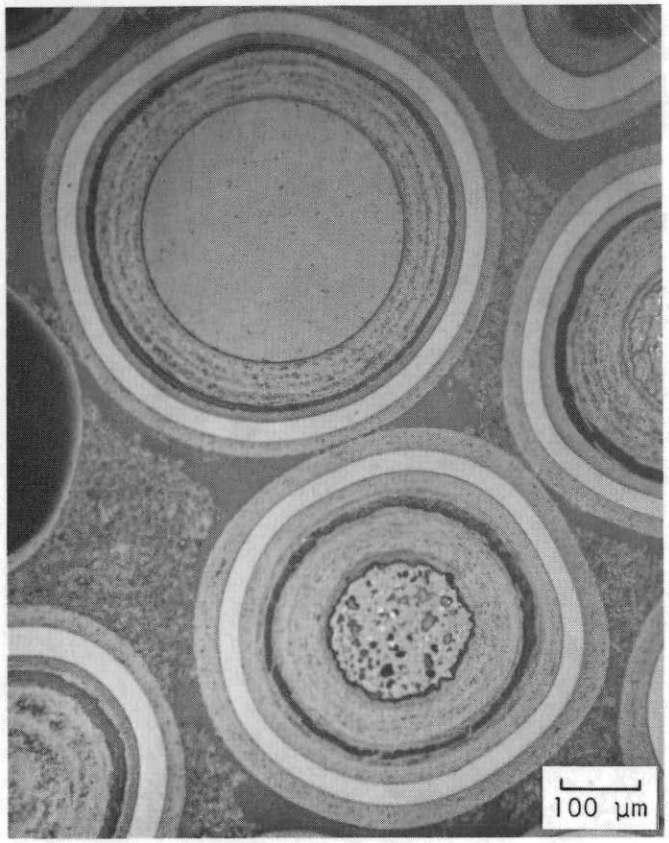

L7437-135 (a)

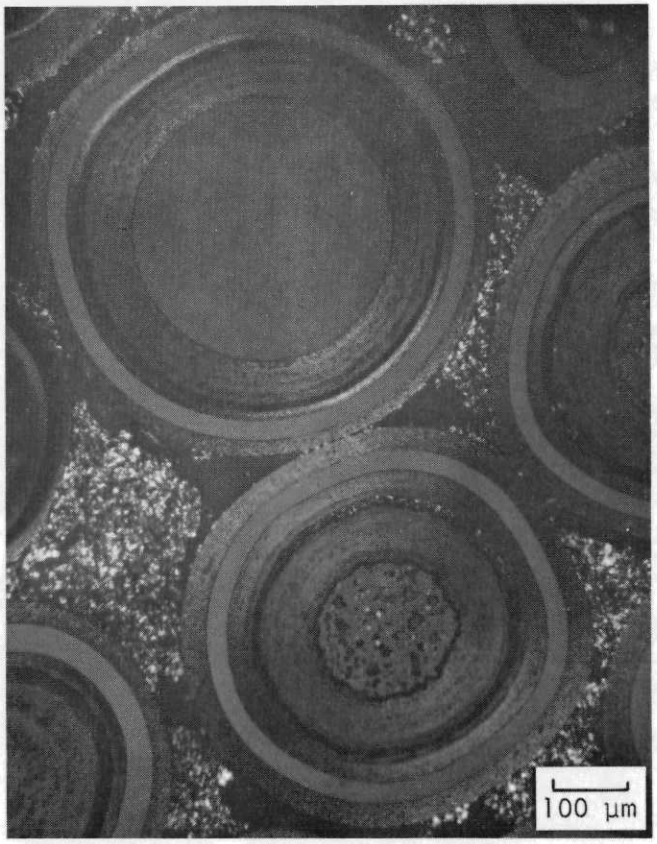

L7437-136 (b)

Fig. 9-48. Photomicrographs of representative fertile ThO_2 TRISO and fissile UO_2 TRISO fuel particles from FTE-15 fuel rod 2-6-5. Irradiation conditions 2.5 x 10^{25} n/m^2 $(E \geq 29\ fJ)_{HTGR}$ at 1516°C. (a) light field and (b) dark field.

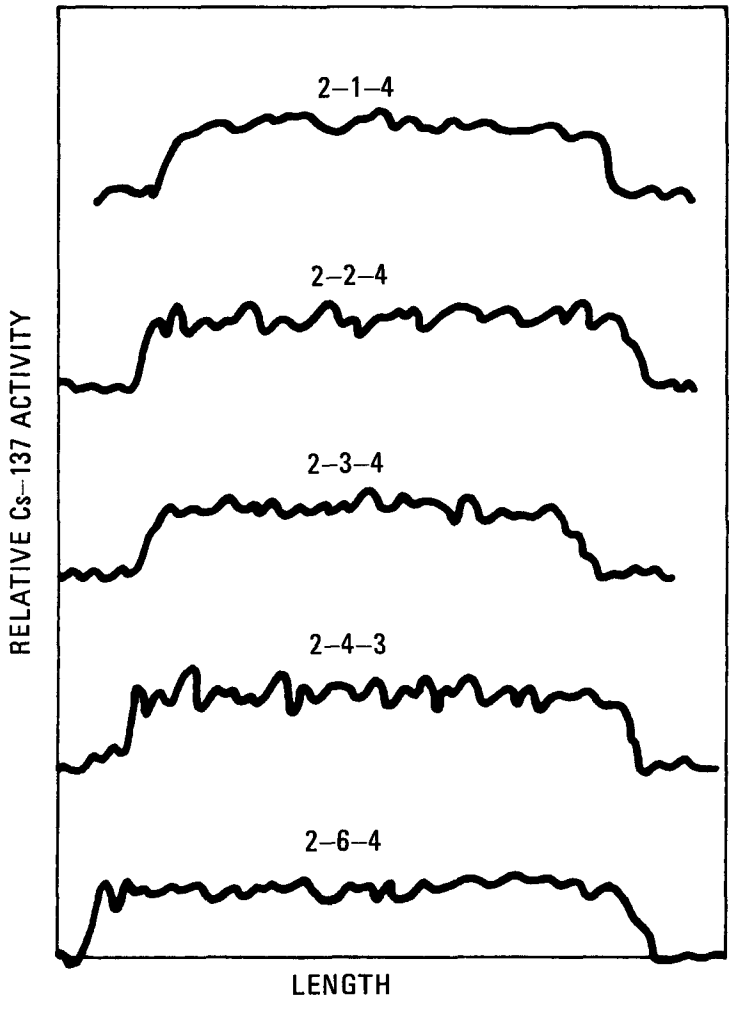

Fig. 9-49. FTE-15 single-channel gamma scans of representative fuel rods used in the fuel examination

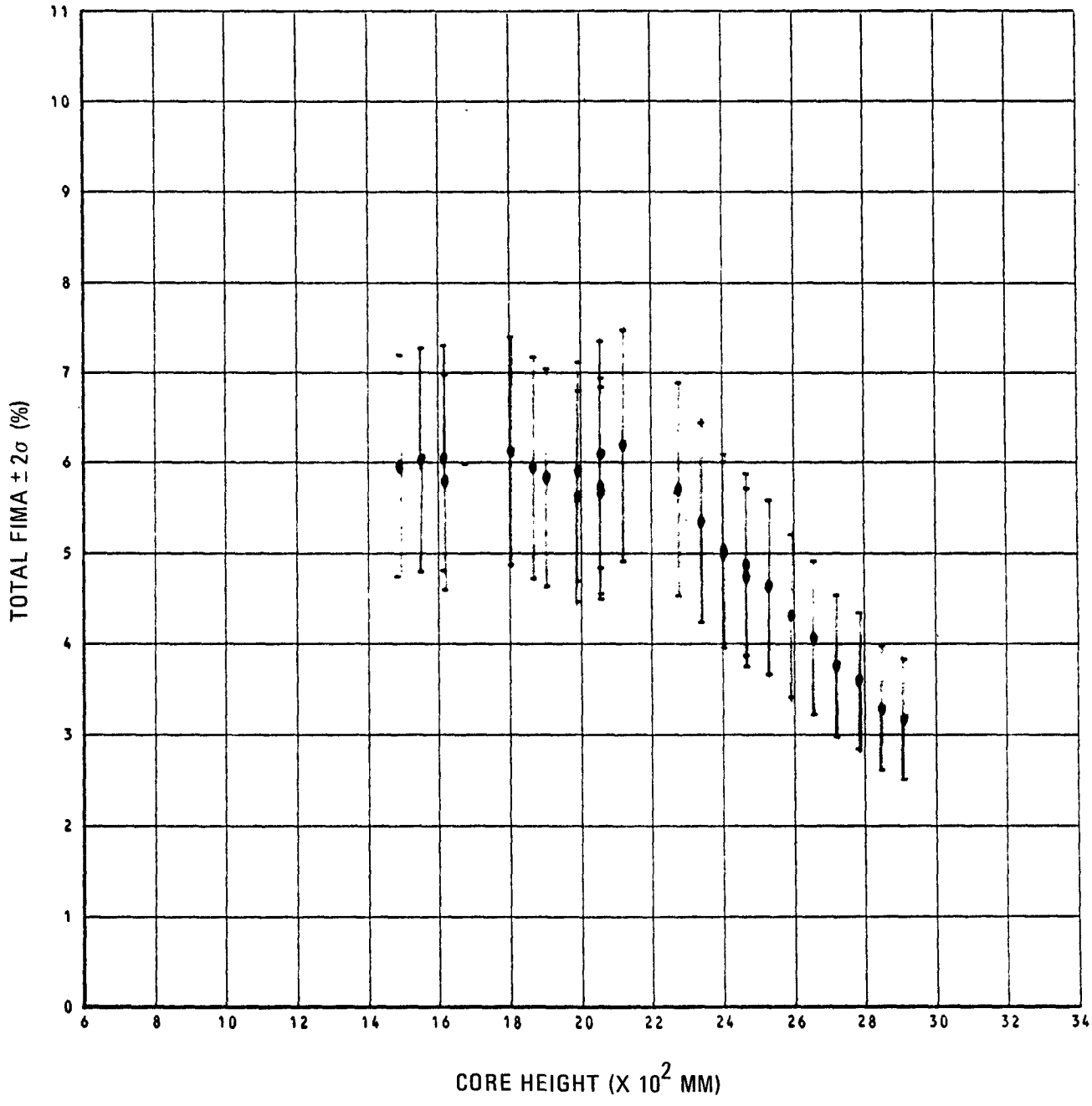

Fig. 9-50. Gamma-spectroscopy-measured total FIMA in fuel stacks having BOL Th/U ratios of 6.33 to 6.60

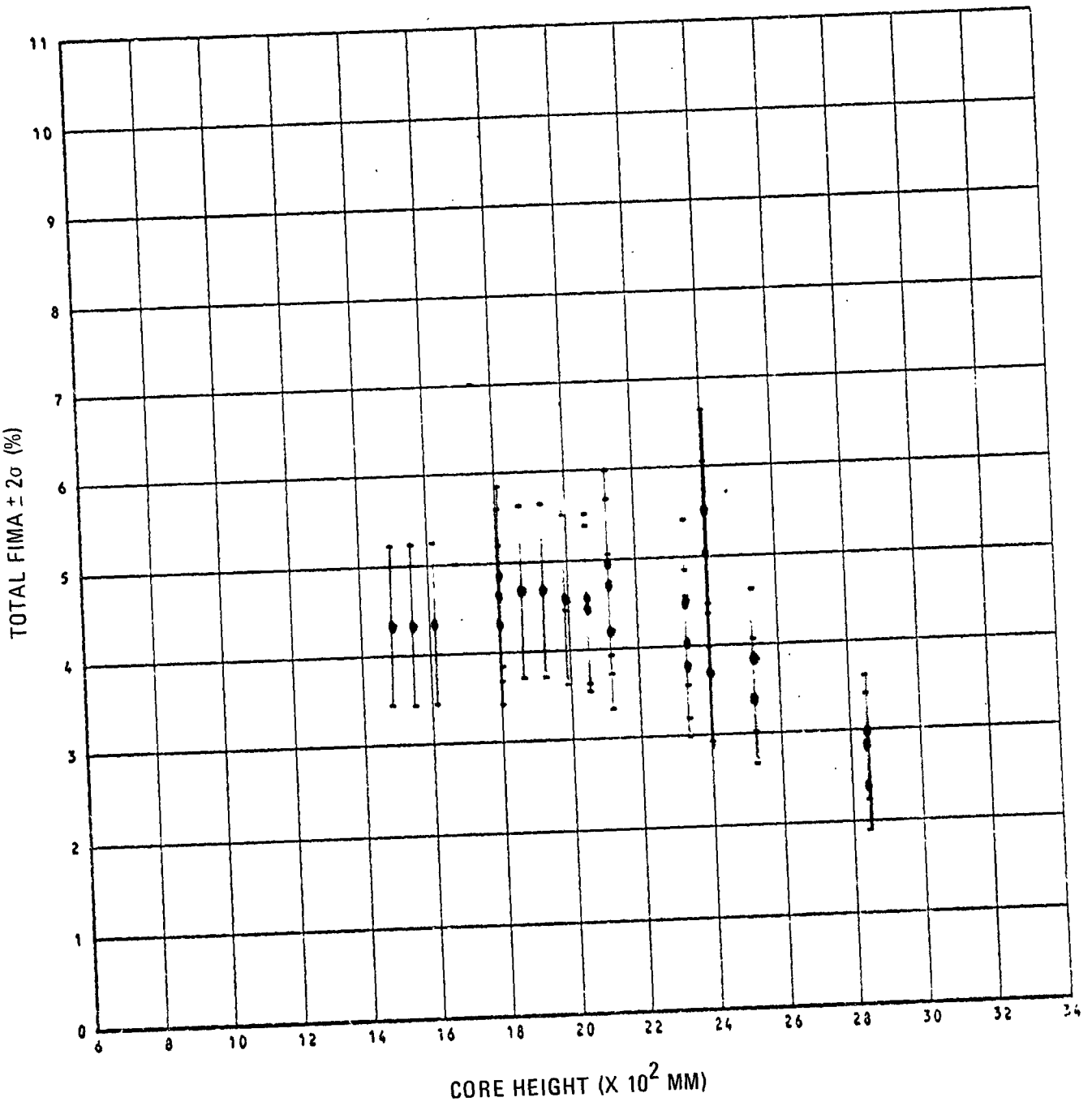

Fig. 9-51. Gamma-spectroscopy-measured total FIMA in fuel stacks having BOL Th/U ratios of 7.82-8.94

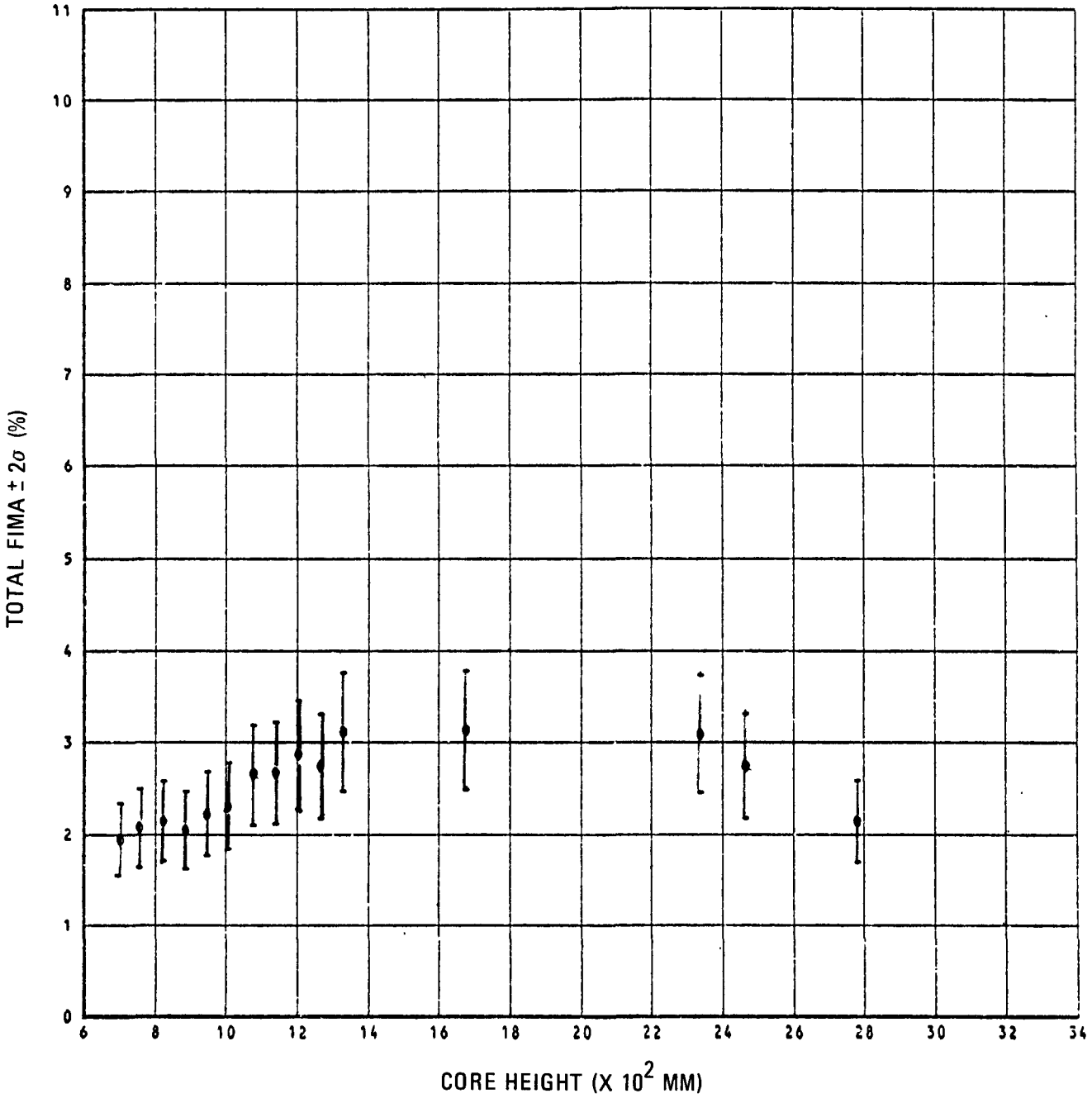

Fig. 9-52. Gamma-spectroscopy-measured total FIMA in fuel stacks having BOL Th/U ratios of 12.03-13.82

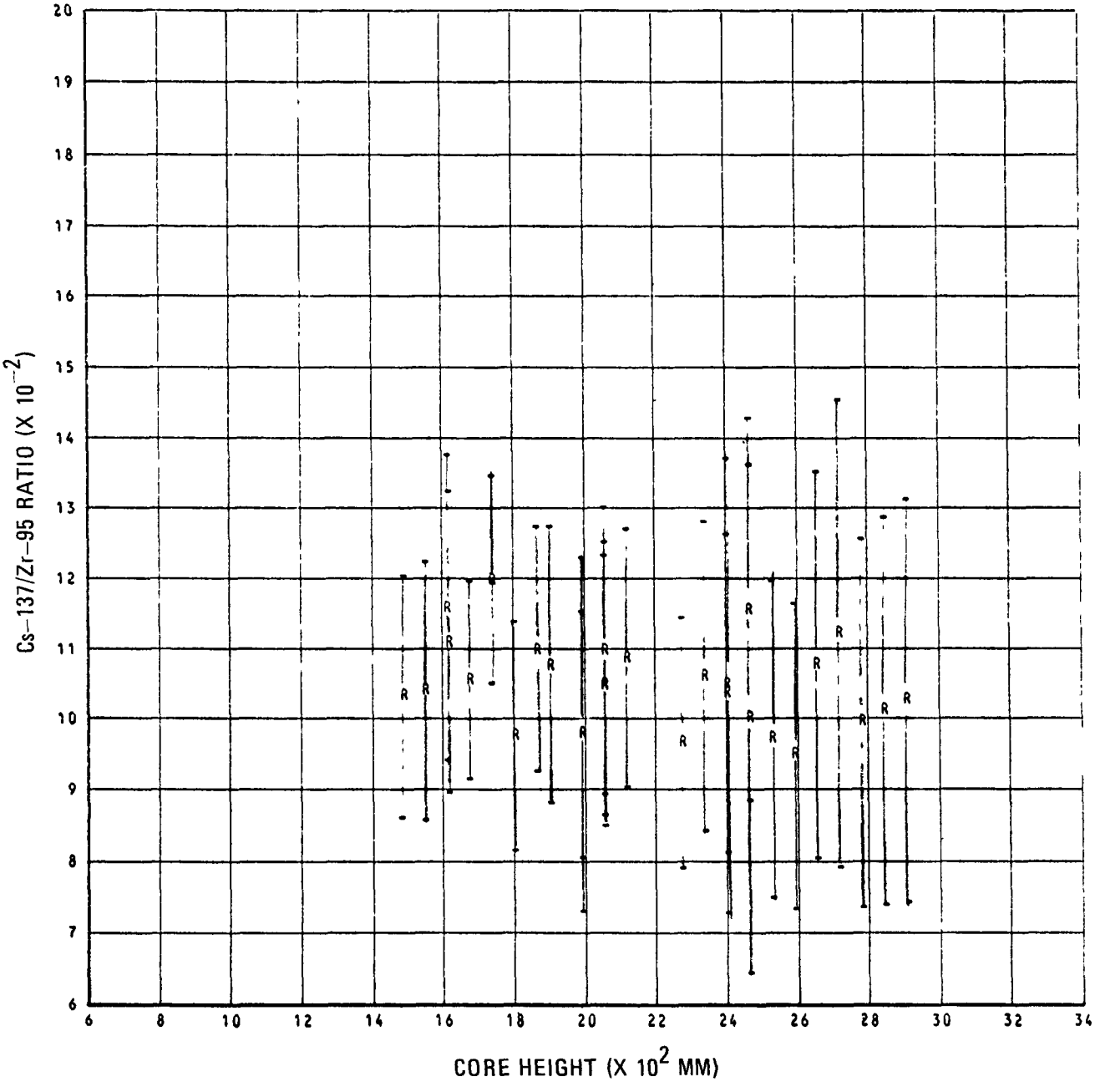

Fig. 9-53. CS-137/Zr-95 ratio for fuel rods having BOL Th/U ratios of 6.33 to 6.60

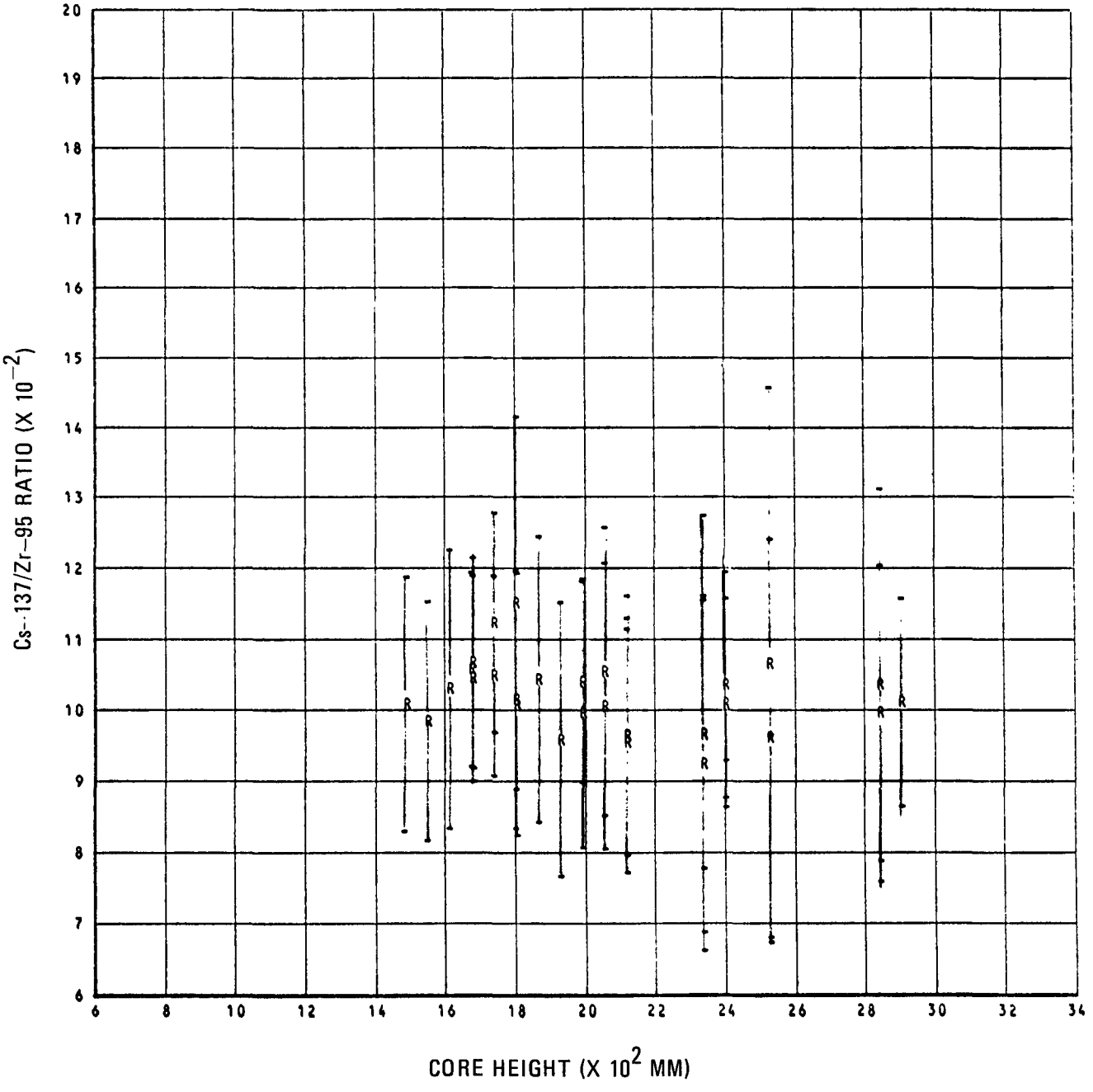

Fig. 9-54. Cs-137/Zr-95 ratio for fuel rods having BOL Th/U ratios of 7.82-8.94

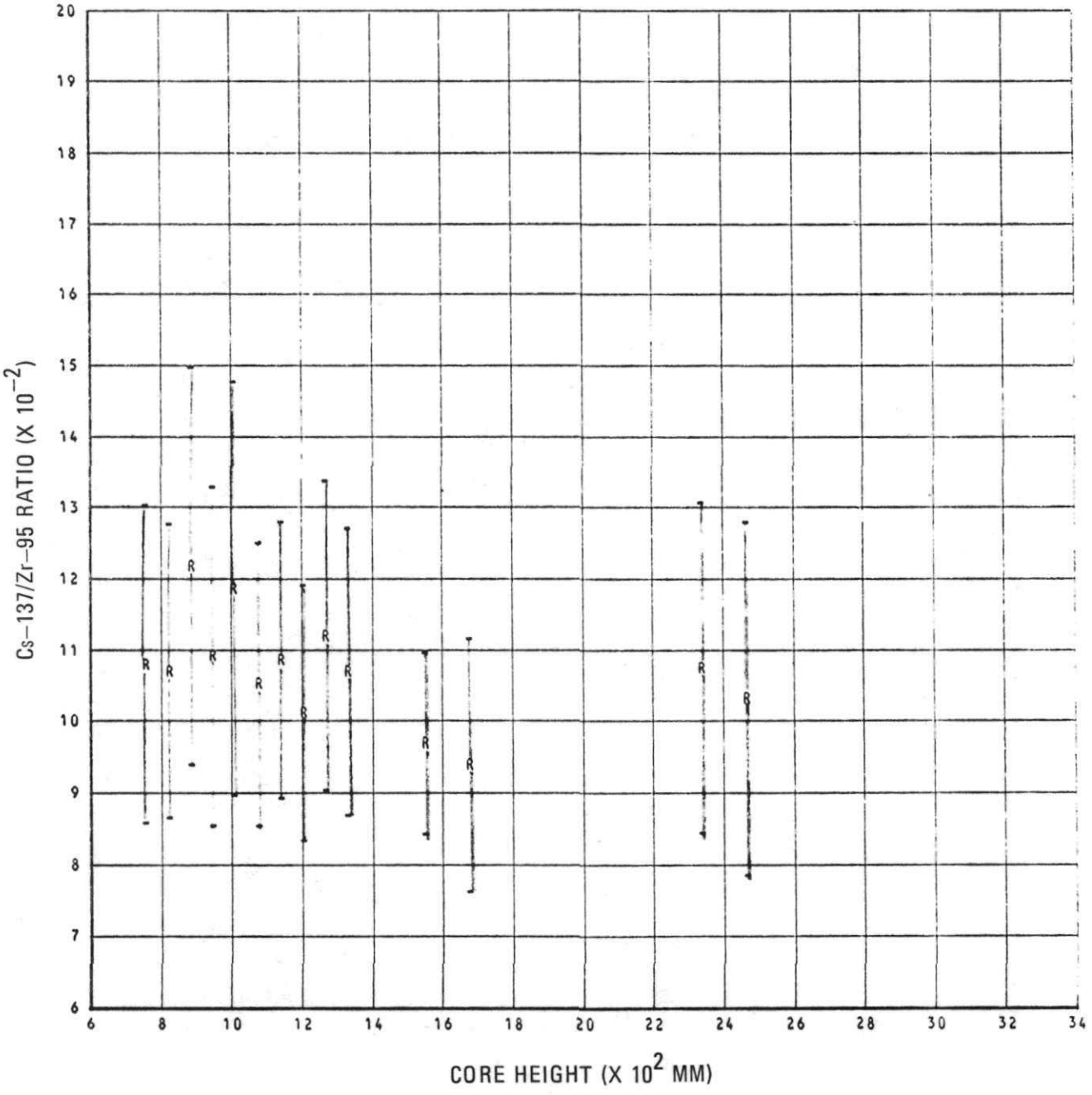

Fig. 9-55. Cs-137/Zr-95 ratio for fuel rods having BOL Th/U ratios of 12.03-13.82

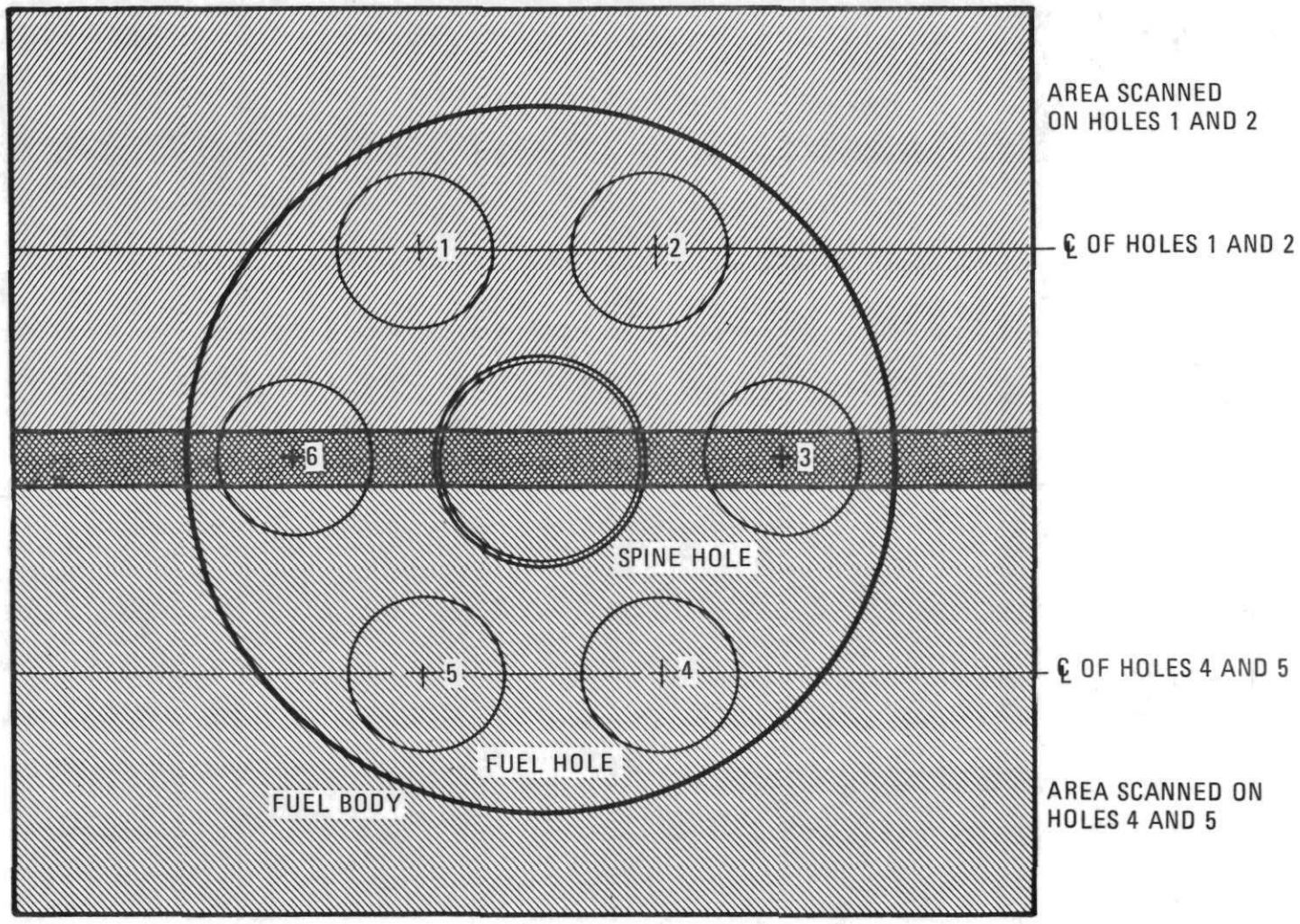

Fig. 9-56. FTE-15 graphite fuel body gamma scanned areas

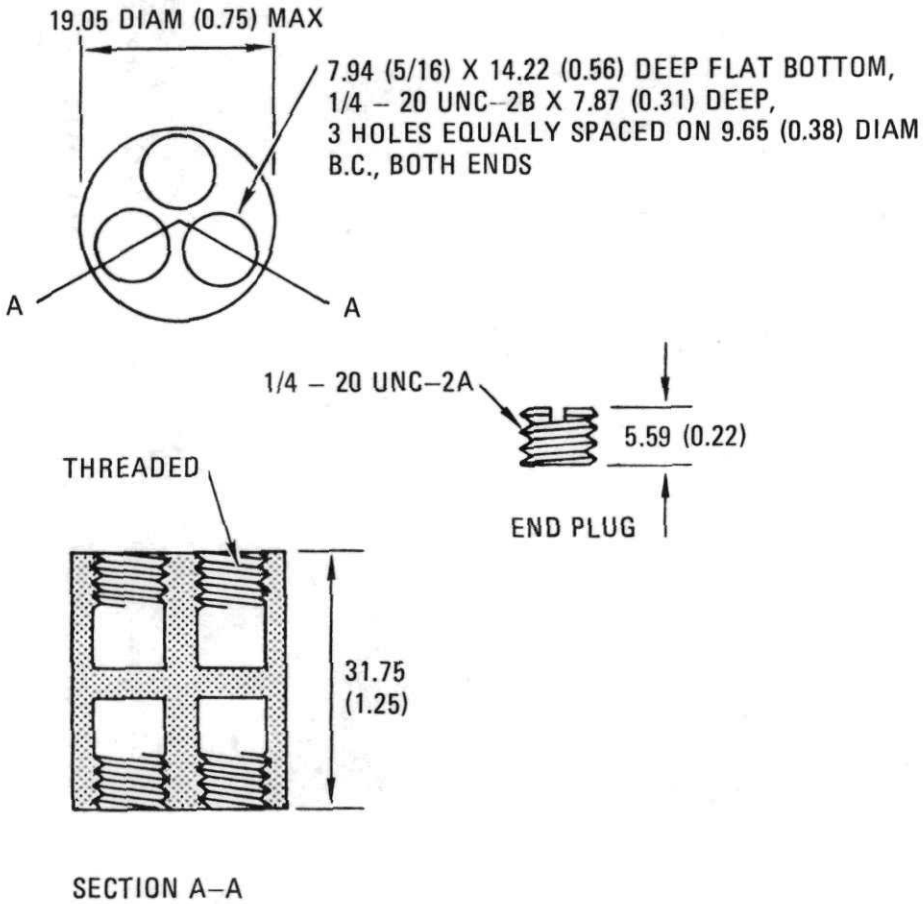

Fig. 9-57. Thermal stability center hole sample

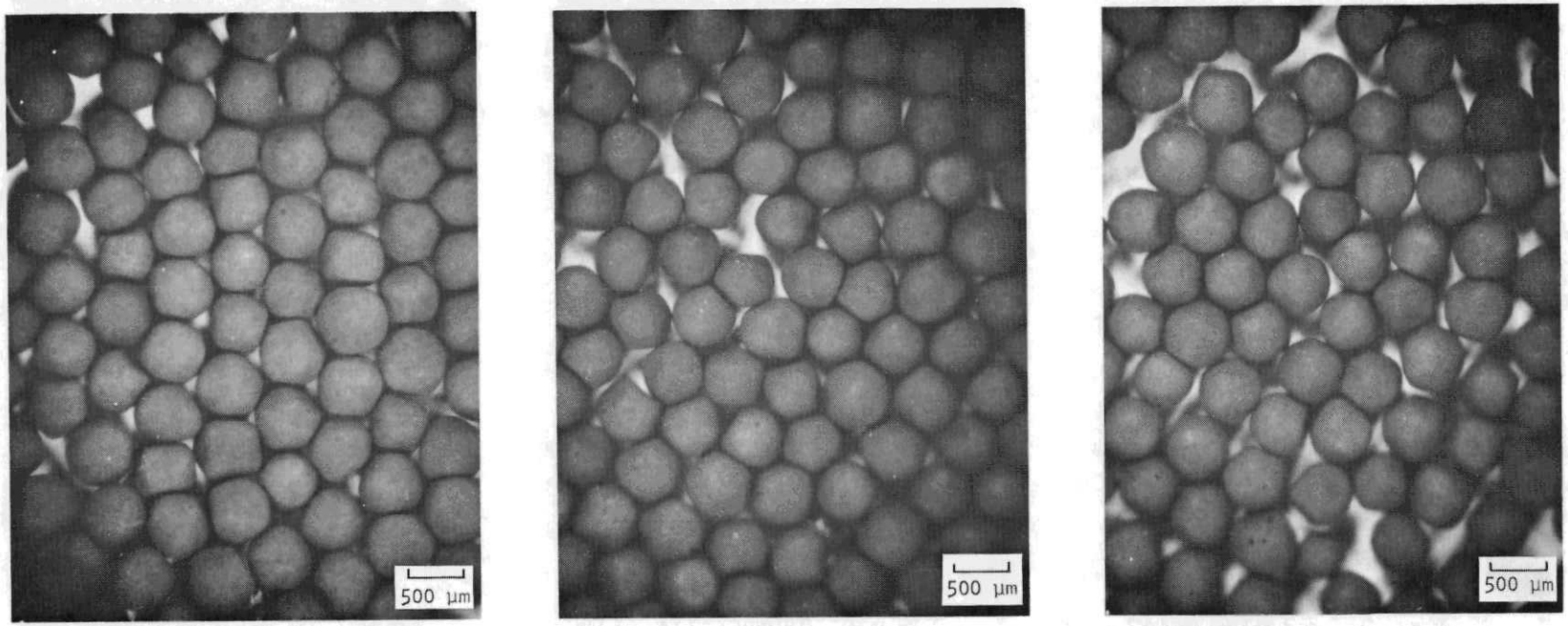

S7437-118 (a) S7437-120 (b) S7437-112 (c)

Fig. 9-58. Stereophotographs of FTE-15 UC_2 TRISO fissile particle batch 4161-01-030. (a) spine sample TS 3-6 irradiated to 1.8 x 10^{25} n/m^2 $(E \geq 29\ fJ)_{HTGR}$ ∿1230°C, (b) spine sample TS 4-6 irradiated to 2.0 x 10^{25} n/m^2 $(E \geq 29\ fJ)_{HTGR}$ at ∿1540°C, and (c) spine sample TS 5-6 irradiated to 2.0 x 10^{25} n/m^2 $(E \geq 29\ fJ)_{HTGR}$ at ∿1640°C.

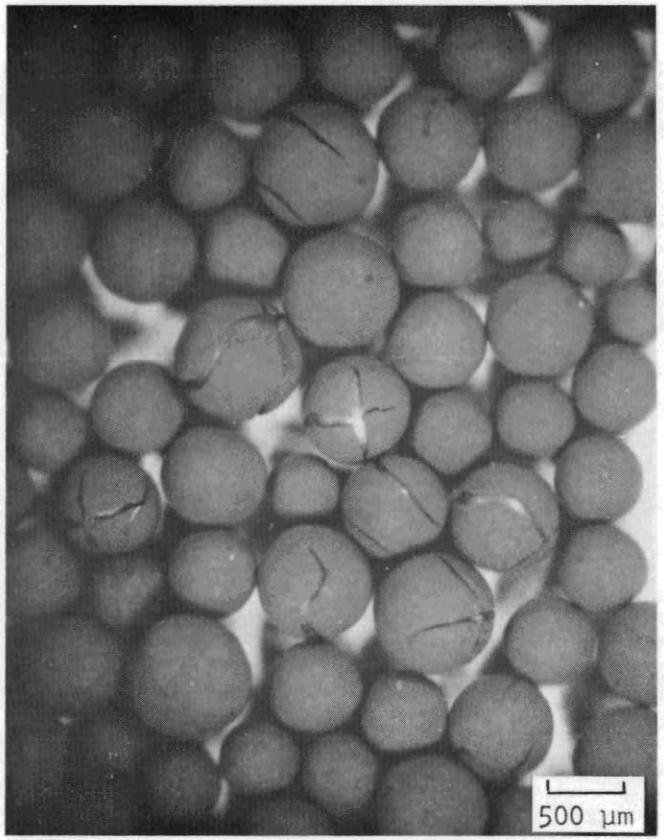

L7437-115 (a)

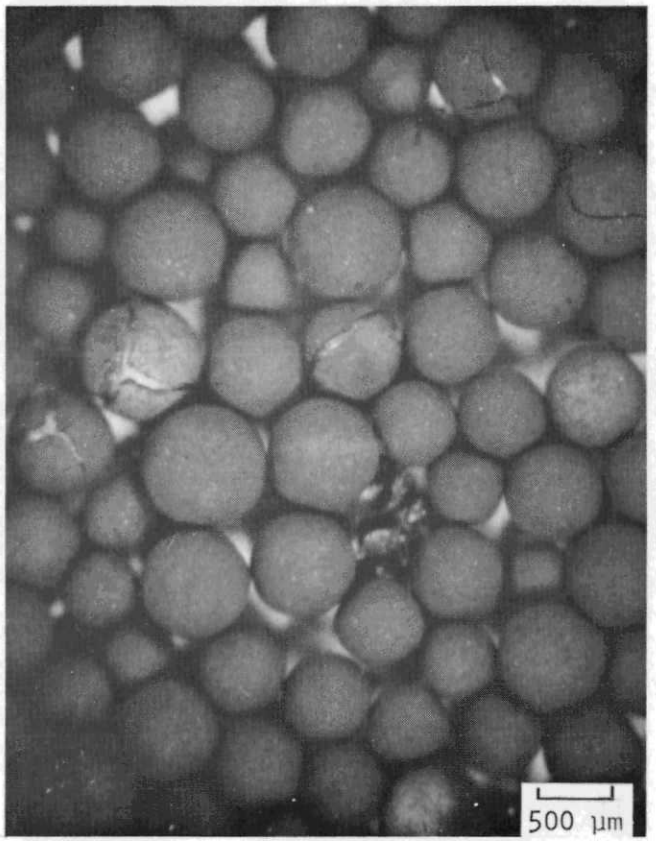

L7437-110 (b)

Fig. 9-59. Stereophotographs of FTE-15 UC_xO_y TRISO (WAR) fissile batch OR-1694. (a) spine sample TS 2-6 irradiated to 1.8×10^{25} n/m^2 $(E \geq 29 \text{ fJ})_{HTGR}$ at ∿1210°C and (b) spine sample TS 6-6 irradiated to 2.0×10^{25} n/m^2 $(E \geq 29 \text{ fJ})_{HTGR}$ at ∿1550°C.

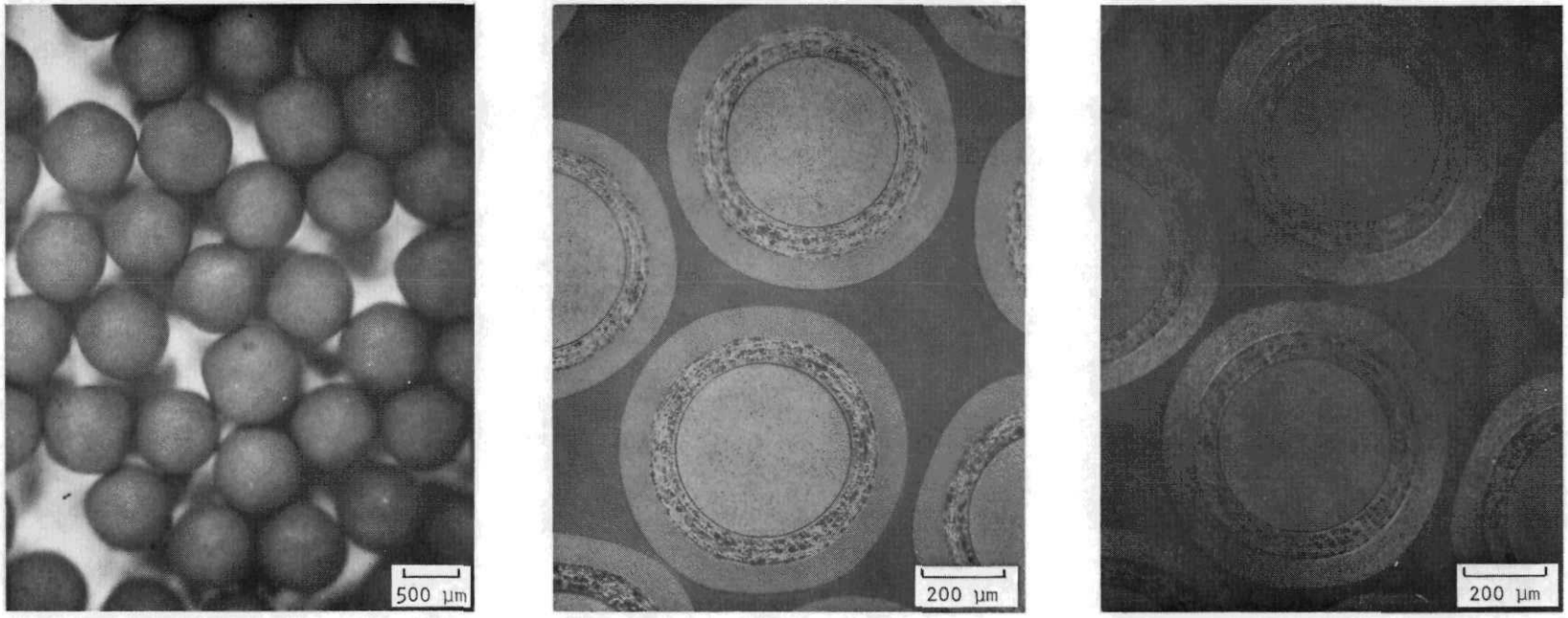

S7437-106 (a) L7437-21 (b) L7437-22 (c)

Fig. 9-60. Photomicrographs of FTE-15 ThO_2 BISO fertile batch 4252-02-070 from spine sample TS-6-1. Irradiation conditions 2.0 x 10^{25} n/m^2 $(E \geq 29\ fJ)_{HTGR}$ at ∿1550°C. (a) stereophotograph, (b) bright field, and (c) dark field.

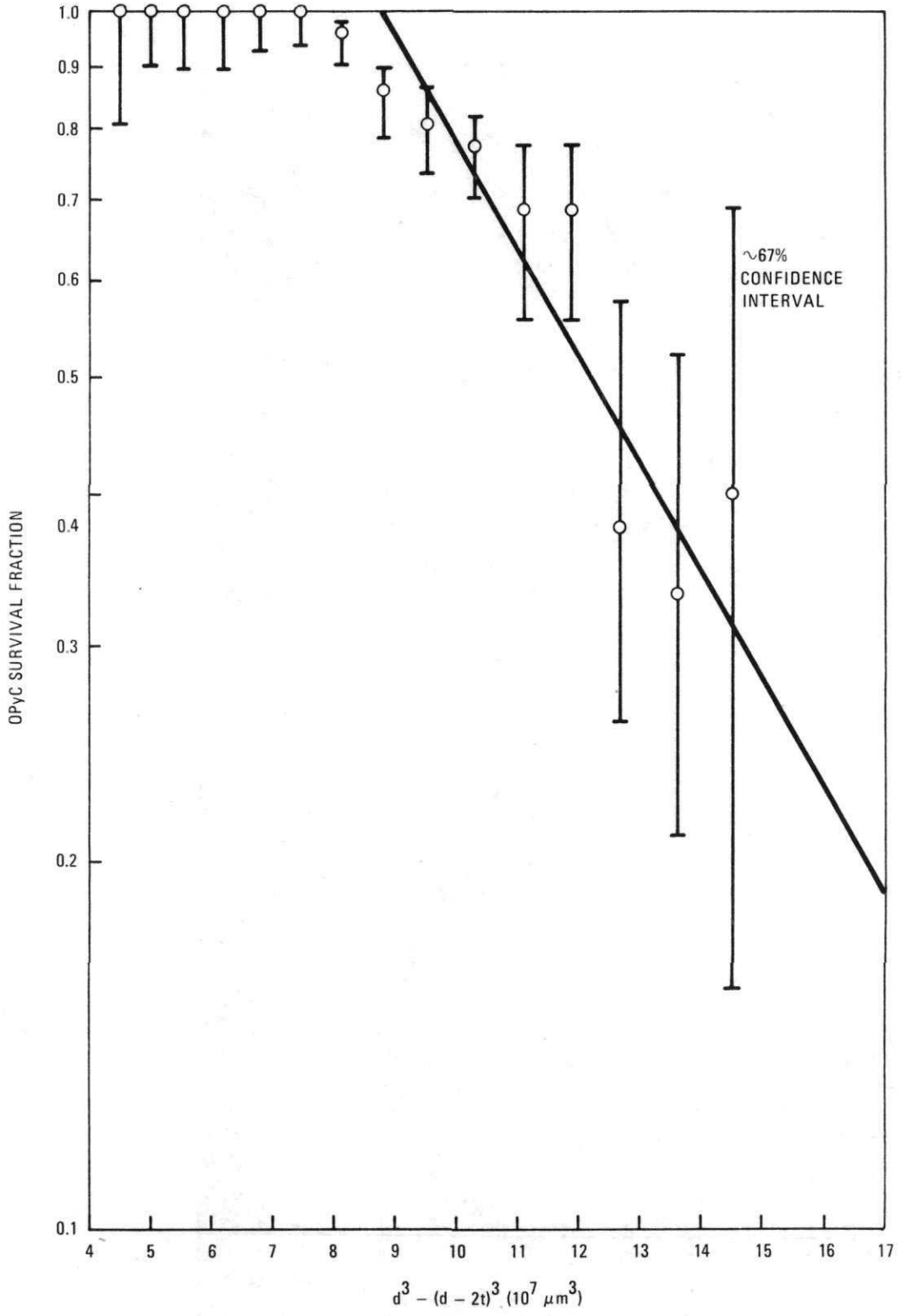

Fig. 9-61. Particle size effect on OPyC failure

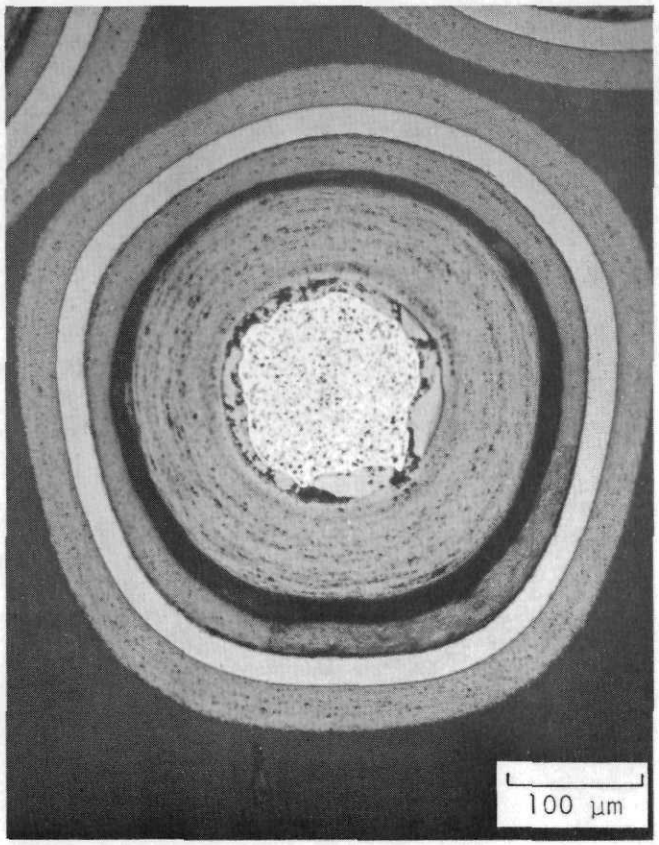

L7437-36 (a)

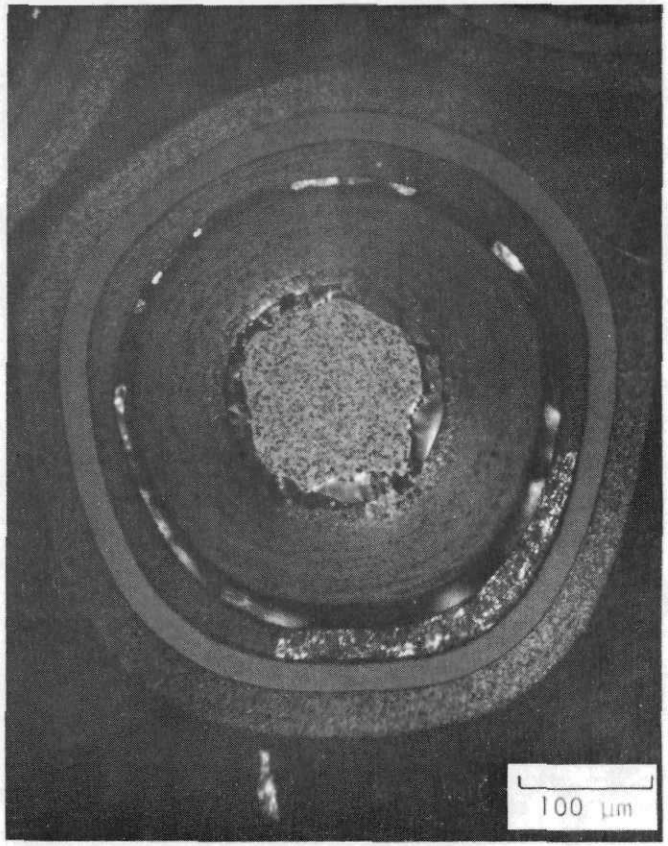

L7437-37 (b)

Fig. 9-62. Photomicrographs of FTE-15 UC_2 TRISO (VSM) fissile particle batch 4161-01-030 from spine sample TS 3-6. Irradiation conditions 1.8 x 10^{25} n/m^2 $(E \geq 29\ fJ)_{HTGR}$ at ∿1230°C. (a) bright field and (b) dark field showing concentration of metallic fission products in the IPyC.

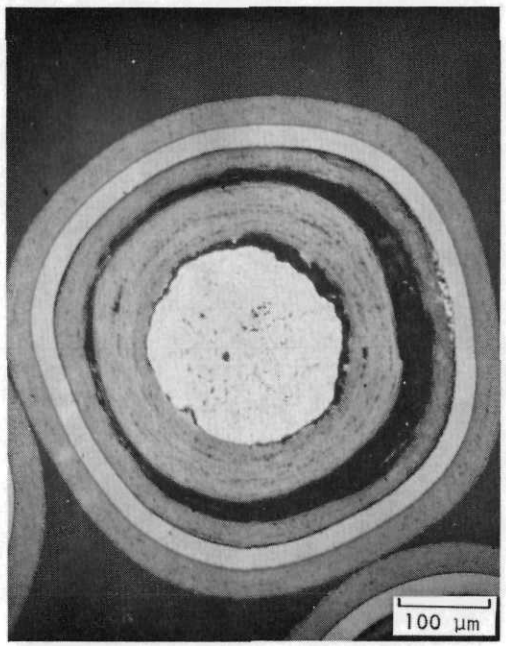

L7437-46 (a)

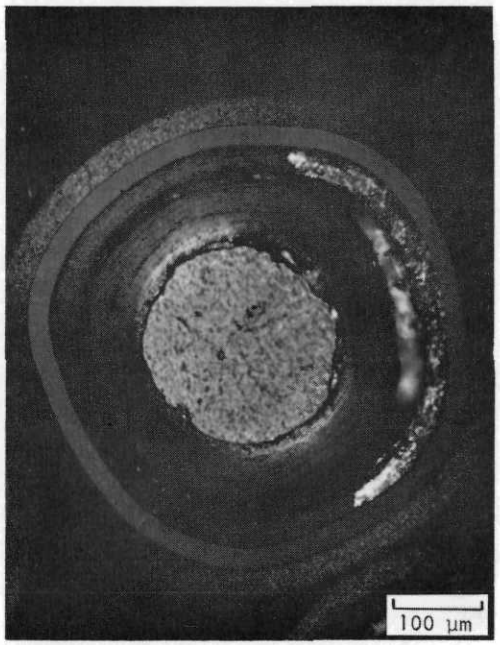

L7437-47 (b)

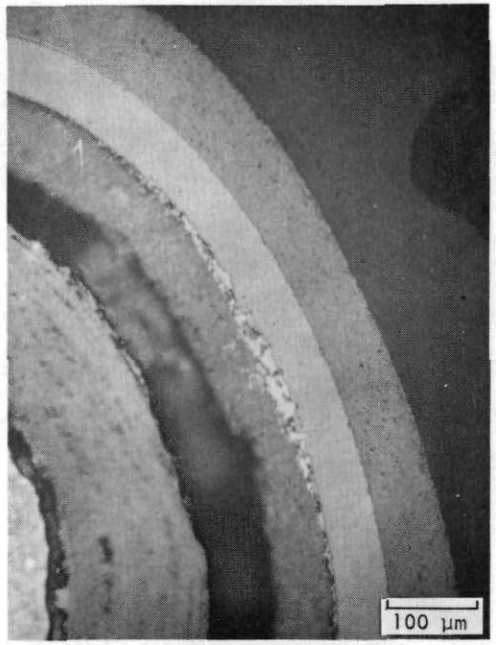

L7437-48 (c)

Fig. 9-63. Photomicrographs of FTE-15 UC_2 TRISO (VSM) fissile particle batch 4161-01-030 from spine sample TS 4-6. Irradiation conditions 2.0 x 10^{25} n/m^2 $(E \geq 29\ fJ)_{HTGR}$ at 1540°C. (a) bright field, (b) dark field, and (c) high magnification of SiC attack.

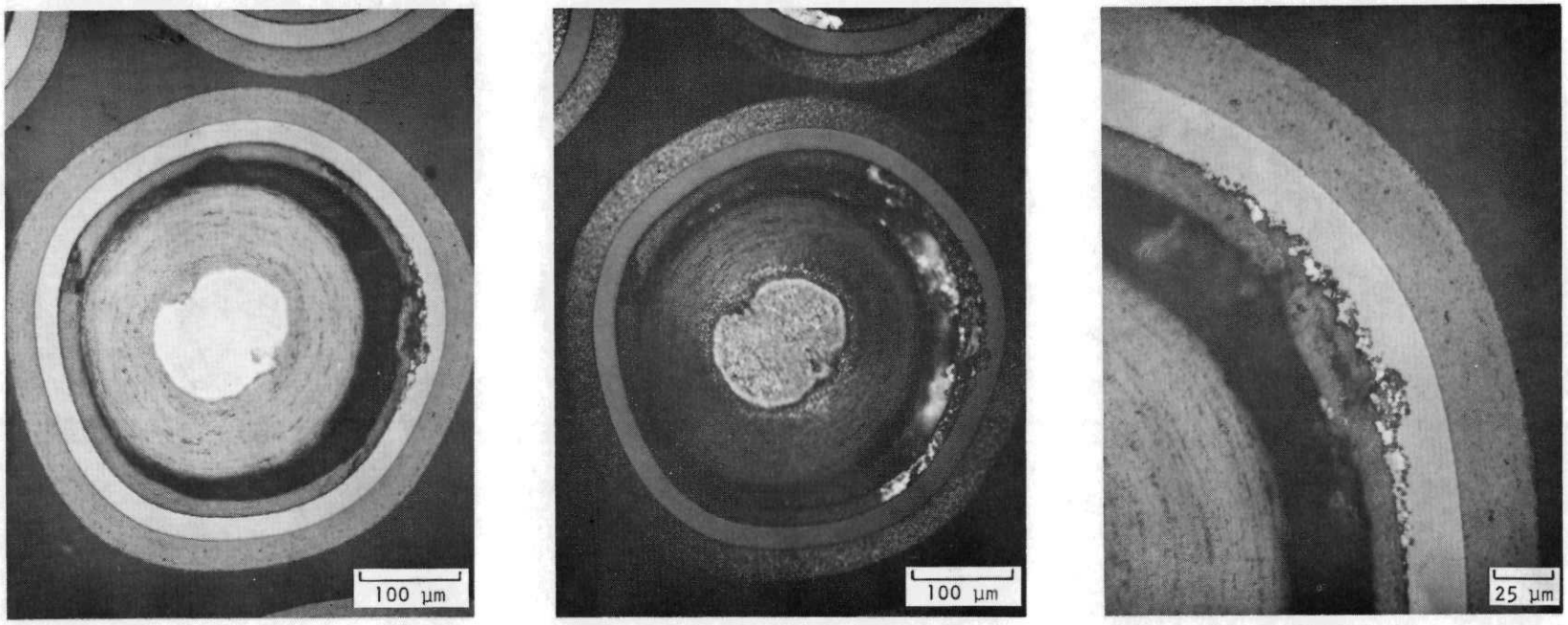

L7437-63 (a) L7437-64 (b) L7437-22 (c)

Fig. 9-64. Photomicrographs of FTE-15 UC_2 TRISO (VSM) fissile particle batch 4161-01-030 from spine sample TS 5-6. Irradiation conditions 2.0 x 10^{25} n/m^2 $(E \geq 29\ fJ)_{HTGR}$ at 1640°C. (a) bright field, (b) dark field, and (c) high magnification of SiC attack.

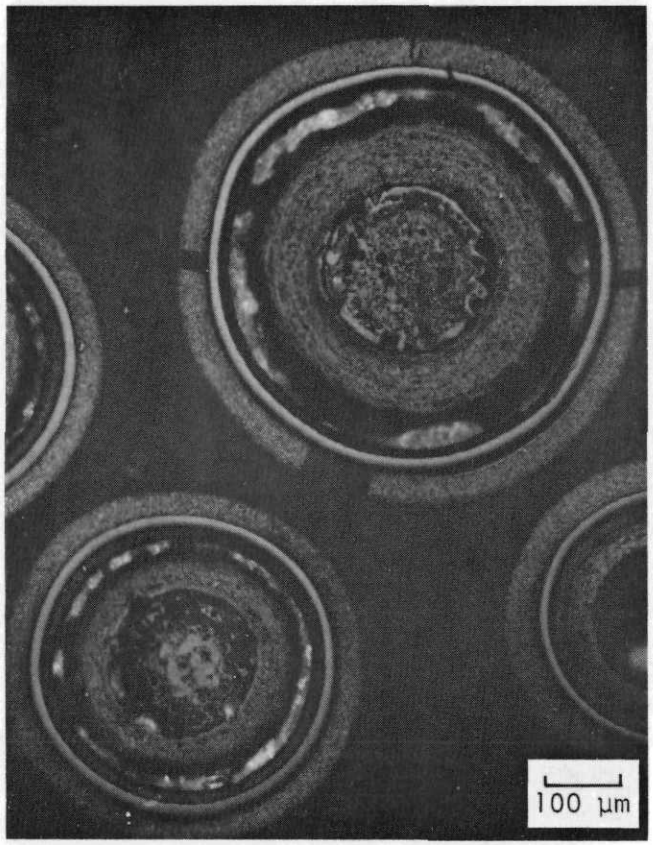

L7437-13 (a)

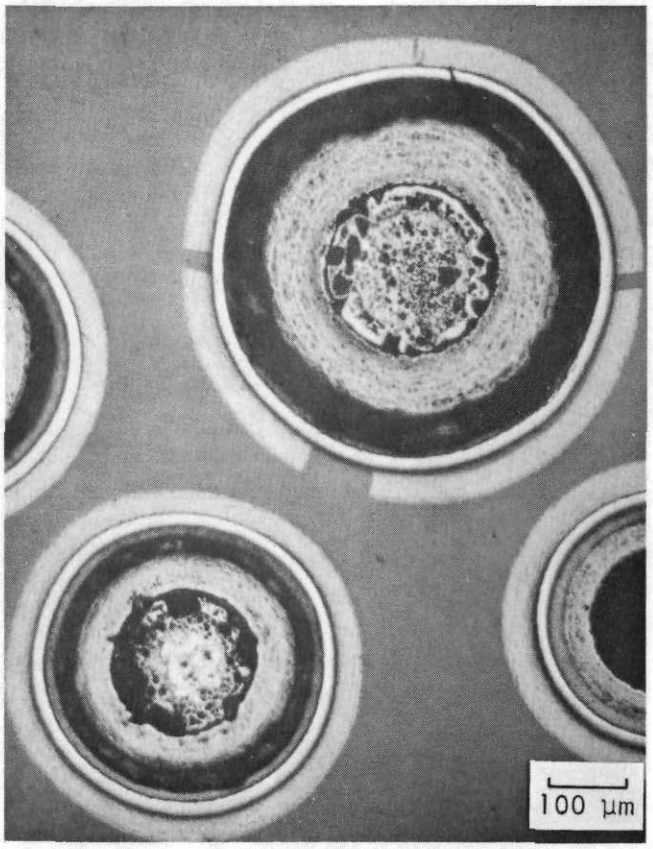

L7437-14 (b)

Fig. 9-65. Photomicrographs of FTE-15 UC_xO_y TRISO (WAR) fissile particle batch OR-1694 from spine sample TS 2-6. Irradiation conditions 1.8×10^{25} n/m^2 $(E \geq 29 \text{ fJ})_{HTGR}$ at ∿1210°C. (a) bright field and (b) dark field.

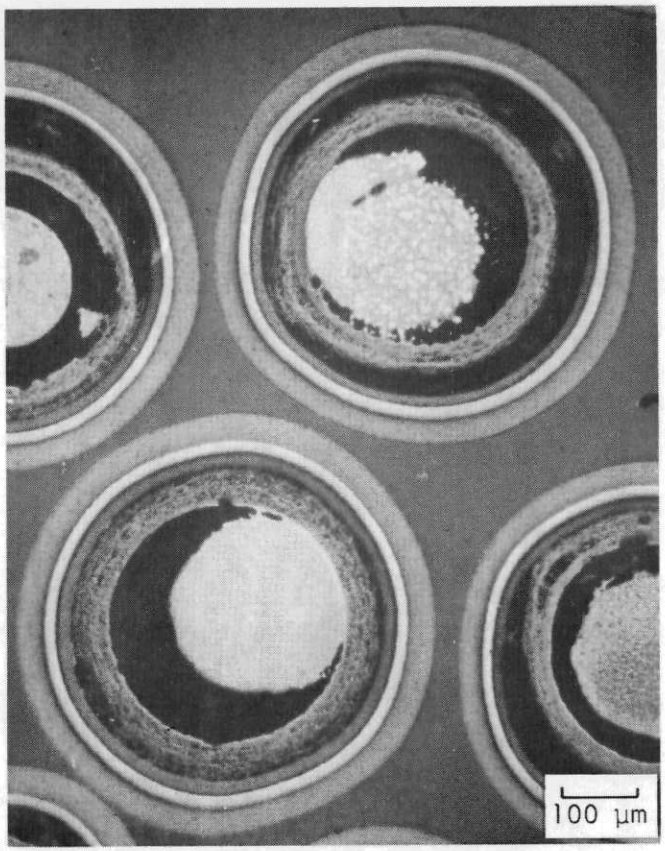

L7437-30 (a)

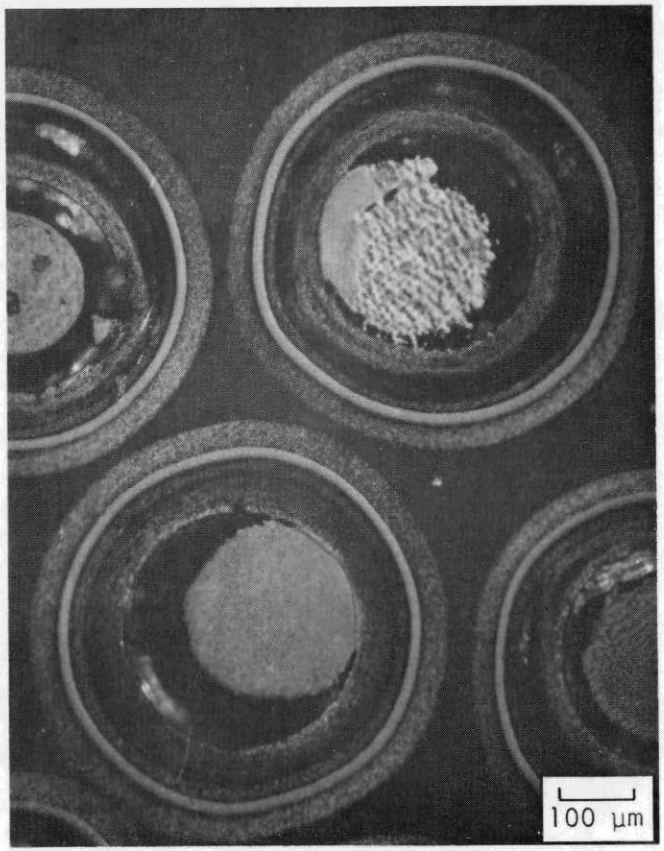

L7437-31 (b)

Fig. 9-66. Photomicrographs of FTE-15 UC_xO_y TRISO (WAR) fissile particle batch OR-1694 from spine sample TS 6-6. Irradiation conditions 2.0 x 10^{25} n/m^2 $(E \geq 29 \text{ fJ})_{HTGR}$ at ∿1550°C. (a) bright field and (b) dark field.

11. GRAPHITE DEVELOPMENT
189a NO. SU004

The characterization and irradiation of materials for replaceable fuel and reflector elements were continued. Characterization of core support and side reflector graphites was begun.

TASK 100: FABRICATION AND OPERATION OF IRRADIATION CAPSULES

Capsule OG-5

Work on capsule OG-5 has been suspended due to uncertainty in the operation of the Oak Ridge Reactor during FY-77. Design documents, drawings, and completed hardware will be stored pending resolution of the ORR operating schedule.

TASK 200: GRAPHITE SPECIMEN PREPARATION AND PROPERTY MEASUREMENTS FOR CAPSULE IRRADIATION

Capsule OG-3

Postirradiation measurements on specimens irradiated in capsule OG-3 have been completed and analysis is in progress. A complete data tabulation and discussion of the results will be included in a forthcoming topical report. Those results that are currently available are included in this report.

Thermal Expansivity

Measurements of the thermal expansivity of graphite specimens irradiated in capsule OG-3 were made with a silica dilatometer between ambient temperature and 100 K less than the irradiation temperature. Specimens of H-451 graphite (lots 266 and 426), H-429 graphite, TS-1240 graphite, and

S0818 graphite irradiated to a variety of fluences and temperatures were measured. Results for the mean thermal expansivity between ambient temperature and 773 K are tabulated in Tables 11-1 through 11-5. The average thermal expansivity changes in H-429 and TS-1240 graphites irradiated in capsules OG-1, OG-2, and OG-3 are summarized in Tables 11-6 and 11-7. Similar tables for H-451 and S0818 graphites will be prepared when final control tests have been completed. The thermal expansivity of all the near-isotropic graphites decreases with irradiation. The decrease is greater at high irradiation temperatures than at low temperatures; at irradiation temperatures above 1300 K and fluences of 10^{26} n/m^2, a reduction of about 40% is found.

Tensile Properties

Tensile tests at ambient temperature were performed on 215 specimens of H-451, TS-1240, and H-327 graphite irradiated in capsule OG-3. The specimens were cylinders 6.4 mm in diameter by 23 mm long which were cemented between metal end pieces and extended to failure. The strain was measured with a clip-on extensometer. The tensile test results are given in Tables 11-8 through 11-12. Tables 11-13 through 11-15 are summary tables consolidating the results of tensile tests for capsules OG-1, OG-2, and OG-3.

The fractional increases in strength and Young's modulus are plotted as functions of fast neutron fluence in Figs. 11-1 through 11-3. The curves through the Young's modulus points in Figs. 11-1 and 11-2 are the current design curves based on Dragon Project data. The present measurements on near-isotropic graphites are consistent with the design curves. The measurements on needle-coke grade H-327 do not show the second rise in Young's modulus found with near-isotropic graphites irradiated at around 1173 K (900°C). New design curves were prepared for H-327 graphite based on Dragon data for an anisotropic petroleum coke graphite (reference code 120). The curves are indicated in Fig. 11-3 and are in good agreement with the measurements. Design curves for the fractional increase in tensile strength are based on the relationship:

$$S/S_o = (E/E_o)^k \quad ,$$

where S is the irradiated strength, S_o is the unirradiated strength, E is the irradiated Young's modulus, and E_o is the unirradiated Young's modulus. The exponent k was measured for each data set. The following average values for k were obtained:

	k
H-451	0.64
TS-1240	0.48
H-327, axial	0.67
H-327, radial	0.41

The design curves shown for the tensile strength data in Figs. 11-1 through 11-3 are based on these k values. When modulus and strength values are expressed as fractional increases above the preirradiation level, the data for all log locations, orientations, and production lots fall on the same line.

The distribution of the strength values is an important factor in the mechanical design of graphite components. It was found that the standard deviation of the tensile strengths tends to increase upon irradiation (Tables 11-13 through 11-15). However, the coefficient of variation (standard deviation divided by the mean) remains roughly constant except possibly after the highest exposures. Figures 11-4 and 11-5 show the coefficients of variation of the tensile strength, with 95% confidence intervals, as a function of neutron fluence. There is no significant trend in the coefficient of variation, although there is some suggestion of an increase at fluences above 6×10^{25} n/m^2.

Thermal Conductivity

Thermal diffusivity measurements were made on discs of H-451 graphite (lots 266 and 426), TS-1240 graphite, and S0818 graphite irradiated at

three temperatures. The thermal conductivity was obtained by multiplying by the heat capacity and the density. The data are shown in Tables 11-16 through 11-19. Figure 11-6 shows the thermal conductivity extrapolated to the irradiation temperature plotted against the fast neutron fluence for all near-isotropic graphite specimens irradiated to date. Irradiation reduces the conductivity to a saturation level which increases with the irradiation temperature. Axial specimens have consistently higher conductivities than radial specimens. After irradiation, the data for all three grades of near-isotropic graphite fall in the same band.

Two sets of radial H-451 graphite specimens were irradiated successively at different temperatures. The first set was irradiated at 1625 K to 3×10^{25} n/m^2, followed by 1.8×10^{25} n/m^2 at 925 K; the second set was irradiated first at 875 K to 2×10^{25} n/m^2 and then at 1615 K for an additional 2.9×10^{25} n/m^2. The data are shown in Table 11-20. In both cases the specimens achieved a conductivity equivalent to the saturation level for the second irradiation period.

All the thermal conductivity data obtained to date on grades H-451, TS-1240, and SO818 irradiated in the OG-series capsules are summarized in Tables 11-21 through 11-23.

TASK 300: CHARACTERIZATION OF CANDIDATE GRAPHITES FOR PROPERTIES AND PURITY

Replaceable Fuel Element and Reflector Graphites

Characterization of Great Lakes Carbon Corporation's (GLCC) preproduction lots of grade H-451 has been completed. Characterization work on Union Carbide Corporation's (UCC) preproduction lot 1 of grade TS-1240 and AirCo Speer's (AS) preproduction lot 4B of grade SO818 has been completed. Further characterization work on these materials has been suspended and the characterization effort shifted to core support structures. Future characterization work on replaceable fuel element and reflector graphites will be concentrated on production H-451.

Grade H-451 (GLCC)

Characterization of GLCC grade H-451 lots 266, 408, and 426 has been completed and reported in Ref. 11-1. Additional strength, thermal conductivity, and purity measurements have been made on specimens from lot 426; these data along with the results from lot 440 will be reported in Ref. 11-2, which is currently being written. The publication of Ref. 11-2 will complete the characterization work on preproduction logs of H-451.

Approximately 350 logs of H-451 are under production for Fort St. Vrain reload elements. This production order has been carried through the bake stage, and 256 of the logs were held there pending further clarification of the operating schedule for Fort St. Vrain. However, approximately 100 logs are being graphitized and will be delivered in September of 1976.

Grade SO818 (AS)

The characterization of the first lot (AS lot 4B) of grade SO818 graphite has been completed and will be reported in Ref. 11-2. At this time no further work is planned on SO818.

Side Reflector Graphites

A half log of HLM graphite (GA No. 6484-78), a candidate for the side reflector block, was purchased from GLCC. Grade HLM is a coarse-grained graphite manufactured by a conventional extrusion process. The full-size HLM log is 1.14 m in diameter by 1.83 m long.

Impurity content based on spectrographic analysis is given in Table 11-24. Ash and sulfur contents are given in Table 11-25. The lithium content was 0.5 ppm measured on a composite sample which was a mixture of all sampling locations. These data show the inhomogeneity of the large HLM block. The ash is highest at the center in both slabs. The average for

slab 1 (end) is 3683 ppm whereas the average for slab 6 (center) is only 1112 ppm. Iron, which is an important impurity with respect to oxidation resistance, showed a lower content at the edge and slab 1 averaged higher than slab 6.

Core Support Post and Seat Graphites

Two logs of commercial grade 2020 have been purchased from the Stackpole Carbon Company (SC) and a half log of preproduction H-440 graphite has been purchased from GLCC for characterization measurements. An additional small sample of H-440P (ash content about 300 ppm) has also been acquired for evaluation. Grades 2020 and H-440 are fine-grained graphites manufactured by an isotstatic molding procedure as 0.254 m diameter by 1.83 to 2.1 m long logs.

The impurity content based on spectrochemical analysis is given in Table 11-26. Ash and sulfur contents are given in Table 11-27. The lithium content was 0.3 ppm measured on a composite sample which was a mixture of all sampling locations. These data show the ash and iron contents to be highest at the end of the log. Averaging the values in Table 11-27, ash in slab 1 was 1950 ppm versus 1150 ppm in slab 6 and iron was 400 ppm in slab 1 versus 40 ppm in slab 6.

One block of commercial-grade ATJ graphite has been purchased for characterization measurements. ATJ graphite is a fine-grained graphite manufactured by a conventional molding process. The ATJ block is 0.2 m by 0.43 m by 1.83 m.

A block of grade PGX graphite, a candidate graphite for the core support floor blocks, has been purchased for characterization measurements. PGX is a coarse-grained graphite manufactured by a conventional process. The PGX log is 1.14 m in diameter by 1.83 m long. Characterization work is under way on the PGX graphite.

TASK 400: STATISTICAL STUDY OF GRAPHITE STRENGTH

A topical report entitled "Statistical Study of the Strength of Near-Isotropic Graphite," by R. J. Price (Ref. 11-3) was issued. Publication of this report completes the first phase of the work scheduled under this task.

TASK 500: FATIGUE BEHAVIOR OF GRAPHITE

Ambient temperature uniaxial fatigue tests are being conducted on radial specimens of PGX graphite. The test procedures are the same as those used for the H-451 graphite fatigue tests described in the previous quarterly report (Ref. 11-4).

Two series of tests have been completed. In the first, 35 specimens were tested to failure in uniaxial tension while mounted in the fatigue machine to provide baseline data. The second series consisted of 40 fatigue tests with a tension-zero-tension loading cycle ($R = 0$). The results of the tests are given in Tables 11-28 and 11-29.

Figure 11-7 is the S-N curve for the $R = 0$ test series, plotted with log-log coordinates. The data were statistically analyzed to obtain the lower tolerance limits for the population of data points. The tolerance limits are included in Fig. 11-7. The statistical model used is the same as the one given in Ref. 11-4. The endurance limit for 50% survival to 100,000 cycles was 84% of the mean tensile strength, and the lower tolerance limit for 99% survival to 100,000 cycles with 95% confidence was 64% of the mean tensile strength. These limits are appreciably higher than the factors for H-451 graphite fatigue tested under the same conditions (Ref. 11-4).

TASK 600: STRUCTURAL INTEGRITY OF GRAPHITE BLOCKS

Residual Stress Analysis

During the last quarter, residual stress analyses were performed on a six-hole teledial test element, FTE-14. In addition, stresses were recalculated for the eight-hole teledial element, FTE-4. (Previous results for FTE-4 were reported in Ref. 11-4.) The recalculations were made to determine the effects of changes in material properties and of a refinement in the finite element mesh to gain a more accurate estimate of stresses at a sharp notch in the teledial specimen.

Analyses of FTE-14

A preliminary stress analysis of Peach Bottom fuel test element FTE-14 has been conducted. Residual stresses at the end-of-life and stresses due to primary loadings were calculated. It was calculated that a 0.45-m-long strip will bow as much as 3.8 mm when the bending moment due to residual stresses is relieved.

The analysis was performed before the revisions in material properties described below for FTE-4 were made available. The analysis will be rerun with the revised material data. The preliminary results, however, have indicated what experiments should be performed to verify the calculated effects of the residual stresses.

The GTEPC computer code, a two-dimensional finite element program (Ref. 11-5), was used for temperature and stress computations. In computing residual stresses, a 0.524-rad sector of the eight-hole teledial element was idealized by a mesh of triangular elements (Fig. 11-8). A standard solid model (Ref. 11-6) was adopted to account for the irradiation-induced creep in graphite. New material constants were obtained from the recent irradiation experiment OG-3.

The residual stress depends on the thermal and irradiation history. In calculating the thermal boundary conditions and neutron doses at various times during Core 2 operation, a one-dimensional computer program was used (Ref. 11-7). A typical result at axial position 5 (approximately 0.343 m from the bottom of the core) is given in Table 11-30.

The finite element mesh used for thermal and stress calculations is shown in Fig. 11-8. In addition to the model for the graphite, the fuel rod and the graphite sleeve were also included for thermal computations. The heat transfer across the gap between the fuel rod and the graphite was treated by defining the emissivities (0.89 for fuel and 0.87 for graphite) and the gas conductivity ($3.32 \times 10^{-3}\ T^{0.674}$, W/m^2-K), where T is the computed gas temperature in K. Because of the small temperature variation along the gap between the graphite and the sleeve, the constant gas conductances given in Table 11-30 were used in the computation. The coolant temperature and the film coefficient were used to define the boundary condition at the outer surface of the sleeve. The thermal computations were carried out using the thermal conductivities and the heat generation rates given in Table 11-30. Assuming the graphite was subjected to no external forces, the operating and the shutdown stress fields resulting from the temperature differential and the neutron dose were computed.

In computing stress under primary loadings, a 1.57-rad sector model was used.

The residual stress contours are given in Figs. 11-9 through 11-11. A maximum in-plane stress of 4.1 MPa was calculated next to the fuel hole (Fig. 11-10).

The axial residual stress contours shown in Fig. 11-9 are used to estimate the bow for strip cutting experiments. Since the axial stress varies approximately linearly in the radial direction, strips cut as indicated in Fig. 11-9 will bow to relieve most of their residual stress. The radius of curvature for the strip is estimated to be 13.7 m, which gives a displacement at the midlength of a 0.45-m-long strip of 3.8 mm.

The stress contours under a compression load are given in Figs. 11-12 and 11-13, and the stress contours under a hydrostatic pressure load applied to the walls of the fuel holes are given in Figs. 11-14 and 11-15. A maximum stress of 3.6 MPa occurs at the outer web of the fuel hole under the compression loading of 25.4 kN/m (Fig. 11-12). A 100-kPa pressure load at the inner surface of a fuel hole produces a maximum stress of 394 kPa at the outer web of the fuel hole (Fig. 11-14).

The results suggest that primary loading tests be carried out in such a way that failure across a section with low residual stress, such as section A-A in Fig. 11-9, can also be induced by a measured primary load. This would allow the comparison of the primary stress at failure in the absence of significant residual stress with the primary stress at failure in the presence of high residual stresses, on the order of the strength of the graphite. Tests on unirradiated specimens will be performed to establish the feasibility of the test methods.

Analyses of FTE-4

The changes in physical properties that were studied resulted from incorporation of the analyses of recent irradiation data obtained from capsule OG-3 with previous data on H-327. Properties analyzed for design were irradiation-induced dimensional changes, tensile strength, elastic modulus, thermal expansivity, and thermal conductivity.

In addition, a change was made in the creep data used for H-327 graphite. In previous calculations, such as those reported in Ref. 11-4, Poisson's ratio was assumed to be the same for creep deformation as for elastic deformation (i.e., $\nu = 0.117$). This assumption is consistent with the model described in Ref. 11-6. According to Ref. 11-8, however, constant volume creep has been observed for graphite during irradiation under uniaxial stress conditions. To more nearly simulate the constant volume creep condition, a ratio of 0.45 was used for creep deformation and 0.117 for elastic deformation.

The revised Poisson's ratio in creep and the other changes in properties of H-327 graphite described above were used to calculate the operating and shutdown stresses for FTE-4 at axial position 23. The results, shown in Figs. 11-16 and 11-17, were compared with results reported in Ref. 11-4 which were obtained before the changes in material properties had been made. The shutdown stresses at the end-of-life differed by at most 5% in the axial direction and 15% in the in-plane direction from those calculated before the graphite properties were changed.

In order to obtain a better estimate of the peak stress next to the slot, a more detailed finite element mesh was constructed in this area, as shown in Fig. 11-18. The resulting in-plane stress distribution is shown in Fig. 11-19. A comparison of these results with the results calculated with the coarse mesh (as shown in Fig. 11-17) shows that the peak in-plane stress has increased by about 65% to 14.1 MPa.

TASK 700: PROGRAM PLAN

There was no work on this task during the quarter.

REFERENCES

11-1. Johnson, W. R., and G. B. Engle, "Properties of Unirradiated Fuel Element Graphites H-451 and TS-1240," ERDA Report GA-A13752, General Atomic, January 31, 1976.

11-2. Engle, G. B., and W. R. Johnson, "Properties of Unirradiated Fuel Element Graphites H-451 and SO818," ERDA Report GA-A14068, General Atomic, to be published.

11-3. Price, R. J., "Statistical Study of the Strength of Near-Isotropic Graphite," ERDA Report GA-A13955, General Atomic, May 24, 1976.

11-4. "HTGR Fuels and Core Development Program Quarterly Progress Report for the Period Ending May 31, 1976," ERDA Report GA-A13941, General Atomic, June 30, 1976.

11-5. Tzung, F. K., "GTEPC-2D, A Computer Program for Two-Dimensional Graphite Thermal-Elastic-Plastic-Creep Analysis, User's Manual," General Atomic Report GA-A13532, to be published.

11-6. Head, J. L., "The Transient Creep of Graphite in a Reactor Environment," paper presented at the Third International Conference on Structural Mechanics in Reactor Technology, London, September 1-5, 1975.

11-7. Saurwein, J. J., "Peach Bottom Test Element Thermal Analysis," General Atomic unpublished data, April 19, 1976.

11-8. Gray, W. J., "Constant Stress Irradiation-Induced Compressive Creep of Graphite at High Fluences," Carbon 11, 383 (1973).

TABLE 11-1
THERMAL EXPANSIVITY OF H-451 GRAPHITE, LOT 266,
IRRADIATED IN CAPSULE OG-3

LOT NUMBER: 266 LOG NUMBER(S): 5651-28

ORIEN-TATION	LOCA-TION	CRUC-IBLE	MOLE	MEAN IRR. TEMP. (K)	FLUENCE (10EXP25 N/M**2, E>.18MEV)	SPECIMEN NUMBER	C.T.E. (10EXP-6/K) 295K-773K (22C-500C)
AXIAL	MLC	1	1	935	5.5	.301.	3.65
			1	(662 C)		.302.	3.69
			2			.303.	3.70
						MEAN:	3.67
						STD. DEV:	.04
AXIAL	MLC	8	1	1170	6.4	.371.	2.85
			1	(897 C)		.372.	2.98
			2			.373.	2.83
						MEAN:	2.89
						STD. DEV:	.09
AXIAL	MLC	3	1	1270	8.5	.405.	2.43
			1	(997 C)		.632.	2.38
			1			.406.	2.20
						MEAN:	2.34
						STD. DEV:	.12
AXIAL	MLE	4	1	1515	9.2	.581.	2.18
			1	(1242 C)		.582.	2.22
			2			.583.	2.19
						MEAN:	2.20
						STD. DEV:	.02
AXIAL	MLC	5	1	1660	9.0	.331.	2.12
			1	(1387 C)		.332.	1.90
						MEAN:	2.01
						STD. DEV:	.15

TABLE 11-1 (Continued)

LOT NUMBER: 266 LOG NUMBER(S): 5651-28

ORIEN-TATION	LOCA-TION	CRUC-IBLE	HOLE	MEAN IRR. TEMP. (K)	FLUENCE (10EXP25 N/M**2, E>.18MEV)	SPECIMEN NUMBER	C.T.E. (10EXP-6/K) 295K-773K (22C-500C)
RADIAL	MLC	1	1	935	5.5	.426.	4.61
			1	(662 C)		.427.	4.69
			2			.428.	4.75
						MEAN:	4.68
						STD. DEV:	.07
RADIAL	MLC	8	1	1170	6.4	.496.	3.54
			1	(897 C)		.497.	3.70
			2			.498.	3.54
						MEAN:	3.60
						STD. DEV:	.09
RADIAL	MLC	3	1	1270	8.5	.530.	2.81
			1	(997 C)		.732.	2.48
			1			.531.	2.68
						MEAN:	2.66
						STD. DEV:	.16
RADIAL	MLE	4	1	1515	9.2	.681.	2.66
			1	(1242 C)		.682.	2.73
			2			.683.	3.07
						MEAN:	2.82
						STD. DEV:	.22
RADIAL	MLC	5	1	1660	9.0	.456.	2.48
			1	(1387 C)		.457.	2.60
						MEAN:	2.54
						STD. DEV:	.08

TABLE 11-2
THERMAL EXPANSIVITY OF H-451 GRAPHITE, LOT 426,
IRRADIATED IN CAPSULE OG-3

LOT NUMBER: 426 LOG NUMBER(S): 6484-34

ORIEN-TATION	LOCA-TION	CRUC-IBLE	HOLE	MEAN IRR. TEMP. (K)	FLUENCE (10EXP25 N/M**2, E>.18MEV)	SPECIMEN NUMBER	C.T.E. (10EXP-6/K) 295K-773K (22C-500C)
AXIAL	MLC	1	7	970	1.8	34-2A-8A	3.67
			7	(697 C)		34-2A-8B	3.86
			8			34-2A-8C	3.65
						MEAN:	3.73
						STD. DEV:	.12
AXIAL	MLC	2	4	1040	2.4	34-2B-5C	3.89
			5	(767 C)		34-2B-5D	3.78
			6			34-2B-6A	3.63
						MEAN:	3.77
						STD. DEV:	.13
AXIAL	MLC	5	2	1655	2.9	34-2B-6C	3.92
			3	(1382 C)		34-2B-6D	3.87
			4			34-2B-7A	3.89
						MEAN:	3.90
						STD. DEV:	.03
RADIAL	MLC	1	7	970	1.8	34-2B-39A	4.41
			7	(697 C)		34-2B-39B	4.40
			8			34-2B-39C	4.43
						MEAN:	4.41
						STD. DEV:	.01
RADIAL	MLC	2	9	1010	2.4	34-2B-36C	4.26
			10	(737 C)		34-2B-36D	4.39
			11			34-2B-36A	4.49
						MEAN:	4.38
						STD. DEV:	.12
RADIAL	MLC	5	7	1655	2.9	34-2B-40D	4.60
			8	(1382 C)		34-2B-37C	4.42
			9			34-2B-37D	4.67
						MEAN:	4.56
						STD. DEV:	.13

TABLE 11-3
THERMAL EXPANSIVITY OF H-429 GRAPHITE IRRADIATED
IN CAPSULE OG-3

LOT NUMBER: -- LOG NUMBER(S): 4974- 04A

ORIENTATION	LOCATION	CRUCIBLE	HOLE	MEAN IRR. TEMP. (K)	FLUENCE (10EXP25 N/M**2, E>.18MEV)	SPECIMEN NUMBER	C.T.E. (10EXP-6/K) 295K-773K (22C-500C)
AXIAL		8	7	1170 (897 C)	7.2	392	3.20
			7			393	3.44
			7			397	3.46
						MEAN:	3.38
						STD. DEV:	.15
AXIAL		4	5	1480 (1207 C)	11.4	404	2.57
			5			405	2.67
			6			406	2.33
						MEAN:	2.52
						STD. DEV:	.17
RADIAL		8	6	1170 (897 C)	7.2	419	3.90
			6			420	4.05
			6			421	4.20
						MEAN:	4.05
						STD. DEV:	.15
RADIAL		4	5	1480 (1207 C)	11.4	434	3.09
			5			435	3.05
			6			436	3.04
						MEAN:	3.06
						STD. DEV:	.03

TABLE 11-4
THERMAL EXPANSIVITY OF TS-1240 GRAPHITE
IRRADIATED IN CAPSULE OG-3

LOT NUMBER: 1 LOG NUMBER(S): 5651-73

ORIEN-TATION	LOCA-TION	CRUC-IBLE	HOLE	MEAN IRR. TEMP. (K)	FLUENCE (10EXP25 N/M**2, E>.18MEV)	SPECIMEN NUMBER	C.T.E. (10EXP-6/K) 295K-773K (22C-500C)
AXIAL	MLE	10	10	880	2.3	T40241	4.62
			10	(607 C)		T40243	4.50
			11			T40245	4.55
						MEAN:	4.55
						STD. DEV:	.06
AXIAL	MLC	7	8	1250	4.9	T40037	2.60
			8	(977 C)		T40039	2.86
			9			T40041	2.66
						MEAN:	2.71
						STD. DEV:	.13
AXIAL	MLC	4	29	1415	5.9	T40001	2.91
			29	(1142 C)		T40003	2.63
			30			T40005	3.00
						MEAN:	2.85
						STD. DEV:	.19
RADIAL	MLC	10	15	880	2.3	T40149	5.08
			15	(607 C)		T40151	5.15
			16			T40153	4.82
						MEAN:	5.02
						STD. DEV:	.17
RADIAL	MLC	7	29	1200	4.9	T40121	3.77
			29	(927 C)		T40123	4.04
			30			T40125	3.79
						MEAN:	3.87
						STD. DEV:	.15
RADIAL	MLC	4	7	1500	5.9	T40157	2.64
			7	(1227 C)		T40159	2.57
			8			T40161	2.56
						MEAN:	2.59
						STD. DEV:	.04

TABLE 11-5
THERMAL EXPANSIVITY OF SO818 GRAPHITE
IRRADIATED IN CAPSULE OG-3

LOT NUMBER: 4-B LOG NUMBER(S): 6484-22

ORIENTATION	LOCATION	CRUCIBLE	HOLE	MEAN IRR. TEMP. (K)	FLUENCE (10EXP25 N/M**2, E>.18MEV)	SPECIMEN NUMBER	C.T.E. (10EXP-6/K) 295K-773K (22C-500C)
AXIAL	MLC	2	5	1040	2.4	22-1A-1A	4.71
			6	(767 C)		22-1A-1B	4.75
			7			22-1A-1C	4.49
						MEAN:	4.65
						STD. DEV:	.14
AXIAL	MLC	5	3	1655	2.9	22-1A-2A	4.16
			4	(1382 C)		22-1A-2B	3.89
			5			22-1A-2C	3.95
						MEAN:	4.00
						STD. DEV:	.14
RADIAL	MLC	2	10	1010	2.4	22-1A-61A	5.53
			11	(737 C)		22-1A-61B	5.26
			12			22-1A-61C	5.50
						MEAN:	5.43
						STD. DEV:	.15
RADIAL	MLC	5	8	1655	2.9	22-1A-68A	4.55
			9	(1382 C)		22-1A-68B	4.54
			10			22-1A-68C	4.47
						MEAN:	4.52
						STD. DEV:	.04

TABLE 11-6
SUMMARY OF IRRADIATION-INDUCED CHANGES IN THERMAL EXPANSIVITY OF H-429 GRAPHITE IRRADIATED IN CAPSULES OG-1, OG-2, AND OG-3

Log No.	Orientation	Mean Irradiation Temperature (K)	Fluence (X 10^{25} n/m^2) $(E > 29\ fJ)_{HTGR}$	Average Percent Change in CTE (295-773 K)
4974-04A	Axial	1165	3.0	-8
		1180	5.2	-4
		1170	7.2	-21
		1435	5.6	-13
		1460	8.6	-28
		1480	11.4	-41
		1705	6.6	-22
		1675	8.8	-30
	Radial	1165	3.0	+2
		1145	5.6	+1
		1170	7.2	-19
		1435	5.6	-9
		1460	8.6	-29
		1480	11.4	-39
		1705	6.6	-17
		1675	8.8	-27

TABLE 11-7
SUMMARY OF IRRADIATION-INDUCED CHANGES IN THERMAL EXPANSIVITY OF TS-1240 GRAPHITE IRRADIATED IN CAPSULES OG-2 AND OG-3

Log No.	Orientation	Location in Log	Mean Irradiation Temperature (K)	Fluence (X 10^{25} n/m^2) $(E > 29\ fJ)_{HTGR}$	Average Percent Change in CTE (295-773 K)
5651-73	Axial	Midlength-center	895	1.2	+7
			1040	1.7	+2
			1195	2.5	-1
			1250	4.9	-36
			1380	2.9	+1
			1415	5.9	-33
		Midlength-edge	880	2.3	+6
	Radial	Midlength-center	865	1.2	-1
			1080	1.7	-4
			1195	2.5	-4
			1200	4.9	-20
			1475	2.9	-11
			1500	5.9	-47
		Midlength-edge	880	2.3	+4

TABLE 11-8
TENSILE PROPERTIES OF H-451 GRAPHITE, LOT 266,
IRRADIATED IN CAPSULE OG-3

GRAPHITE GRADE: H-451

LOT NUMBER: 266

LOG NUMBER(S): 5651-28

ORIENTATION: AXIAL CRUCIBLE NO: 1

LOG LOCATION: MIDLENGTH-CENTER FLUENCE: 5.50*10EXP 25 N/M**2, E>0.18 MEV

HOLE NO.	MEAN IRR. TEMP. (K)	SPECIMEN NUMBER	TENSILE STRENGTH (MPA)	FRACTURE STRAIN (PCT)	YOUNG'S MODULUS (GPA)
16	885	T-111	17.2	.133	15.3
16	(612 C)	T-112	15.5	.105	18.1
22	870	T-113	17.6	.131	18.1
22	(597 C)	T-114	18.5		19.1
23	*	T-115	19.9	.125	20.7
23	*	T-116	18.3		14.4
24	*	T-117	18.9	.132	16.4
24	*	T-118	19.3	.167	12.6
		MEAN:	18.2 MPA (2633. PSI)	.132 PCT	16.8 GPA (2.44 MPSI)
		STD. DEV:	1.4 MPA (199. PSI)	.020 PCT	2.7 GPA (.39 MPSI)

ORIENTATION: AXIAL CRUCIBLE NO: 3

LOG LOCATION: MIDLENGTH-CENTER FLUENCE: 8.50*10EXP 25 N/M**2, E>0.18 MEV

HOLE NO.	MEAN IRR. TEMP. (K)	SPECIMEN NUMBER	TENSILE STRENGTH (MPA)	FRACTURE STRAIN (PCT)	YOUNG'S MODULUS (GPA)
16	1205	T-131	15.4	.100	24.5
16	(932 C)	T-132	20.2	.135	17.8
17	*	T-133	20.9	.120	22.4
17	*	T-134	14.9	.105	19.7
26	1190	T-135	21.0	.140	20.4
26	(917 C)	T-136	26.5	.152	20.9
27	*	T-137	15.9	.083	25.6
27	*	T-138	16.1	.112	18.4
		MEAN:	18.9 MPA (2735. PSI)	.118 PCT	21.2 GPA (3.08 MPSI)
		STD. DEV:	4.0 MPA (582. PSI)	.023 PCT	2.6 GPA (.41 MPSI)

TABLE 11-8 (Continued)

GRAPHITE GRADE: H-451

LOT NUMBER: 266

LOG NUMBER(S): 5651-28

ORIENTATION: AXIAL — CRUCIBLE NO: 5

LOG LOCATION: MIDLENGTH-CENTER — FLUENCE: 9.00*10EXP 25 N/M**2, E>0.18 MEV

HOLE NO.	MEAN IRR. TEMP. (K)	SPECIMEN NUMBER	TENSILE STRENGTH (MPA)	FRACTURE STRAIN (PCT)	YOUNG'S MODULUS (GPA)
21	1600	T-147	21.0	.193	11.5
21	(1327 C)	T-148	23.8	.143	22.7
22	*	T-149	18.4	.129	14.7
22	*	T-150	16.8	.115	15.7
23	*	T-151	20.5	.121	18.5
23	*	T-152	21.6	.110	23.6
24	*	T-153	18.4	.160	16.0
24	*	T-154	16.1	.103	16.1
		MEAN:	19.6 MPA (2842. PSI)	.134 PCT	17.3 GPA (2.52 MPSI)
		STD. DEV:	2.6 MPA (379. PSI)	.030 PCT	4.1 GPA (.59 MPSI)

ORIENTATION: RADIAL — CRUCIBLE NO: 3

LOG LOCATION: MIDLENGTH-CENTER — FLUENCE: 8.50*10EXP 25 N/M**2, E>0.18 MEV

HOLE NO.	MEAN IRR. TEMP. (K)	SPECIMEN NUMBER	TENSILE STRENGTH (MPA)	FRACTURE STRAIN (PCT)	YOUNG'S MODULUS (GPA)
14	1220	T-201	23.3	.145	20.8
14	(947 C)	T-202	22.9	.121	22.2
14	*	T-203	21.1	.115	21.2
15	*	T-204	25.5	.122	25.0
15	1205	T-205	26.7	.143	24.0
15	(932 C)	T-206	23.2	.123	25.5
16	*	T-207	24.1	.145	19.9
17	*	T-208	28.9	.167	21.0
26	1190	T-209	26.5	.139	23.3
27	(917 C)	T-210	19.9	.100	28.6
		MEAN:	24.2 MPA (3511. PSI)	.132 PCT	23.2 GPA (3.36 MPSI)
		STD. DEV:	2.7 MPA (397. PSI)	.019 PCT	2.7 GPA (.39 MPSI)

TABLE 11-9
TENSILE PROPERTIES OF H-451 GRAPHITE, LOT 408,
IRRADIATED IN CAPSULE OG-3

GRAPHITE GRADE: H-451

LOT NUMBER: 408

LOG NUMBER(S): 5651-86

ORIENTATION: AXIAL CRUCIBLE NO: 1

LOG LOCATION: MIDLENGTH-CENTER FLUENCE: 4.60*10EXP 25 N/M**2, E>0.10 MEV

HOLE NO.	MEAN IRR. TEMP. (K)	SPECIMEN NUMBER	TENSILE STRENGTH (MPA)	FRACTURE STRAIN (PCT)	YOUNG'S MODULUS (GPA)
10	940	T-40501	20.4	.173	15.0
10	(667 C)	T-40503	15.8	.145	14.2
11	*	T-40505	17.3	.160	11.6
11	*	T-40507	12.8	.111	12.4
12	*	T-40509	18.5	.184	12.2
12	*	T-40511	17.8	.155	12.0
13	*	T-40513	16.2	.140	13.5
13	*	T-40515	19.0	.184	12.2
14	*	T-40517	18.2	.159	12.6
14	*	T-40519	13.7	.110	16.0
15	*	T-40521	18.3	.182	12.1
15	*	T-40523	18.5	.166	11.0
		MEAN:	17.2 MPA (2497. PSI)	.159 PCT	12.5 GPA (1.82 MPSI)
		STD. DEV:	2.2 MPA (322. PSI)	.028 PCT	1.6 GPA (.23 MPSI)

ORIENTATION: AXIAL CRUCIBLE NO: 1

LOG LOCATION: MIDLENGTH-EDGE FLUENCE: 4.60*10EXP 25 N/M**2, E>0.10 MEV

HOLE NO.	MEAN IRR. TEMP. (K)	SPECIMEN NUMBER	TENSILE STRENGTH (MPA)	FRACTURE STRAIN (PCT)	YOUNG'S MODULUS (GPA)
25	900	T-40741			
25	(627 C)	T-40743	25.1	.200	14.4
26	*	T-40745	26.9	.215	14.1
26	*	T-40747	23.8	.188	15.7
27	*	T-40749	25.5	.145	22.0
27	*	T-40751	26.4	.170	21.4
28	*	T-40753	19.5	.119	24.3
28	*	T-40755	26.8	.182	16.4
29	*	T-40757	26.4	.160	19.1
29	*	T-40759	24.7	.220	12.4
30	*	T-40761	22.7	.178	17.2
30	*	T-40763	25.4	.155	16.8
		MEAN:	24.8 MPA (3602. PSI)	.176 PCT	17.6 GPA (2.55 MPSI)
		STD. DEV:	2.2 MPA (319. PSI)	.030 PCT	3.7 GPA (.54 MPSI)

TABLE 11-9 (Continued)

GRAPHITE GRADE: H-451

LOT NUMBER: 408

LOG NUMBER(S): 5651-86

ORIENTATION: AXIAL CRUCIBLE NO: 6

LOG LOCATION: MIDLENGTH-CENTER FLUENCE: 4.10*10EXP 25 N/M**2, E>0.18 MEV

HOLE NO.	MEAN IRR. TEMP. (K)	SPECIMEN NUMBER	TENSILE STRENGTH (MPA)	FRACTURE STRAIN (PCT)	YOUNG'S MODULUS (GPA)
8	1160	T-40597	17.7	.196	10.8
9	(887 C)	T-40599	17.8	.162	12.7
10	*	T-40601	14.7	.131	12.7
11	*	T-40603	14.7	.189	9.0
12	*	T-40605	18.7	.171	15.2
13	*	T-40607	14.5	.133	15.5
14	1130	T-40609	17.2	.183	10.6
15	(857 C)	T-40611	15.5	.193	11.9
16	*	T-40613	19.0	.130	16.5
23	*	T-40615	18.9	.223	10.7
		MEAN:	16.9 MPA (2447. PSI)	.171 PCT	12.6 GPA (1.82 MPSI)
		STD. DEVT	1.8 MPA (267. PSI)	.032 PCT	2.9 GPA (.36 MPSI)

ORIENTATION: AXIAL CRUCIBLE NO: 8

LOG LOCATION: MIDLENGTH-EDGE FLUENCE: 4.10*10EXP 25 N/M**2, E>0.18 MEV

HOLE NO.	MEAN IRR. TEMP. (K)	SPECIMEN NUMBER	TENSILE STRENGTH (MPA)	FRACTURE STRAIN (PCT)	YOUNG'S MODULUS (GPA)
8	1160	T-40765	28.8	.248	13.4
9	(887 C)	T-40767	26.5	.195	18.2
10	*	T-40769	25.5	.155	24.4
11	*	T-40771	24.2	.183	15.5
12	*	T-40773	26.6	.235	12.3
13	*	T-40775	22.9	.212	12.7
14	1130	T-40777	21.9	.210	11.6
15	(857 C)	T-40779	22.3	.202	15.1
16	*	T-40781	24.9	.212	14.8
23	*	T-40783	26.2	.202	14.7
		MEAN:	25.0 MPA (3622. PSI)	.205 PCT	15.3 GPA (2.21 MPSI)
		STD. DEVT	2.2 MPA (319. PSI)	.026 PCT	3.7 GPA (.54 MPSI)

TABLE 11-9 (Continued)

GRAPHITE GRADE: H-451

LOT NUMBER: 408

LOG NUMBER(S): 5651-86

ORIENTATION: AXIAL CRUCIBLE NO: 3

LOG LOCATION: MIDLENGTH-CENTER FLUENCE: 5.50*10EXP 25 N/M**2, E>0.18 MEV

HOLE NO.	MEAN IRR. TEMP. (K)	SPECIMEN NUMBER	TENSILE STRENGTH (MPA)	FRACTURE STRAIN (PCT)	YOUNG'S MODULUS (GPA)
10	1245	T-40525	18.9	.109	24.7
10	(972 C)	T-40527	19.1	.161	14.3
10	*	T-40529	22.4	.176	14.7
11	*	T-40531	22.1	.156	18.0
11	*	T-40533	21.6	.160	17.6
11	*	T-40535	23.6	.177	16.8
12	*	T-40537	17.4	.159	12.8
12	*	T-40539	21.8	.175	16.3
12	*	T-40541	20.3	.170	15.3
13	*	T-40543	18.2	.131	17.1
13	*	T-40545	23.3	.163	20.6
13	*	T-40547	18.1	.125	17.5
		MEAN:	20.6 MPA (2984. PSI)	.155 PCT	17.1 GPA (2.49 MPSI)
		STD. DEV:	2.2 MPA (315. PSI)	.022 PCT	3.1 GPA (.45 MPSI)

ORIENTATION: AXIAL CRUCIBLE NO: 5

LOG LOCATION: MIDLENGTH-CENTER FLUENCE: 5.80*10EXP 25 N/M**2, E>0.18 MEV

HOLE NO.	MEAN IRR. TEMP. (K)	SPECIMEN NUMBER	TENSILE STRENGTH (MPA)	FRACTURE STRAIN (PCT)	YOUNG'S MODULUS (GPA)
12	1635	T-40549	22.0	.150	16.2
12	(1362 C)	T-40551	17.5	.167	13.2
13	*	T-40553	23.1	.183	14.1
13	*	T-40555	21.1	.223	13.3
14	*	T-40557	21.9	.150	17.8
14	*	T-40559	23.3	.165	16.3
15	*	T-40561	13.6	.173	11.3
15	*	T-40563	20.0	.247	9.8
20	1620	T-40565	22.2	.250	10.9
20	(1347 C)	T-40567	23.3	.151	20.3
		MEAN:	20.8 MPA (3015. PSI)	.186 PCT	14.3 GPA (2.08 MPSI)
		STD. DEV:	3.1 MPA (447. PSI)	.039 PCT	3.3 GPA (.48 MPSI)

TABLE 11-9 (Continued)

GRAPHITE GRADE: H-451

LOT NUMBER: 408

LOG NUMBER(S): 5651-86

ORIENTATION: RADIAL CRUCIBLE NO: 8

LOG LOCATION: MIDLENGTH-CENTER FLUENCE: 4.10*10EXP 25 N/M**2, E>0.18 MEV

HOLE NO.	MEAN IRR. TEMP. (K)	SPECIMEN NUMBER	TENSILE STRENGTH (MPA)	FRACTURE STRAIN (PCT)	YOUNG'S MODULUS (GPA)
24	1115	T-40661	21.4	.206	11.2
24	(842 C)	T-40663	15.8	.186	11.2
25	*	T-40665	12.8	.100	13.9
25	*	T-40667	17.0	.167	12.7
		MEAN:	16.7 MPA (2429. PSI)	.165 PCT	12.3 GPA (1.78 MPSI)
		STD. DEV:	3.6 MPA (519. PSI)	.046 PCT	1.3 GPA (.19 MPSI)

ORIENTATION: RADIAL CRUCIBLE NO: 3

LOG LOCATION: MIDLENGTH-CENTER FLUENCE: 5.50*10EXP 25 N/M**2, E>0.18 MEV

HOLE NO.	MEAN IRR. TEMP. (K)	SPECIMEN NUMBER	TENSILE STRENGTH (MPA)	FRACTURE STRAIN (PCT)	YOUNG'S MODULUS (GPA)
28	1200	T-40621	25.5	.192	16.4
28	(927 C)	T-40623	16.1	.131	14.8
28	*	T-40625	23.5	.162	17.6
29	*	T-40627	17.5	.158	13.1
29	*	T-40629	24.5	.171	18.4
29	*	T-40631	22.3	.195	12.7
30	*	T-40633	21.7	.194	12.7
30	*	T-40635	22.0	.147	20.1
30	*	T-40637	23.2	.167	16.8
31	*	T-40639	22.5	.205	12.7
31	*	T-40641	23.3	.203	15.0
31	*	T-40643	18.3	.149	14.8
		MEAN:	21.7 MPA (3145. PSI)	.173 PCT	15.4 GPA (2.24 MPSI)
		STD. DEV:	2.9 MPA (419. PSI)	.025 PCT	2.5 GPA (.36 MPSI)

TABLE 11-10
TENSILE PROPERTIES OF H-451 GRAPHITE, LOT 426,
IRRADIATED IN CAPSULE OG-3

GRAPHITE GRADE: H-451

LOT NUMBER: 426

LOG NUMBER(S): 6484-33

ORIENTATION: AXIAL CRUCIBLE NO: 6

LOG LOCATION: MIDLENGTH-CENTER FLUENCE: 2.70*10EXP 25 N/M**2, E>0.18 MEV

HOLE NO.	MEAN IRR. TEMP. (K)	SPECIMEN NUMBER	TENSILE STRENGTH (MPA)	FRACTURE STRAIN (PCT)	YOUNG'S MODULUS (GPA)
24	1210	33-2A-1A	27.8	.229	12.5
28	(937 C)	33-2A-1B	21.4	.201	14.2
30	*	33-2A-2A	26.0	.228	16.5
36	*	33-2A-2B	21.1	.183	14.5
34	*	33-2A-3A	22.4	.213	13.9
		MEAN:	23.7 MPA (3442. PSI)	.211 PCT	14.3 GPA (2.08 MPSI)
		STD. DEV:	3.0 MPA (434. PSI)	.019 PCT	1.5 GPA (.21 MPSI)

LOG NUMBER(S): 6484-34

28	1210	34-2A-1A	21.8	.197	12.5
26	(937 C)	34-2A-1B	20.7	.200	11.1
32	*	34-2A-2A	22.6	.210	11.8
34	*	34-2A-2B	22.7	.192	14.6
38	*	34-2A-3A	16.3	.174	10.8
		MEAN:	20.8 MPA (3020. PSI)	.195 PCT	12.1 GPA (1.76 MPSI)
		STD. DEV:	2.6 MPA (382. PSI)	.013 PCT	1.5 GPA (.22 MPSI)

LOG NUMBER(S): 6484-41

24	1210	41-2A-1A	18.3	.165	15.8
26	(937 C)	41-2A-1B	21.3	.192	14.6
30	*	41-2A-8A	19.9	.163	15.4
32	*	41-2A-8B	21.5	.242	10.3
36	*	41-2A-10A	19.5	.184	12.9
		MEAN:	20.1 MPA (2914. PSI)	.189 PCT	13.8 GPA (2.00 MPSI)
		STD. DEV:	1.3 MPA (193. PSI)	.032 PCT	2.2 GPA (.32 MPSI)

TABLE 11-10 (Continued)

GRAPHITE GRADE: H-451

LOT NUMBER: 426

LOG NUMBER(S): 6484-33

ORIENTATION: AXIAL CRUCIBLE NO: 6

LOG LOCATION: MIDLENGTH-EDGE FLUENCE: 2.70*10EXP 25 N/M**2, E>0.18 MEV

HOLE NO.	MEAN IRR. TEMP. (K)	SPECIMEN NUMBER	TENSILE STRENGTH (MPA)	FRACTURE STRAIN (PCT)	YOUNG'S MODULUS (GPA)
25	1210	33-2A-101A	27.9	.218	15.4
27	(937 C)	33-2A-101B	18.5	.143	19.2
31	*	33-2A-102A	24.0	.240	11.3
33	*	33-2A-102B	24.1	.186	18.3
37	*	33-2B-101A	32.0	.313	10.8
		MEAN:	25.3 MPA (3669. PSI)	.220 PCT	15.0 GPA (2.17 MPSI)
		STD. DEV:	5.0 MPA (732. PSI)	.064 PCT	3.9 GPA (.56 MPSI)

LOG NUMBER(S): 6484-34

25	1210	34-2A-101A	30.9	.271	16.9
29	(937 C)	34-2A-101B	28.1	.235	14.5
31	*	34-2A-102A	26.8	.230	14.5
35	*	34-2A-102B	27.0	.251	10.5
37	*	34-2B-103A	26.2		14.3
		MEAN:	27.8 MPA (4033. PSI)	.247 PCT	14.1 GPA (2.05 MPSI)
		STD. DEV:	1.9 MPA (272. PSI)	.018 PCT	2.3 GPA (.34 MPSI)

LOG NUMBER(S): 6484-41

27	1210	41-2A-101A	25.3	.221	15.4
29	(937 C)	41-2A-101B	24.3	.185	16.5
33	*	41-2A-102A	25.5	.280	10.3
35	*	41-2A-102B	24.7	.263	11.3
38	*	41-2B-101A	28.4	.231	15.9
		MEAN:	25.6 MPA (3718. PSI)	.236 PCT	13.9 GPA (2.01 MPSI)
		STD. DEV:	1.6 MPA (237. PSI)	.037 PCT	2.8 GPA (.41 MPSI)

TABLE 11-10 (Continued)

GRAPHITE GRADE: H-451

LOT NUMBER: 426

LOG NUMBER(S): 6484-33

ORIENTATION: RADIAL CRUCIBLE NO: 3

LOG LOCATION: MIDLENGTH-CENTER FLUENCE: 2.80*10EXP 25 N/M**2, E>0.18 MEV

HOLE NO.	MEAN IRR. TEMP. (K)	SPECIMEN NUMBER	TENSILE STRENGTH (MPA)	FRACTURE STRAIN (PCT)	YOUNG'S MODULUS (GPA)
32	1205	33-2A-33A	14.1	.143	12.5
34	(932 C)	33-2A-33B	13.2	.130	13.1
36	*	33-2A-34A	12.0	.137	10.1
38	*	33-2A-34B	14.1	.155	11.3
		MEAN:	13.3 MPA (1935. PSI)	.141 PCT	11.7 GPA (1.70 MPSI)
		STD. DEV:	1.0 MPA (141. PSI)	.011 PCT	1.3 GPA (.19 MPSI)

LOG NUMBER(S): 6484-34

32	1205	34-2A-33A	17.9	.188	10.3
34	(932 C)	34-2A-33B	18.4	.172	12.2
38	*	34-2A-34A	17.7	.185	12.2
36	*	34-2A-34B	17.5	.186	11.7
		MEAN:	17.9 MPA (2595. PSI)	.183 PCT	11.6 GPA (1.68 MPSI)
		STD. DEV:	.4 MPA (57. PSI)	.007 PCT	.9 GPA (.13 MPSI)

LOG NUMBER(S): 6484-41

32	1205	41-2A-40A	18.3	.183	11.8
34	(932 C)	41-2A-40B	18.2	.192	11.4
36	*	41-2B-56A	18.0	.205	10.0
38	*	41-2B-56B	19.6	.177	14.2
		MEAN:	18.5 MPA (2685. PSI)	.189 PCT	11.9 GPA (1.72 MPSI)
		STD. DEV:	.7 MPA (103. PSI)	.012 PCT	1.7 GPA (.25 MPSI)

TABLE 11-10 (Continued)

GRAPHITE GRADE: H-451

LOT NUMBER: 426

LOG NUMBER(S): 6484-33

ORIENTATION: RADIAL CRUCIBLE NO: 8

LOG LOCATION: MIDLENGTH-EDGE FLUENCE: 2.00*10EXP 25 N/M**2, E>0.18 MEV

HOLE NO.	MEAN IRR. TEMP. (K)	SPECIMEN NUMBER	TENSILE STRENGTH (MPA)	FRACTURE STRAIN (PCT)	YOUNG'S MODULUS (GPA)
27	1105	33-2A-133A	17.1	.113	21.5
35	(832 C)	33-2A-133B	22.0	.240	10.4
33	*	33-2A-134A	21.7	.189	14.1
38	*	33-2A-134B	20.7	.171	18.1
29	*	33-2A-135A	24.4	.221	14.1
		MEAN:	21.2 MPA (3073. PSI)	.187 PCT	15.6 GPA (2.26 MPSI)
		STD. DEV:	2.7 MPA (388. PSI)	.049 PCT	4.2 GPA (.61 MPSI)

LOG NUMBER(S): 6484-34

27	1105	34-2A-133A	27.3	.265	11.6
31	(832 C)	34-2A-133B	18.8	.226	9.5
33	*	34-2A-134A	23.9	.243	15.0
37	*	34-2A-134B	17.1	.138	16.0
		MEAN:	21.8 MPA (3155. PSI)	.218 PCT	13.0 GPA (1.89 MPSI)
		STD. DEV:	4.7 MPA (680. PSI)	.056 PCT	3.0 GPA (.44 MPSI)

LOG NUMBER(S): 6484-41

29	1105	41-2A-160A	21.8	.256	12.1
31	(832 C)	41-2A-160B	19.4	.248	9.0
35	*	41-2A-162A	22.0	.270	9.8
37	*	41-2A-162B	17.3	.151	17.6
		MEAN:	20.1 MPA (2922. PSI)	.231 PCT	12.1 GPA (1.76 MPSI)
		STD. DEV:	2.2 MPA (319. PSI)	.054 PCT	3.9 GPA (.56 MPSI)

TABLE 11-11
TENSILE PROPERTIES OF TS-1240 GRAPHITE IRRADIATED
IN CAPSULE OG-3

GRAPHITE GRADE: TS1240

LOT NUMBER: 1

LOG NUMBER(S): 5651-73

ORIENTATION: RADIAL CRUCIBLE NO: 4

LOG LOCATION: MIDLENGTH-CENTER FLUENCE: 5.90*10EXP 25 N/M**2, E>0.18 MEV

HOLE NO.	MEAN IRR. TEMP. (K)	SPECIMEN NUMBER	TENSILE STRENGTH (MPA)	FRACTURE STRAIN (PCT)	YOUNG'S MODULUS (GPA)
7	1515	T-40157	13.2	.110	13.2
7	(1242 C)	T-40159	13.9	.119	14.1
8	*	T-40161	16.0	.117	14.6
8	*	T-40163	15.9	.112	15.6
9	1500	T-40165	16.8	.154	12.0
9	(1227 C)	T-40167	13.9	.120	13.0
10	*	T-40169	14.7	.099	21.1
10	*	T-40171	17.4	.160	12.6
		MEAN:	15.2 MPA (2209. PSI)	.124 PCT	14.5 GPA (2.11 MPSI)
		STD. DEV:	1.5 MPA (221. PSI)	.022 PCT	2.9 GPA (.42 MPSI)

TABLE 11-12
TENSILE PROPERTIES OF H-327 GRAPHITE IRRADIATED
IN CAPSULE OG-3

GRAPHITE GRADE: H-327

LOT NUMBER: --

LOG NUMBER(S): 4974-03

ORIENTATION: AXIAL CRUCIBLE NO: 2

LOG LOCATION: MIDLENGTH-CENTER FLUENCE: 7.20*10EXP 25 N/M**2, E>0.18 MEV

HOLE NO.	MEAN IRR. TEMP. (K)	SPECIMEN NUMBER	TENSILE STRENGTH (MPA)	FRACTURE STRAIN (PCT)	YOUNG'S MODULUS (GPA)
29	960	T-251	16.8	.110	19.1
29	(687 C)	T-252	10.9	.078	17.7
30	*	T-253	16.2	.154	14.7
30	*	T-254	16.8	.147	14.4
31	940	T-255	15.5	.113	18.1
31	(667 C)	T-256	18.4	.135	20.2
32	*	T-257	12.1	.121	13.8
32	*	T-258	15.1	.135	15.0
33	*	T-259	14.4	.090	22.7
33	*	T-260	14.9	.090	22.0
		MEAN:	15.1 MPA (2194. PSI)	.117 PCT	17.8 GPA (2.58 MPSI)
		STD. DEV:	2.3 MPA (327. PSI)	.026 PCT	3.2 GPA (.47 MPSI)

ORIENTATION: AXIAL CRUCIBLE NO: 2

LOG LOCATION: MIDLENGTH-CENTER FLUENCE: 4.60*10EXP 25 N/M**2, E>0.18 MEV

HOLE NO.	MEAN IRR. TEMP. (K)	SPECIMEN NUMBER	TENSILE STRENGTH (MPA)	FRACTURE STRAIN (PCT)	YOUNG'S MODULUS (GPA)
14	1015	T-317	16.2	.140	18.0
14	(742 C)	T-318	13.6	.105	16.3
15	*	T-319	17.2	.135	14.6
15	*	T-320	12.7	.114	18.0
16	985	T-321	13.5	.116	18.0
16	(712 C)	T-322	17.2	.110	21.2
17	*	T-323	16.7	.126	17.5
17	*	T-324	15.4	.115	18.4
		MEAN:	15.6 MPA (2257. PSI)	.120 PCT	17.8 GPA (2.58 MPSI)
		STD. DEV:	2.1 MPA (303. PSI)	.012 PCT	1.9 GPA (.27 MPSI)

TABLE 11-12 (Continued)

GRAPHITE GRADE: H-327

LOT NUMBER: **

LOG NUMBER(S): 4974-03

ORIENTATION: RADIAL CRUCIBLE NO: 2

LOG LOCATION: MIDLENGTH-CENTER FLUENCE: 4.60*10EXP 25 N/M**2, E>0.18 MEV

HOLE NO.	MEAN IRR. TEMP. (K)	SPECIMEN NUMBER	TENSILE STRENGTH (MPA)	FRACTURE STRAIN (PCT)	YOUNG'S MODULUS (GPA)
24	955	T-411	10.3	.121	9.6
24	(682 C)	T-412	4.1	.165	
25	*	T-413	2.4	.054	
25	*	T-414	9.8	.160	7.5
26	*	T-415	7.8	.100	9.5
26	*	T-416	8.9	.135	6.7
27	*	T-417	7.8	.161	5.6
27	*	T-418	4.5	.100	
28	*	T-419	10.6	.134	11.1
28	*	T-420	7.5	.100	8.6
		MEAN:	7.4 MPA (1070. PSI)	.123 PCT	8.4 GPA (1.21 MPSI)
		STD. DEV:	2.8 MPA (408. PSI)	.035 PCT	1.9 GPA (.27 MPSI)

ORIENTATION: RADIAL CRUCIBLE NO: 6

LOG LOCATION: MIDLENGTH-CENTER FLUENCE: 5.40*10EXP 25 N/M**2, E>0.18 MEV

HOLE NO.	MEAN IRR. TEMP. (K)	SPECIMEN NUMBER	TENSILE STRENGTH (MPA)	FRACTURE STRAIN (PCT)	YOUNG'S MODULUS (GPA)
14	1250	T-421	9.1	.145	8.0
14	(977 C)	T-422	10.8	.163	9.0
15	*	T-423	10.5	.150	9.2
15	*	T-424	8.6	.148	8.0
16	*	T-425	5.9	.090	
16	*	T-426	9.2	.140	8.5
23	1220	T-427	3.8	.161	
23	(947 C)	T-428	7.6	.148	7.1
		MEAN:	8.2 MPA (1184. PSI)	.143 PCT	8.3 GPA (1.20 MPSI)
		STD. DEV:	2.3 MPA (339. PSI)	.023 PCT	.8 GPA (.11 MPSI)

TABLE 11-13
SUMMARY OF TENSILE PROPERTY DATA FOR H-451 GRAPHITE IRRADIATED IN CAPSULES OG-1, OG-2, AND OG-3

Lot	Log No.	Orientation	Location in Log	Irradiation Conditions		Ultimate Tensile Strength			Young's Modulus		
				Mean Irrad. Temp. (K)	Fluence ($\times 10^{25}$ n/m^2) ($E > 29$ fJ)$_{HTGR}$	Observed Value ± Std. Dev. (MPa)	Percent Increase ± Std. Dev.	Coefficient of Variation (%)	Observed Value ± Std. Dev. (GPa)	Percent Increase ± Std. Dev.	Coefficient of Variation (%)
266	5651-28	Axial	Midlength-center	--	0	10.8 ± 0.9	--	8	7.9 ± 0.6	--	8
				890	1.4	16.7 ± 1.8	55 ± 17	11	18.1 ± 1.4	131 ± 18	8
				870	2.0	17.1 ± 1.2	59 ± 11	7	15.3 ± 0.8	95 ± 10	5
				860	2.6	17.1 ± 2.2	59 ± 21	13	17.5 ± 1.4	123 ± 18	8
				880	5.5	18.2 ± 1.4	68 ± 13	8	16.8 ± 2.7	114 ± 34	16
				1200	3.0	16.3 ± 1.9	52 ± 17	12	14.2 ± 1.7	81 ± 21	12
				1200	5.3	19.1 ± 1.8	78 ± 17	9	17.6 ± 1.0	124 ± 13	6
				1200	8.5	18.9 ± 4.0	75 ± 37	21	21.2 ± 2.8	170 ± 36	13
				1630	3.2	15.4 ± 0.8	43 ± 7	5	13.0 ± 0.9	65 ± 11	7
				1600	9.0	19.6 ± 2.6	81 ± 24	13	17.3 ± 4.1	119 ± 52	24
		Radial	Midlength center	--	0	11.5 ± 1.7	--	15	7.0 ± 0.3	--	4
				1190	2.8	18.3 ± 1.9	58 ± 16	10	13.0 ± 0.9	88 ± 13	7
				1200	8.5	24.2 ± 2.7	110 ± 24	11	23.2 ± 2.7	236 ± 39	12
408	5651-86	Axial	Midlength-center	--	0	12.9 ± 1.7	--	13	7.4 ± 0.7	--	9
				940	4.6	17.2 ± 2.2	33 ± 17	13	12.5 ± 1.6	69 ± 21	13
				1150	4.1	16.9 ± 1.8	31 ± 14	11	12.6 ± 2.5	70 ± 34	20
				1250	5.5	20.6 ± 2.2	59 ± 17	11	17.1 ± 3.1	131 ± 42	18
				1630	5.8	20.8 ± 3.1	61 ± 24	15	14.3 ± 3.3	93 ± 45	23
			Midlength-edge	--	0	17.4 ± 1.5	--	9	8.3 ± 0.7	--	8
				900	4.6	24.8 ± 2.2	43 ± 13	9	17.6 ± 3.7	111 ± 45	21
				1150	4.1	25.0 ± 2.2	44 ± 13	9	15.3 ± 3.7	84 ± 45	24
		Radial	Midlength-center	--	0	12.2 ± 1.6	--	13	7.2 ± 0.8	--	11
				1120	4.1	16.7 ± 3.6	37 ± 30	22	12.3 ± 1.3	71 ± 18	11
				1200	5.5	21.7 ± 2.9	77 ± 24	13	15.4 ± 2.5	115 ± 35	16
426	6484-33	Axial	Midlength-center	--	0	16.4 ± 1.4	--	8	7.8 ± 0.8	--	10
				1210	2.7	23.7 ± 3.0	45 ± 18	13	14.3 ± 1.5	83 ± 19	10
			Midlength-edge	--	0	18.6 ± 1.9	--	10	9.3 ± 1.4	--	15
				1210	2.7	25.3 ± 5.0	36 ± 27	20	15.0 ± 3.9	61 ± 42	26
		Radial	Midlength-center	--	0	8.5 ± 2.4	--	28	6.3 ± 0.5	--	8
				1210	2.8	13.3 ± 1.0	56 ± 12	8	11.7 ± 1.3	86 ± 21	11
			Midlength-edge	--	0	16.6 ± 1.2	--	7	7.6 ± 0.7	--	9
				1110	2.0	21.2 ± 2.7	28 ± 16	13	15.6 ± 4.2	105 ± 55	27
	6484-34	Axial	Midlength-center	--	0	12.9 ± 2.2	--	17	7.5 ± 0.7	--	9
				1210	2.7	20.8 ± 2.6	61 ± 20	13	12.1 ± 1.5	61 ± 20	12
			Midlength-edge	--	0	18.5 ± 1.3	--	7	8.7 ± 0.9	--	10
				1210	2.7	27.8 ± 1.9	50 ± 10	7	14.1 ± 2.3	62 ± 26	16
		Radial	Midlength-center	--	0	13.3 ± 0.9	--	6	7.0 ± 0.5	--	6
				1210	2.8	17.9 ± 0.4	35 ± 3	2	11.6 ± 0.9	66 ± 13	8
			Midlength-edge	--	0	16.5 ± 1.7	--	10	7.3 ± 0.5	--	7
				1110	2.0	21.8 ± 4.7	32 ± 28	22	13.0 ± 3.0	78 ± 41	23
	6484-41	Axial	Midlength-center	--	0	14.0 ± 1.3	--	9	7.7 ± 0.6	--	8
				1210	2.7	20.1 ± 1.3	44 ± 9	6	13.8 ± 2.2	79 ± 29	16
			Midlength-edge	--	0	16.8 ± 1.3	--	8	8.1 ± 0.7	--	8
				1210	2.7	25.6 ± 1.6	52 ± 10	6	13.9 ± 2.8	72 ± 35	20
		Radial	Midlength-center	--	0	11.6 ± 1.7	--	14	6.4 ± 0.6	--	9
				1210	2.8	18.5 ± 0.7	59 ± 6	4	11.9 ± 1.7	86 ± 27	14
			Midlength-edge	--	0	14.5 ± 1.1	--	8	7.0 ± 0.6	--	9
				1110	2.0	20.1 ± 2.2	39 ± 15	11	12.1 ± 3.9	73 ± 56	32

TABLE 11-14
SUMMARY OF TENSILE PROPERTY DATA FOR TS-1240 GRAPHITE IRRADIATED IN CAPSULES OG-1, OG-2, AND OG-3

Lot	Log No.	Orientation	Location in Log	Irradiation Conditions		Ultimate Tensile Strength			Young's Modulus		
				Mean Irrad. Temp. (K)	Fluence ($\times 10^{25}$ n/m^2) ($E > 29$ fJ)$_{HTGR}$	Observed Value ± Std. Dev. (MPa)	Percent Increase ± Std. Dev.	Coefficient of Variation (%)	Observed Value ± Std. Dev. (GPa)	Percent Increase ± Std. Dev.	Coefficient of Variation (%)
1	5651-73	Axial	Midlength-center	--	0	10.8 ± 1.7	--	16	6.2 ± 0.7	--	11
				890	1.2	12.7 ± 3.1	17 ± 29	24	11.9 ± 2.2	91 ± 36	18
				1040	1.7	14.3 ± 2.7	32 ± 25	19	11.9 ± 1.2	91 ± 19	10
				1190	2.5	14.6 ± 1.8	35 ± 16	12	11.4 ± 0.9	84 ± 14	8
				1380	2.9	13.1 ± 3.7	21 ± 34	28	11.7 ± 1.4	88 ± 23	12
		Radial	Midlength-center	--	0	9.5 ± 2.1	--	22	6.2 ± 0.8	--	13
				1080	1.7	13.5 ± 2.3	41 ± 24	17	10.3 ± 1.8	67 ± 29	17
				1515	5.9	15.2 ± 1.5	60 ± 16	10	14.5 ± 2.9	134 ± 47	20

TABLE 11-15
SUMMARY OF TENSILE PROPERTY DATA FOR H-327 GRAPHITE IRRADIATED IN CAPSULES OG-1, OG-2, AND OG-3

Lot	Log No.	Orientation	Location in Log	Irradiation Conditions		Ultimate Tensile Strength			Young's Modulus		
				Mean Irrad. Temp. (K)	Fluence ($\times 10^{25}$ n/m^2) $(E > 29\ fJ)_{HTGR}$	Observed Value ± Std. Dev. (MPa)	Percent Increase ± Std. Dev.	Coefficient of Variation (%)	Observed Value ± Std. Dev. (GPa)	Percent Increase ± Std. Dev.	Coefficient of Variation (%)
FSV-42	4974-03	Axial	Midlength-center	--	0	9.1 ± 1.1	--	12	9.0 ± 0.8	--	9
				1010	2.2	13.4 ± 2.6	47 ± 29	19	15.5 ± 2.8	73 ± 31	18
				1000	4.6	15.6 ± 2.1	71 ± 23	13	17.8 ± 1.9	98 ± 21	11
				950	7.2	15.1 ± 2.3	66 ± 25	15	17.8 ± 3.2	98 ± 36	18
				1060	3.6	16.7 ± 2.4	83 ± 26	14	19.1 ± 3.4	113 ± 38	18
				1110	4.5	16.8 ± 2.5	84 ± 27	15	17.6 ± 2.2	96 ± 25	13
				1150	2.3	14.7 ± 1.9	61 ± 21	13	20.8 ± 1.9	132 ± 21	9
				1270	2.7	13.4 ± 2.3	47 ± 25	17	17.1 ± 2.8	91 ± 31	16
				1260	5.7	15.3 ± 3.2	68 ± 35	21	16.0 ± 2.1	78 ± 24	13
				1390	6.3	13.8 ± 4.0	52 ± 44	29	16.0 ± 2.1	78 ± 23	13
			Midlength-edge	--	0	15.1 ± 2.0	--	13	13.3 ± 1.7	--	13
				940	2.6	21.7 ± 1.9	44 ± 13	9	26.5 ± 2.3	99 ± 17	9
				1060	1.9	19.2 ± 1.7	27 ± 11	9	21.4 ± 1.8	61 ± 13	8
				1340	3.3	19.5 ± 1.8	29 ± 12	9	22.3 ± 1.3	67 ± 10	6
		Radial	Midlength-center	--	0	5.7 ± 2.0	--	35	4.4 ± 0.6	--	14
				960	4.6	7.4 ± 2.8	30 ± 50	38	8.4 ± 1.9	91 ± 42	23
				1260	3.0	6.6 ± 1.4	17 ± 24	21	8.5 ± 1.4	92 ± 31	16
				1240	5.4	8.2 ± 2.3	44 ± 40	28	8.3 ± 0.8	89 ± 18	10

TABLE 11-16
THERMAL CONDUCTIVITY OF H-451 GRAPHITE, LOT 266,
IRRADIATED IN CAPSULE OG-3

LOT NUMBER: 266 LOG NUMBER(S):5651-28

ORIENTATION: AXIAL LOG LOCATION: MIDLENGTH-CENTER

CRUCTBLE NO: 1 FLUENCE: 5.50*EXP25
N/M**2, E>.18MEV

MEAN IRR. TEMP. (K)	SPECIMEN NUMBER	THERMAL CONDUCTIVITY (W/M-K) AT: 295K (22 C)	473K (200C)	673K (400C)	873K (600C)	1073K (800C)	IRRAD. TEMP.
300	201	30.8	36.1	38.7			33.9
(427 C)	202	29.3	32.2	34.9			30.2
*	203	30.6	37.9	38.5			33.9
*	204	27.7	31.9	30.8			28.2
	MEAN:	29.6	35.0	35.7			31.5
	STD. DEV:	1.4	3.4	3.7			4.4

CRUCTBLE NO: 7 FLUENCE: 7.70*EXP25
N/M**2, E>.18MEV

MEAN IRR. TEMP. (K)	SPECIMEN NUMBER	THERMAL CONDUCTIVITY (W/M-K) AT: 295K (22 C)	473K (200C)	673K (400C)	873K (600C)	1073K (800C)	IRRAD. TEMP.
1210	205	35.7	38.4	37.0	33.7	32.8	29.8
(937 C)	206	40.5	41.5	39.1	33.3	31.0	30.2
*	207	51.3	50.2	52.9	50.8	45.6	39.6
*	208	46.8	53.1	48.3	45.4	39.1	36.8
	MEAN:	43.6	45.8	44.3	40.8	37.1	34.1
	STD. DEV:	6.8	7.0	7.5	8.7	6.6	5.9

CRUCTBLE NO: 5 FLUENCE: 9.00*EXP25
N/M**2, E>.18MEV

MEAN IRR. TEMP. (K)	SPECIMEN NUMBER	THERMAL CONDUCTIVITY (W/M-K) AT: 295K (22 C)	473K (200C)	673K (400C)	873K (600C)	1073K (800C)	IRRAD. TEMP.
1620	210	61.0	66.2	56.8	52.6	50.8	33.0
(1347 C)	211	66.8	69.7	61.4	55.7	54.2	34.1
*	212	65.4	68.1	59.3	55.2	50.7	33.5
*	213	82.1	82.4	75.9	63.2	67.7	37.3
	MEAN:	68.9	71.6	63.3	56.7	55.8	34.5
	STD. DEV:	9.2	7.3	8.6	4.6	8.1	1.8

TABLE 16 (Continued)

LOT NUMBER: 266 LOG NUMBER(S):5651-28

ORIENTATION: RADIAL LOG LOCATION: MIDLENGTH-CENTER

CRUCIBLE NO: 1 FLUENCE: 5.50*EXP25 N/M**2, E>.18MEV

MEAN IRR. TEMP. (K)	SPECIMEN NUMBER	THERMAL CONDUCTIVITY (W/M-K) AT: 295K (22 C)	473K (200C)	673K (400C)	873K (600C)	1073K (800C)	IRRAD. TEMP.
900 (627 C)	221	26.7	34.2	33.0			29.9
	222	25.1	33.0	33.4			29.9
*	223	25.4	27.5	27.8			25.8
*	224	26.3	29.4	29.6			26.6
	MEAN:	25.9	31.0	31.0			28.0
	STD. DEV:	.8	3.1	2.7			4.7

CRUCIBLE NO: 7 FLUENCE: 7.70*EXP25 N/M**2, E>.18MEV

MEAN IRR. TEMP. (K)	SPECIMEN NUMBER	THERMAL CONDUCTIVITY (W/M-K) AT: 295K (22 C)	473K (200C)	673K (400C)	873K (600C)	1073K (800C)	IRRAD. TEMP.
1210 (937 C)	231	32.1	41.2	39.9	38.8	38.3	32.8
	232	24.6	30.4	28.4	27.4	27.2	24.9
*	233	31.1	37.6	36.3	36.7	33.6	29.9
*	234	37.0	45.4	41.6	44.2	44.4	35.2
	MEAN:	31.2	38.6	36.6	36.8	35.9	30.7
	STD. DEV:	5.1	6.3	5.9	7.0	7.3	6.1

CRUCIBLE NO: 5 FLUENCE: 9.00*EXP25 N/M**2, E>.18MEV

MEAN IRR. TEMP. (K)	SPECIMEN NUMBER	THERMAL CONDUCTIVITY (W/M-K) AT: 295K (22 C)	473K (200C)	673K (400C)	873K (600C)	1073K (800C)	IRRAD. TEMP.
1620 (1347 C)	242	56.5	63.7	59.4	53.4	48.4	33.5
	243	53.9	62.0	51.6	49.1	44.6	31.8
*	244	60.0	68.3	60.6	56.8	51.7	34.7
*	245	54.4	62.0	56.1	50.7	46.3	32.6
	MEAN:	56.2	64.0	56.9	52.5	47.8	33.1
	STD. DEV:	2.8	3.0	4.0	3.4	3.1	4.4

TABLE 11-17
THERMAL CONDUCTIVITY OF H-451 GRAPHITE, LOT 426,
IRRADIATED IN CAPSULE OG-3

LOT NUMBER: 426 LOG NUMBER(S): 6484-34

ORIENTATION: AXIAL LOG LOCATION: MIDLENGTH-CENTER

CRUCTBLE NO: 1 FLUENCE: 1.80*EXP25 N/M**2, E>.18MEV

MEAN IRR. TEMP. (K)	SPECIMEN NUMBER	THERMAL CONDUCTIVITY (W/M-K) AT: 295K (22 C)	473K (200C)	673K (400C)	873K (600C)	1073K (800C)	IRRAD. TEMP.
925 (652 C)	34-2B-L-1A	30.5	37.0	33.6			30.1
	34-2B-L-1B	35.6	38.6	36.5			31.6
*	34-2B-L-1C	35.7	41.6	40.7			34.4
	MEAN:	34.0	39.1	36.9			32.0
	STD. DEV:	3.0	2.3	3.6			6.6

CRUCTBLE NO: 7 FLUENCE: 2.40*EXP25 N/M**2, E>.18MEV

MEAN IRR. TEMP. (K)	SPECIMEN NUMBER	THERMAL CONDUCTIVITY (W/M-K) AT: 295K (22 C)	473K (200C)	673K (400C)	873K (600C)	1073K (800C)	IRRAD. TEMP.
1220 (947 C)	34-2B-L1G	65.7	63.7	54.4	46.3	43.3	38.4
	34-2B-L1H	63.3	67.6	57.1	51.4	46.2	40.1
*	34-2B-L1I	60.4	65.1	60.8	53.4	50.6	41.2
*	34-2B-L1J	53.8	59.9	51.4	43.5	38.8	36.1
	MEAN:	60.8	64.1	55.9	48.7	44.7	39.0
	STD. DEV:	5.1	3.2	4.0	4.6	5.0	6.7

CRUCTBLE NO: 5 FLUENCE: 2.90*EXP25 N/M**2, E>.18MEV

MEAN IRR. TEMP. (K)	SPECIMEN NUMBER	THERMAL CONDUCTIVITY (W/M-K) AT: 295K (22 C)	473K (200C)	673K (400C)	873K (600C)	1073K (800C)	IRRAD. TEMP.
1615 (1342 C)	34-2B-L1D	81.6	82.5	71.2	63.2	58.7	33.1
	34-2B-L1E	82.1	81.8	71.4	62.7	56.3	32.8
*	34-2B-L1F	83.6	73.9	65.2	56.4	52.3	31.5
	MEAN:	82.4	79.4	69.3	60.7	55.8	32.5
	STD. DEV:	1.1	4.8	3.5	3.8	3.2	6.3

TABLE 17 (Continued)

LOT NUMBER: 426 LOG NUMBER(S): 6484-34

ORIENTATION: RADIAL LOG LOCATION: MIDLENGTH-CENTER

CRUCIBLE NO: 1 FLUENCE: 1.80*EXP25 N/M**2, E>.18MEV

MEAN IRR. TEMP. (K)	SPECIMEN NUMBER	THERMAL CONDUCTIVITY (W/M-K) AT: 295K (22 C)	473K (200C)	673K (400C)	873K (600C)	1073K (800C)	IRRAD. TEMP.
925	34-2B-L-6A	24.9	33.0	29.2			27.1
(652 C)	34-2B-L-6B	31.6	36.2	35.2			30.8
*	34-2B-L-6C	32.4	37.5	36.2			31.4
	MEAN:	29.6	35.6	33.5			29.8
	STD. DEV:	4.1	2.3	3.8			6.7

CRUCIBLE NO: 7 FLUENCE: 2.40*EXP25 N/M**2, E>.18MEV

MEAN IRR. TEMP. (K)	SPECIMEN NUMBER	THERMAL CONDUCTIVITY (W/M-K) AT: 295K (22 C)	473K (200C)	673K (400C)	873K (600C)	1073K (800C)	IRRAD. TEMP.
1220	34-2B-L-6G	55.8	52.5	47.8	44.9	41.0	35.6
(947 C)	34-2B-L-6H	59.7	60.6	52.9	44.0	41.5	37.1
*	34-2B-L-6I	62.9	53.1	48.3	41.1	39.1	35.0
*	34-2B-L-6J	57.2	53.9	47.0	40.2	35.6	34.0
	MEAN:	58.9	55.0	49.0	42.6	39.3	35.4
	STD. DEV:	3.1	3.7	2.7	2.3	2.7	6.4

CRUCIBLE NO: 5 FLUENCE: 2.90*EXP25 N/M**2, E>.18MEV

MEAN IRR. TEMP. (K)	SPECIMEN NUMBER	THERMAL CONDUCTIVITY (W/M-K) AT: 295K (22 C)	473K (200C)	673K (400C)	873K (600C)	1073K (800C)	IRRAD. TEMP.
1615	34-2B-L6D	73.2	77.1	65.7	57.8	55.2	32.1
(1342 C)	34-2B-L6E	70.8	81.7	64.6	56.2	53.4	32.1
*	34-2B-L6F	73.0	74.1	65.0	55.6	53.3	31.5
	MEAN:	72.4	77.6	65.1	56.5	54.0	31.9
	STD. DEV:	1.3	3.8	.6	1.2	1.1	6.3

TABLE 11-18
THERMAL CONDUCTIVITY OF TS-1240 GRAPHITE
IRRADIATED IN CAPSULE OG-3

LOT NUMBER: 1 LOG NUMBER(S):5651-73

ORIENTATION: AXIAL LOG LOCATION: MIDLENGTH-CENTER

CRUCIBLE NO: 1 FLUENCE: 3.50*EXP25 N/M**2, E>.18MEV

MEAN IRR. TEMP. (K)	SPECIMEN NUMBER	THERMAL CONDUCTIVITY (W/M-K) AT: 295K (22 C)	473K (200C)	673K (400C)	873K (600C)	1073K (800C)	IRRAD. TEMP.
915 (642 C)	74D63	26.3	29.8	26.8			26.0
*	74D64	27.7	33.5	30.9			28.6
*	74D65	26.4	36.0	36.6			31.5
*	74D66	25.6	28.5	27.0			25.4
	MEAN:	26.5	32.0	30.3			27.9
	STD. DEV:	.9	3.4	4.6			5.0

CRUCIBLE NO: 7 FLUENCE: 4.90*EXP25 N/M**2, E>.18MEV

MEAN IRR. TEMP. (K)	SPECIMEN NUMBER	THERMAL CONDUCTIVITY (W/M-K) AT: 295K (22 C)	473K (200C)	673K (400C)	873K (600C)	1073K (800C)	IRRAD. TEMP.
1220 (947 C)	74D71	50.1	48.2	47.7	44.0	37.6	36.4
*	74D72	54.3	53.2	51.3	48.2	44.0	39.4
*	74D73	51.7	47.7	43.7	38.6	35.4	34.4
*	74D74	49.8	48.0	47.4	41.2	35.6	35.6
	MEAN:	51.5	49.3	47.5	43.0	38.2	36.5
	STD. DEV:	2.1	2.7	3.1	4.1	4.0	4.0

CRUCIBLE NO: 5 FLUENCE: 5.80*EXP25 N/M**2, E>.18MEV

MEAN IRR. TEMP. (K)	SPECIMEN NUMBER	THERMAL CONDUCTIVITY (W/M-K) AT: 295K (22 C)	473K (200C)	673K (400C)	873K (600C)	1073K (800C)	IRRAD. TEMP.
1615 (1342 C)	74D067	72.4	76.7	66.1	57.5	55.1	39.1
*	74D068	62.8	69.6	58.3	54.6	49.0	36.9
*	74D069	72.5	75.5	64.7	58.5	56.8	39.1
*	74D070	56.3	63.2	54.7	48.6	46.6	35.0
	MEAN:	66.0	71.2	61.0	54.8	51.9	37.5
	STD. DEV:	7.9	6.2	5.4	4.4	4.8	4.6

TABLE 18 (Continued)

LOT NUMBER: 1 LOG NUMBER(S):5651-73

ORIENTATION: RADIAL LOG LOCATION: MIDLENGTH-CENTER

CRUCTBLE NO: 1 FLUENCE: 3.50*EXP25 N/M**2, E>.18MEV

MEAN IRR. TEMP. (K)	SPECIMEN NUMBER	THERMAL CONDUCTIVITY (W/M-K) AT: 295K (22 C)	473K (200C)	673K (400C)	873K (600C)	1073K (800C)	IRRAD. TEMP.
915	74D93	27.0	30.0	28.4			26.2
(642 C)	74D94	26.5	29.3	25.3			25.0
*	74D95	27.9	29.8	26.2			24.8
*	74D96	28.4	27.8	26.7			24.4
	MEAN:	27.5	29.2	26.7			25.1
	STD. DEV:	.8	1.0	1.3			3.4

CRUCTBLE NO: 7 FLUENCE: 4.90*EXP25 N/M**2, E>.18MEV

MEAN IRR. TEMP. (K)	SPECIMEN NUMBER	THERMAL CONDUCTIVITY (W/M-K) AT: 295K (22 C)	473K (200C)	673K (400C)	873K (600C)	1073K (800C)	IRRAD. TEMP.
1220	74D109	48.9	52.4	48.4	43.0	40.9	37.9
(947 C)	74D110	49.0	59.2	52.9	46.0	43.4	40.3
*	74D111	50.6	48.7	48.2	39.5	34.6	35.9
*	74D112	51.8	47.8	47.3	42.3	35.5	36.2
	MEAN:	50.1	52.0	49.2	42.7	38.6	37.6
	STD. DEV:	1.4	5.2	2.5	2.7	4.2	4.7

CRUCTBLE NO: 5 FLUENCE: 5.80*EXP25 N/M**2, E>.18MEV

MEAN IRR. TEMP. (K)	SPECIMEN NUMBER	THERMAL CONDUCTIVITY (W/M-K) AT: 295K (22 C)	473K (200C)	673K (400C)	873K (600C)	1073K (800C)	IRRAD. TEMP.
1615	74D101	66.5	71.6	61.4	54.5	54.1	36.8
(1342 C)	74D102	63.2	66.6	57.7	53.6	51.8	35.6
*	74D103	68.8	74.1	64.9	60.2	55.9	38.1
*	74D104	63.2	73.8	63.7	56.2	53.3	37.6
	MEAN:	65.4	71.5	61.9	56.1	53.8	37.0
	STD. DEV:	2.8	3.5	3.2	2.9	1.7	3.5

TABLE 11-19
THERMAL CONDUCTIVITY OF SO818 GRAPHITE
IRRADIATED IN CAPSULE OG-3

LOT NUMBER: 4-B LOG NUMBER(S):6484-22

ORIENTATION: AXIAL LOG LOCATION: MIDLENGTH-CENTER

CRUCTBLE NO: 1 FLUENCE: 1.80*EXP25 N/M**2, E>.18MEV

MEAN IRR. TEMP. (K)	SPECIMEN NUMBER	THERMAL CONDUCTIVITY (W/M-K) AT: 295K (22 C)	473K (200C)	673K (400C)	873K (600C)	1073K (800C)	IRRAD. TEMP.
925 (652 C) *	22-3A-L51A	27.7	30.4	29.3			26.7
	22-3A-L51B	28.9	28.6	26.7			24.7
	22-3A-L51C	29.2	32.8	31.5			28.6
	MEAN:	28.6	30.6	29.2			26.7
	STD. DEV:	.8	2.1	2.4			4.6

CRUCTBLE NO: 7 FLUENCE: 2.40*EXP25 N/M**2, E>.18MEV

MEAN IRR. TEMP. (K)	SPECIMEN NUMBER	THERMAL CONDUCTIVITY (W/M-K) AT: 295K (22 C)	473K (200C)	673K (400C)	873K (600C)	1073K (800C)	IRRAD. TEMP.
1220 (947 C) *	22-3A-L55A	51.1	58.6	49.3	42.7	39.4	36.7
	22-3A-L55B	49.7	55.2	50.4	44.4	40.1	37.0
	22-3A-L55C	50.7	54.5	51.0	42.7	38.4	36.4
	MEAN:	50.5	56.1	50.2	43.3	39.3	36.7
	STD. DEV:	.8	2.2	.9	1.0	.8	4.2

CRUCTBLE NO: 5 FLUENCE: 2.90*EXP25 N/M**2, E>.18MEV

MEAN IRR. TEMP. (K)	SPECIMEN NUMBER	THERMAL CONDUCTIVITY (W/M-K) AT: 295K (22 C)	473K (200C)	673K (400C)	873K (600C)	1073K (800C)	IRRAD. TEMP.
1615 (1342 C) *	22-3A-L81A	69.6	75.5	69.8	63.0	58.7	35.2
	22-3A-L81B	59.8	68.6	61.5	53.7	49.8	32.6
	22-3A-L81C	64.1	77.3	68.9	62.0	57.4	35.1
	MEAN:	64.5	73.8	66.7	59.6	55.3	34.3
	STD. DEV:	4.9	4.6	4.5	5.1	4.8	4.4

TABLE 19 (Continued)

LOT NUMBER: 4-R LOG NUMBER(S): 6484-22

ORIENTATION: RADIAL LOG LOCATION: MIDLENGTH-CENTER

CRUCIBLE NO: 1 FLUENCE: 1.80*EXP25 N/M**2, E>.18MEV

MEAN IRR. TEMP. (K)	SPECIMEN NUMBER	THERMAL CONDUCTIVITY (W/M-K) AT: 295K (22 C)	473K (200C)	673K (400C)	873K (600C)	1073K (800C)	IRRAD. TEMP.
925	22-3A-L78A	27.4	28.0	25.7			24.3
(652 C)	22-3A-L78B	29.0	31.6	30.2			27.0
*	22-3A-L78C	28.8	34.5	32.6			29.6
	MEAN:	28.4	31.4	29.5			27.0
	STD. DEV:	.8	3.2	3.5			5.0

CRUCIBLE NO: 7 FLUENCE: 2.40*EXP25 N/M**2, E>.18MEV

MEAN IRR. TEMP. (K)	SPECIMEN NUMBER	THERMAL CONDUCTIVITY (W/M-K) AT: 295K (22 C)	473K (200C)	673K (400C)	873K (600C)	1073K (800C)	IRRAD. TEMP.
1220	22-3B-L90A	39.7	45.1	42.9	37.3	34.2	31.6
(947 C)	22-3B-L90B	43.4	47.0	42.3	35.4	36.0	31.9
*	22-3B-L90C	48.0	50.3	44.0	37.5	37.0	33.3
	MEAN:	43.7	47.5	43.0	36.7	35.7	32.3
	STD. DEV:	4.2	2.6	.9	1.2	1.4	4.3

CRUCIBLE NO: 5 FLUENCE: 2.90*EXP25 N/M**2, E>.18MEV

MEAN IRR. TEMP. (K)	SPECIMEN NUMBER	THERMAL CONDUCTIVITY (W/M-K) AT: 295K (22 C)	473K (200C)	673K (400C)	873K (600C)	1073K (800C)	IRRAD. TEMP.
1615	22-3B-L62A	67.8	70.3	62.5	57.9	53.8	33.4
(1342 C)	22-3B-L62B	63.3	68.6	60.0	52.9	52.3	32.6
*	22-3B-L62C	66.4	70.4	63.9	59.0	49.6	33.1
	MEAN:	65.8	69.8	62.1	56.6	51.9	33.0
	STD. DEV:	2.3	1.0	2.0	3.3	2.2	4.2

TABLE 11-20

THERMAL CONDUCTIVITY OF H-451 GRAPHITE IRRADIATED AT TWO DIFFERENT TEMPERATURES: (1) 3 x 10^{25} n/m^2 AT 1625 K, THEN 1.8 x 10^{25} n/m^2 AT 925 K; (2) 2 x 10^{25} n/m^2 at 875 K, THEN 2.9 x 10^{25} n/m^2 AT 1615 K

LOT NUMBER: 266 LOG NUMBER(S):5651-2A

ORIENTATION: RADIAL LOG LOCATION: MIDLENGTH-CENTER

CRUCIBLE NO: 5-1 FLUENCE: 4.80*EXP25 N/M**2, E>.18MEV

MEAN IRR. TEMP. (K)	SPECIMEN NUMBER	THERMAL CONDUCTIVITY (W/M-K) AT: 295K (22 C)	473K (200C)	673K (400C)	873K (600C)	1073K (800C)	IRRAD. TEMP.
1625-925 STEP DOWN	250	26.5	28.3	29.2			25.5
	251	25.2	30.6	29.9			27.0
	MEAN:	25.8	29.4	29.5			26.2
	STD. DEV:	.9	1.6	.5			4.3

CRUCIBLE NO: 1-5 FLUENCE: 4.90*EXP25 N/M**2, E>.18MEV

MEAN IRR. TEMP. (K)	SPECIMEN NUMBER	THERMAL CONDUCTIVITY (W/M-K) AT: 295K (22 C)	473K (200C)	673K (400C)	873K (600C)	1073K (800C)	IRRAD. TEMP.
875-1615 STEP UP	229	71.5	80.0	64.9	55.5	53.2	36.0
	230	71.7	77.8	62.9	59.3	53.4	36.4
	MEAN:	71.6	78.9	63.9	57.4	53.3	36.2
	STD. DEV:	.1	1.6	1.5	2.7	.1	4.2

TABLE 11-21
SUMMARY OF IRRADIATION-INDUCED CHANGES IN THERMAL CONDUCTIVITY OF H-451 GRAPHITE IRRADIATED IN CAPSULES OG-1, OG-2, AND OG-3
(ALL SPECIMENS FROM MIDLENGTH-CENTER)

Lot	Log No.	Orientation	Mean Irradiation Temperature (K)	Fluence x 10^{-25} (n/m^2) $(E > 29\ fJ)_{HTGR}$	Mean Thermal Conductivity (W/m-K) ± Std. Dev.	
					At 293 K	At Irradiation Temperature
266	5651-28	Axial	--	0	145.2 ± 1.3	--
			875	2.0	34.7 ± 1.4	33.3 ± 2.7
			890	3.7	30.1 ± 0.9	32.5 ± 4.3
			900	5.5	29.6 ± 1.4	31.5 ± 4.4
			1195	2.8	48.8 ± 1.8	40.0 ± 1.7
			1205	5.3	41.3 ± 8.4	39.8 ± 3.0
			1210	7.7	43.6 ± 6.8	34.1 ± 5.9
			1625	3.2	79.8 ± 4.2	41.1 ± 1.2
			1625	6.1	80.9 ± 4.0	40.7 ± 0.6
			1620	9.0	68.9 ± 9.2	34.5 ± 3.8
266	5651-28	Radial	--	0	123.0 ± 7.1	--
			875	2.0	32.0 ± 1.9	33.3 ± 2.7
			890	3.7	27.8 ± 3.1	29.5 ± 3.2
			900	5.5	25.9 ± 0.8	28.0 ± 4.7
			1195	2.8	42.9 ± 3.3	36.1 ± 2.8
			1205	5.3	34.2 ± 4.3	29.5 ± 2.0
			1210	7.7	31.2 ± 5.1	30.7 ± 6.1
			1625	3.2	83.5 ± 7.2	39.3 ± 3.4
			1625	6.1	65.7 ± 8.2	36.4 ± 2.0
			1620	9.0	56.2 ± 2.8	33.1 ± 4.4
426	6484-34	Axial	--	0	136.0 ± 17.2	--
			925	1.8	34.0 ± 3.0	32.0 ± 6.6
			1220	2.4	60.8 ± 5.1	39.0 ± 6.7
			1615	2.9	82.4 ± 1.1	32.5 ± 6.3
			--	0	128.9 ± 10.0	--
			925	1.8	29.6 ± 4.1	29.8 ± 6.7
			1220	2.4	58.9 ± 3.1	35.4 ± 6.4
			1615	2.9	72.4 ± 1.3	31.9 ± 6.3

TABLE 11-22
SUMMARY OF IRRADIATION-INDUCED CHANGES IN THERMAL CONDUCTIVITY OF TS-1240 GRAPHITE IRRADIATED IN CAPSULES OG-2 AND OG-3
(ALL SPECIMENS FROM MIDLENGTH-CENTER)

Lot	Log No.	Orientation	Mean Irradiation Temperature (K)	Fluence x 10^{-25} (n/m^2) $(E > 29\ fJ)_{HTGR}$	Mean Thermal Conductivity (W/m-K) ± Std. Dev.	
					At 293 K	At Irradiation Temperature
	5651-73	Axial	--	0	97.9 ± 8.4	--
			910	1.7	30.5 ± 1.2	34.1 ± 1.7
			915	3.5	26.5 ± 0.9	27.9 ± 5.0
			1220	2.5	45.5 ± 3.7	38.2 ± 2.4
			1220	4.9	51.5 ± 2.1	36.5 ± 4.0
			1620	2.9	68.8 ± 3.4	37.2 ± 1.5
			1615	5.8	66.0 ± 7.9	37.5 ± 4.6
	5651-73	Radial	--	0	103.3 ± 4.2	--
			910	1.7	28.5 ± 2.8	32.6 ± 0.3
			915	3.5	27.5 ± 0.8	25.1 ± 3.4
			1220	2.5	37.0 ± 2.2	29.9 ± 1.7
			1220	4.9	50.1 ± 1.4	37.6 ± 4.7
			1620	2.9	64.5 ± 5.5	33.5 ± 1.2
			1615	5.8	65.4 ± 2.8	37.0 ± 3.5

TABLE 11-23
SUMMARY OF IRRADIATION-INDUCED CHANGES IN THERMAL CONDUCTIVITY OF SO818 GRAPHITE IRRADIATED IN CAPSULE OG-3
(ALL SPECIMENS FROM MIDLENGTH-CENTER)

Lot	Log No.	Orientation	Mean Irradiation Temperature (K)	Fluence x 10^{-25} (n/m^2) ($E > 29$ fJ)$_{HTGR}$	Mean Thermal Conductivity (W/m-K) ± Std. Dev.	
					At 293 K	At Irradiation Temperature
4-B	6484-22	Axial	--	0	135.1 ± 5.0	--
			925	1.8	28.6 ± 0.8	26.7 ± 4.6
			1220	2.4	50.5 ± 0.8	36.7 ± 4.2
			1615	2.9	64.5 ± 4.9	34.3 ± 4.4
4-B	6484-22	Radial	--	0	125.9 ± 5.0	--
			925	1.8	28.4 ± 0.8	27.0 ± 5.0
			1220	2.4	43.7 ± 4.2	32.3 ± 4.3
			1615	2.9	65.8 ± 2.3	33.0 ± 4.2

TABLE 11-24
IMPURITY CONTENT OF HLM GRAPHITE
LOG NO. 6484-78, SPECTROGRAPHIC ANALYSIS

LAB. NO. 44247 — REPORT TO: G ENGLE — DATE: 6-21-76
SAMPLE: GRAPHITE 6484-78-E708 — PROJECT NO. 3224146005 — DILUTION: 1.0000 — PLATE NO. 76-066

ELEMENT	CONCENTRATION, PPM	ELEMENT	CONCENTRATION, PPM	ELEMENT	CONCENTRATION, PPM
AG	< .50	AL	60.00	B	2.00
BA	60.00	BE	< .50	BI	< 2.00
CA	400.00	CD	< 10.00	CE	< 80.00
CO	< 4.00	CR	10.00	CS	< 100.00
CU	< 1.00	DY	< 20.00	ER	< 6.00
EU	< 10.00	FE	1000.00	GD	< 10.00
HF	< 20.00	HO	< 10.00	IN	< 1.00
K	20.00	LA	< 10.00	LI	< 1.00
LU	< .50	MG	2.00	MN	< 1.00
MO	< 1.00	NA	10.00	NB	< 6.00
ND	< 200.00	NI	20.00	P	< 100.00
PB	< 6.00	PR	< 100.00	RB	< 40.00
SB	< 8.00	SC	< 1.00	SI	100.00
SM	< 100.00	SN	< 6.00	SR	< 40.00
TA	< 40.00	TB	< 40.00	TI	60.00
TL	< 20.00	TM	< 4.00	V	60.00
W	< 40.00	YB	< 10.00	ZN	< 20.00
ZR	< .50				

LAB. NO. 44247 — REPORT TO: G ENGLE — DATE: 6-21-76
SAMPLE: GRAPHITE 6484-78-E40B — PROJECT NO. 3224146005 — DILUTION: 1.0000 — PLATE NO. 76-066

ELEMENT	CONCENTRATION, PPM	ELEMENT	CONCENTRATION, PPM	ELEMENT	CONCENTRATION, PPM
AG	< .50	AL	60.00	B	2.00
BA	40.00	BE	< .50	BI	< 2.00
CA	200.00	CD	< 10.00	CE	< 80.00
CO	< 4.00	CR	20.00	CS	< 100.00
CU	< 1.00	DY	< 20.00	ER	< 6.00
EU	< 10.00	FE	> 1000.00	GD	< 10.00
HF	< 20.00	HO	< 10.00	IN	< 1.00
K	10.00	LA	< 10.00	LI	1.00
LU	< .50	MG	6.00	MN	4.00
MO	< 1.00	NA	10.00	NB	< 6.00
ND	< 200.00	NI	40.00	P	< 100.00
PB	< 6.00	PR	< 100.00	RB	< 40.00
SB	< 8.00	SC	< 1.00	SI	80.00
SM	< 100.00	SN	< 6.00	SR	< 40.00
TA	< 40.00	TB	< 40.00	TI	40.00
TL	< 20.00	TM	< 4.00	V	40.00
W	< 40.00	YB	< 10.00	ZN	< 20.00
ZR	40.00				

CONCENTRATION BASED ON ORGINAL SAMPLE BEFORE DILUTION WITH DILUENT
> MEANS GREATER THAN
< MEANS LESS THAN THE SENSITIVITYOF THE SPECTROGRAPHIC PROCEDURE USE
RESULTS ARE CORRECT WITHIN A FACTOR OF 40% (ONE STANDARD DEVIATION)

TABLE 11-24 (Continued)

LAB. NO. 44247 REPORT TO: G ENGLE DATE: 6-21-76
SAMPLE: GRAPHITE 6484-78-E168 PROJECT NO. 3224146005 DILUTION: 1.0000 PLATE NO. 76-066

ELEMENT	CONCENTRATION, PPM	ELEMENT	CONCENTRATION, PPM	ELEMENT	CONCENTRATION, PPM
AG	< .50	AL	80.00	B	20.00
BA	40.00	BE	< .50	BI	< 2.00
CA	200.00	CD	< 10.00	CE	< 80.00
CO	< 4.00	CR	20.00	CS	< 100.00
CU	< 1.00	DY	< 20.00	ER	< 6.00
EU	< 10.00	FE	> 1000.00	GD	< 10.00
HF	< 20.00	HO	< 10.00	IN	< 1.00
K	10.00	LA	< 10.00	LI	< 1.00
LU	< .50	MG	2.00	MN	4.00
MO	< 1.00	NA	10.00	NB	< 6.00
ND	< 200.00	NI	40.00	P	< 100.00
PB	< 6.00	PR	< 100.00	RB	< 40.00
SB	< 8.00	SC	< 1.00	SI	60.00
SM	< 100.00	SN	< 6.00	SR	< 40.00
TA	< 40.00	TB	< 40.00	TI	40.00
TL	< 20.00	TM	< 4.00	V	40.00
W	< 40.00	YB	< 10.00	ZN	< 20.00
ZR	< .50				

LAB. NO. 44247 REPORT TO: G ENGLE DATE: 6-21-76
SAMPLE: GRAPHITE 6484-78-E888 PROJECT NO. 3224146005 DILUTION: 1.0000 PLATE NO. 76-066

ELEMENT	CONCENTRATION, PPM	ELEMENT	CONCENTRATION, PPM	ELEMENT	CONCENTRATION, PPM
AG	< .50	AL	40.00	B	2.00
BA	40.00	BE	< .50	BI	< 2.00
CA	200.00	CD	< 10.00	CE	< 80.00
CO	< 4.00	CR	20.00	CS	< 100.00
CU	< 1.00	DY	< 20.00	ER	< 6.00
EU	< 10.00	FE	> 1000.00	GD	< 10.00
HF	< 20.00	HO	< 10.00	IN	< 1.00
K	60.00	LA	< 10.00	LI	2.00
LU	< .50	MG	4.00	MN	4.00
MO	< 1.00	NA	40.00	NB	< 6.00
ND	< 200.00	NI	40.00	P	< 100.00
PB	200.00	PR	< 100.00	RB	< 40.00
SB	60.00	SC	< 1.00	SI	60.00
SM	< 100.00	SN	< 6.00	SR	< 40.00
TA	< 40.00	TB	< 40.00	TI	40.00
TL	< 20.00	TM	< 4.00	V	40.00
W	< 40.00	YB	< 10.00	ZN	< 20.00
ZR	< .50				

CONCENTRATION BASED ON ORGINAL SAMPLE BEFORE DILUTION WITH DILUENT
> MEANS GREATER THAN
< MEANS LESS THAN THE SENSITIVITYOF THE SPECTROGRAPHIC PROCEDURE USED
RESULTS ARE CORRECT WITHIN A FACTOR OF 40% , (ONE STANDARD DEVIATION)

TABLE 11-24 (Continued)

LAB. NO. 44247 REPORT TO: G ENGLE DATE: 6-21-76
SAMPLE: GRAPHITE 6484-78-E1248 PROJECT NO. 3224146005 DILUTION: 1.0000 PLATE NO. 76-066

ELEMENT	CONCENTRATION, PPM	ELEMENT	CONCENTRATION, PPM	ELEMENT	CONCENTRATION, PPM
AG	< .50	AL	20.00	B	2.00
BA	40.00	BE	< .50	BI	< 2.00
CA	200.00	CD	< 10.00	CE	< 80.00
CO	< 4.00	CR	20.00	CS	< 100.00
CU	< 1.00	DY	< 20.00	ER	< 6.00
EU	< 10.00	FE	> 1000.00	GD	< 10.00
HF	< 20.00	HO	< 10.00	IN	< 1.00
K	< 10.00	LA	< 10.00	LI	1.00
LU	< .50	MG	2.00	MN	4.00
MO	< 1.00	NA	< 10.00	NB	< 6.00
ND	< 200.00	NI	40.00	P	< 100.00
PB	< 6.00	PR	< 100.00	RB	< 40.00
SB	< 8.00	SC	< 1.00	SI	80.00
SM	< 100.00	SN	< 6.00	SR	< 40.00
TA	< 40.00	TB	< 40.00	TI	40.00
TL	< 20.00	TM	< 4.00	V	60.00
W	< 40.00	YB	< 10.00	ZN	< 20.00
ZR	40.00				

LAB. NO. 44247 REPORT TO: G ENGLE DATE: 6-21-76
SAMPLE: GRAPHITE 6484-78-E1548 PROJECT NO. 3224146005 DILUTION: 1.0000 PLATE NO. 76-066

ELEMENT	CONCENTRATION, PPM	ELEMENT	CONCENTRATION, PPM	ELEMENT	CONCENTRATION, PPM
AG	< .50	AL	< 1.00	B	2.00
BA	40.00	BE	< .50	BI	< 2.00
CA	100.00	CD	< 10.00	CE	< 80.00
CO	< 4.00	CR	< 10.00	CS	< 100.00
CU	< 1.00	DY	< 20.00	ER	< 6.00
EU	< 10.00	FE	800.00	GD	< 10.00
HF	< 20.00	HO	< 10.00	IN	< 1.00
K	< 10.00	LA	< 10.00	LI	< 1.00
LU	< .50	MG	4.00	MN	< 1.00
MO	< 1.00	NA	< 10.00	NB	< 6.00
ND	< 200.00	NI	10.00	P	< 100.00
PB	< 6.00	PR	< 100.00	RB	< 40.00
SB	< 8.00	SC	< 1.00	SI	80.00
SM	< 100.00	SN	< 6.00	SR	< 40.00
TA	< 40.00	TB	< 40.00	TI	40.00
TL	< 20.00	TM	< 4.00	V	20.00
W	< 40.00	YB	< 10.00	ZN	< 20.00
ZR	< .50				

CONCENTRATION BASED ON ORGINAL SAMPLE BEFORE DILUTION WITH DILUENT
> MEANS GREATER THAN
< MEANS LESS THAN THE SENSITIVITYOF THE SPECTROGRAPHIC PROCEDURE USED
RESULTS ARE CORRECT WITHIN A FACTOR OF 40% , (ONE STANDARD DEVIATION)

TABLE 11-24 (Continued)

LAB. NO. 44247 REPORT TO: G ENGLE DATE: 6-21-76
SAMPLE: GRAPHITE 6484-78-M708 PROJECT NO. 3224146005 DILUTION: 1.0000 PLATE NO. 76-066

ELEMENT	CONCENTRATION, PPM	ELEMENT	CONCENTRATION, PPM	ELEMENT	CONCENTRATION, PPM
AG	< .50	AL	< 1.00	B	2.00
BA	40.00	BE	< .50	BI	< 2.00
CA	80.00	CD	< 10.00	CE	< 80.00
CO	< 4.00	CR	< 10.00	CS	< 100.00
CU	< 1.00	DY	< 20.00	ER	< 6.00
EU	< 10.00	FE	100.00	GD	< 10.00
HF	< 20.00	HO	< 10.00	IN	< 1.00
K	< 10.00	LA	< 10.00	LI	2.00
LU	< .50	MG	2.00	MN	< 1.00
MO	< 1.00	NA	< 10.00	NB	< 6.00
ND	< 200.00	NI	< 4.00	P	< 100.00
PB	< 6.00	PR	< 100.00	RB	< 40.00
SB	< 8.00	SC	< 1.00	SI	60.00
SM	< 100.00	SN	< 6.00	SR	< 40.00
TA	< 40.00	TB	< 40.00	TI	20.00
TL	< 20.00	TM	< 4.00	V	10.00
W	< 40.00	YB	< 10.00	ZN	< 20.00
ZR	< .50				

LAB. NO. 44247 REPORT TO: G ENGLE DATE: 6-21-76
SAMPLE: GRAPHITE 6484-78-M408 PROJECT NO. 3224146005 DILUTION: 1.0000 PLATE NO. 76-066

ELEMENT	CONCENTRATION, PPM	ELEMENT	CONCENTRATION, PPM	ELEMENT	CONCENTRATION, PPM
AG	< .50	AL	60.00	B	2.00
BA	40.00	BE	< .50	BI	< 2.00
CA	200.00	CD	< 10.00	CE	< 80.00
CO	< 4.00	CR	< 10.00	CS	< 100.00
CU	< 1.00	DY	< 20.00	ER	< 6.00
EU	< 10.00	FE	600.00	GD	< 10.00
HF	< 20.00	HO	< 10.00	IN	< 1.00
K	< 10.00	LA	< 10.00	LI	1.00
LU	< .50	MG	4.00	MN	2.00
MO	< 1.00	NA	< 10.00	NB	< 6.00
ND	< 200.00	NI	20.00	P	< 100.00
PB	< 6.00	PR	< 100.00	RB	< 40.00
SB	< 8.00	SC	< 1.00	SI	100.00
SM	< 100.00	SN	< 6.00	SR	< 40.00
TA	< 40.00	TB	< 40.00	TI	40.00
TL	< 20.00	TM	< 4.00	V	40.00
W	< 40.00	YB	< 10.00	ZN	< 20.00
ZR	10.00				

CONCENTRATION BASED ON ORGINAL SAMPLE BEFORE DILUTION WITH DILUENT
> MEANS GREATER THAN
< MEANS LESS THAN THE SENSITIVITYOF THE SPECTROGRAPHIC PROCEDURE USED
RESULTS ARE CORRECT WITHIN A FACTOR OF 40% , (ONE STANDARD DEVIATION)

TABLE 11-24 (Continued)

LAB. NO. 44247 REPORT TO: G ENGLE DATE: 6-21-76
SAMPLE: GRAPHITE 6484-78-M1BB PROJECT NO. 3224146005 DILUTION: 1.0000 PLATE NO. 76-066

ELEMENT	CONCENTRATION, PPM	ELEMENT	CONCENTRATION, PPM	ELEMENT	CONCENTRATION, PPM
AG	< .50	AL	80.00	B	2.00
BA	40.00	BE	< .50	BI	< 2.00
CA	100.00	CD	< 10.00	CE	< 80.00
CO	< 4.00	CR	> 1000.00	CS	< 100.00
CU	10.00	DY	< 20.00	ER	< 8.00
EU	< 10.00	FE	> 1000.00	GD	< 10.00
HF	< 20.00	MO	< 10.00	IN	< 1.00
K	< 10.00	LA	< 10.00	LI	6.00
LU	< .50	MG	4.00	MN	100.00
MO	< 1.00	NA	< 10.00	NB	< 8.00
ND	< 200.00	NI	> 1000.00	P	< 100.00
PB	< 8.00	PR	< 100.00	RB	< 40.00
SB	< 8.00	SC	< 1.00	SI	200.00
SM	< 100.00	SN	< 8.00	SR	< 40.00
TA	< 40.00	TB	< 40.00	TI	80.00
TL	< 20.00	TM	< 4.00	V	20.00
W	< 40.00	YB	< 10.00	ZN	< 20.00
ZR	40.00				

LAB. NO. 44247 REPORT TO: G ENGLE DATE: 6-21-76
SAMPLE: GRAPHITE 6484-78-M1008 PROJECT NO. 3224146005 DILUTION: 1.0000 PLATE NO. 76-066

ELEMENT	CONCENTRATION, PPM	ELEMENT	CONCENTRATION, PPM	ELEMENT	CONCENTRATION, PPM
AG	< .50	AL	40.00	B	2.00
BA	20.00	BE	< .50	BI	< 2.00
CA	100.00	CD	< 10.00	CE	< 80.00
CO	< 4.00	CR	200.00	CS	< 100.00
CU	< 1.00	DY	< 20.00	ER	< 8.00
EU	< 10.00	FE	100.00	GD	< 10.00
HF	< 20.00	MO	< 10.00	IN	< 1.00
K	< 10.00	LA	< 10.00	LI	1.00
LU	< .50	MG	4.00	MN	20.00
MO	< 1.00	NA	< 10.00	NB	< 8.00
ND	< 200.00	NI	200.00	P	< 100.00
PB	200.00	PR	< 100.00	RB	< 40.00
SB	40.00	SC	< 1.00	SI	80.00
SM	< 100.00	SN	< 8.00	SR	< 40.00
TA	< 40.00	TB	< 40.00	TI	20.00
TL	< 20.00	TM	< 4.00	V	29.00
W	< 40.00	YB	< 10.00	ZN	< 20.00
ZR	10.00				

CONCENTRATION BASED ON ORGINAL SAMPLE BEFORE DILUTION WITH DILUENT
> MEANS GREATER THAN
< MEANS LESS THAN THE SENSITIVITY OF THE SPECTROGRAPHIC PROCEDURE USED
RESULTS ARE CORRECT WITHIN A FACTOR OF 40% , (ONE STANDARD DEVIATION)

TABLE 11-24 (Continued)

LAB. NO. 44247 REPORT TO: G ENGLE DATE: 6-21-76
SAMPLE: GRAPHITE 6484-78-M122B PROJECT NO. 3224146005 DILUTION: 1.0000 PLATE NO. 76-066

ELEMENT	CONCENTRATION, PPM	ELEMENT	CONCENTRATION, PPM	ELEMENT	CONCENTRATION, PPM
AG	< .50	AL	100.00	B	2.00
BA	40.00	BE	< .50	BI	< 2.00
CA	100.00	CD	< 10.00	CE	< 80.00
CO	< 4.00	CR	< 10.00	CS	< 100.00
CU	< 1.00	DY	< 20.00	ER	< 6.00
EU	< 10.00	FE	400.00	GD	< 10.00
HF	< 20.00	HO	< 10.00	IN	< 1.00
K	10.00	LA	< 10.00	LI	1.00
LU	< .50	MG	2.00	MN	< 1.00
MO	< 1.00	NA	< 10.00	NB	< 6.00
ND	< 200.00	NI	10.00	P	< 100.00
PB	< 6.00	PR	< 100.00	RB	< 40.00
SB	< 8.00	SC	< 1.00	SI	80.00
SM	< 100.00	SN	< 6.00	SR	< 40.00
TA	< 40.00	TB	< 40.00	TI	20.00
TL	< 20.00	TM	< 4.00	V	20.00
W	< 40.00	YB	< 10.00	ZN	< 20.00
ZR	< .50				

LAB. NO. 44247 REPORT TO: G ENGLE DATE: 6-21-76
SAMPLE: GRAPHITE 6484-78-M1528 PROJECT NO. 3224146005 DILUTION: 1.0000 PLATE NO. 76-066

ELEMENT	CONCENTRATION, PPM	ELEMENT	CONCENTRATION, PPM	ELEMENT	CONCENTRATION, PPM
AG	< .50	AL	< 1.00	B	2.00
BA	40.00	BE	< .50	BI	< 2.00
CA	80.00	CD	< 10.00	CE	< 80.00
CO	< 4.00	CR	< 10.00	CS	< 100.00
CU	< 1.00	DY	< 20.00	ER	< 6.00
EU	< 10.00	FE	80.00	GD	< 10.00
HF	< 20.00	HO	< 10.00	IN	< 1.00
K	< 10.00	LA	< 10.00	LI	< 1.00
LU	< .50	MG	2.00	MN	< 1.00
MO	< 1.00	NA	< 10.00	NB	< 6.00
ND	< 200.00	NI	10.00	P	< 100.00
PB	< 6.00	PR	< 100.00	RB	< 40.00
SB	< 8.00	SC	< 1.00	SI	80.00
SM	< 100.00	SN	< 6.00	SR	< 40.00
TA	< 40.00	TB	< 40.00	TI	20.00
TL	< 20.00	TM	< 4.00	V	20.00
W	< 40.00	YB	< 10.00	ZN	< 20.00
ZR	< .50				

CONCENTRATION BASED ON ORGINAL SAMPLE BEFORE DILUTION WITH DILUENT
> MEANS GREATER THAN
< MEANS LESS THAN THE SENSITIVITYOF THE SPECTROGRAPHIC PROCEDURE USED
RESULTS ARE CORRECT WITHIN A FACTOR OF 40% , (ONE STANDARD DEVIATION)

TABLE 11-25
ASH AND SULFUR CONTENT OF HLM GRAPHITE, LOG 8464-78

Element (ppm)	1A[a]			1B[a]			6A[a]			6B[a]		
	E70B[b]	E40B	E16B	E88B	E124B	E154B	M70B	M40B	M16B	M100B	M122B	M152B
Ash	2400	4900	4500	4600	4500	1200	670	1900	1000	1100	1100	900
Sulfur	179	<4	<4	59	18	15	42	<4	<4	25	24	9
	170	<4	<4	57	18	16	47	<4	<4	21	20	9

Edge Center Edge
Slab 1
Edge Center Edge
Slab 6

(a) Slab 1 or 6, side A or B; slab 1 was from the top of the log and slab 6 from the center. A and B are sides chosen arbitrarily.

(b) Specimen number; the B signifies it is the B half, or bottom specimen, from the specimen core.

TABLE 11-26
IMPURITY CONTENT OF 2020 GRAPHITE
LOG NO. 6484-110, SPECTROCHEMICAL ANALYSIS

LAB. NO. 44389 — REPORT TO: GLEN ENGLE — DATE: 8-3-76
SAMPLE: 6484-110 2020 L168 GRAP — PROJECT NO. H3224146005 — DILUTION: 1.0000 — PLATE NO. 76-71

ELEMENT	CONCENTRATION, PPM	ELEMENT	CONCENTRATION, PPM	ELEMENT	CONCENTRATION, PPM
AG	< .50	AL	60.00	B	4.00
BA	40.00	BE	< .50	BI	< 2.00
CA	600.00	CD	< 10.00	CE	< 80.00
CO	< 4.00	CR	< 10.00	CS	< 100.00
CU	< 1.00	DY	< 20.00	ER	< 6.00
EU	< 10.00	FE	400.00	GD	< 10.00
HF	< 20.00	HO	< 10.00	IN	< 1.00
K	80.00	LA	< 10.00	LI	< 1.00
LU	< .50	MG	4.00	MN	2.00
MO	< 1.00	NA	10.00	NB	< 6.00
ND	< 200.00	NI	< 4.00	P	< 100.00
PB	< 6.00	PR	< 100.00	RB	< 40.00
SB	< 8.00	SC	< 1.00	SI	200.00
SM	< 100.00	SN	< 6.00	SR	40.00
TA	< 40.00	TB	< 40.00	TI	40.00
TL	< 20.00	TM	< 4.00	V	20.00
W	< 40.00	YB	< 10.00	ZN	< 20.00
ZR	< .50				

LAB. NO. 44389 — REPORT TO: GLEN ENGLE — DATE: 8-3-76
SAMPLE: 6484-110 2020 L288 GRAP — PROJECT NO. H3224146005 — DILUTION: 1.0000 — PLATE NO. 76-71

ELEMENT	CONCENTRATION, PPM	ELEMENT	CONCENTRATION, PPM	ELEMENT	CONCENTRATION, PPM
AG	< .50	AL	60.00	B	2.00
BA	40.00	BE	< .50	BI	< 2.00
CA	600.00	CD	< 10.00	CE	< 80.00
CO	< 4.00	CR	< 10.00	CS	< 100.00
CU	< 1.00	DY	< 20.00	ER	< 6.00
EU	< 10.00	FE	400.00	GD	< 10.00
HF	< 20.00	HO	< 10.00	IN	< 1.00
K	60.00	LA	< 10.00	LI	< 1.00
LU	< .50	MG	2.00	MN	1.00
MO	< 1.00	NA	10.00	NB	< 6.00
ND	< 200.00	NI	< 4.00	P	< 100.00
PB	< 6.00	PR	< 100.00	RB	< 40.00
SB	< 8.00	SC	< 1.00	SI	200.00
SM	< 100.00	SN	< 6.00	SR	< 40.00
TA	< 40.00	TB	< 40.00	TI	20.00
TL	< 20.00	TM	< 4.00	V	10.00
W	< 40.00	YB	< 10.00	ZN	< 20.00
ZR	< .50				

CONCENTRATION BASED ON ORGINAL SAMPLE BEFORE DILUTION WITH DILUENT
> MEANS GREATER THAN
< MEANS LESS THAN THE SENSITIVITYOF THE SPECTROGRAPHIC PROCEDURE USED
RESULTS ARE CORRECT WITHIN A FACTOR OF 40% , (ONE STANDARD DEVIATION)

TABLE 11-26 (Continued)

LAB. NO. 44389 REPORT TO: GLEN ENGLE DATE: 8-3-76
SAMPLE: 6484-110 2020 L64R GRAP PROJECT NO. H3224146005 DILUTION: 1.0000 PLATE NO. 76-71

ELEMENT	CONCENTRATION, PPM	ELEMENT	CONCENTRATION, PPM	ELEMENT	CONCENTRATION, PPM
AG	< .50	AL	20.00	B	4.00
BA	40.00	BE	< .50	BI	< 2.00
CA	400.00	CD	< 10.00	CE	< 80.00
CO	< 4.00	CR	< 10.00	CS	< 100.00
CU	< 1.00	DY	< 20.00	ER	< 6.00
EU	< 10.00	FE	20.00	GD	< 10.00
HF	< 20.00	HO	< 10.00	IN	< 1.00
K	20.00	LA	< 10.00	LI	< 1.00
LU	< .50	MG	4.00	MN	< 1.00
MO	< 1.00	NA	10.00	NB	< 6.00
ND	< 200.00	NI	< 4.00	P	< 100.00
PB	< 6.00	PR	< 100.00	RB	< 40.00
SB	< 8.00	SC	< 1.00	SI	20.00
SM	< 100.00	SN	< 6.00	SR	< 40.00
TA	< 40.00	TB	< 40.00	TI	100.00
TL	< 20.00	TM	< 4.00	V	20.00
W	< 40.00	YB	< 10.00	ZN	< 20.00
ZR	< .50				

LAB. NO. 44389 REPORT TO: GLEN ENGLE DATE: 8-3-76
SAMPLE: 6484-110 2020 L76R GRAP PROJECT NO. H3224146005 DILUTION: 1.0000 PLATE NO. 76-71

ELEMENT	CONCENTRATION, PPM	ELEMENT	CONCENTRATION, PPM	ELEMENT	CONCENTRATION, PPM
AG	< .50	AL	60.00	B	4.00
BA	20.00	BE	< .50	BI	< 2.00
CA	400.00	CD	< 10.00	CE	< 80.00
CO	< 4.00	CR	< 10.00	CS	< 100.00
CU	< 1.00	DY	< 20.00	ER	< 6.00
EU	< 10.00	FE	60.00	GD	< 10.00
HF	< 20.00	HO	< 10.00	IN	< 1.00
K	60.00	LA	< 10.00	LI	8.00
LU	< .50	MG	4.00	MN	< 1.00
MO	< 1.00	NA	20.00	NB	< 6.00
ND	< 200.00	NI	< 4.00	P	< 100.00
PB	< 6.00	PR	< 100.00	RB	< 40.00
SB	< 8.00	SC	< 1.00	SI	100.00
SM	< 100.00	SN	< 6.00	SR	< 40.00
TA	< 40.00	TB	< 40.00	TI	100.00
TL	< 20.00	TM	< 4.00	V	20.00
W	< 40.00	YB	< 10.00	ZN	< 20.00
ZR	< .50				

CONCENTRATION BASED ON ORGINAL SAMPLE BEFORE DILUTION WITH DILUENT
> MEANS GREATER THAN
< MEANS LESS THAN THE SENSITIVITYOF THE SPECTROGRAPHIC PROCEDURE USED
RESULTS ARE CORRECT WITHIN A FACTOR OF 40% , (ONE STANDARD DEVIATION)

TABLE 11-27
ASH AND SULFUR CONTENT OF 2020 GRAPHITE, LOG 8464-110

Element (ppm)	Slab 1[a]		Slab 6[a]	
	L16B[b]	L28B	L64B	L76B
Ash	2000	1900	1100	1200
Sulfur	25	12	10	12
	21	13	11	11

[a] Slab 1 was from the top of the log and slab 6 from the center.

[b] Specimen number; the B signifies it is the B half, or bottom specimen, from the specimen core.

TABLE 11-28
FATIGUE TESTS ON PGX GRAPHITE
CONTROL TENSILE TESTS

LOT NO: -- LOG NO: 6484-74
ORIENTATION: RADIAL LOCATION: END-ONE THIRD RADIUS

CONTROL TENSILE TESTS

SPECIMEN NO.	DENSITY (KG/M**3)	DIA. (MM)	FRACTURE LOAD (KN)	TENSILE STRENGTH (MPA)
1A	1.766	12.69	1.21	9.6
3B	1.765	12.69	1.29	10.2
5C	1.762	12.70	1.37	10.8
7D	1.760	12.70	1.34	10.6
9A	1.761	12.70	1.26	10.0
11B	1.768	12.71	1.26	9.9
13C	1.763	12.71	1.16	9.1
15D	1.754	12.70	1.29	10.2
17A	1.761	12.70	1.21	9.5
19B	1.754	12.70	1.26	10.0
21C	1.756	12.70	1.31	10.4
23D	1.765	12.70	1.26	10.0
25A	1.745	12.70	1.05	8.3
27B	1.762	12.70	1.31	10.4
29C	1.756	12.70	1.21	9.5
31D	1.769	12.70	.79	6.2
33A	1.759	12.70	1.16	9.1
35B	1.762	12.70	1.24	9.8
37C	1.757	12.70	1.18	9.3
39D	1.770	12.70	1.00	7.9
41A	1.761	12.70	1.31	10.4
43B	1.762	12.70	1.34	10.6
45C	1.764	12.70	1.00	7.9
47D	1.757	12.70	1.31	10.4
49A	1.756	12.70	1.16	9.1
51B	1.772	12.68	1.18	9.4
53C	1.763	12.68	1.26	10.0
55D	1.760	12.68	1.31	10.4
57A	1.763	12.70	1.24	9.7
59B	1.758	12.70	1.16	9.1
61C	1.755	12.71	1.16	9.1
63D	1.769	12.68	1.10	8.7
65A	1.757	12.70	1.03	8.1
67B	1.770	12.68	1.21	9.6
69C	1.762	12.68	1.10	8.7
MEAN:	1.761		MEAN:	9.5 MPA (1376.PSI)
STD. DEV:	.006		STD. DEV:	1.0 MPA (139.PSI)

TABLE 11-29
FATIGUE TESTS ON PGX GRAPHITE
STRESS RATIO, R = 0

LOT NO: ** LOG NO: 6484-74
ORIENTATION: RADIAL LOCATION: END-ONE THIRD RADIUS

STRESS RATIO, R (MIN. STRESS / MAX. STRESS): .0

SPECIMEN NO.	DENSITY (KG/M**3)	MAX. STRESS (MPA)	MIN. STRESS (MPA)	CYCLES TO FAILURE
13B	1.765	6.6	.0	>141200 (RUNOUT)
7C	1.759	6.6	.0	>123100 (RUNOUT)
59C	1.761	6.6	.0	>182700 (RUNOUT)
27D	1.756	6.6	.0	>145100 (RUNOUT)
45A	1.760	6.6	.0	>163300 (RUNOUT)
39B	1.760	6.6	.0	>121200 (RUNOUT)
35C	1.758	6.6	.0	>100400 (RUNOUT)
19A	1.756	6.6	.0	>135400 (RUNOUT)
1D	1.769	6.7	.0	>100400 (RUNOUT)
53D	1.770	6.7	.0	>118300 (RUNOUT)
13A	1.760	7.5	.0	3800
61B	1.761	7.5	.0	>102000 (RUNOUT)
7B	1.762	7.5	.0	>302700 (RUNOUT)
21D	1.763	7.5	.0	>337800 (RUNOUT)
27C	1.757	7.5	.0	>118500 (RUNOUT)
49D	1.757	7.5	.0	>101900 (RUNOUT)
39A	1.758	7.5	.0	>118300 (RUNOUT)
33B	1.770	7.5	.0	>109800 (RUNOUT)
1C	1.770	7.5	.0	>135600 (RUNOUT)
55C	1.767	7.5	.0	11600
7A	1.752	8.7	.0	170
61A	1.755	8.7	.0	746
17D	1.760	8.7	.0	29
35A	1.753	8.7	.0	1748
25C	1.764	8.7	.0	3
29B	1.761	8.7	.0	168
49C	1.754	8.7	.0	286
43D	1.758	8.7	.0	69
1B	1.762	8.7	.0	1165
55B	1.774	8.7	.0	48
65D	1.766	9.1	.0	2
29A	1.766	9.1	.0	< 1 (FIRST CYCLE)
3A	1.765	9.1	.0	< 1 (FIRST CYCLE)
11D	1.763	9.5	.0	1
17C	1.761	9.5	.0	75
25B	1.764	9.5	.0	27
45C	1.758	9.5	.0	9
37D	1.758	9.5	.0	36
49B	1.760	9.5	.0	29
55A	1.768	9.6	.0	3

TABLE 11-30
DATA FOR AXIAL POSITION 5

Power Day	Heat Generation[a] (MW/m^3)		Conductivity ($W/m \cdot K$)		Conductance ($W/m^2 \cdot K$) Sleeve-Graphite	Gap Length, Fuel-Graphite (mm)	Coolant Temp (K)	Film Coeff. ($W/m^2 \cdot K$)
	Fuel	Sleeve or Graphite	Fuel	Sleeve or Graphite				
435	31.9	0.79	9.67	79.9	1926	0.17	631	1094
581	35.2	0.88	7.87	32.3	2052	0.168	650	1138
662	40.5	1.01	7.47	23.4	2220	0.163	660	1161
713	38.6	0.96	7.28	21.3	2182	0.165	651	1178
812	40.3	1.00	7.04	18.9	2286	0.16	651	1176

[a] All of the numbers under this heading in Table 11-25 of the previous quarterly report (Ref. 11-4) were in error by a factor of 10^4. The correct heat generation rates can be obtained by dividing the numbers in Table 11-25 of Ref. 11-4 by 10^4.

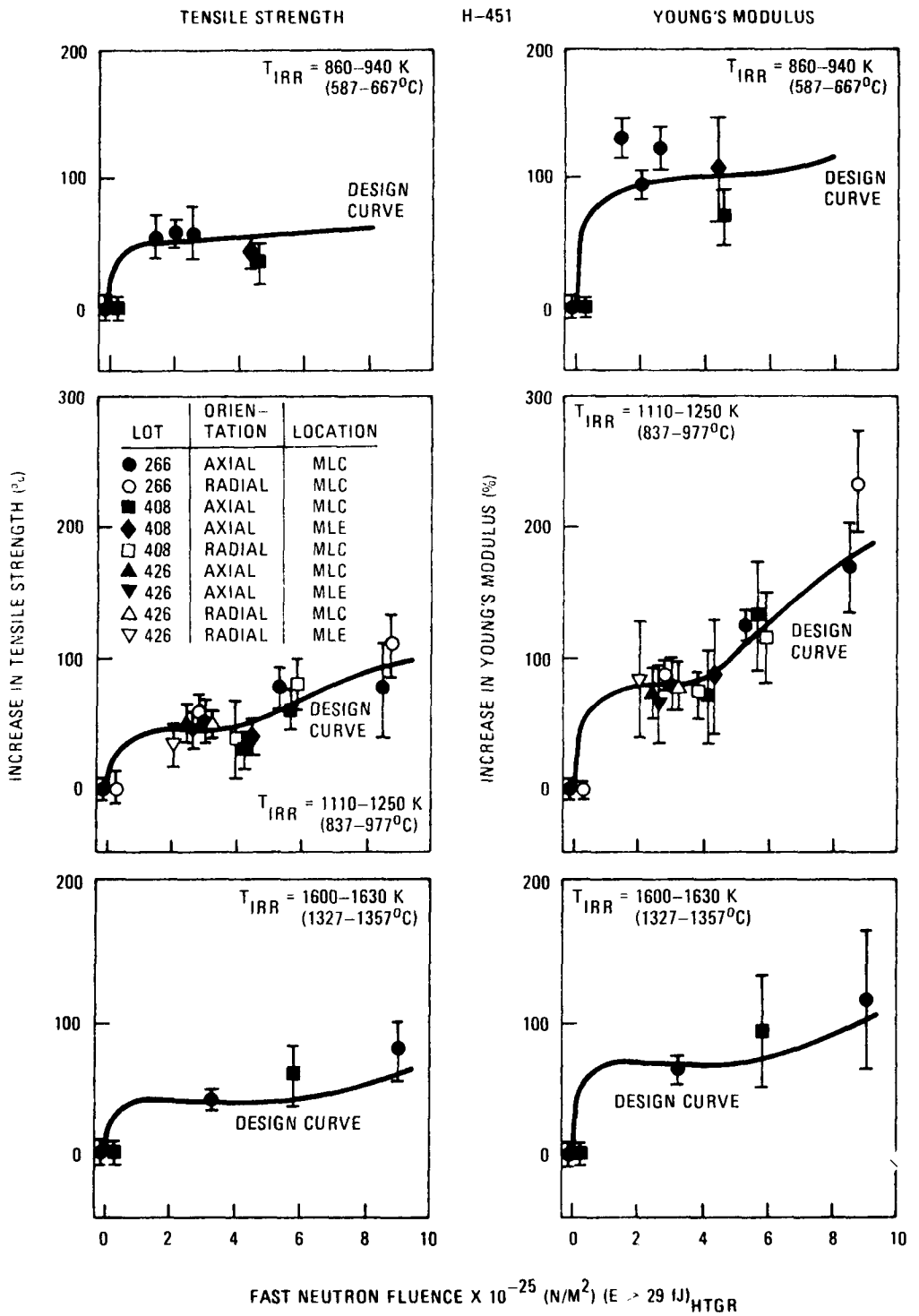

Fig. 11-1. Tensile strength and Young's modulus of H-451 graphite as a function of fast neutron fluence. Error bars denote plus or minus one standard deviation.

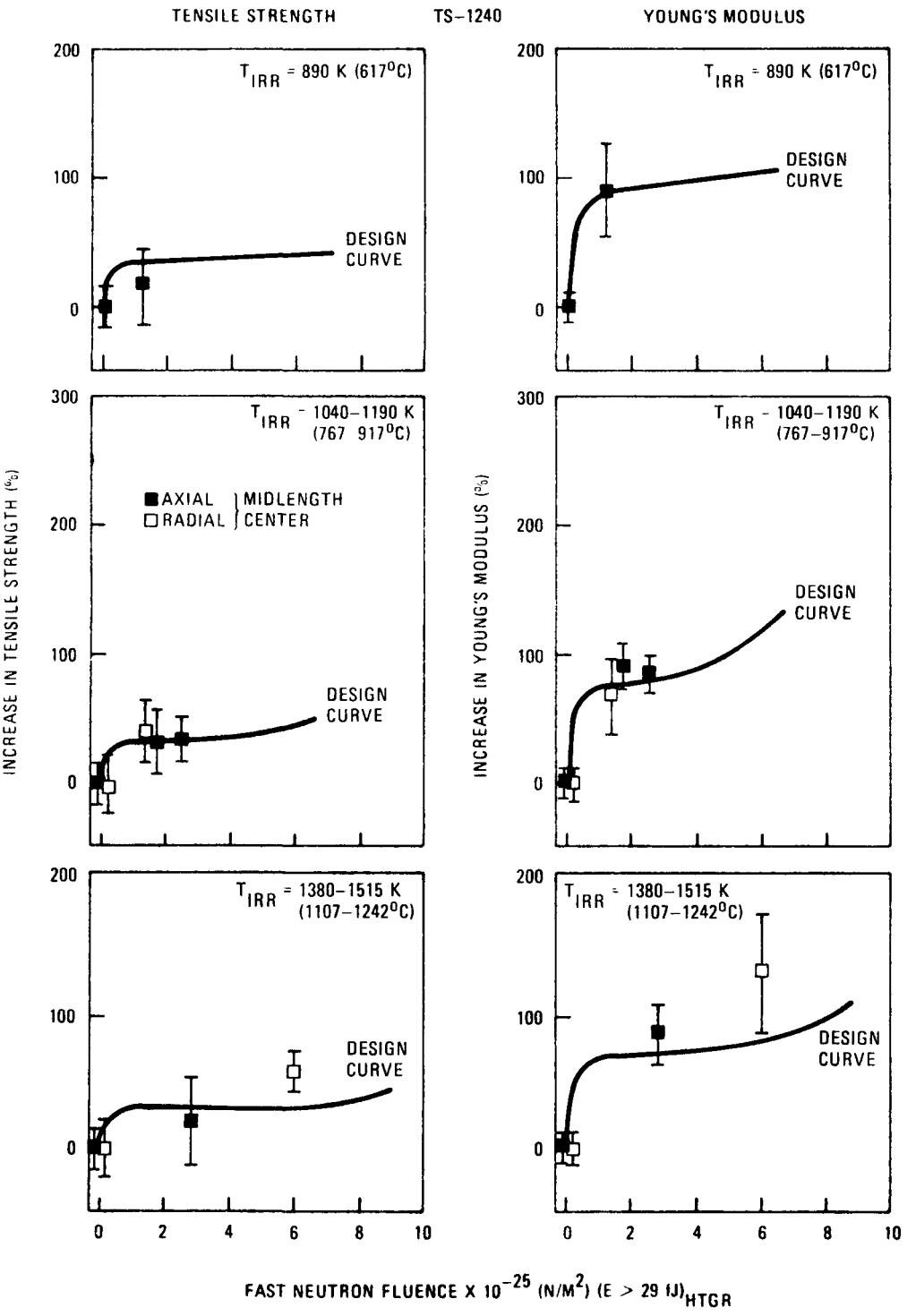

Fig. 11-2. Tensile strength and Young's modulus of TS-1240 graphite as a function of fast neutron fluence. Error bars denote plus or minus one standard deviation.

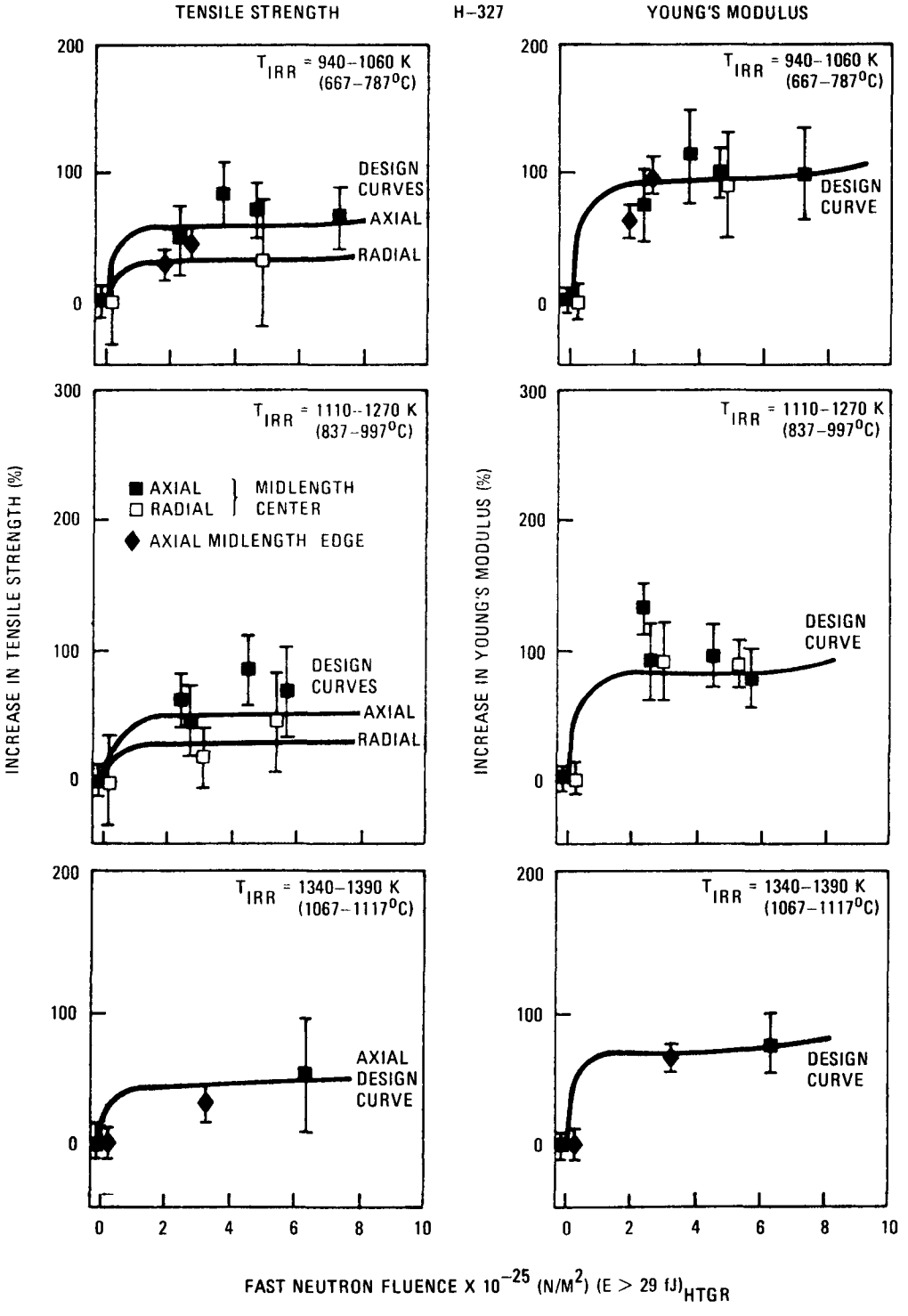

Fig. 11-3. Tensile strength and Young's modulus of H-327 graphite as a function of fast neutron fluence. Error bars denote plus or minus one standard deviation.

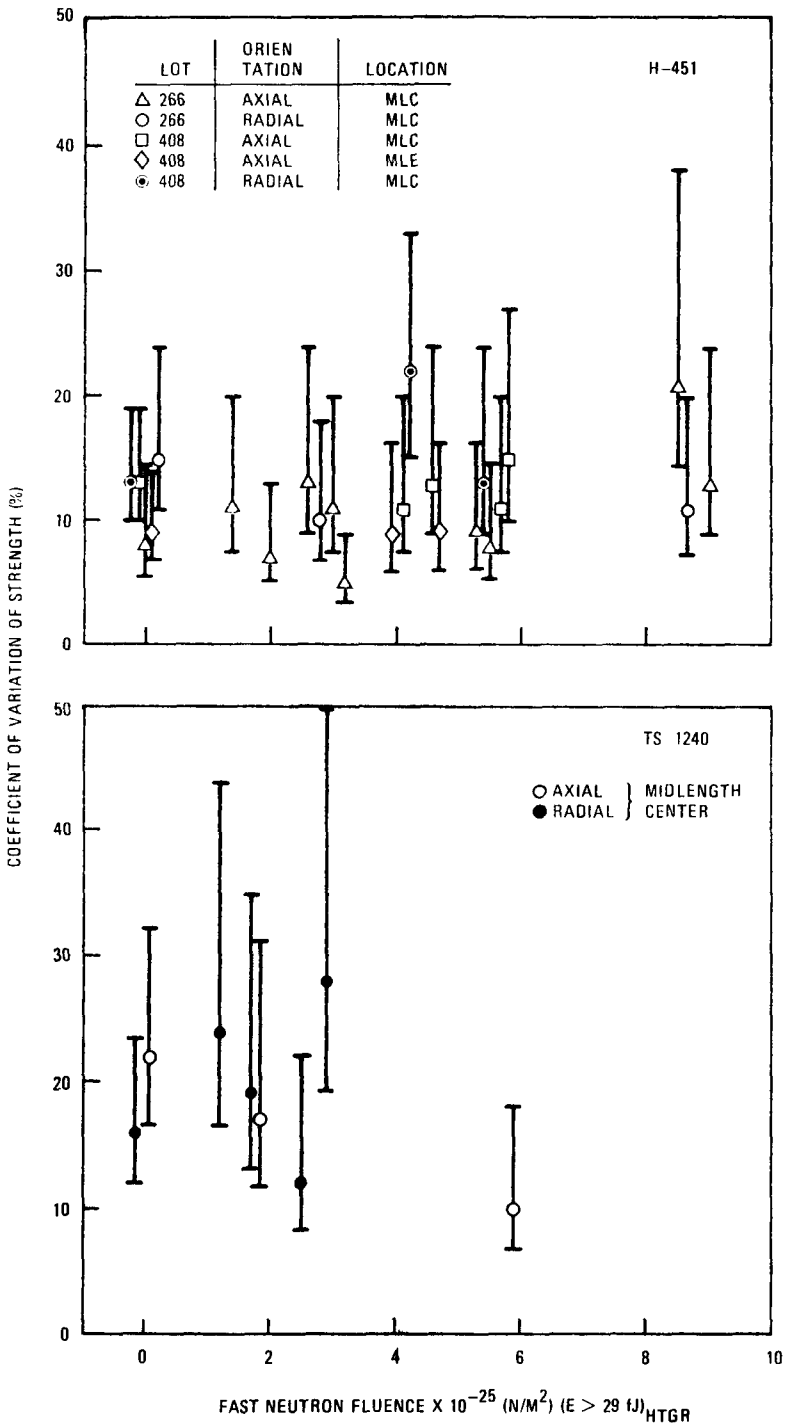

Fig. 11-4. Coefficient of variation of the tensile strength of H-451 and TS-1240 graphites as a function of fast neutron fluence. Error bars denote 95% confidence interval.

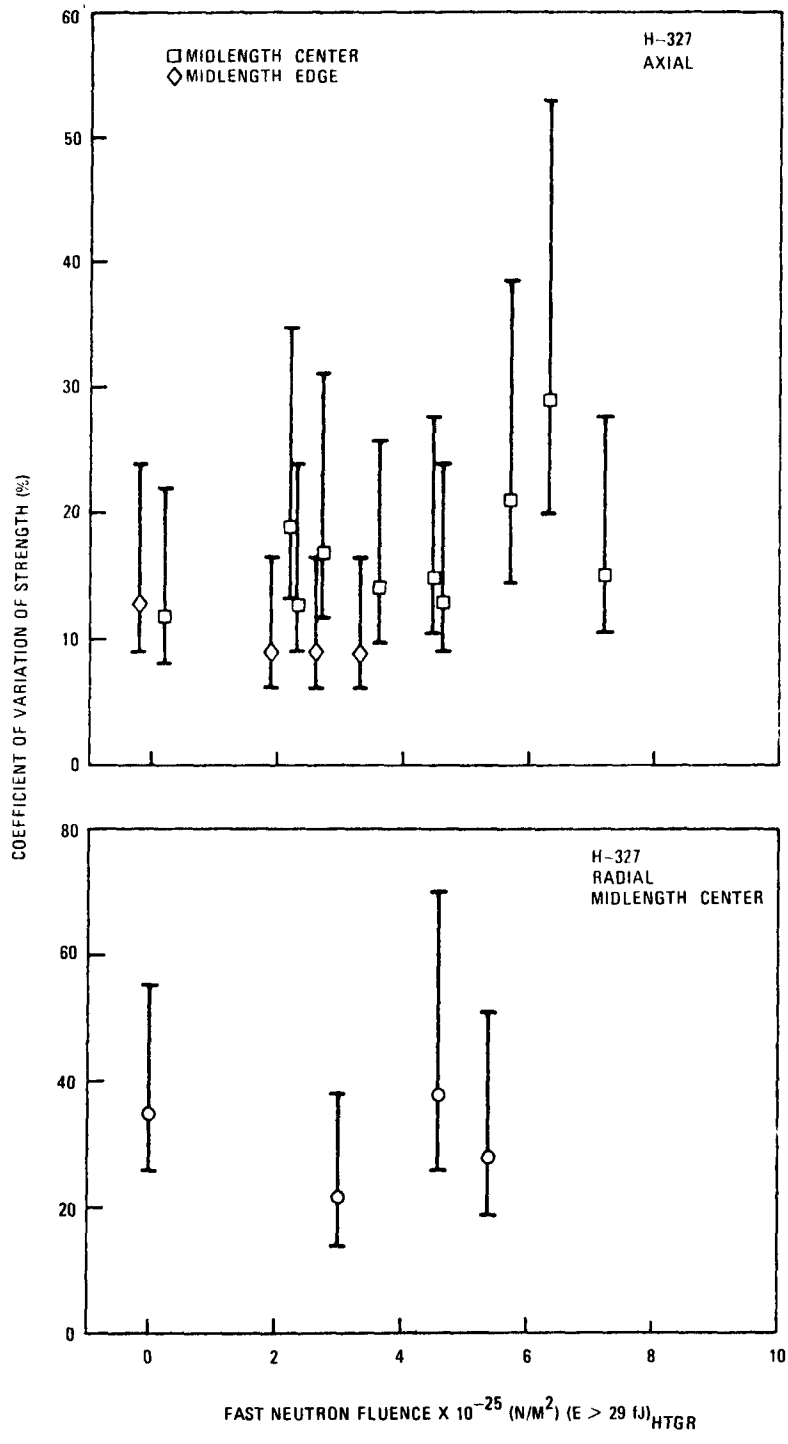

Fig. 11-5. Coefficient of variation of the tensile strength of H-327 graphite as a function of fast neutron fluence. Error bars denote 95% confidence interval.

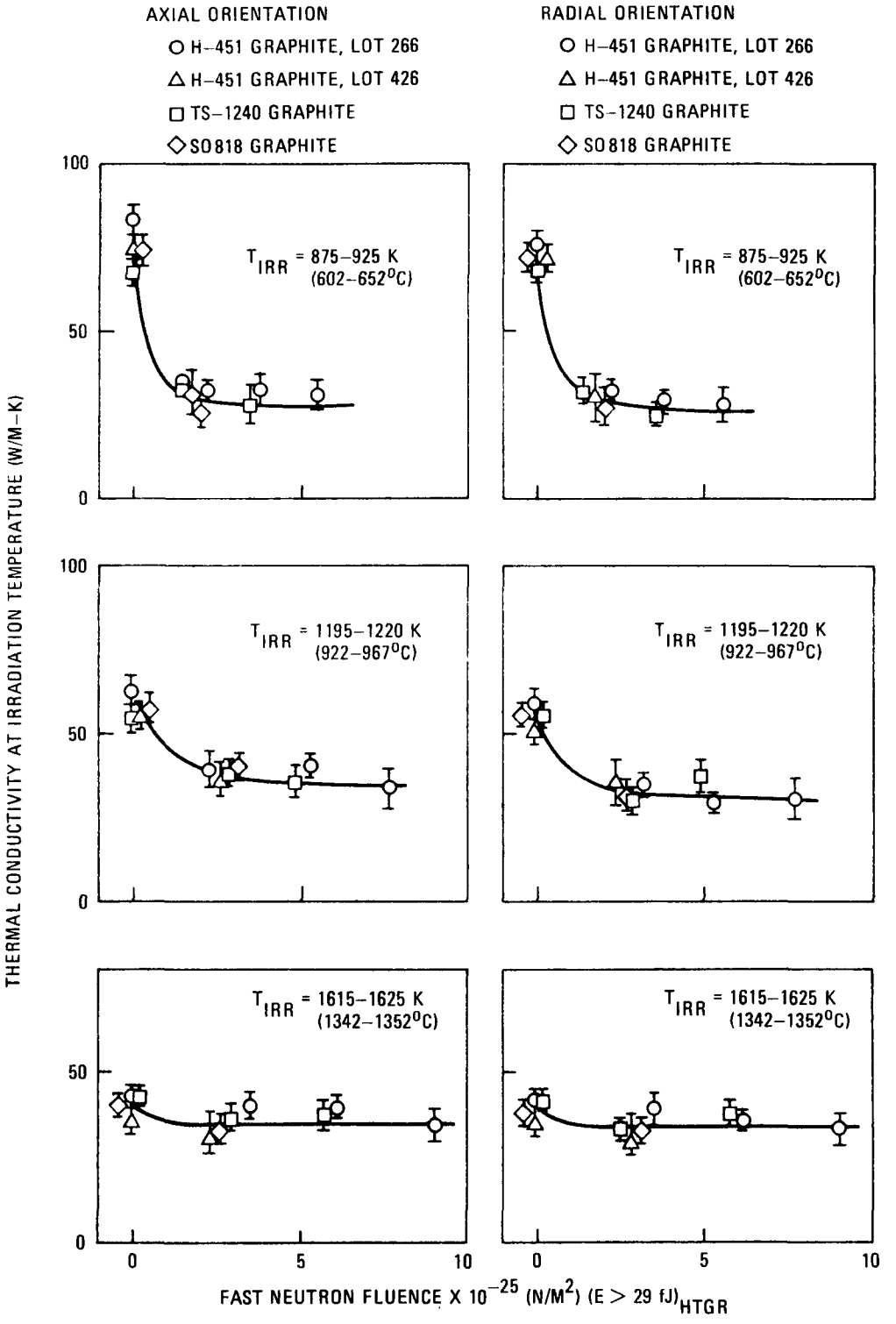

Fig. 11-6. Thermal conductivity at the irradiation temperature of near-isotropic graphites H-451, TS-1240, and SO818 as a function of fast neutron fluence. Error bars indicate plus or minus one standard deviation.

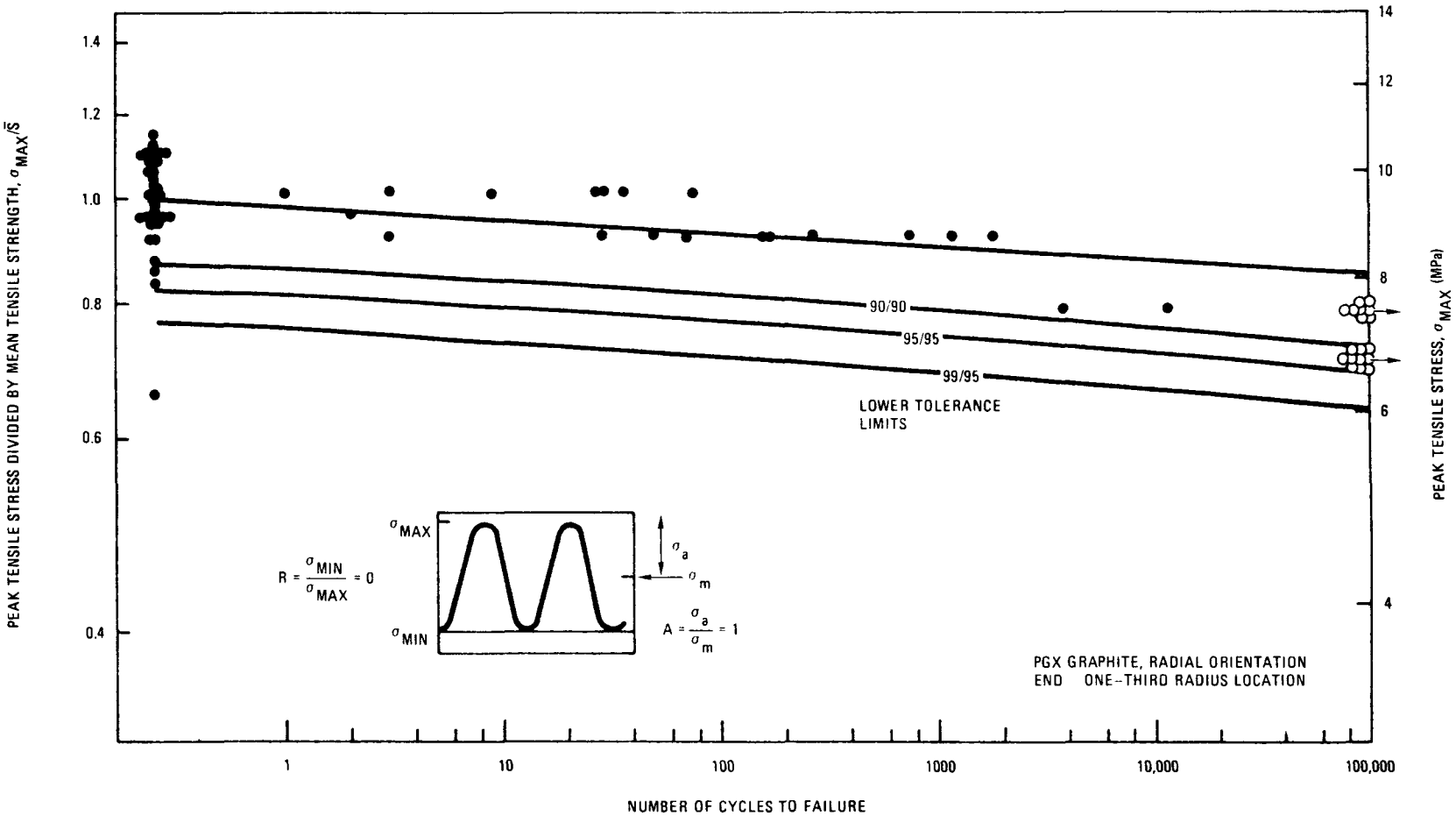

Fig. 11-7. Fatigue test data for PGX graphite, radial orientation, end - one-third radius location, in air at ambient temperature. Log-log plot of normalized maximum stress versus number of cycles to failure with stress ratio R = 0. Lower x/y tolerance limits represent the limits above which at least x% of the points fall, with y% confidence. Open circles represent runouts.

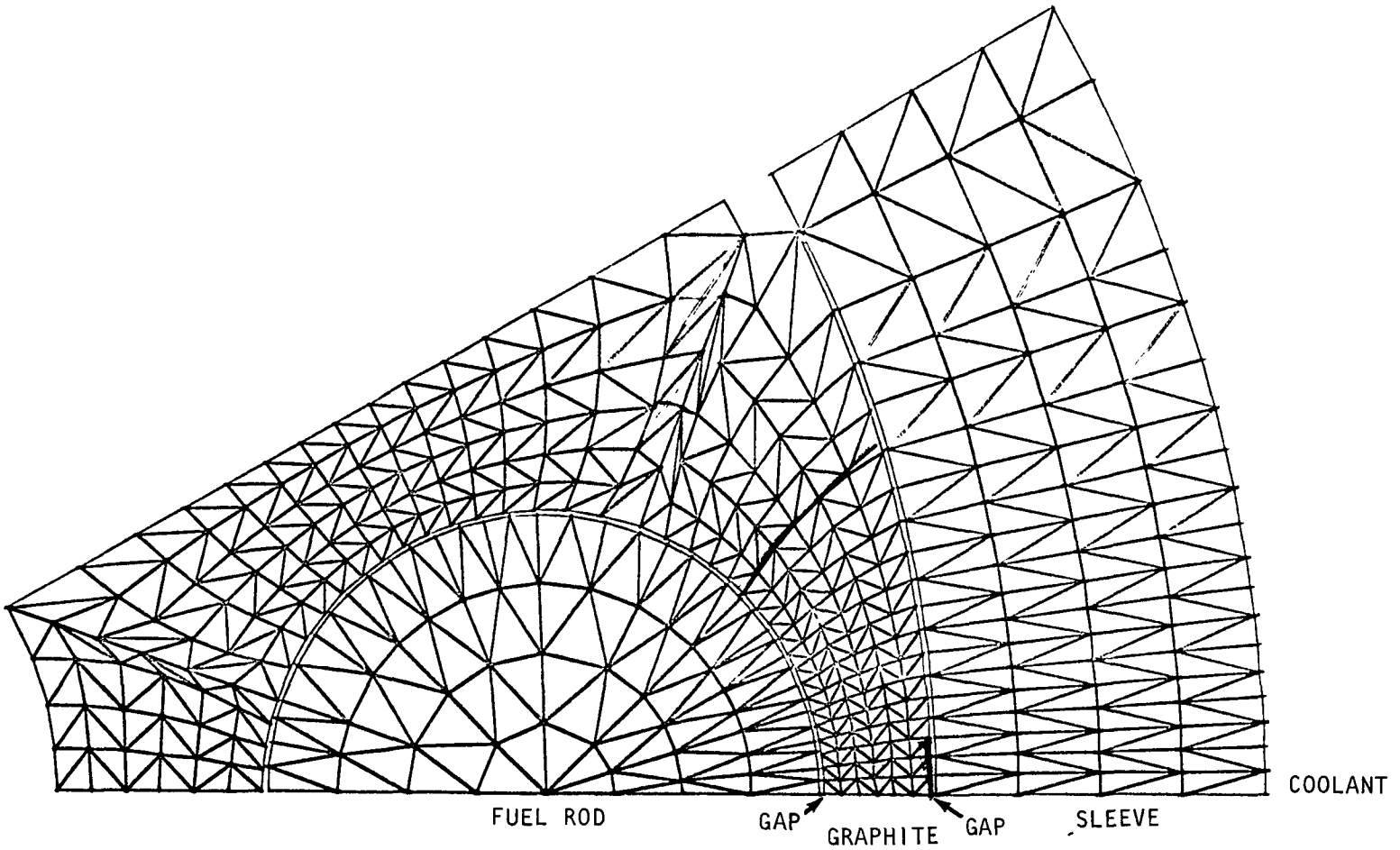

Fig. 11-8. Finite element model for residual stress analysis

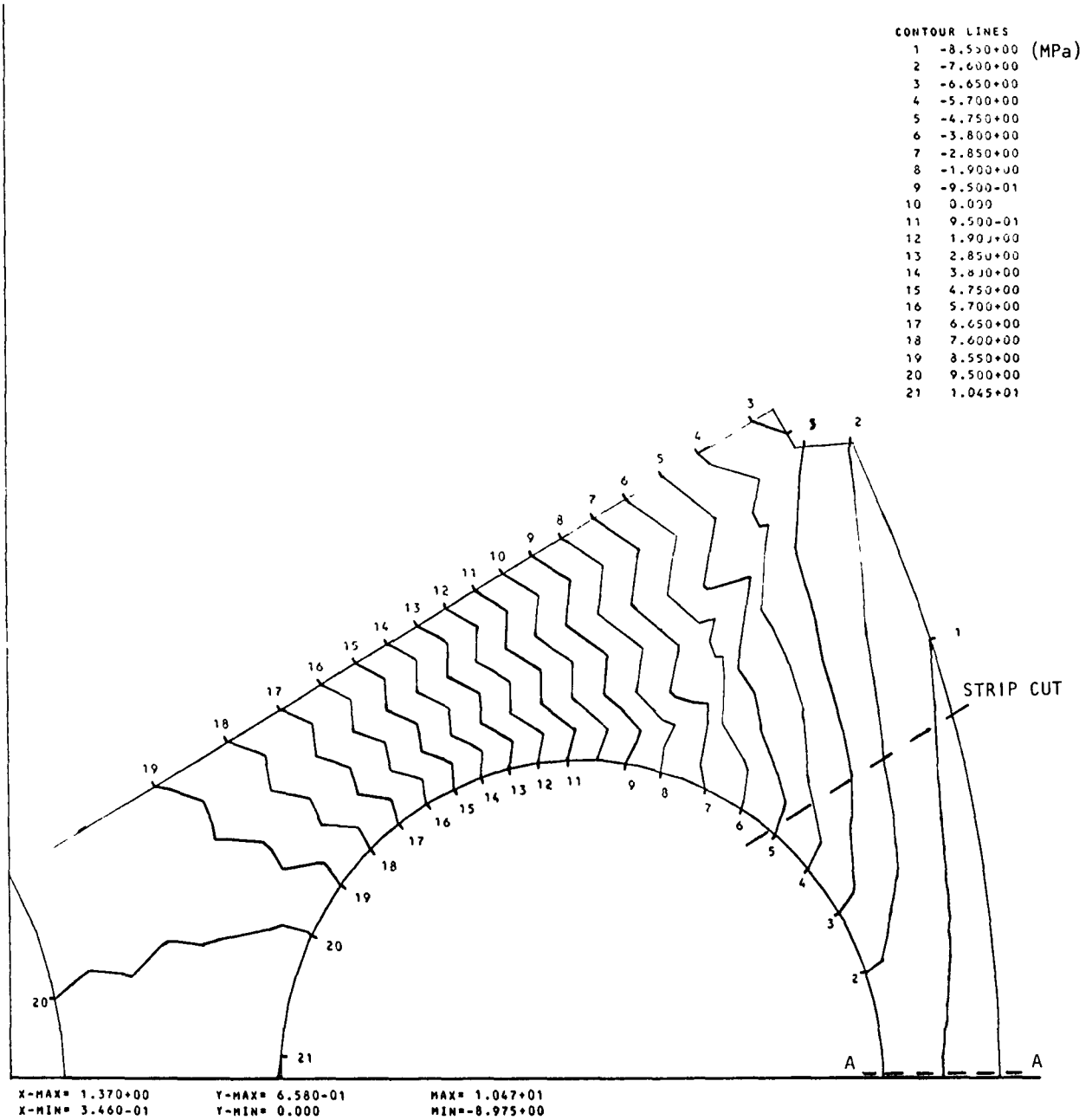

Fig. 11-9. Residual axial stress for FTE-14 at axial position 5

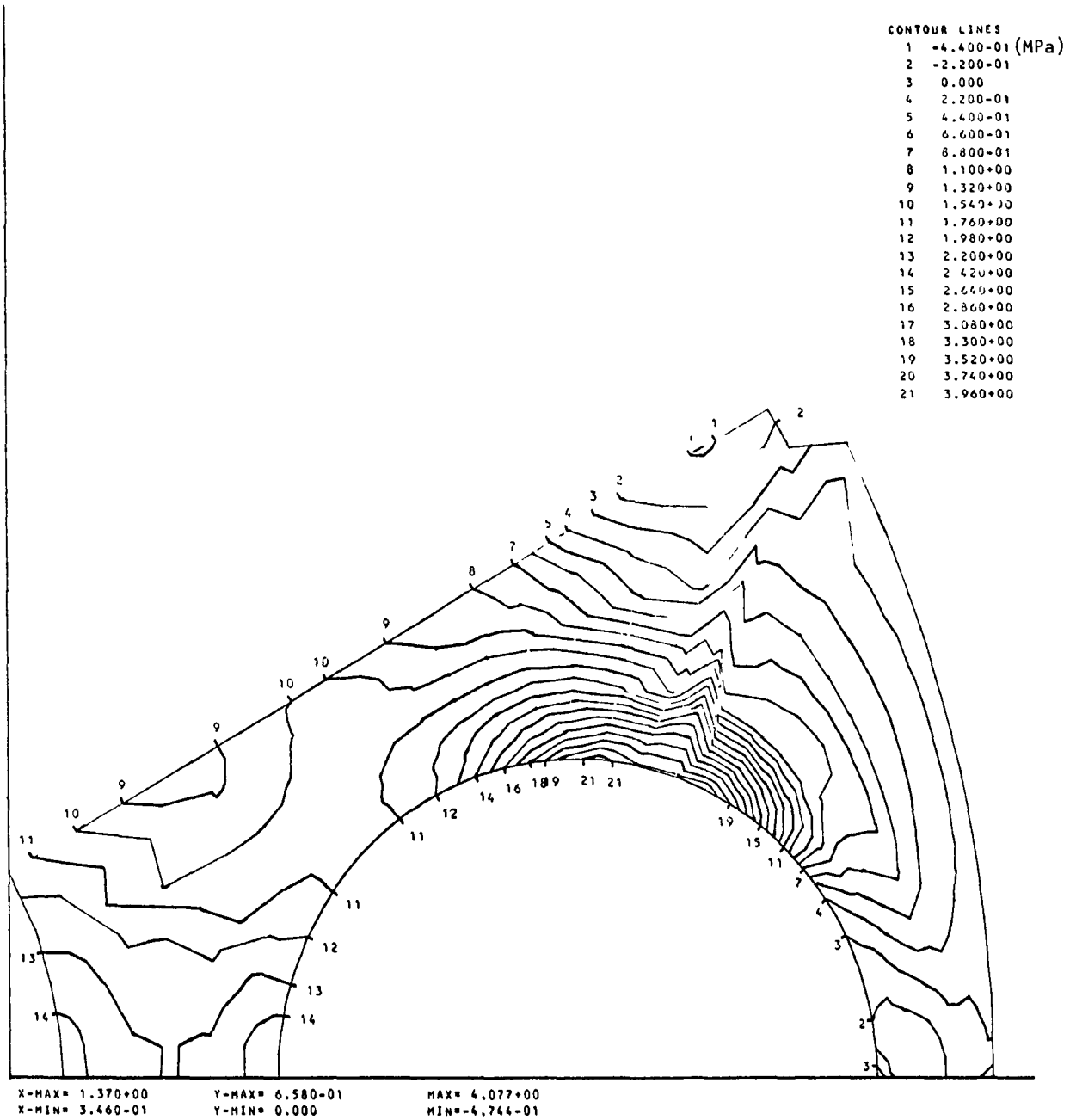

Fig. 11-10. Residual stress, $\sigma_{\text{max principal}}$, for FTE-14 at axial position 5

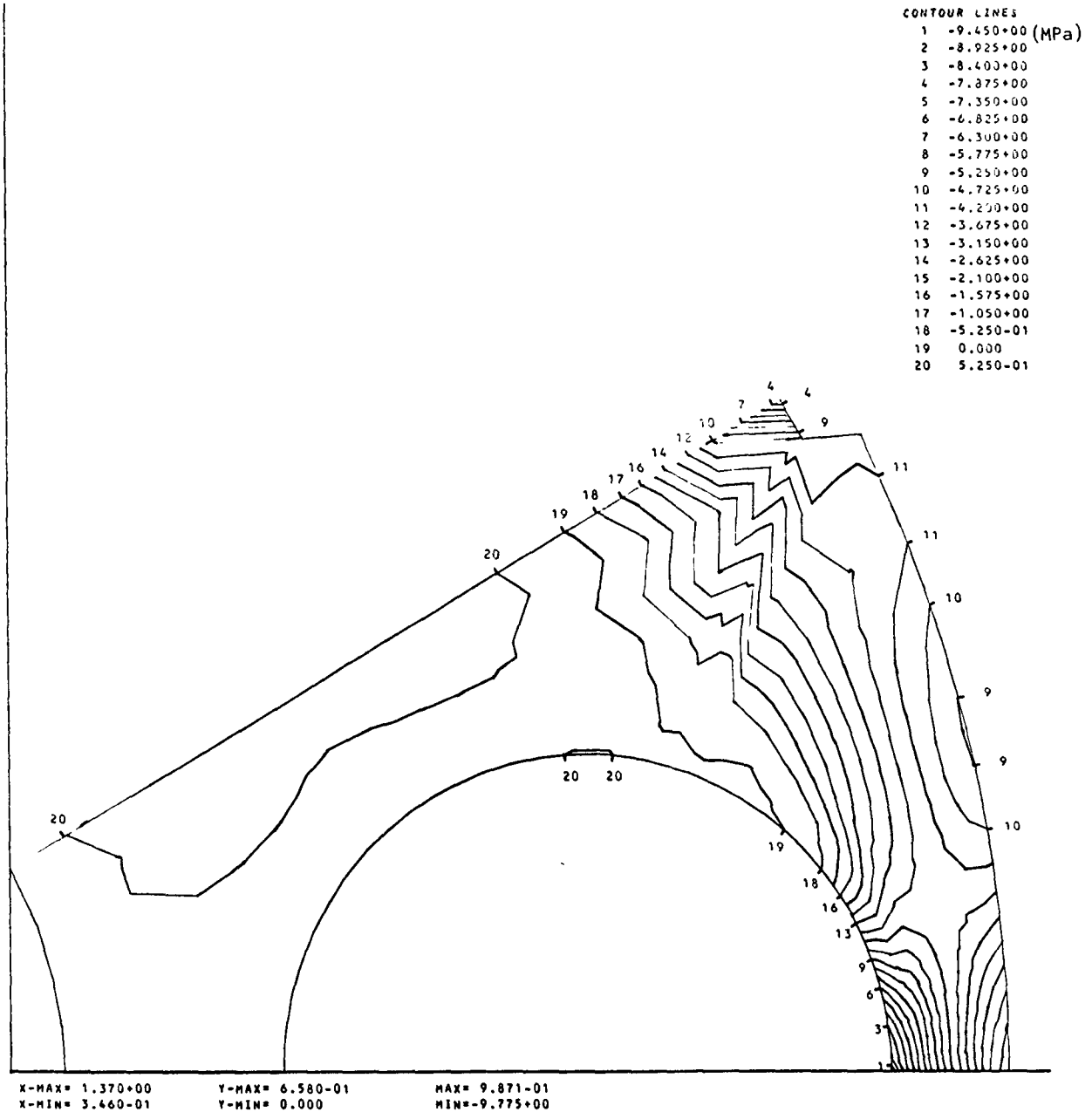

Fig. 11-11. Residual stress, $\sigma_{\text{min principal}}$, for FTE-14 at axial position 5

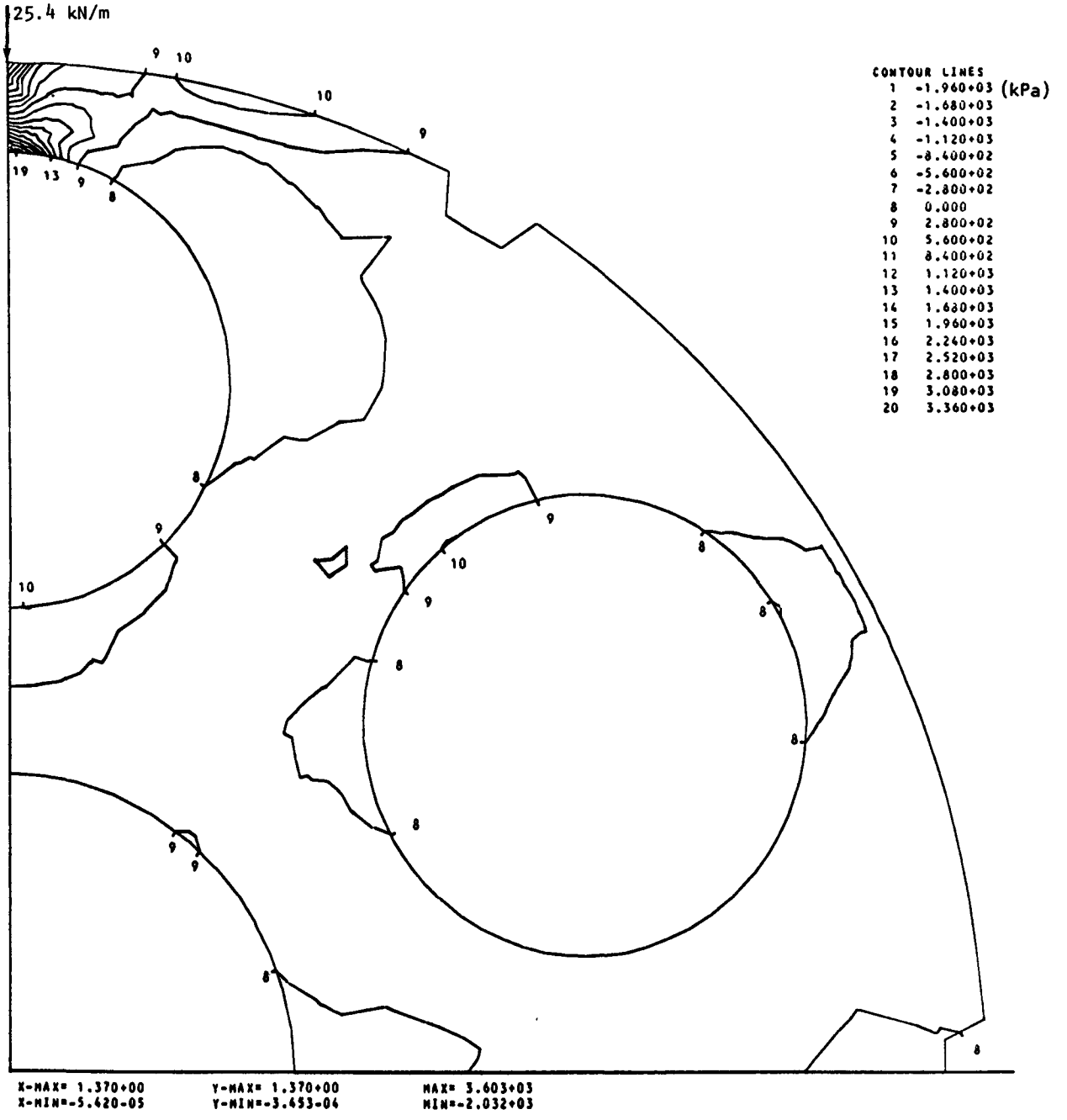

Fig. 11-12. Maximum principal stress contour under 25.4 kN/m compression load

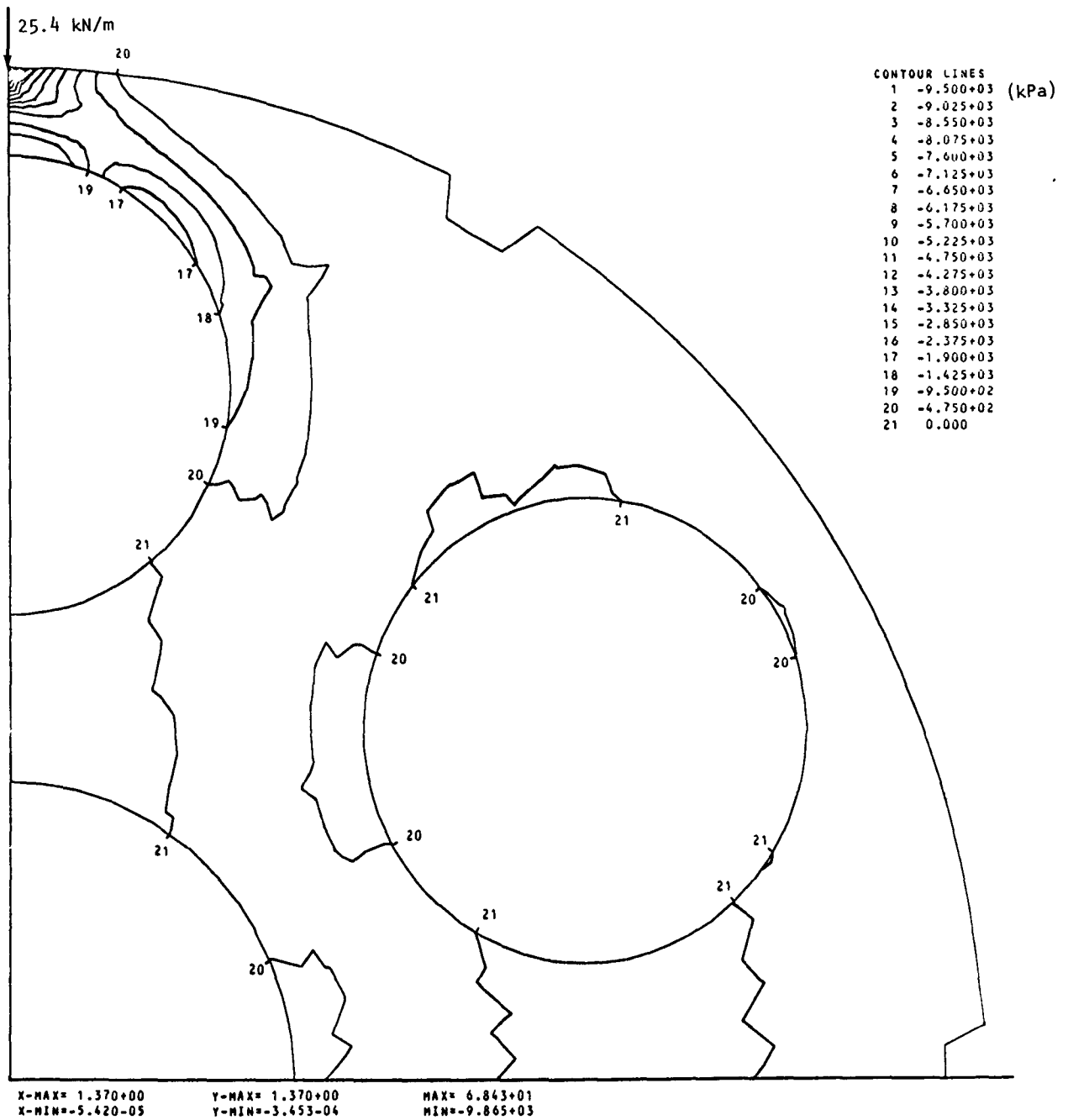

Fig. 11-13. Minimum principal stress contour under 25.4 kN/m compression load

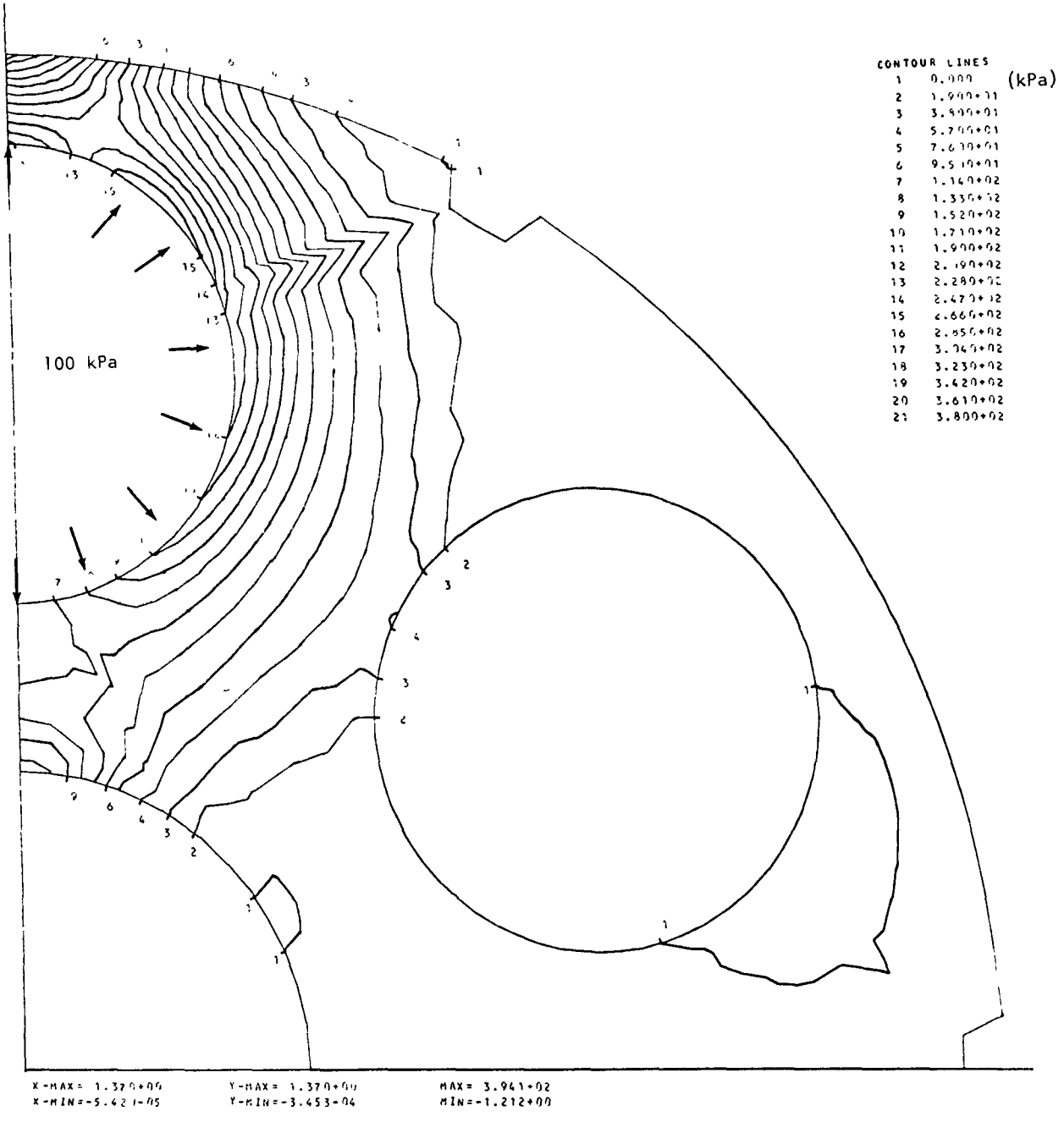

Fig. 11-14. Maximum principal stress under 100-kPa pressure loading

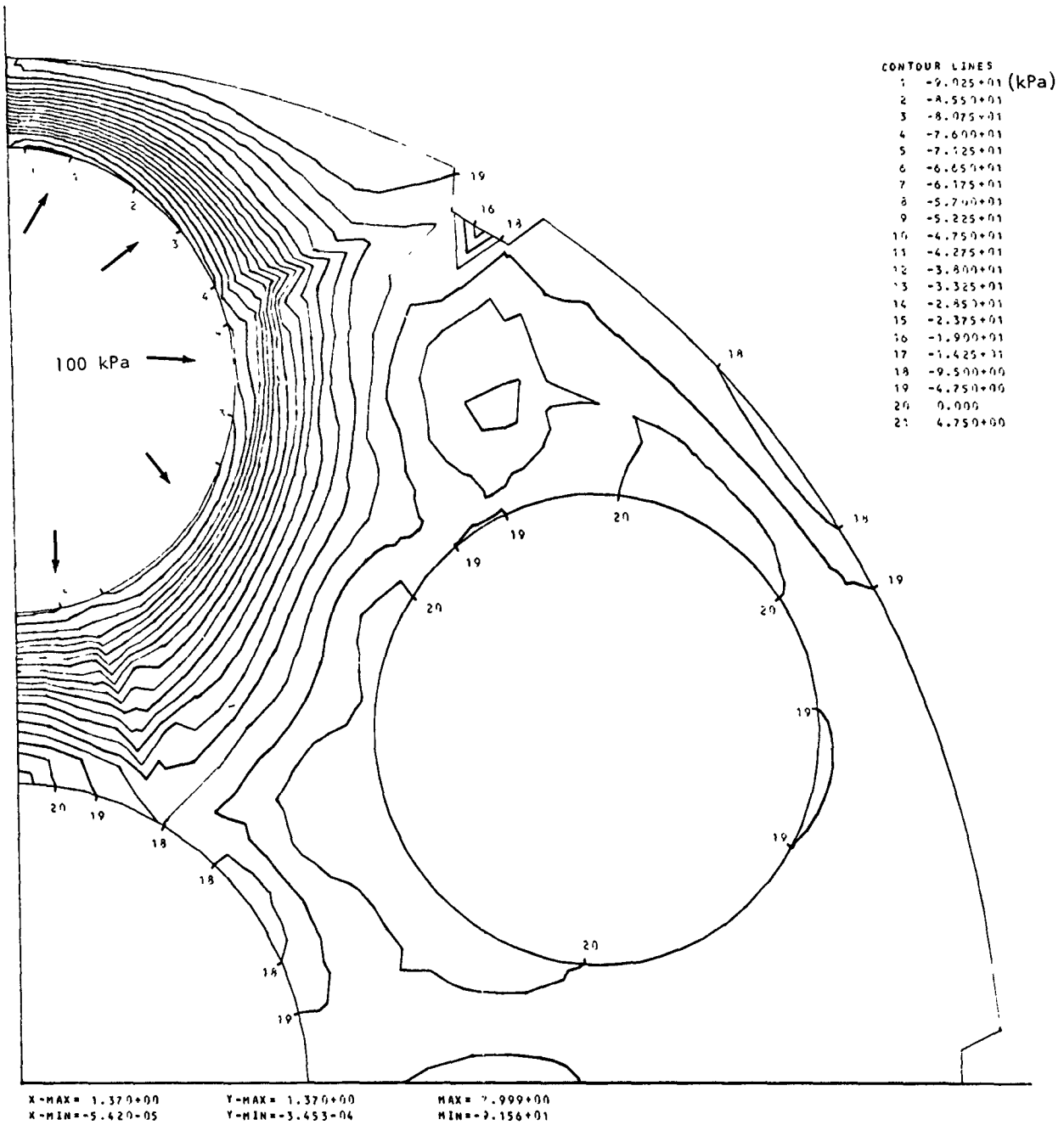

Fig. 11-15. Minimum principal stress under 100-kPa pressure loading

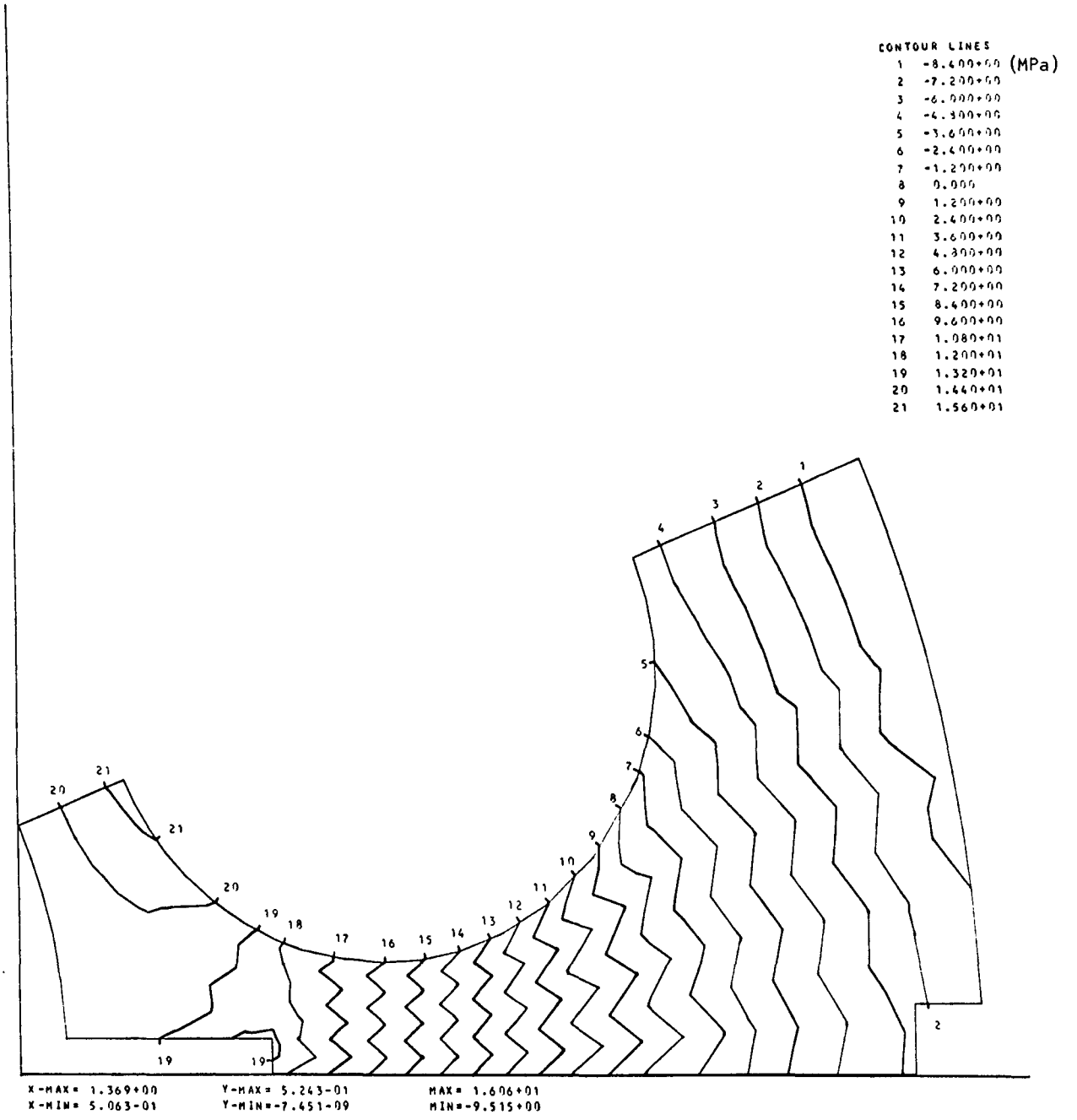

Fig. 11-16. Axial stress for FTE-4 with revised graphite properties

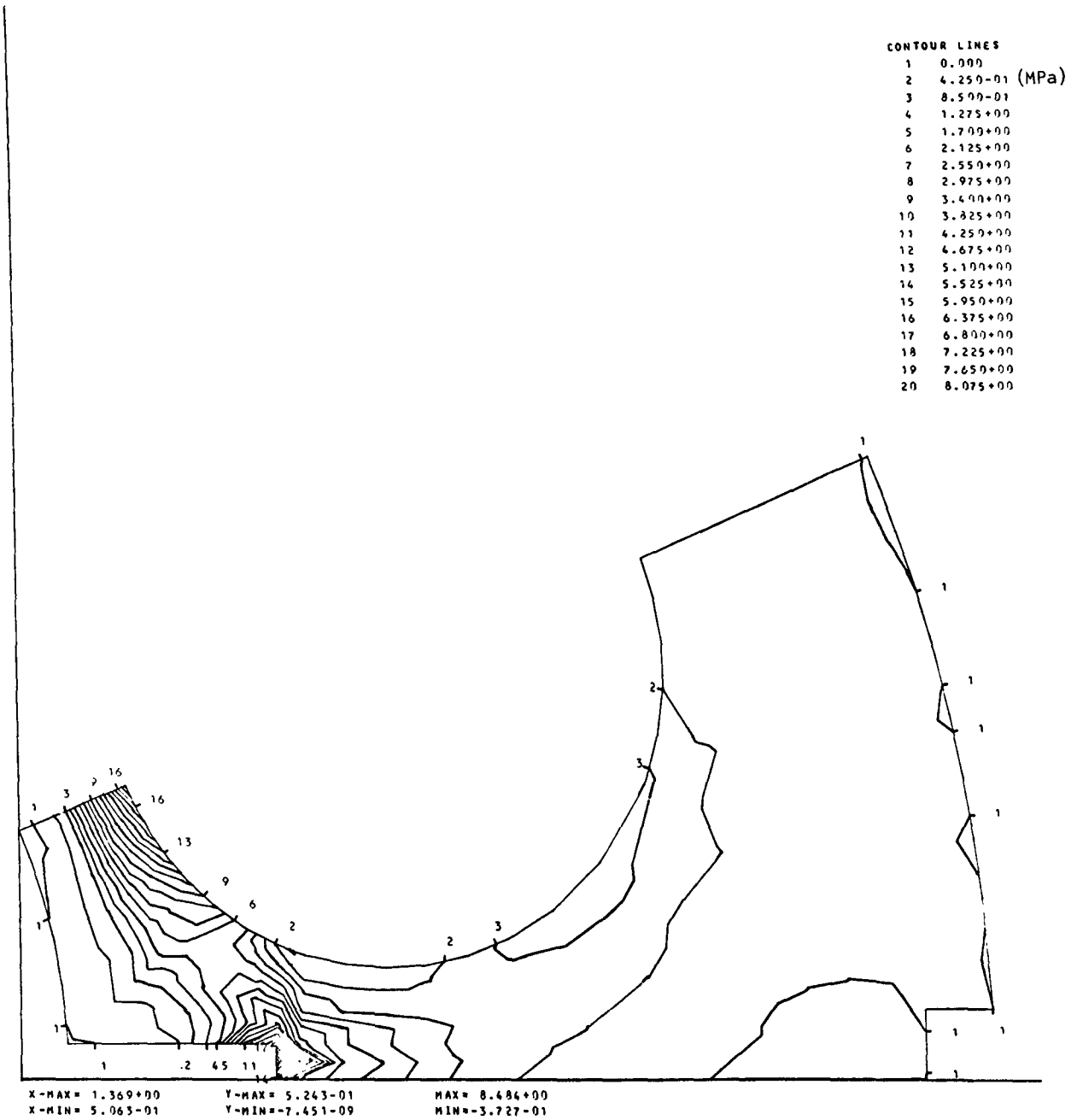

Fig. 11-17. Maximum principal in-plane stress for FTE-4 with revised graphite properties

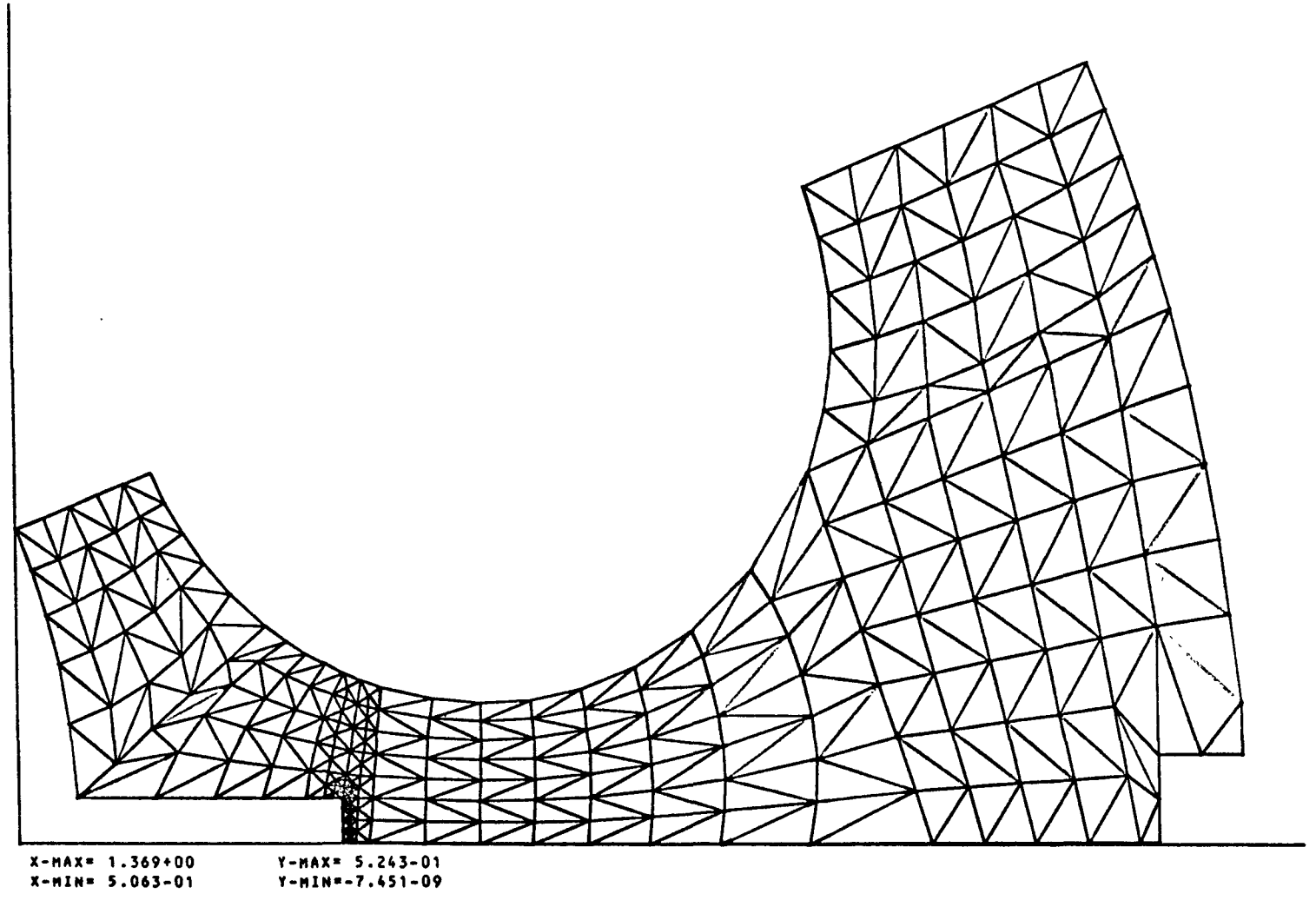

Fig. 11-18. Finite element mesh with refined mesh at slot

Fig. 11-19. Maximum principal in-plane stress for FTE-4 calculated with refined mesh

APPENDIX
TOPICAL REPORTS PUBLISHED DURING THE QUARTER

Price, R. J., "Statistical Study of the Strength of Near-Isotropic Graphite," ERDA Report GA-A13955, General Atomic, May 24, 1976.